Negative Hydrogen Ions in a Helicon Plasma Source

Riccardo AGNELLO

Abstract

There is nowadays a large interest to employ helicon plasmas as sources of negative ions for Neutral Beam Injectors (NBIs). Helicon plasma sources offer a number of advantages compared to current Inductive Couple Plasma (ICP) negative ions source, such as high energy efficiency, high plasma density production, low electron temperature and a considerable amount of H^- and D^- produced through volumetric processes, without caesium. Therefore, helicon plasma sources are promising candidates to be employed as a negative ion source for future NBIs, such as in DEMO, a next generation tokamak closer to commercial devices. However, many physics and technical aspects of helicon plasmas have to be deeply investigated, before their possible integration in future NBIs.

The goal of this thesis is to advance the understanding of the physics of helicon-based negative ion sources in the helicon plasma source RAID (Resonant Antenna Ion Device) at the Swiss Plasma Center of École Polytéchnique Fédérale de Lausanne, Switzerland. The investigations are carried out by employing a variety of diagnostics, and the results are interpreted and compared to numerical models.

To investigate the negative ion production we have extensively developed two negative ion diagnostics: the Cavity Ring-Down Spectroscopy (CRDS), to the best of the author's knowledge, for the first time in a helicon plasma device, and the Langmuir Probe assisted laser photodetachment. The combined use of the two techniques shows that H^- and D^- ions are distributed in a shell around the plasma column with densities of $2 \times 10^{16}\,\mathrm{m}^{-3}$ with only a few kW power, in a Cs-free plasma. These results show that helicon plasma columns have a hot core favorable for the ro-vibrational excitation of H_2 molecules and a cooler edge where slow electrons (<1 eV) can attach to rovibrationally excited H_2, a process known as *dissociative attachment*, and produce H^- in the plasma volume. The elongated plasma column would be suitable for the extraction of negative ion blade-like beams, which are adapted to photoneutralization systems.

To characterize the plasma we used Langmuir Probes (LPs), microwave interferometry and Thomson Scattering (TS) diagnostics. A two-axis LP system was employed to characterize the plasma column in several conditions of input power, magnetic field and neutral pressure. We have measured the characteristics of hydrogen and deuterium plasma discharges showing that these are typically density peaked on axis, reaching about $2 \times 10^{18}\mathrm{m}^{-3}$ with 3 kW power. Temperature profiles are also peaked reaching 7 eV in front of the antenna source and radially

Abstract

decaying to 1 eV at $r = 5\,cm$. To investigate high power plasma discharges, LPs are sometimes not robust enough, therefore, we developed a Thomson Scattering system to measure plasma density and temperature in Ar plasmas. These can attain density of $10^{19}\,m^{-3}$ and exhibit a bright "blue core", due to Ar ion emission which is as indirect signature of the propagation of helicon waves. The TS system developed on RAID will be employed to characterize the helicon plasma cell for AWAKE source at CERN which is one promising candidate for particle wake field acceleration.

The propagation of helicon waves and the power deposition mechanisms are not fully understood phenomena. We developed a movable B-dot probe to measure the helicon wave field. We confirmed that plasma is sustained by the propagation of the helicon wave and we performed measurements of the axial wavelength and we compared to a numerical model.

To better understand the characteristics of RAID helicon plasma, we have developed a hydrogen transport fluid model. The electron density and temperature profiles, measured by LPs and interferometry, are introduced as input parameters. The model takes into account a full chemistry reaction set, and the plasma transport in a magnetized collisional plasma. The model is then able to calculate the profiles of different plasma species such as H, H^+, H_2^+, H_3^+ and H^-, showing a qualitatively good agreement with the experimental results.

This work broadens our knowledge of helicon plasma sources by exploring the feasibility to employ helicon plasmas as sources of negative ions for NBIs and a provides some new interesting insights on helicon wave physics supported by numerical simulations.

Keywords: plasma physics, nuclear fusion, neutral beam injection (NBI), negative ions, helicon source, helicon waves, Langmuir probe, microwave interferometry, Cavity Ring-Down Spectroscopy (CRDS), Langmuir Probe Laser Photodetachment, Optical Emission Spectroscopy, Thomson Scattering, AWAKE project, B-dot probe, H model, plasma transport, negative ion extractor.

Résumé

Les sources plasma hélicon sont actuellement considérées comme une des directions possibles pour la production volumique d'ions negatifs pour les injecteurs de faisceaux atomiques en fusion nucléaire. Les sources hélicon possédent de nombreux avantages par rapport aux sources de plasma inductives conventionelles : grande efficacité énergetique, haute densité plasma, basse température électronique et production d'ions H$^-$ et D$^-$ sans recours au caesium. Les sources hélicon pourraient être employées pour la prochaine génération d'injecteurs de faisceaux atomiques, par exemple pour DEMO, le future réacteur à fusion destiné à la production d'électricité. Toutefois, nombreux défis techniques et de compréhension quant à la physique fondamentale des sources hélicon, demeurent.

Le but de ce travail de thèse est de progresser dans la compréhension de la physique des sources hélicon et des mechanismes de production d'ions negatifs dans ces dernières. Les mesures effectuées sur l'experience RAID (Resonant Antenna Ion Device) au Swiss Plasma Center de l'Ecole Polytéchnique Fédérale de Lausanne, ont impliqué la mise en oeuvre de différents diagnostiques plasma. Premiérment, nous avons développé deux techniques pour mesurer la densité produite d'ions négatifs dans des plasmas d'hydrogène et de deuterium : la *Spectroscopie Cavity Ring-Down (CRDS)*, jamais utilisée encore sur un plasma hélicon, et le *photodetachment avec sonde de Langmuir*. Le résultat le plus marquant est l'observation d'une distribution d'ions négatifs sur un anneau au bord de la colonne plasma. Leur densité atteint 2×10^{16}m^{-3} avec 3 kW de puissance RF et ce sans utilisation de cesium. Ce résultat s'explique par le fait que la colonne plasma présente un profil de temperature électronique très piqué, 5 eV au centre et < 1eV au bord, à 5 cm du centre. La zone centrale de temperature électronique élevée favorise l'excitation rovibrationelle de l'hydrogène moleculaire (H$_2$). Ces molecules excitées diffusent alors dans la zone de basse temperature électronique (<1eV), en bord de colonne, où le processus connu comme *association dissociative*, à l'origine de la production de H$^-$, est plus probable. Par ailleurs, la forme allongée du plasma est compatible avec l'extraction de faisceaux d'ions négatifs longs et fins, bien adaptée aux systèmes de photoneutralisation.

La caracterisation de la colonne de plasma a été effectuée par l'analyse de sondes de Langmuir, d'interferomètrie à microonde et de diffusion Thomson des électrons. Une sonde de Langmuir à deplacement bidirectionelle à été utilisée pour étudier l'ensemble de la colonne dans différentes conditions de puissance RF livré à l'antenne, de champs magnétiques et de pres-

sion du gas. Etant donné que les sondes de Langmuir n'arrivent pas à soutenir des courants électronique élevés sans être abîmées, nous avons mis en place un système de mesure de la densité et de la température électronique basé sur la mesure du spectre de diffusion Thomson des électrons. Ce système à été développé dans le cadre d'une collaboration avec le projet AWAKE au CERN, ayant pour objectif la caracterisation de la source helicon envisagée pour l'accélération des particules avec le plasma. Typiquement nous avons obtenu des décharges d'hydrogène ou de deuterium fortment piquées au centre de la colonne, avec des densités atteignant $2 \times 10^{18} \mathrm{m}^{-3}$ pour 3 kW de puissance RF.
Par ailleurs, l'utilisation d'une sonde magnetique à 3 composantes (sondes B-dot) a permis la mise en evidence indubitable de la progation d'ondes hélicon tout au long de la colonne.

Enfin, pour mieux comprendre le transport du plasma dans cette décharge, nous avons développé un modèle numerique fluide en symétrie cylindrique. Partant des profils experimentaux de densité et temperature électronique et en prenant en compte un ensemble de réactions chimiques assez complet, ce modèle fluide permet l'obtention des profiles d'équilibre de toutes les espèces ioniques et neutres.

Mots-cléfs : physique du plasma, fusion nucléaire, injection de faisceaux neutres, ions negatifs, source hélicon, ondes hélicon, sonde de Langmuir, interferometrie à microondes, Spectroscopie Cavity Ring-Down (CRDS), Laser Photodetachment avec sonde de Langmuir, Spectroscopie optique, Diffusion Thomson, projet AWAKE, sonde B-dot, model H, model 2D-Axysimmetrique, transport du plasma, exctracteur d'ions negatifs.

Sommario

Le sorgenti di plasmi helicon sono attualmente considerate come una possibile alternativa per la produzione di ioni negativi per la futura generazione di iniettori di fasci di particelle neutre, conosciuti come "Neutral Beam Injectors" (NBIs), nel contesto della fusione termonucleare controllata. Le sorgenti helicon posseggono numerosi vantaggi rispetto alle sorgenti convezionali ICP (Inductive Couple Plasmas) per la produzione di ioni negativi, tra questi annoveriamo: la migliore efficienza energetica, l'alta densità di plasma e la considerevole quantità di ioni H^- e D^- prodotti in volume senza l'utilizzo di cesio. Tali caratteristiche le renderebbero promettenti per lo sviluppo di una futura filiera di sorgenti di ioni negativi ad alta efficienza destinate al reattore DEMO, il primo prototipo di reattore a fusione in grado di produrre energia elettrica da fusione nucleare. Allo stato attuale, tuttavia, sussistono diversi aspetti di fisica di base delle helicon che non sono del tutto esplorati, senza parlare della possibile ingegnerizzazione di una sorgente helicon in un reattore a fusione.

L'obiettivo di questa tesi è di ampliare la comprensione della fisica delle sorgenti helicon per la produzione di ioni negativi per mezzo di investigazioni sperimentali effettuate sulla sorgente di plasma helicon RAID, situata presso lo Swiss Plasma Center, del Politecnico Federale di Losanna. I risultati presentati in questo lavoro di tesi sono il prodotto dello sviluppo, l'utilizzo e l'interpretazione dei risultati sperimentali ottenuti da diverse diagnostiche di plasma.

Due argomenti centrali sono lo svilluppo di due tecniche mirate alla misura in volume della densità di ioni negativi: la *Spettroscopia Cavity Ring-Down (CRDS)*, che non era mai stata impiegata su un plasma helicon e il *photodetachment con sonda di Langmuir*. Combinando le due diagnostiche, il risultato più notevole è l'osservazione di una distribuzione di ioni negativi di forma anulare sul bordo della colonna di plasma. La densità misurata è di circa $2 \times 10^{16} \mathrm{m}^{-3}$ con 3kW di potenza RF e senza fare ricorso al cesio. Tale risultato si spiega per la presenza di un profilo radiale di temperatura elettronica fortemente piccato, che raggiunge i 5 eV al centro e scende a < 1eV sul bordo, a 5 cm dal centro. La zona centrale del plasma ad alta temperatura elettronica, infatti, favorisce l'eccitazione vibrazionale dell'idrogeno molecolare (H_2). Le molecole eccitate, in seguito, migrano verso il bordo della colonna dove un processo noto come *associazione dissociativa*, principale responsabile della produzione volumetrica di H^-, è più probabile. Un'altra caratteristica intrinseca dei plasmi helicon è la loro forma elongata che la rende adatta a sistemi di estrazione di fasci lunghi e stretti di ioni negativi, a loro volta compatibili a sistemi di fotoneutralizzazione ad alta efficienza.

Sommario

Per caratterizzare la colonna di plasma sono state utilizzate diverse sonde di Langmuir, l'interferometria a microonde e la diffusione Thomson degli elettroni. Una sonda di Langmuir su un sistema a due assi ha consentito, in primo luogo, di studiare la struttura globale della colonna per diversi valori di potenza RF, di campi magnetici e di pressioni del gas. Valori tipici di densità in plasma di idrogeno o deuterio sono di $2 \times 10^{18} \mathrm{m}^{-3}$ con 3kW di potenza RF. Poiché, per i plasmi tipicamente prodotti in RAID, le sonde di Langmuir sono spesso soggette a notevoli flussi di calore quando tirano della corrente elettronica rischiando quindi di essere danneggiate, è stata installata una diagnostica indiretta, non invasiva e locale per misure di densità e temperature electtronica, basata sull'analisi dello spettro di diffusione Thomson. Questo sistema è stato sviluppato nel contesto di una collaborazione col progetto AWAKE del CERN mirato allo studio del prototipo della sorgente helicon destinata a futuri sistemi di accelerazione di particelle per mezzo di plasmi.

Tra l'altro, l'utilizzo di una sonda magnetica, detta *sonda B-dot*, ha consentito di dimostrare in maniera diretta la propagazione di un'onda helicon lungo la colonna di plasma.

Infine, per indagare più nel dettaglio il trasporto del plasma in RAID, è stato sviluppato un modello numerico fluido per un plasma di idrogeno a simmetria cilindrica. Introducendo come paramentri di input i profili di densità e temperatura elettronica sperimentali e facendo riferimento ad un insieme di reazioni chimiche in un plasma di idrogeno, tale modello è in grado di calcolare i profili di equilibrio di tutte le specie ioniche e neutre. Simulazioni numeriche di tal genere rappresentano un valido strumento di supporto per guidare il design e l'ottimizzazione delle sorgenti di plasmi per la fusione.

Parole-chiave: fisica del plasma, fusione nucleare, iniettore di fasci neutri, ioni negativi, sorgenti helicon, onde helicon, sonde di Langmuir, interferometria a microonde, Spettroscopia Cavity Ring-Down (CRDS), Laser Photodetachment con sonda di Langmuir, Spettroscopia ottica, Thomson Scattering, progetto AWAKE, sonda B-dot, modello H, trasporto del plasma, estrattore di ioni negativi.

Contents

Contents

Contents

1 Introduction

The purpose of this chapter is to introduce the reader to the basic concepts of thermonuclear fusion, which is the framework of this thesis work. In the first part we will describe the fundamental nuclear reactions and the general structure of a tokamak, the device where controlled fusion is achieved. The status of the biggest fusion project ITER and DEMO will be also presented. In the second part of the chapter we will progressively go towards the topics of this work by presenting why neutral beam heating (NBH) is important to achieve the plasma conditions required for thermonuclear fusion and by describing the components of a negative ion source, which is the first stage of neutral beam injectors (NBIs). In the last part of this chapter we will describe helicon plasmas and how these could be helpful to develop a next generation of negative ion sources for future NBI. Finally, we outline the thesis structure.

1.1 Controlled Thermonuclear Fusion

The increase of the level of CO_2 is one of the biggest issues that mankind has to deal with during this century. This will surely lead to large population displacements and change of everyday lifestyle. It is nowadays recognised that the cause of the global warming is mainly due to the release of the products of combustion of fossil products in the atmosphere. "Within a few centuries we are returning to the atmosphere and oceans the concentrated organic carbon stored in sedimentary rocks over hundreds of millions of years"[129]. Moreover, fossil fuels might be sufficient just for a few generations. We therefore must find energy sources that can replace the current fossil ones and without CO_2 emissions. This appears to be a hard task if we think that our current civilization is based on fossil resources, from transport to the production of plastic materials. The renewable sources of energy such as the solar and wind are a limited solution since they are intermittent in time and require large areas. Although renewable energy sources are a good solution for single houses and remote places, a base load supply and constant energy source is required to power modern society. Nuclear fission with conventional reactors is already a mature technology and currently provides about 10 % of world energy demand. However, the risk of accident due to the chain reaction, and the management of the storage of nuclear waste, remain controversial issues. The production

of energy by controlled nuclear fusion could be an alternative for future large scale energy production.

The production of energy by controlled thermonuclear fusion reactions is one the most ambitious challenges of mankind. The increasing world energy demand and the recent issues related to climate change require the use of an abundant and clean source of energy. The raw materials for thermonuclear fusion are deuterium and lithium, which are worldwide available, and no radioactive long-lived isotopes are produced. The Sun is a self-sustained gravitationally confined fusion reactor. On Earth, nuclear fusion is achieved by heating magnetically confined plasmas up to 150 million degrees in reactors called "*Tokamak*". A crucial step in the development of fusion power is the reactor ITER, currently being constructed in France, whose aim is to demonstrate the production of 500 MW of fusion power, 10 times the input power. To achieve the temperatures required for thermonuclear reactions (10 - 15 keV), plasma must be heated up either by electromagnetic waves or beams of energetic neutral particles called *Neutral Beam Injectors* (NBI). NBIs consist of of high energy H or D atoms which are accelerated up to an energy of 1 MeV. The production of beams of H or D is based on the acceleration of the respective negative ions H^-/D^- and their neutralization with gas. Negative ions are usually produced in Inductively Coupled Plasma (ICP) sources where Cs is deposited to enhance the production of H^-/D^- on vessel walls. For the next generation of NBIs, negative ion sources capable of producing high throughputs of negative ions are required.

1.1.1 Concepts of thermonuclear fusion

The production of energy from controlled nuclear fusion is one of the main goals of mankind in this century. In the long term, this source of energy could replace fossil fuels since it presents many advantages. First, the raw materials deuterium and lithium atoms, are available world wide, contrary to fossil fuels which are localized in a few and often politically unstable areas. Secondly, fusion does not produce any long-life radioactive waste (apart from the activation of the reactor itself), but only He ash. Nuclear fusion is the process where light nuclei fuse to form heavier nuclei. The energy released by a fusion reaction is given by the well know equation $\Delta E = \Delta mc^2$. In order to achieve fusion, nuclei have to overcome their electric repulsion, then they can fuse through quantum tunneling. The process requires a temperature of about 10 keV, corresponding to 100 million degrees centigrade. At such a temperature the matter is fully ionized meaning that it is made of a mixture of charged particles: electrons an ions. This state of matter is called *plasma*. At these high temperatures, plasma cannot be enclosed in material walls and other ways to confined plasma have to be employed. In the universe, stars are made of plasma, which are self-confined by gravity. On Earth, presently, there are two ways to achieve fusion: the first is the *inertial confinement* consisting of laser-induced implosion of fuel pellets; the second, the *magnetic confinement*, is achieved by using magnetic fields. The second method is obtained in devices named *Tokamaks*, which are shortly described in the
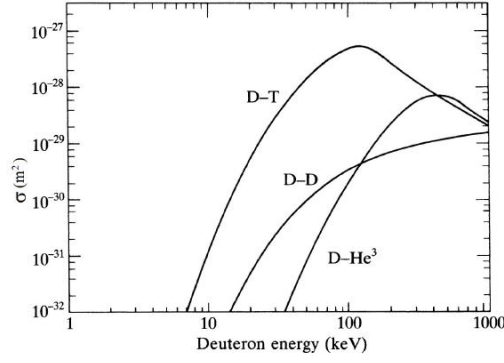
Figure 1.1 – Cross sections of the fusion reactions of D-T, D-He and D-D, from [145].

next paragraph. The fusion reactions that can be reproduced on Earth are:

$$D^+ + T^+ \rightarrow {}^4He^{2+} + n, \tag{1.1}$$

$$D^+ + He^+ \rightarrow {}^4He^+ + p, \tag{1.2}$$

$$D^+ + D^+ \rightarrow T^+ + p, \tag{1.3}$$

The cross section as a function of energy of the above reactions are shown in Fig. 1.1 (taken from [145]). We can clearly see that the most convenient reaction is that for D-T since it is the one reaching the largest cross sections at lowest energies. The D-T reaction is the reaction envisaged to be employed in fusion experiments. The ${}^4He^{2+}$ resulting from the $D^+ - T^+$ reaction, being charged, is confined by the magnetic field keeping the plasma hot, while the neutrons leave the plasma. The high temperature is not the only ingredient required to achieve controlled thermonuclear fusion. Nuclei must be confined in the plasma as long as possible so that they can react, therefore plasmas have to be confined for enough time. On Earth, nuclear fusion in plasmas can be achieved in devices called *Tokamak* consisting of toroidal-shape magnetic fields. The goal of fusion devices is to achieve *ignition* where the burning process are self-sustained. The condition for plasma ignition is described by the following triple product known as *Lawson criterion* [84]:

$$n\tau T > 5 \times 10^{21} \, [\text{m}^{-3} \, \text{s} \, \text{keV}], \tag{1.4}$$

where n and T are the peak ion density and temperature and τ is the energy confinement time. From the D-T reaction, the fusion-generated ${}^4He$ has 3.5 MeV energy and the neutron has 14.1 MeV.

The deuterium needed to fuel fusion is relatively easy to find in nature, indeed the amount of deuterium in oceans is 0.014% of all the naturally occurring hydrogen. The tritium, however, exists in a tiny amount in nature ($\sim$ 30 kg in the entire Earth atmosphere) because it has a

short life time (12.5 years of half life), therefore it has to be produced artificially. There are two possible nuclear reactions to produce tritium from the two stable isotopes of lithium (^{6}Li and ^{7}Li):

$$n + {}^6\text{Li} \rightarrow T + {}^4\text{He}, \tag{1.5}$$

$$n + {}^7\text{Li} \rightarrow T + {}^4\text{He} + n, \tag{1.6}$$
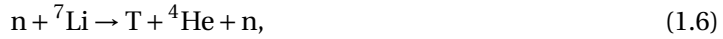
these reactions could take place in the internal walls of a future fusion reactor; this process is called *tritium breeding* and it is accomplished by the neutron released by fusion reactions and escaping the plasma. It is nowadays recognized that ignition can occur in Tokamak, described more in details in the next paragraph, however there are still a lot of unexplored phenomena like instabilities, materials and tritium breeding problems which remain important issues to be addressed to make controlled nuclear fusion possible.

1.1.2 Tokamaks

During the past 60 years, a variety of plasma devices to achieve fusion have been proposed. The mirror and Z-pinch devices were initially proposed as promising candidates to produce fusion energy but these geometries were then abandoned because of their intrinsic considerable plasma losses.

Nowadays, the most promising fusion device is the tokamak, a transliteration of the Russian acronym "TOKAMAK", **to**roidalnaya **ka**mera **ma**gnitnaya **k**atushka, meaning "toroidal chamber with magnetic coils". A sketch of a tokamak is shown in Fig. 1.2. The main components of a tokamak are the toroidal, the poloidal and the inner field coils. The toroidal field coils produce the main magnetic field for plasma confinement, which has a typical value of a few Tesla. The toroidal field alone is not enough to achieve sufficient plasma confinement due to the 1/R magnetic field scaling, where R is the outer radius of the torus, causing particle vertical losses and magnetic instabilities. In order to achieve a stable configuration, a poloidal magnetic field component is required. A poloidal component is produced by a current flowing through the plasma itself along the toroidal direction. This current can be induced by the inner poloidal coils (see Fig.1.2), which acts as a current transformer, where the plasma is the secondary circuit. The effect of this current is also to heat up the plasma though *Ohmic heating*. However, the plasma cannot be heated up indefinitely by ohmic heating because of the limited current ramp up and also because the resistivity of the plasma is proportional to $T_e^{-3/2}$ making ohmic heating inefficient at high electron temperatures.

The combination of the toroidal and the poloidal magnetic field produces helical trajectories producing a stabilizing configuration. In addition, some outer poloidal field coils are also present. These are required to counterbalance the *hoop force* and the *tire tube* forces, which tend to make the plasma expand in the outer direction; moreover, these coils are used for plasma positioning and shaping.
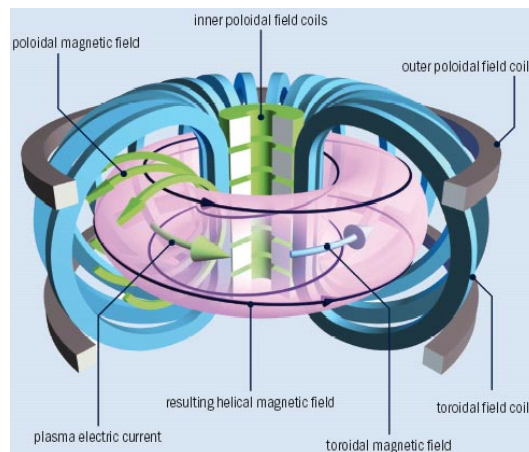
Figure 1.2 – Schematic of a Tokamak showing the coils generating the magnetic field. The toroidal magnetic field are field lines closed. The addition of a poloidal magnetic field produces helical magnetic lines leading to a stabilizing plasma configuration. The outer poloidal field coils are used to position and shape the plasma (from *www.iter.org*).

The longer the plasma is confined in the vacuum vessel, the more energy can be produced by fusion reactions. From early '60s, research on tokamaks has been focused on how to increase the plasma confinement time as much as possible. In early tokamaks, the confinement time was of the order of 1 ms. Since then, a lot of progress has been made till nowadays with a few seconds achieved. Apart from the confinement time, many physics aspects have been investigated during previous decades. For example, it was initially believed that the increase of plasma density n and the consequent increasing thermal transport due to collisions would lead to higher losses. This was in contradiction with experiment where an improvement of the confinement time with n was observed: as bigger machines were built, plasmas were confined for longer times. The largest tokamak ever built is the Joint European Torus (JET), in the United Kingdom.

Due to the inefficiency of ohmic heating at high electron temperatures, other heating mechanisms have been investigated. The most explored heating mechanisms are those by RF waves and the injection of fast neutral particles. RF waves are lunched by antennas and interact resonantly with the plasma. The neutral fast particles interact by collisions with plasma and are progressively slowed down. Thanks to these other mechanisms of plasma heating it was possible to increase the plasma temperature till the requirement for fusion and the discovery of a more stable operation regime, compared to normal operation, called (High confinement) H-mode, leading to longer confinement times. Unfortunately, because of plasma instabilities, energy is released by so called "disruptions" leading to a sudden loss of plasma energy and subsequent shut down of the discharge, or the "sawtooth" instabilities characterized by periodical energy relaxation of the plasma core, leading to loss of energetic particle from the plasma core. All these phenomena should be studied and controlled to achieve long time operation needed for the production of fusion energy. A milestone in fusion power in tokamak are the experimental campaigns in JET during the 90s. The production of 16.1 MW fusion
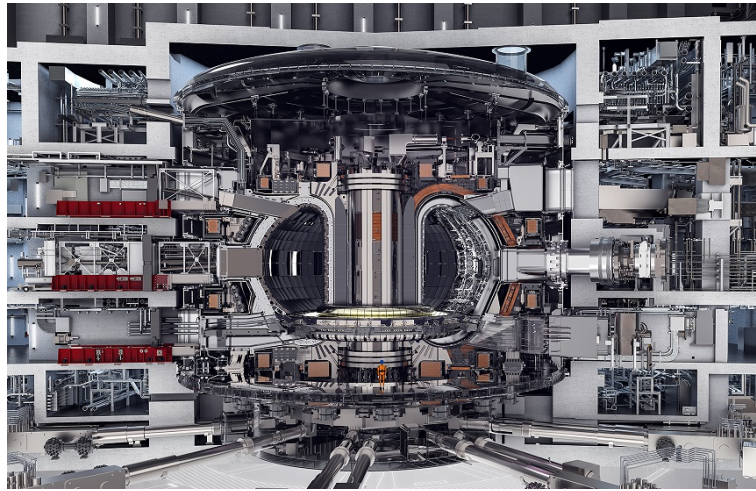
Figure 1.3 – ITER, the largest experimental tokamak in the world, will explore the physics of self-sustained fusion plasmas, producing 500 MW power, 10 times the input power (from *www.iter.org*)

.

power from a 50-50 mixture of deuterium-tritium and a record value of the ratio of fusion power to total input power, $Q_{in} = P_{fus}/P_{in} = 0.62$, was achieved [44].

The goal of the next generation of fusion devices is to build a self-sustaining plasma. It is now confirmed that the performance of tokamaks scale with machine size and magnetic field. The future step will be the International Thermonuclear Experimental Reactor (ITER), larger and more complex than any other existing tokamaks, which is currently being built in the Cadarache site of CEA (Commissariat à l'Énergie Atomique), in France.

1.1.3 ITER experimental thermonuclear reactor

ITER represents the culmination of many decades of research in fusion and a necessary step before the next generation of commercial-like fusion reactors. The main goal of the project is to produce a self sustained D-T plasma producing 500 MW power, 10 times the input power. The ITER project is a huge international scientific and technological effort to demonstrate the possibility to produce a self sustained fusion reactor. A drawing of the ITER Tokamak showing the main components of the device and the plant is shown in Fig. 1.3. The construction of ITER started in 2014 [98] in the Cadarache site and it is under the responsibility of the European Union, and carried out by the French Nuclear Authority.

ITER will push the limits of current technologies of the superconductive coils, the vacuum vessels and nuclear materials. Superconductive coils are made by twisted Ni_3Ti strands into stainless jacket. They will be D-shaped and treated in huge furnaces. The vacuum vessel will be the largest in the world (8000 t of steel, 840 m^3, 6 m major radius) and will have to comply with ultra vacuum requirements. A crucial mechanical component of ITER will be the plasma facing surface, named *blanket*. This will have to withstand the surface heat flux, the electromagnetic

loads, the plasma interaction consequent to disruption, shield the coils from high neutron flux and be able to remove 850 MW of power. All this must respect the highest vacuum standards and allow remote handling. The rapid release of fast electrons during disruption may cause local melting of the vessel wall. To minimize this risk, an injection system of high-Z impurities will be implemented, able to cool down the plasma in a few milliseconds and dissipate the thermal and magnetic energy. Furthermore, since ITER provides the opportunity to test the tritium breeding, blankets able to produce tritium from typical fusion powers, will be tested. Another crucial component is the divertor which serves to absorb the impurities and, in a burning plasma, it removes the He ash produced by fusion reactions. The divertor converts the ions into neutrals, which are then pumped out by the vacuum system. Therefore, the divertor has to withstand extreme heat loads ($20 \, \mathrm{MW/m^2}$), the highest among plasma facing materials. According to current planning, ITER first operation in deuterium plasma is expected in 2025, then the experiments in D-T plasmas are expected for 2035. Although ITER will not convert fusion power to electricity energy, it will address many unsolved issues of controlled fusion. First of all, it will produce for the first time in history, a net fusion power in long plasma pulses (400s). ITER will also be the opportunity to study controlled fusion in a device closer to future fusion power plants. Moreover, it will be possible to study a self-sustained plasma, a burning plasma, heated by the alpha particles produced by fusion reactions. One crucial mission for last ITER operations, is to study the production of tritium with blankets since the world supply is not sufficient to cover the ITER burning plasma operations. Moreover, ITER will demonstrate the safety of the production of fusion energy and the negligible impact on the environment. The step after ITER is a reactor capable of producing net electric power; this belongs to a second generation of fusion devices. Scientists are already studying the conceptual design of a fusion power plant, named DEMO, which is shortly described in the next paragraph.

1.1.4 DEMOnstration Fusion Power Plant

To bridge the gap between ITER and commercial fusion reactors, a fusion reactor able to demonstrate the production of commercially competitive electricity from fusion power is required. The European Union is currently developing the preconceptual design of such a device, whose name is DEMOnstration Fusion Power Plant (DEMO) [47]. DEMO is a crucial step after ITER and its main physics goal is to demonstrate the production of a few hundreds MWs electrical energy and achieve a closed-tritium cycle. A schematic design of DEMO is shown in Fig.1.4. Nowadays there is no definitive design for DEMO and many plant designs are being considered. Very likely, DEMO development strategy will be based on modest extrapolations from ITER in order to minimize the risks. DEMO will be developed in the framework of nuclear technologies (like fission reactors) and will have to comply with strict nuclear safety regulations.
The timescale of DEMO's development will proceed in parallel with the know-how acquired during ITER's exploitation. DEMO's design will rely on the constant flow of knowledge from ITER operation, from physics to material science. A pre-conceptual design phase started in
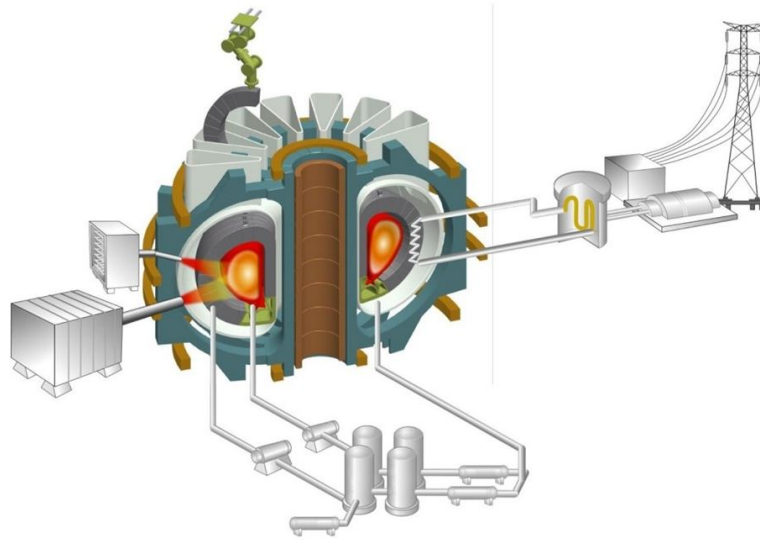
Figure 1.4 – DEMO will demonstrate the production of net electrical power from fusion power. This reactor will bridge the gap between ITER and commercial fusion plants (from *www.iter.org*)

.

2014 and will probably be frozen in 2020. This phase will consist of the assessment of the power plant requirements (the electrical energy output requirement, for example) and the exploration of several possible designs. This will be followed by the conceptual design development phase. The most critical point in DEMO's design will come from the D-T results from ITER, which are scheduled to start in 2035. After these preliminary phases, the engineering design will freeze plant features. The construction of DEMO is nowadays expected for the beginning of the 2040s. The main designs for DEMO, which are currently considered, are DEMO-1 and flexi-DEMO, which are both solutions based on medium-size tokamaks, to reduce the size of the entire power plant, and making fusion plants cheaper and faster to build. The biggest technological challenge that can be forecast at the present status of development are the maximum field in the toroidal coils and the divertor thermal load. Indeed, reducing the size of the vessel will require stronger magnetic field. The threshold of superconductor performance and the huge mechanical stress of coils may pose serious problems, as well as the heat fluxes on the divertor, larger even than those in ITER. Overall, DEMO will have to increase the efficiency of technologies to make fusion electricity competitive. In this context, the optimization of heating plasma systems is highly desirable, among these the neutral beam injection, which will be discussed in more detail in the next paragraph.

1.2 Neutral Beam Injection

A self-sustained D-T plasma is heated by α-particles (He nuclei) resulting from fusion reactions and confined in the plasma volume. Since ohmic heating drops at the temperature required for

the ignition, auxiliary heating systems are necessary. In Tokamaks, two methods are employed for plasma heating: the launching of RF waves and the injection of neutral particle beams. The RF heating is based on the resonance of the RF waves with the electron or ion cyclotron frequency. The particle beams used for plasma heating have to be neutral since otherwise if they were electrically charged, they would be deflected by the confining magnetic field. A schematic design of a Neutral Beam Injection (NBI) System is shown in Fig.1.5.
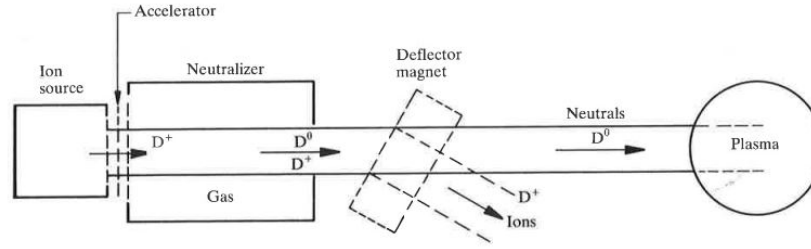
Figure 1.5 – Schematic of a Neutral Beam Injector showing the main components: the source of ions, the accelerator grids, the neutralizer (where ions are converted to neutrals) and the magnetic deflector (to filter out residual ions) (taken from [145])

.

The production of neutral particles starts from the production of ions, for example, H^+ or D^+, in the ion source. The ions are then electrostatically accelerated by high voltage grids to an energy of a few hundred keV. Then, the ions pass through a chamber filled with a low pressure gas (<0.3 Pa) where they are neutralized by charge exchange. A deflecting magnet filters out the residual charged particles after the neutralizer. Once the neutral beam particle enters the plasma region, it can interact by charge exchange, or it can be ionized either by ion or electron collisions. The processes in the plasma are summarized as follows, where "b" stands for the beam and "p" for the plasma:

- Charge exchange $\quad\quad H_b + H_p{}^+ \rightarrow H_b{}^+ + H_p,$

- Ionization by ions $\quad\quad H_b + H_p{}^+ \rightarrow H_b{}^+ + H_p{}^+ + e,$

- Ionization by electrons $\quad\quad H_b + e \rightarrow H_b{}^+ + 2e.$

A very crucial step is the neutralization of ions before they are injected in the tokamak plasma. Most NBIs start from positive ions and the resulting H^+ or D^+ ions are neutralized by passing through H_2 or D_2 gas, however their neutralization efficiency quickly drops to negligible values for energies larger than $\sim 100\,\mathrm{keV}$. Since ITER NBI will require an energy of about 1 MeV of D^0 and 0.87 MeV of H^0, positive ions cannot, therefore, be employed. Fortunately, the neutralization efficiency for negative ions (H^- or D^-) at the required energy is around 60%, as can be seen in Fig. 1.6 [68], making NBIs feasible with negative ion sources. More advanced concepts, based on laser photo-neutralization schemes, are expected to reach neutralization efficiency even of 93% but these schemes are completely unexplored yet [127]. If on one
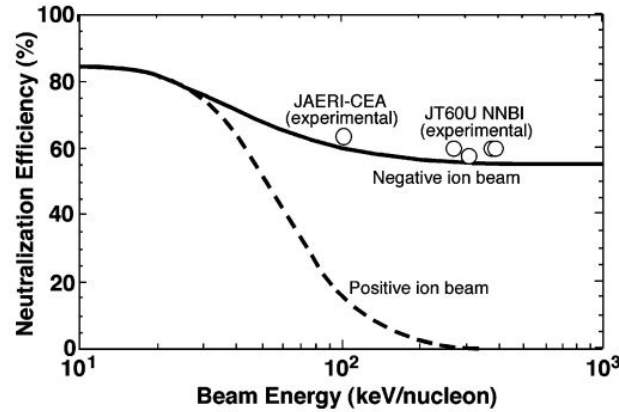
Figure 1.6 – Neutralization efficiency for positive and negative ion beams, showing the need for negative ions for NBIs.

hand, it is relatively easy to neutralize H^- or D^- ions, on the other hand, their production is challenging. The most external electron of H^- or D^- has an electron affinity of 0.75 eV making it very fragile since this electron can be easily stripped by collision with neutrals. This imposes that negative plasma sources for NBIs must operate at low pressure, making plasma discharges more difficult to achieve. In the case of ITER negative ion source, the maximum allowed operating pressure is 0.3 Pa. Moreover, the extraction of negative ions from a plasma source is much more problematic than positive ions since undesired electrons are co-extracted as well and may disturb the negative ion extraction and increase heat load on extraction components. Therefore, a large effort is ongoing to optimize the current technology of negative ion sources to reach the highest throughput and find alternative/more efficient ways for producing and neutralizing negative ions both for ITER and for the next generation of future NBIs.

1.2.1 The negative ion source

Volume and Surface production of negative ions

As previously discussed, the production and extraction of hydrogen or deuterium negative ions is a more complex operation than for positive ions. One reason already mentioned is the low electron affinity of H^- of 0.75 eV making H^- and D^- very fragile to survive in a plasma environment, since even in a cold plasma source the typical electron temperature is a few eV. Secondly, the electronegativity of the plasma, namely the ratio of negative ions compared to electrons, is intrinsically quite low in plasmas. Therefore, when trying to extract negative ions, there is a large amount of co-extracted electrons, which are undesired because they add thermal loads.

There are two mechanisms to produce negative hydrogen or deuterium ions in plasmas: the *volume production* and the *surface production* mechanisms. In the following discussion, we will consider only the case for hydrogen, but similar processes apply to deuterium with very

similar cross sections. The volume production mechanism consists in the attachment of low energy electrons ($< 1\,\text{eV}$) to ro-vibrationally excited H_2 molecules [18], leading to the formation of negative hydrogen ions as described by the following reaction:

$$\textit{Volume production} \qquad e + H_2(v) \rightarrow H^- + H, \tag{1.7}$$
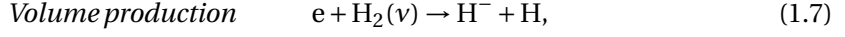
where $H_2(v)$ denotes a hydrogen molecule in the ro-vibrational state v. This process is commonly known as *dissociative attachment.* The other process, the surface production mechanism, is based on the conversion of a neutral atomic hydrogen which, when impinging onto the wall of a vacuum chamber, acquires an extra electron from the surface and then goes back to plasma or is directly extracted:

$$\textit{Surface production} \qquad H + e(\text{wall}) \rightarrow H^-. \tag{1.8}$$
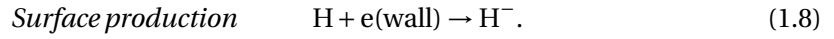
Both mechanisms can be used in conventional negative ion sources, where plasma and geometrical parameters are optimized for the highest production of negative ions.

Excitation of the H_2 molecule

The vibrational excitation of H_2 molecules requires high temperature electrons ($T_e > 5\,\text{eV}$). There are two processes in plasmas which can ro-vibrationally excite the H_2 molecule. One is the *stepwise vibrational excitation* of molecules in collision with electrons (e-V process):

$$e + H_2 \rightarrow H_2^- \rightarrow e + H_2(v + \Delta v), \tag{1.9}$$
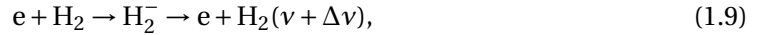
where H_2^- is a transitory negative ion. This mechanism requires many collisions, and so high electron densities, to increase the vibrational state v, since the most probable change in v is $\Delta v = \pm 1$ [13].
Another important mechanism for $H_2(v)$ production at the low pressures typical of NBIs is the radiative decay from the singlet state, the so called *E-V process* [69]:

$$H_2(X^1\Sigma_g^+, v) + e \rightarrow H_2(B^1\Sigma_u; C^1\Pi_u) + e \tag{1.10}$$
$$\rightarrow H_2(X^1\Sigma_g^+, v'') + e + h\nu. \tag{1.11}$$

.
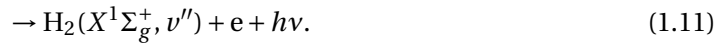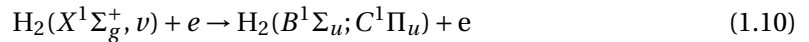
Therefore, for the volume production of H^-, the co-existence in the source volume of high
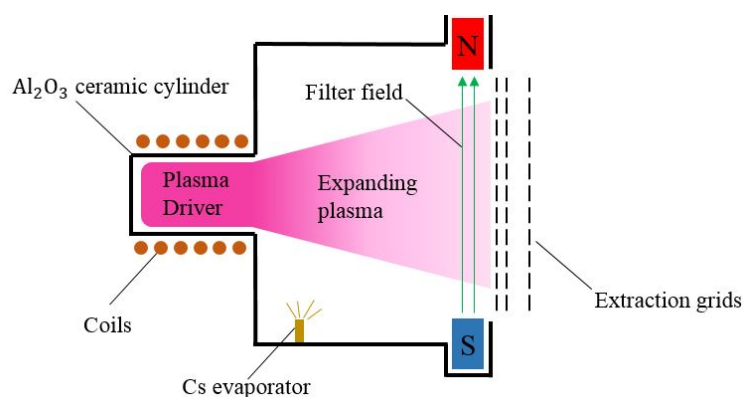
Figure 1.7 – Schematic of a conventional negative ion source for NBIs. The plasma is produced by inductive coupling inside a ceramic cylinder, then it expands to the extraction grid where negative ions are formed and then accelerated. The magnetic filter field is necessary to filter out the hot electrons. The surface production of negative ions is enhanced by the evaporation of Cs on the first extraction grid.

energy electrons ($> 5\,\mathrm{eV}$) to increase the vibrational state of the molecule, and low energy electrons ($< 1\,\mathrm{eV}$) to enhance the dissociative attachment is required. It is evident that it is not a easy task to maintain two electron populations at different temperatures in the same plasma source.

Features of a conventional negative ion source

Due to the intrinsic limitations of volume production in conventional ICP (Inductively Coupled Plasma) ion sources, such as the limited skin depth, negative ion sources for fusion rely on low work function materials to enhance the surface negative ion production (see Eq. 1.8). This is normally performed by depositing a thin layer of Cs, which is the material with the lowest work function [80], on the walls of the vacuum vessel. A schematic of a conventional ICP negative ion source for NBIs is shown in Fig. 1.7 [131]. The concept of this source geometry is based on the separation of a hot region, the ICP plasma driver, which is a hot plasma where H_2 is ro-vibrationally excited, from a low electron temperature region, the extraction region, where H^- generated by surface processes, can survive. The plasma driver is made of water-cooled RF coils producing a plasma inside an alumina cylinder, then plasma exits and expands towards the extraction grids. At the same time, Cs is evaporated onto the internal walls, extraction grid included, forming a very thin layer, a few atoms thick. Thanks to the reduced work function, negative ions are easily produced on the extraction grid. To prevent their destruction and to enhance the dissociative attachment, a magnetic filter field (about 100 G) separates the hot from the cold region. The filter field has also another crucial role: it reduces the amount of co-extracted electrons with the negative ions. If too many electrons were extracted, they would deposit their energy on the extraction grid leading to undesired thermal load. Finally,

the extraction grids accelerates the negative ions to the target energy and they are delivered to the beam duct.

Although the evaporation of Cs enabled conventional ICP sources to reach the requirements for ITER NBIs, [19, 36] there are many drawbacks, which remain major issues in employing Cs negative ion sources. First, the uniformity of the extracted negative ion beams is sensitive to Cs distribution in the source so that source conditioning and beam stability are not easy to achieve and reproduce. Second, Cs has to be continuously evaporated even during plasma operation. This could lead to diffusion and deposition of Cs into the beam duct and could be problematic in particular when ITER (or DEMO) will operate with a mixture of D-T plasma, producing high neutron fluxes, and then making the reactor radioactive. Since the remote handling must be employed for maintenance in these conditions, replacing many parts may pose a serious problem. Third, Cs is difficult to handle and it is polluting for the environment. Therefore, due to the problems related to Cs management, the possibility to use negative ion sources which do not rely on Cs is currently explored [94]. This requires optimization of the volume production mechanisms such as exploring other plasma sources, beyond conventional ICP sources, and perhaps employing alternative magnetic geometries, extractions and injections of negative ions. One currently explored strategy is to employ helicon plasma sources to produce the negative ions, which is nowadays explored by a few research groups [117, 104, 94]. These sources have several advantages, compared to ICP, which will be discussed in detail in Sec. 1.3. Although the source for ITER NBI injector will be based on conventional ICP as previously discussed, since the technology is mature and reliable, alternative concepts for NBIs are currently explored for the next generation of tokamaks, such as for DEMO, which was described in Sec. 1.1.4.

1.2.2 Extraction and Acceleration

The production of negative ions raises more issues compared to positive ions, since negative ions can be easily stripped in plasma environment and their density is much less compared to background plasma density. The ease to destroy negative ions poses also many issues in the extraction because of collisions with neutrals and by the large background of electrons. We show first the scheme of an ion extractor and then we show the issues of negative ion extraction.

In the simplest configuration, an ion extractor is made of a plasma electrode (known as *plasma grid* and an extraction electrode, called *extraction grid*, as shown in Fig. 1.8. The plasma grid is usually electrically biased negatively and the extraction electrode is grounded, so that it can be connected to the tokamak vessel. The interface plasma-vacuum is called the *meniscus* and represents the boundary between the plasma and the beam. The shape of the meniscus depends on the applied bias, the plasma density and the extraction geometry. For example, when the plasma density is low, the meniscus is strongly concave and the focal point is close to the extraction electrode, this is a over focusing situation and the beam will diverge.

The extracted current from a plasma source is limited either by the emission capability or by space charge forces. The maximum extracted current density j can be calculated by the
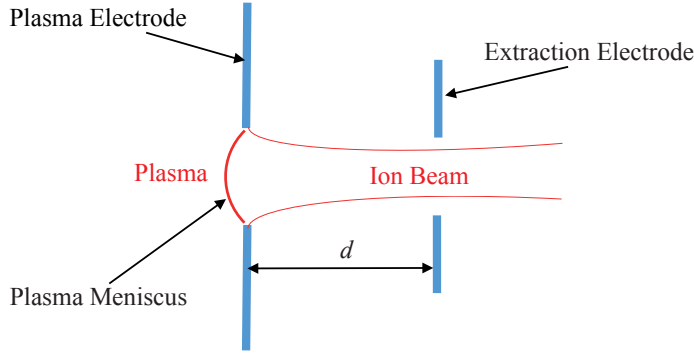
Figure 1.8 – Schematic of a ion extractor. When the plasma electrode is facing the plasma, a plasma meniscus is formed, which is the surface from which ions are extracted.

Child-Langmuir equation [146], for a parallel plates geometry:

$$j[\text{A/m}^2] = \frac{4\epsilon_0}{9}\sqrt{\frac{2q}{m}}\frac{\phi^{\frac{3}{2}}}{d^2}, \tag{1.12}$$

where ϵ_0 is the electrical permittivity in vacuum, q the electric charge, m the particle mass and ϕ is the potential drop across the gap of length d. The beam is subsequently transported by electrical optics and its quality is described by the emittance, namely, the space occupied by the particle beam in the phase space. The extraction capability of an ion source is described by the *perveance P*:

$$P = \frac{I_{ext}}{\phi^{3/2}}, \tag{1.13}$$

where I_{ext} is the extracted current and $\phi^{3/2}$ is the extraction voltage. The perveance is used to compare the extraction capability of different extractors. It is usually normalized with respect to the perveance for current flow between parallel electrodes when the flow is limited just by the space charge:

$$P_c = \frac{4\epsilon_0}{9}\sqrt{\frac{2q}{m}}\frac{A}{d^2}, \tag{1.14}$$

where A is the emitting area. If the acceleration gap is small compared to radius of curvature r_c of the meniscus, and if we consider a spherical radius of curvature and a circular aperture [59]:

$$\frac{I_{ext}}{\phi^{3/2}}\left(\frac{A}{Z}\right)^{1/2} = 1.72 \times 10^{-7}\frac{a^2}{d^2}\left(1 - 1.6\frac{d}{r_c}\right), \tag{1.15}$$

and for a cylindrical curvature and a slit of aperture $2a$:

$$\frac{I_{ext}}{\phi^{3/2}}\left(\frac{A}{Z}\right)^{1/2} = 1.14 \times 10^{-7} \frac{a^2}{d^2}\left(1 - 0.8\frac{d}{r_c}\right), \qquad (1.16)$$

where A is the atomic mass and Z the atomic number. We remark that the geometry of the emitting surface changes the extracted current. In the case of radial extraction from a plasma column, which will be discussed in Sec. 8, Eq. 1.16 is used to estimate the current for a negative ion extractor designed of for RAID.

The differences of extraction between positive and negative ions is depicted in Fig. 1.9, where, the vertical coordinate is the potential along the extraction direction.

Fig 1.9 a) shows the extraction of positive ions: The extraction grid is negatively biased and electrons and negative ions are trapped in the plasma potential well, while positive ions flow from the plasma bulk to the extraction sheath at the Bohm velocity and then they are accelerated. Therefore, positive ions just flow out the plasma and are accelerated by the desired energy by the extraction electrode.

The situation is different in the case of negative ion extraction when they are generated by surface processes, shown in Fig. 1.9 b) or when they are generated in the plasma volume, shown in Fig. 1.9 c). In Fig. 1.9 b), the plasma grid is biased lower compared to the plasma potential, this creates a potential well in the potential profile where positive thermal ions are trapped. Negative ions and electrons in the plasma volume are trapped in the plasma bulk because of the plasma potential, but those produced on the surface of the plasma grid are accelerated by the extraction grid and escape the plasma. In Fig. 1.9 c), showing the extraction of negative ions from the plasma volume, which is the case for RAID, the plasma grid is biased at 20 V, above the plasma potential (12 V). Negative ions and electrons are therefore accelerated to the plasma grid. Electron are then mostly filtered out transverse magnetic fields and negative ions are additionally accelerated by the extraction grid.

In conventional negative ion extractors where negative ions are produced by surface processes, the plasma grid is usually composed of many arrays of circular apertures so that the beam is extracted in forms of many *beamlets*. Just after the PG, there is the Extraction Grid (EG) which pre-accelerates the ions. Once the ions have passed through the PG, they are accelerated by multiple grids to the required energy up to the Grounded Grid (GG).

The EG is usually embedded with permanent magnets to filter out residual electrons. However, the effect of this magnetic field is to slightly deviate the negative ion trajectory. Therefore, the EG has a small tilt to be aligned to the trajectory of extracted ions. The bias of the EG is usually kept at a few kV to limit the power deposition of electrons in case of misalignment.

 There are many issues in negative ion extraction such as: 1) the gas pressure has to be kept as low as possible to minimize stripping losses of H^- and D^- by H_2 and D_2 molecules. The stripping losses produce neutral atoms which cannot be controlled by electric or magnetic field and which could flow to beam duct, and also electrons which could increase the amount of co-extracted electrons and the thermal load onto the walls. 2) The stripping reactions in the accelerator line could create also D_2^+ and D^+ ions which backstream up to the source leading
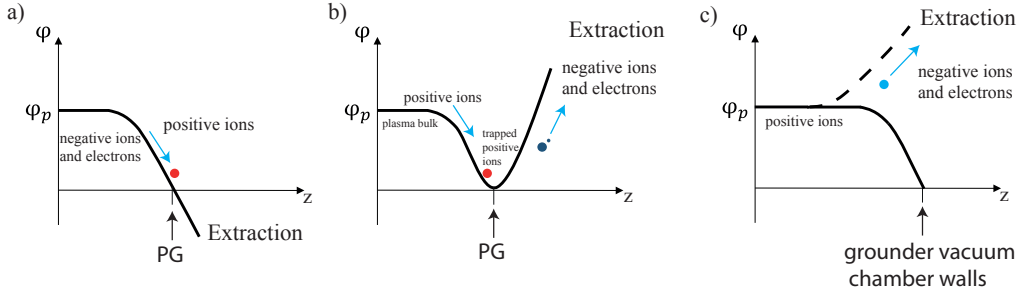
Figure 1.9 – a) Schematic drawing of positive ion extraction. Positive ions are naturally accelerated by the sheath potential drop. b) Schematic drawing of negative ion extractions generated by surface processes: the positively polarized electrode (with respect to ϕ_p) leads to the formation of a potential well for thermal positive ions and a potential barrier for negative ions and electrons. c) Extraction of negative ions generated from volume processes in RAID: the plasma grid has to be biased above the plasma potential ($V_{plasma} = 12\,\text{V}$).

important thermal loads. 3) The presence of a "halo" beam, namely a component of the D^- beamlets that has a high divergence fraction with respect with the rest of the beamlets.

1.2.3 The neutralizer and the residual ion dump

Once the energetic negative ions exit the Grounded Grid (GG), they enter the gas neutralizer where they can collide with gas molecules. The gas neutralizer has been chosen for ITER NBI due to its robustness and known technologies. Alternative ways of ion neutralizers are being explored such as the plasma neutralizers [150], the lithium jet neutralizer [60] or the laser photoneutralizer [127], but these belong to the next generation of NBIs.

We will now consider the case for D but the same reactions occur for H. The gas neutralization is achieved via collisions of D^- ion with gas molecules of D_2. The reactions occurring in the neutralizers are:

$$D^- + D_2 \rightarrow D + D_2 + e, \tag{1.17}$$

$$D^- + D_2 \rightarrow D^+ + D_2 + 2e, \tag{1.18}$$

$$D + D_2 \rightarrow D^+ + D_2 + e, \tag{1.19}$$

where D is the neutral deuterium atom created by the collision. The neutralization cross section as a function of energy is shown in Fig. 1.6. We remark that the D formed by one of the first two reactions can be destroyed again in the neutralizer by collision with gas molecules. The beam exiting the gas neutralizer finally consists of $\approx 60\%$ of D, 20% of D^+ and 20% of D^- [66]. The gas is injected in the center of the neutralizer and it is pumped away from the sides. Moreover, to reduce the gas conductance, the neutralizer is divided into four vertical channels.
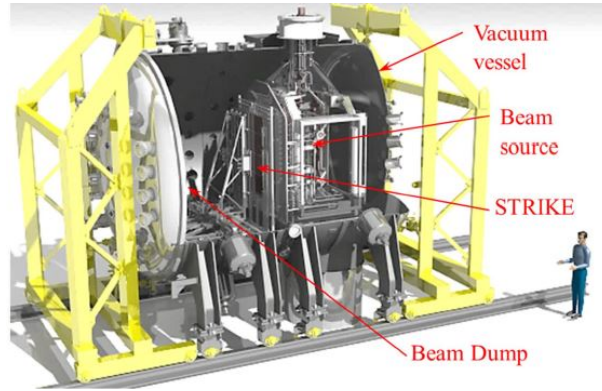
Figure 1.10 – SPIDER negative ion source

As mentioned above, the beam exiting the gas neutralizer is composed of "residual" D^+ and D^-. These ions should be removed from the beam because they would be end up into the duct walls and lead to excessive thermal load. Therefore, they are deflected in a controlled way. This will be achieved in ITER by the Residual Ion Dump (RID) consisting of a volume divided by 4 vertical channels, aligned with the neutralizer channels. A voltage of -20 kV is applied to deflects the ions [67].

1.2.4 SPIDER and MITICA

At the PRIMA (*Padova Research on ITER Megavolt Accelerator*), which is the Neutral Beam Test Facility (NBTF), hosted in Padova, two key infrastructures for the achievement of ITER goals are being built. The first one is SPIDER (*Source for Production of Ions of Deuterium Extracted from an RF plasma*), a full-size negative ion source for ITER NBI; The other is MITICA (*Megavolt ITER Injector and Concept Advancement*), the full scale prototype of the NBI for ITER. Both experiments are crucial for future operation of NBIs to achieve ITER fusion parameters [139]. SPIDER, shown in Fig. 1.10, will provide the production and the acceleration of H^- and D^- up to 100 keV energy for a pulse duration of 3600 s. The plasma is produced by 8 cylindrical RF ICP drivers and the pressure is kept below 0.3 Pa. Plasma diffuses in the expanding region up to the plasma grid, which is covered by a thin layer of Cs to enhance surface production of H^- or D^-. An extraction grid, located 10 mm in front of the plasma grid can be arbitrarily biased to study the effect of the electric fields on the negative ion production and optimize the beam extraction. The grid has a surface area of $2\,m^2$ and has 1280 chamfered holes from where negative ions beamlets are produced. Negative ion beamlets can be absorbed by the STRIKE calorimeter (*Short-Time Retractable Instrumented Kalorimeter Experiment*). SPIDER will work with a magnetic filter field like that employed in ITER and will be equipped with a Cs oven for Cs operation. SPIDER parameters are summarized in the table below: SPIDER will be equipped with a number of diagnostics [105] to monitor and optimize the source with the aim to fulfill the goals relevant for ITER NBI. The knowledge of source parameters is crucial at this stage of development since the high neutron flux expected in ITER ($10^{10}\,n/cm^2/s$) prevents

	H	D	Unit
Beam energy	100	100	keV
Max filling pressure	0.3	0.3	Pa
Extracted negative ion density current	350	285	A/m^2
Min Pulse Duration	400	3600	s
Max co-extracted electron fraction j_e/j_{H^-} and j_e/j_{D^-}	0.5	1	
Max deviation from uniformity	10	10	%
Max divergence of beamlets	30	30	mrad

Table 1.1 – SPIDER parameters

the installation of optics and electronic components. In ITER, the source diagnostics will be limited to thermocouples. In SPIDER and MITICA, however, the much lower neutron flux (2-4 orders of magnitude less than ITER), allows the installation of plasma diagnostics [16]. Therefore, an extensive investigation of SPIDER parameters is necessary to study source plasma parameters, validate physics models and optimize the extracted beam in terms of uniformity and divergence.

- Negative ion density will be measured by Cavity Ring Down Spectroscopy (CRDS) [105], which is also one of the main topic of this thesis, and will be discussed in Sec. 4.1. CRDS will be performed along a 4 m long line in front of the plasma grid using a Nd:YAG laser.

- Cs dynamics will be monitored by a 852 nm tunable diode laser diode.

- Optical Emission Spectroscopy (OES) will be performed by many lines-of-sight (LOS) passing close to the plasma grid, to monitor the plasma in space and time. For the interpretation of OES measured quantities, such as the Balmer lines, collisional radiative codes are required to obtain plasma characteristics [45, 147].

- Beam Emission Spectroscopy (BES), which is based on the Doppler effect of the light emitted when beam particles collide with the background neutral gas, will be used to measure the beam divergence.

- To damp the ion beam, either the water-cooled Beam Dump or the high resolution STRIKE uncooled calorimeter will be used [139].

The experience acquired in SPIDER will be the basis for MITICA: the full-scale NBI line. It represents a large technological step to finally fulfill the requirements for ITER NBI. An overview of MITICA with its main components is shown in Fig. 1.11. The negative ion source for MITICA will have very similar features to SPIDER. The main difference will be the energy of the extracted ions, which will be 1 MeV for hydrogen and 870 keV for deuterium [139]. The operation
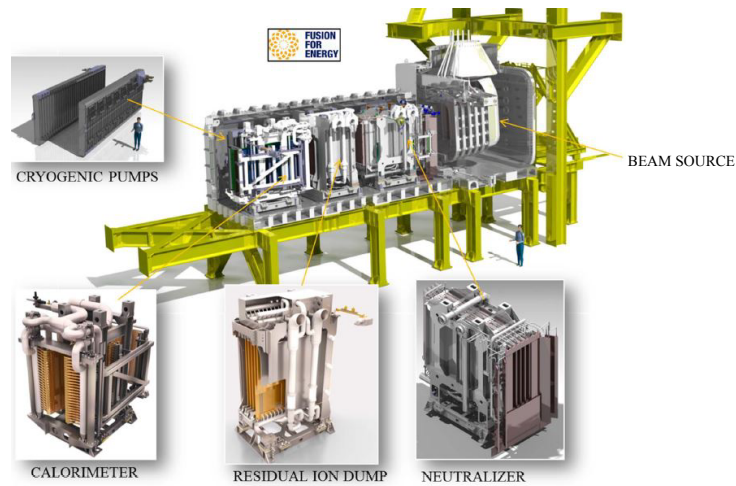
Figure 1.11 – Overview of the NBI prototype MITICA [139].

at a maximum pressure of 0.3 Pa will be crucial since backstreaming positive ion and thermal electrons may induce huge thermal loads at these energies. The extracted H$^-$ or D$^-$ will be neutralized in a gas cell neutralizer and can be dumped in the Residual Ion Dump. MITICA is expected to produce ∼ 17 MW of neutral beam power for 3600 s in the ion dump. Due to the presence of a high energy beam, the system will be subject to much higher neutron flux compared to SPIDER. In this case, optic and electric diagnostics are excluded. Nevertheless, MITICA will be equipped with a large set (about one thousand) thermocouples and thermal sensors installed all along the beam line. These sensors will measure the heat load distribution and could be helpful, apart from preventing thermal damage, to deduce intensity, uniformity and divergence profiles of the beam.

This is the state of the art of the NBI for ITER. It is very likely that the parameters listed in Tab. 1.1 will be achieved by SPIDER, since its working operation is based on many years of experience with RF caesium source. The question now is: can helicon plasmas achieve similar parameters? The goal of this thesis is to try to answer this question. In the next Section, we start by briefly introducing some concepts of helicon plasmas.

1.3 Helicon Plasmas

Helicon plasmas are plasmas sustained by the propagation of helicon waves, a category of whistler waves which can be found in nature such as in the Earth magnetosphere and are associated with lightning strikes [7]. Atmospheric lightning generates an electromagnetic pulse over a large frequency spectrum which propagates along Earth's magnetic field. Since the velocity of propagation depends on the frequency, the signal arrives broadened in time and, when converted to acoustic waves, it sounds like a descending frequency. Helicon plasmas can be produced in the laboratory and are usually long cylindrical magnetized plasma columns

enclosed in dielectric tubes. Plasma discharges are often achieved by means of radiofrequency antennas, usually known as *helicon antennas*, which are used to excite helicon modes.

The generation of helicon plasmas in the laboratory was first achieved by Boswell in 1970 [23] and since then, they have been extensively studied theoretically and experimentally. Helicon waves with cylindrical boundary conditions show a relatively simple dispersion relation. Nevertheless, the mechanism of helicon wave power deposition is not fully understood and simulation efforts are still underway. Nowadays, helicon plasmas are employed in a wide spectrum of fields such as in material processing for industrial applications, as plasma thrusters for space propulsion [125], and in controlled nuclear fusion. Helicon plasmas conditions can indeed reproduce quite well those of the tokamak Scrape-Off-Layer, therefore they are used to test materials subject to severe power fluxes, such as in proto-MPEX [113]. The next generation of tokamaks indeed might consist of more compact and powerful machines, leading to high power fluxes, therefore suitable materials are required.

1.3.1 Helicon Plasmas for Fusion

Another use of helicon plasmas, which is presently under investigation, is for the next generation of negative ions for NBIs, which will be discussed in this thesis.

For the next generation of NBI fusion devices, less power consumption and, perhaps, Cs-free negative ions sources, are envisaged to increase the overall efficiency of the power plant and, in turn, minimize the cost of electricity generated by fusion power. DEMO NBI design will be driven by Reliability, Availability, Maintainability, Inspectability (RAMI) and high efficiency requirements [130]. In this context, helicon plasma sources could be considered as a suitable alternative to current ICP sources for a number of reasons.

First, helicon discharges require less RF power compared to ICP to reach similar plasma density parameters. This is due to the intrinsic nature of helicon coupling which is able to achieve high electron densities, keeping the electron temperature low.

Second, they can operate at the pressures relevant for ITER (<0.3 Pa), required to reduce the negative ion losses by electron stripping.

Third, negative ions are volume produced although it remains to be demonstrated if the amount of negative ions will be sufficient to avoid the use of cesium. The achievement of the required parameters for NBIs without using cesium would be a very important and significant development.

Although helicon plasma sources have been extensively studied for space thrusters, their application in fusion remains largely unexplored today. Therefore, one goal of this thesis is to broaden our current knowledge of the physics of the volume production of negative hydrogen and deuterium ions in plasma sustained by a helicon wave, which has been investigated, as far as we know, by only a very few authors [117, 104].

Helicon plasma sources are currently proposed as a possible candidate as a source of negative ions for systems based on laser photoneutralization. A high power plasma source, such as in RAID (detailed in Sec. 2.1), is an intermediate step to investigate the physics and the techno-

logical challenges of such devices [127]. Although the integration of a helicon-based negative ion source in a neutral beam accelerator and neutralizer requires the study of compatibility of a plasma produced by a helicon wave with an extractor and an acceleration system, a characterization of the helicon source is fundamental for further developments.

One of the the main goals of this thesis is to study the physics of helicon plasma source, and in particular the physics of the volume production of negative ions in helicon plasma sources, which is poorly investigated. RAID is the ideal test testbench for these kind of studies thanks to the wide set of diagnostics and the ease to tune plasma parameters.

1.3.2 Theory of helicon waves

To create a laboratory plasma the usual procedure is to transfer energy from an electromagnetic wave to electrons which ionise a neutral gas, producing a plasma discharge. In radiofrequency discharges, the oscillating electromagnetic field of an antenna couples to electrons which accelerate and heat the plasma by collisions. The most simple kind of coupling is the capacitive coupling where the energy is directly transferred by an external electric field by electrodes in contact with the plasma. The limitation of capacitive discharges led to the development of Inductively Coupled Plasmas (ICP) where the external RF field is coupled across a dielectric wall without any electrical connection. The plasma is therefore heated by ohmic heating of the induced currents allowing high density and low pressure plasma discharges. Although ICP discharges are easy to generate, the electromagnetic wave cannot penetrate the plasma more than a distance λ called *skin depth* $\lambda \sim c/\omega_{pe}$, where ω_{pe} is the plasma frequency. The denser the plasma is, the smaller is λ, therefore the wave tends to be absorbed in a thin surface layer, making these plasmas limited in size. However, an efficient way to transfer energy all along the reactor, is by exciting helicon waves, as described below.

When a plasma is immersed in a sufficiently uniform magnetic field, higher plasma density can be achieved because of the reduction of radial losses. Furthermore, the magnetic field makes it possible to sustain helicon waves, which in turn, can deposit energy in the plasma by wave-particle interaction or particle collisions. The precise mechanism of power deposition is indeed not fully understood and there are many candidates to explain the higher density regimes such as: electron-ion and electron neutral collisions, electron Landau damping and mode conversion of plasma waves. Here, we briefly derive the dispersion relation of helicon waves which has been investigated by experiments in many works [33, 35, 90, 91, 126].

Considering a perfectly conducting plasma, helicon waves can be derived by the following equations:

$$\nabla \times \mathbf{E} = -\frac{\partial \mathbf{B}}{\partial t}, \tag{1.20}$$

$$\nabla \times \mathbf{B} = \mu_0 \mathbf{j}, \tag{1.21}$$

$$\mathbf{E} = \mathbf{j} \times \mathbf{B}_0 / e n_0, \tag{1.22}$$

where $\mathbf{B}_0 = B_0\mathbf{e}_z$ and n_0 are the magnetic field and density at the equilibrium and $\mathbf{B}$, $\mathbf{E}$ and $\mathbf{j}$ are the perturbed magnetic field, electric field and plasma density and μ_0 is the permeability in vacuum. Eq. 1.20 and Eq. 1.21 are the Maxwell's equation, where we have neglected the displacement current term $\frac{1}{c^2}\frac{\partial \mathbf{E}}{\partial t}$ in 1.21. Eq. 1.22 is Ohm's equation without resistivity. Using Eqs. 1.20, 1.21 and 1.22 and assuming a perturbation of the form $e^{i(m\theta + kz - \omega t)}$, which describes wave a pattern rotating clockwise when $m > 0$, or counterclockwise when $m < 0$ around the z-axis, the following relations can be found:

$$\nabla \times \mathbf{B} = \alpha \mathbf{B}, \tag{1.23}$$

$$\alpha = \frac{\omega}{k_\parallel}\frac{\omega_{pe}^2}{\omega_{ce}c^2}, \tag{1.24}$$

where ω, $k_\parallel$, ω_{pe} and $\omega_{ce} = \frac{eB_0}{m_e}$ are the wave angular frequency, the parallel wavenumber, the plasma frequency and the electron cyclotron angular frequency, respectively. Curling Eq. 1.23, we obtain:

$$\nabla^2 \mathbf{B} + \alpha^2 \mathbf{B} = 0. \tag{1.25}$$

The solutions of Eq. 1.25 are combinations of Bessel functions [33]. If cylindrical boundary conditions are defined, for example a cylindrical insulator surface, a standing wave pattern is formed in the radial direction [125]. In this case, we have a bounded whistler wave and α satisfies the equation $\alpha^2 = k_\perp^2 + k_\parallel^2$, where $k_\perp$ is the perpendicular wavenumber. It is then possible to obtain the following dispersion relation [39]:

$$k_\parallel^4 + k_\perp^2 k_\parallel^2 = \left(\frac{\mu_0 e n_0}{B_0}\right)^2 \omega^2. \tag{1.26}$$

Many kinds of antennas have been used to excite azimuthal modes such as single loop, Boswell type, saddle type, Nagoya type, half-helix type and planar type. The most commonly employed mode is $m = 1$ which results in higher plasma density compared to $m = -1$ [31]. The reason for the difference in plasma performance is still under debate.

Apart from the main helicon modes, these antennas can also excite electrostatic modes known as *Trivelpiece-Gould* (TG) modes [125] which are short wavelength radial modes close to the antenna edge which are strongly damped, while the helicon modes have a wavelength of the order of tens of cm and propagate in the plasma core and along the magnetic field lines, efficiently producing high density plasmas peaked on axis. In this thesis, in Sec. 3.6, we will experimentally compare the plasma coupling of a conventional half-helix antenna to an alternative helicon antenna in a birdcage geometry. It is not known what kind of helicon antenna is the best performing for fusion and a comparison with conventional helicon antenna

is needed to understand which antenna would be the most suitable. In Sec. 5, we will devote a particular attention to study the propagation of helicon waves in RAID to understand if the simple dispersion relation is respected, or, if there are more complex mechanisms of propagation. This could be likely the case since the plasma is not radially bounded.

1.4   Thesis Structure

This thesis presents a experimental and numerical investigations carried out on RAID aiming to deepen our knowledge of helicon plasma sources and to study the feasibility of a RAID-like plasma as source of negative ions for future NBIs. The contents of this thesis are structured as follows:

In Chapter 2, we describe the Resonant Antenna Ion Device (RAID) with its diagnostics and the range of operating conditions. We describe the plasma source, the Birdcage antenna, an alternative helicon plasma source, the control and acquisition system. We detail the RF equipment, such as the power generator, the antenna installation and the matching box.

In Chapter 3, we describe the plasma characterization by means of Langmuir probes and a microwave interferometer, to characterize the typical RAID hydrogen and argon plasmas. We study the stability of the plasma column and the plasma fluctuations by Langmuir Probes. We experimentally compare the Birdcage antenna with a more conventional Half-Helix antenna to explore the difference in stability regions on parameter space.

In Chapter 4, we show the experimental investigation of negative ions. We describe the implementation of the Cavity Ring-Down Spectroscopy (CRDS) system, the first time ever in a helicon plasma device. We detail the technical challenges of installing CRDS such as the stability of the optical cavity to thermo-mechanical distortions induced by the plasma, and we show results in hydrogen and deuterium plasmas. We also show the implementation of the LP laser photodetachment to measure the spatial distribution of negative ions and the electronegativity of hydrogen and deuterium plasmas. We combine CRDS and LP photodetachment to obtain the absolute negative ion density.

In Chapter 5, using a magnetic B-dot probe, we investigate the helicon wave field which propagates and sustains the plasma column. We describe the calibration of the probe and provide the wave mapping in the plasma column. We study the effect of various plasma parameters, the wave structure and propagation into the plasma. We numerically simulate the propagation of helicon waves in typical RAID plasmas and we compare with B-dot experimental results.

In Chapter 6, we show the implementation of a Thomson Scattering diagnostic in RAID in the framework of the AWAKE project for innovative acceleration by plasma wakefield, cur-

rently investigated at CERN. We describe the technical details and the results obtained in a high density argon plasma. We show that the experimental apparatus is suitable to measure electron density and temperature for AWAKE limited by the regime of coherent scattering and we provide preliminary estimates of the error.

In Chapter 7, we show numerical simulations to investigate hydrogen plasma discharge in support of experimental campaigns. We describe an hydrogen plasma model which includes a detailed hydrogen plasma chemistry, the transport of a magnetized plasma and the effect of boundary conditions. We show the spatial distribution of plasma species and we compare with experimental results.

In Chapter 8, we show the preliminary design of two negative ion extractors for RAID, a radial and an axial extractor. We discuss the latest advancements of RAID such as the operation with double antenna configuration and the Cybele concept of photoneutralization for a RAID-like plasma.

In Chapter 9, we provide Discussions and Conclusions.

2 The Resonant Antenna Ion Device

In this chapter, we describe the experimental apparatus where experiments have been performed: The Resonant Antenna Ion Device (RAID).

RAID is a helicon plasma device developed at the Swiss Plasma Center of École Polytechnique Fédérale de Lausanne for plasma physics investigations, producing steady-state plasma discharges including H_2 and D_2 relevant for fusion studies [53, 3, 4, 94] as well as He, Ar, N_2 and Ne for broader plasma physics investigations [138]. RAID plasmas are sustained by a non-conventional high power helicon antenna in a birdcage geometry capable to deliver up to 10 kW power. The measurements obtained in this thesis have been collected in RAID mostly in H_2, D_2 and Ar discharges.

RAID is employed on a routine basis for different purposes and the main research areas can be grouped as follows:

1. Study the feasibility of helicon plasmas as a source of negative ions for NBIs.

2. Investigatating the physics of helicon waves.

3. Test bench for diagnostics such as the Thomson Scattering, Laser Induced Fluorescence, Optical Emission Spectroscopy and Microwave Interferometry.

2.1 The RAID device

A picture of RAID is shown in Fig. 2.1. The main vacuum vessel is made of two movable sectors with multiple diagnostic accesses. The red glowing cylinder on the left is a water-cooled ceramic tube surrounded by the antenna source generating the plasma. The ceramic cylinder and the vacuum vessel are surrounded by six coils. Fig. 2.2 shows typical pictures in visible light of RAID plasma discharges, the column on the left and on the right are for hydrogen and argon, respectively. The pictures in Fig. 2.2 (a) and (b), are taken from the end of the plasma column from a porthole displaced by the mechanical axis of the chamber. The plasma column impinges on a target, partially visible in the picture. The pictures in Fig. 2.2 (a) and (b), are
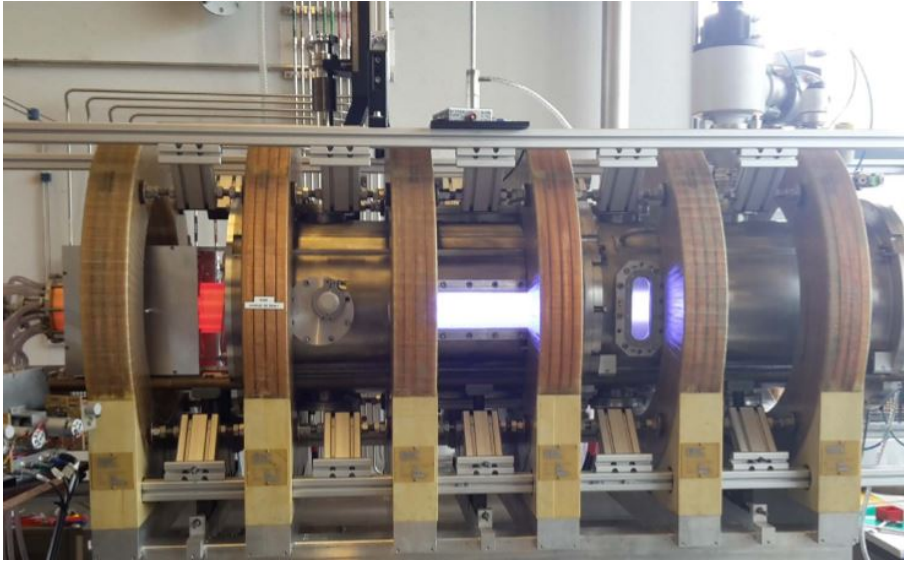
Figure 2.1 – Picture of the RAID experiment at the Swiss Plasma Center of École Polytechnique Fédérale de Lausanne. The RAID vacuum vessel is made of two movable sectors surrounded by six water cooled coils.
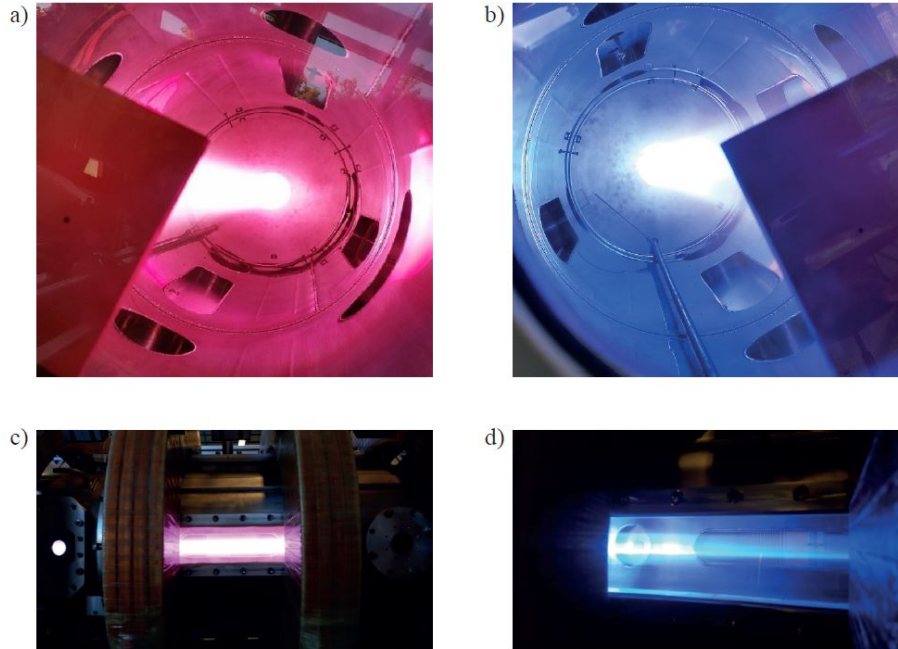

Figure 2.2 – Typical plasma columns produced by RAID in visible light. Downstream and side view for a hydrogen plasma respectively in (a) and (c) and for an argon plasma in (b) and (d).

taken from the side long horizontal port on the first section of the vessel. Fig. 2.3 shows a schematic drawing of RAID. The stainless vacuum vessel is 1.5 m long and 40 cm internal diameter, and the ceramic tube is 40 cm long and 8 cm diameter directly connected to the main vessel. The chamber is equipped with a primary rotary pump and a turbopump located on the top-right of the vessel, the gas pressure is controlled by mass flow controllers at a constant turbo pumping speed of 170 l/s. The vacuum system can reach a base gas pressure of at least 7×10^{-6} mbar. The vessel and the antenna are surrounded by six water-cooled copper coils producing an on-axis magnetic field up to 800 G. The cross section of the conductor is 20.83×15.75 mm^2 and it is made of 9 (radial) $\times$ 4 (axial) turns. The internal diameter is 52 cm, the external diameter is 82.6 cm. Each turn is electrically isolated with resin. Its ohmic resistance is ~ 5 mΩ and its inductance is ~ 6.4 mH. More details on the coils can be found in this reference [99]. The polarity of the source coil (first coil on the left) can be reversed with respect to the other five coils, to create a divergent magnetic field at the antenna position. This helps plasma ignition and stabilizes the helicon regime, resulting in a stable plasma over a wider operational space. The reason for this improvement is not well understood but might be due to the effect of a magnetic field gradient helping to confine slower electrons in the antenna region thus enhancing the ionization. The effect of varying the magnetic field in the antenna region will be investigated in Sec. 3.6 showing how this also affects the downstream plasma.

The plasma source, which consists of a helicon antenna in a birdcage geometry (see Sec. 2.1.2 for further details), is located in the left part of the device, in Fig. 2.3. Its length is 15 cm, its center is at the axial position $z = -0.235$ m and it surrounds the ceramic tube. The ceramic tube also allows installing a Half-Helix antenna, whose dimensions are very similar to the birdcage antenna (see sec. 3.6). The ceramic tube is made of an assembly of two coaxial tubes (internal diameter 9.5 cm and external diameter 11.5 cm) made of alumina (Al$_2$O$_3$). Between the two components, there are 8 equally spaced channels to allow water cooling (needed to avoid vacuum joint melting).

The plasma generated by the antenna mainly propagates along the magnetic field lines up to a water cooled target, made of a copper bulk and covered with a molybdenum foil to minimize ion sputtering. A variety of axial boundary conditions can be implemented, such as with insulators, grounded, floating and biased targets. Most of the results shown in this thesis have been performed with a ceramic cylindrical insulator at the end of the antenna, and the plasma target (shown in Fig. 2.3) electrically floating.

RAID has vacuum ports with various shapes along the main vessel allowing the implementation of a large variety of optical and electromagnetic diagnostics such as Optical Emission Spectroscopy, Cavity Ring-Down Spectroscopy, LP-photodetachment, Thomson Scattering, Laser Induced Fluorescence, B-dot magnetic probes, microwave interferometry and different types of Langmuir Probes. All these diagnostics have been employed to collect the data for this thesis and will be discussed in the next chapters. Tab. 2.1 summarizes the ranges of device and plasma parameters. Plasma columns have peaked n_e and T_e radial profiles with typical FWHM of 6 cm along the radial direction. The source is usually operated with the parameters listed in Tab. 2.2, which we define as *standard conditions* as follows: a base gas pressure of 0.3
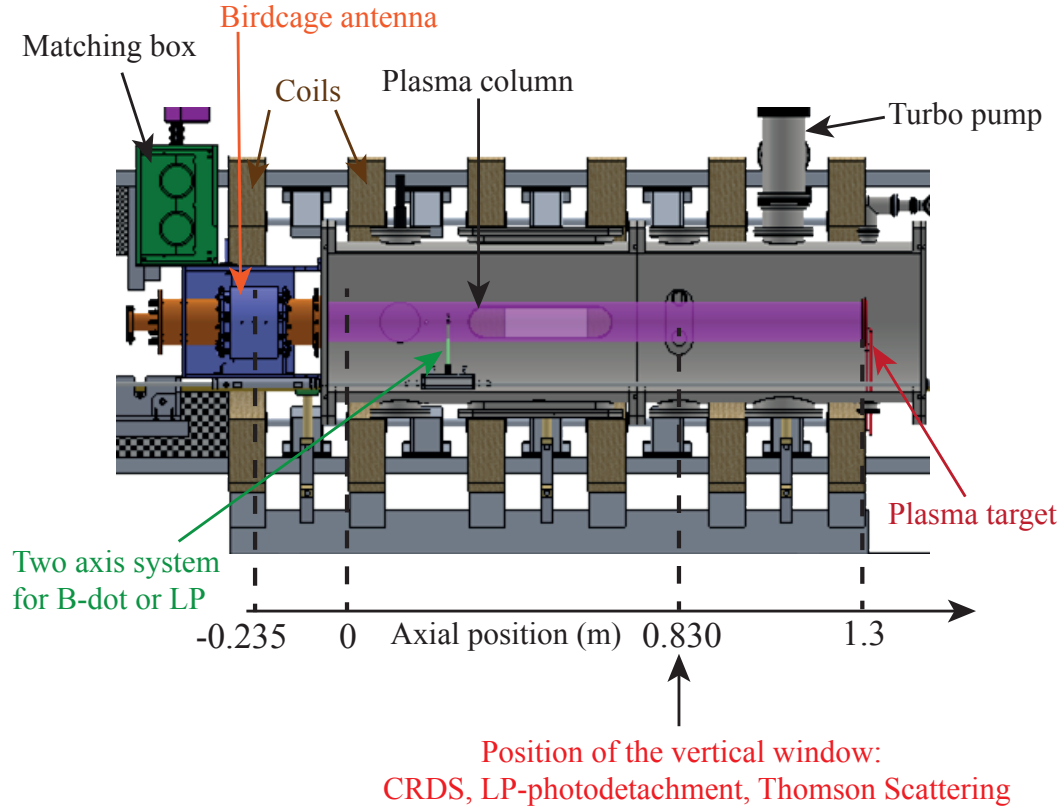
Figure 2.3 – Schematic of the Resonant Antenna Device including the location of the main diagnostics.

Pa, relevant for NBI applications, a current in the vessel coils of 150 A and -40 A in the coil surrounding the antenna, also called *counter field coil*.

When plasma is produced in standard conditions, density fluctuations are reduced and the power required for ignition is minimized. In standard conditions and 3 kW RF power, the peak electron density is about $\sim 2 \times 10^{18} \text{m}^{-3}$ for H_2 or D_2 and $\sim 1 \times 10^{19} \text{m}^{-3}$ for argon. Furthermore, plasma is ignited with 300 W in argon and 1000 W in hydrogen and deuterium. The operation with light ion plasmas is more difficult compared to heavy ion plasmas because: (1) the Bohm velocity, $u_B = \sqrt{k_b T_e / m_i}$, is larger for light ions plasmas, leading to larger axial losses; (2) when molecular gases are used, such as H_2, D_2, N_2 and O_2, a large fraction of the antenna power is used to excite the ro-vibrational channels or to dissociate the molecule. The plot showing the collisional energy loss per electron-ion pair created in Fig. 1 of Ref. [70] clearly shows the large difference between Ar and H_2. In RAID, the ignition of a H_2 plasma cannot be achieved with H_2 alone. The antenna is powered in the presence of a mixture of H_2 and Ar, then the Ar gas flow is stopped resulting in a H_2 plasma with low contamination.

Device Parameters		Plasma Parameters	
Antenna type	Birdcage/Half-Helix	**Electron density**	10^{16} to $10^{19}\,\mathrm{m}^{-3}$
Antenna length	15 cm	**Plasma n_e diameter (FWHM)**	6 cm
RF power (nominal)	0.3 - 10 kW (steady state)	**Electron Temperature**	1 - 10 eV
Magnetic field on axis	50 - 800 G	**Ion Temperature**	$\sim 0.1\,\mathrm{eV}$
Gas species	H_2, D_2, Ar, He, N_2, Ne	**Ion Flux (on target)**	$\sim 10^{21}\,\mathrm{m}^{-2}\mathrm{s}^{-1}$
Pressure	0.15 - 1 Pa	**Power Flux (on target)**	$\sim 100\,\mathrm{kW/m}^2$

Table 2.1 – RAID general machine and plasma parameters.

Antenna type	Birdcage
RF power	1 - 8 kW
Gas pressure	0.3 Pa
Vessel coils current	150 A
Vessel peak field	200 G
First coil current	-40 A
Field in antenna center	30 G
Antenna boundary condition	Dielectric
Downstream boundary	Floating

Table 2.2 – RAID *"standard conditions"* for a H_2 or D_2 plasma discharge.

2.1.1 Magnetic Field

The axial magnetic field is necessary for the propagation of helicon waves and to radially confine the plasma. RAID operates with two separate groups of coils, a source coil and the vessel coils. Each coil is made of $4\,\mathrm{axial} \times 9\,\mathrm{layers}$ of loops, with a central channel for water cooling. Two DC power supplies feed the two sets of coils with a current ripple lower than 1%. The solenoids are cooled by forced water convection in copper pipes and can be continuously operated up to 800 A. The distance between each coil is $21(\pm 0.5)\,\mathrm{cm}$ to optimize the axial homogeneity of the magnetic field. Fig. 2.4 shows the spatial and on-axis magnetic field produced in standard conditions, namely with -40 A in the source electromagnet (producing a counterfield) and 150 A in the vessel electromagnets. The on-axis magnetic field intensity shows a strong gradient in the antenna region, a peak at 20 mT in the center of the vessel, and a decay to 10 mT at the target position. Most helicon sources operate with uniform magnetic fields, even thought the propagation of helicon waves in divergent magnetic field geometries was also investigated [135]. When only the source coil is turned on, the plasma is partially transported in the main chamber; when all coils are turned off, the plasma coupling is purely inductive and the plasma is confined in the region of the ceramic tube corresponding to the antenna length.
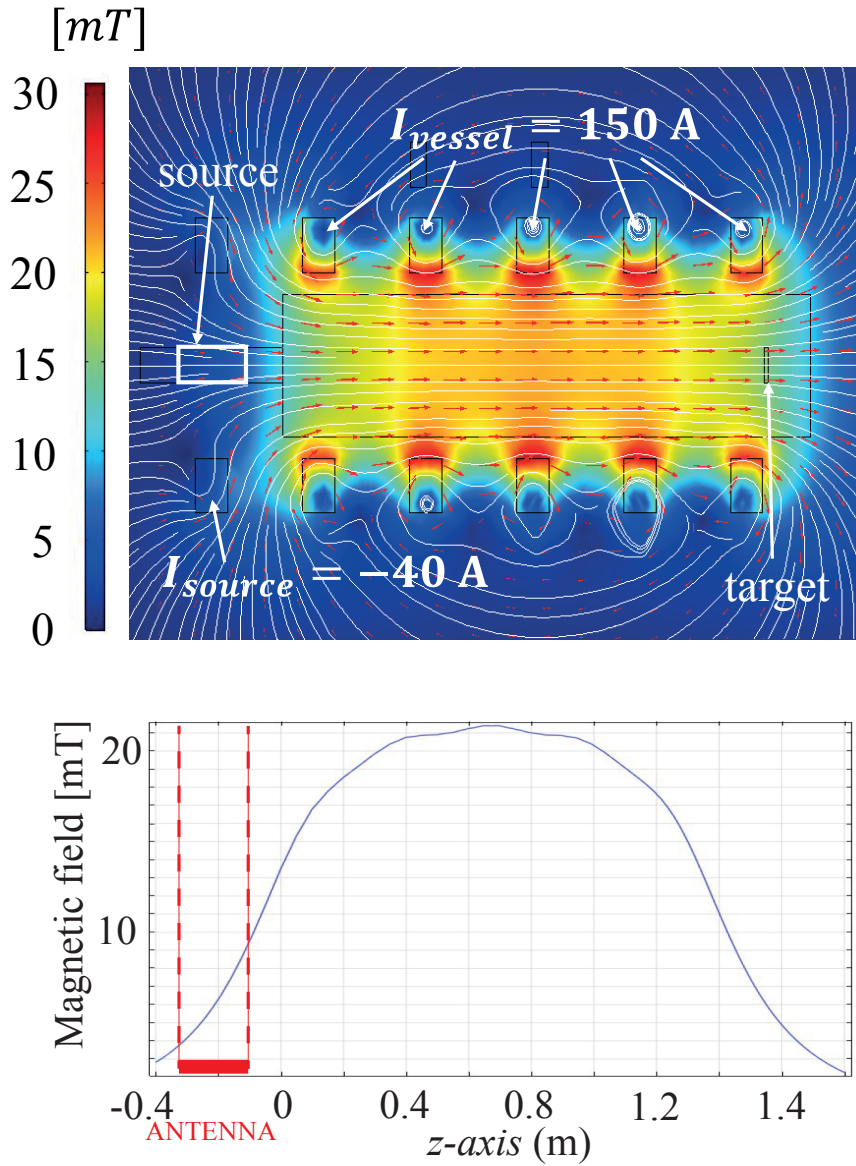
Figure 2.4 – (a) Magnetic field mapping on *"standard conditions"*: -40 A in the source coil (counter field) and 150 A in the vessel coils and (b) Intensity of the magnetic field on axis for same parameters and axial position of the antenna in red.

a)

b)
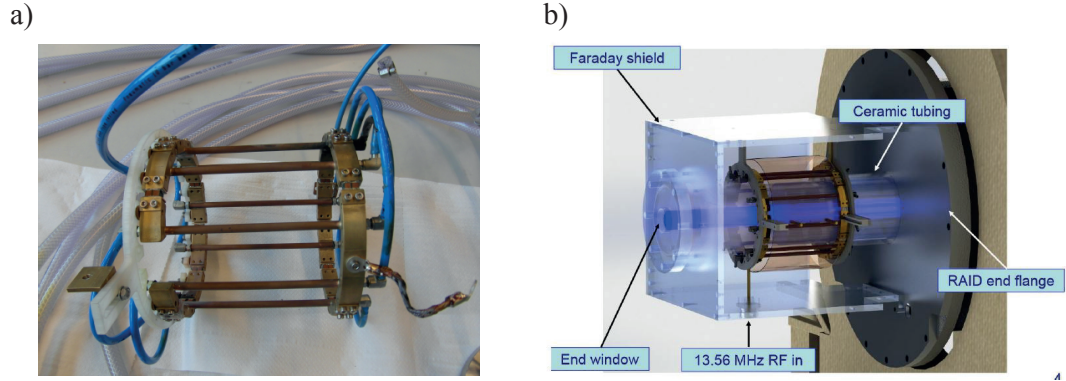
Figure 2.5 – (a) Picture of the birdcage antenna showing the copper legs, the position of the capacitors and the tubes for water cooling. (b) Location of the birdcage antenna mounted on the ceramic tubing at the RAID and flange. The antenna is enclosed in a Faraday screen to limit RF emissions.

2.1.2 The Birdcage Antenna

RAID plasmas are produced and sustained by an innovative resonant helicon antenna in a birdcage geometry [61], shown in Fig. 2.5. The birdcage antenna geometry is commonly used in nuclear magnetic resonance (NMR) for excitation and detection. In helicon wave physics, different antenna configurations were developed with the main idea to match the RF field generated to the helicon wave field in plasma, such as Nagoya, half-helix, Boswell type and paddle shaped [31]. Since the helicon field has a rotating pattern, these antennas are usually in a twisted geometry to enhance the matching. The birdcage antenna has been created with the idea that, to well match the helicon wave field, one should then have an azimuthal distribution of RF current. Indeed, the birdcage antenna is made of 9 conducting parallel copper bars, inductance L and resistance R, in a cylindrical geometry. Each leg is connected with its closest neighbours at the extremities with mica capacitors with capacitance C = 3840 pF. The birdcage antenna has a resonant frequency which is specific to the geometric arrangement and the impedance value of its components. When it is excited by a radiofrequency source, an azimuthal sinusoidal distribution of oscillating currents is generated in the antenna legs. The L, C, R values are chosen so that it resonates close to 13.56 MHz, a standard industrial frequency, which makes it easier to use commercial RF equipment.

We briefly describe here the principle of the planar antenna, whose structure and operation are similar to the birdcage antenna but it is unwrapped on a plane as shown in Fig. 2.6. Solving the Kirchhoff equations in open boundary conditions of the planar network, one finds that there are $N-1$ resonant modes m. Each mode has a characteristic frequency ω_m given by:

$$\omega_m = \frac{1}{\sqrt{C\left(M + 2L\sin^2\left(\frac{m\pi}{2N}\right)\right)}}, \qquad \text{with} \quad m \in [1, N-1]. \tag{2.1}$$
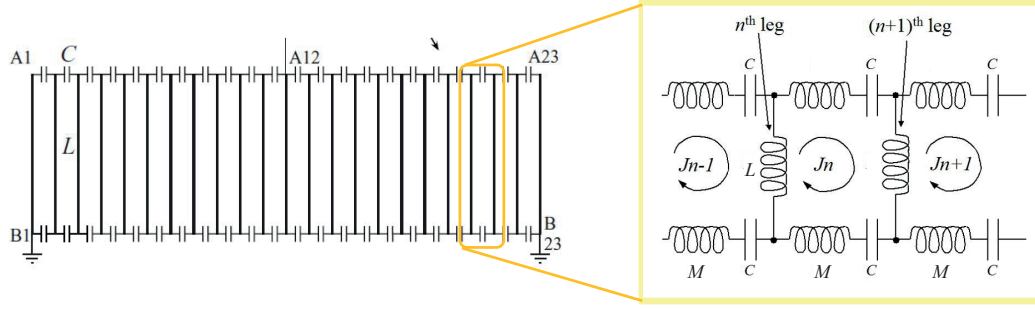
Figure 2.6 – Electrical scheme of the unwrapped birdcage antenna.

Suppose that the antenna is excited at one resonance frequency by a potential $V_{in} = V_0 \cos(\omega t)$ in one node, and grounded in another. The current through the legs I_n and the capacitors is:

$$I_n = \frac{2V_0}{DL\omega_m} \dot{\cos}(k_m(2n-1)) \sin(\omega t) \tag{2.2}$$

$$M_n = \frac{V_0}{DL\omega_m} \left(\frac{\sin(2k_m n)}{\sin(k_m)} \right) \sin(\omega t) \tag{2.3}$$

with $k_m = \frac{m\pi}{2N}$. The voltages to the nodes A_n and B_n can be expressed as:

$$A_n = \frac{V_0}{D} (\cos(k_m(2n-1)) - \cos(k_m(2N_g-1))) \cos(\omega t) \tag{2.4}$$

$$B_n = -\frac{V_0}{D} (\cos(k_m(2n-1)) + \cos(k_m(2N_g-1))) \cos(\omega t) \tag{2.5}$$

where:

$$D = \cos(k_m(2N_f-1)) - \cos(k_m(2N_g-1)). \tag{2.6}$$

We remark that a sinusoidal distribution of currents and potential is present in the resonant network. Before installing the antenna on the ceramic tube, the resonance spectrum of the antenna is usually measured. An example of the measured magnitude of the real and imaginary part of the impedance of the RAID birdcage antenna without plasma is shown in Fig. 2.7; it resonates close to 13.56 MHz with a peak value of about 110 Ω. The peak position can be finely tuned in a range of 2 MHz, by means of two metal half cylindrical screens. When the birdcage antenna is operated in the presence of a plasma, the position of the resonance peak shifts to higher frequencies and the curve tends to broaden [71]. Since the impedance of the system antenna-plasma changes with operating conditions, a matching system is needed
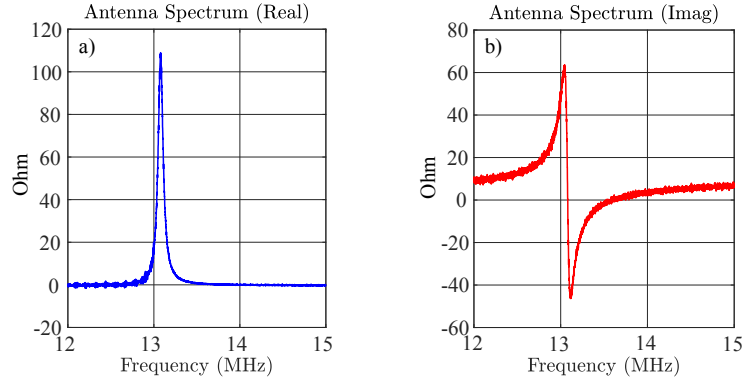
Figure 2.7 – (a) Real and (b) Imaginary part of the impedance of the birdcage antenna measured with a spectrum analyzer.

to minimize the reflected power to the power generator. In RAID this is performed by a T-type matching network, described in Sec. 2.1.3.

2.1.3   Control and acquisition

Pumps, vacuum valves, vents, water valves and water flows data are not acquired neither controlled numerically. The pumping status and the pressure inside the chamber are controlled by the operator before the experiments. Also the water cooling, for the antenna, the matching box, the ceramic tube, the RF power generator and the target, are manually controlled by the operator by means of mechanical knobs. The safety system shuts down immediately the power generator if cooling water in not flowing.

Automatic RF matching system

To deliver the power to the antenna and to minimize the reflected power, RAID is equipped with an automatic matching system developed by Helyssen®. Since the plasma can be represented as a non-perfect conductor for the antenna, depending on the plasma parameters, its impedance changes, requiring a feedback control to adjust the impedance of the transmission line. The IVPhi head (shown in Fig. 2.8), measures the current, the voltage and the phase at the input of the matching box, whose internal components are shown in Fig. 2.9. Then, a micro controller calculates the real (Re) and imaginary (Im) parts of the impedance, and adjusts the variable capacitors C1 and C2 to reach Re = 50 ohm and Im = 0 ohm, corresponding the output impedance of the generator. By minimizing the length of the coaxial cable between the matching box and the antenna, the reflected power is typically < 1% with respect to the total delivered power.

Since the impedance of the antenna does not vary without plasma, when no current flows through the IVPhi device (no power delivered from the RF power generator), the capacitors C1 and C2 are turned to a reference initial position. Once the RF power is delivered to the antenna,
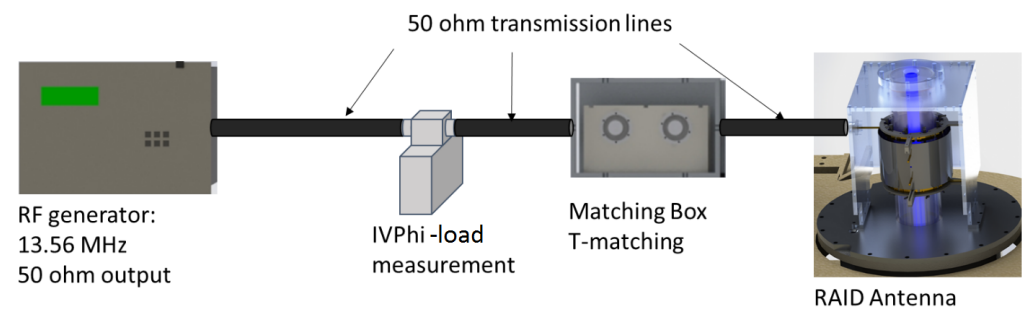
Figure 2.8 – Block schematic of the matching system in RAID. The power is delivered by a 15 kW, 13.56 MHz RF generator to the birdcage antenna. The matching box automatically adjusts its impedance to minimize reflected power to the RF generator.
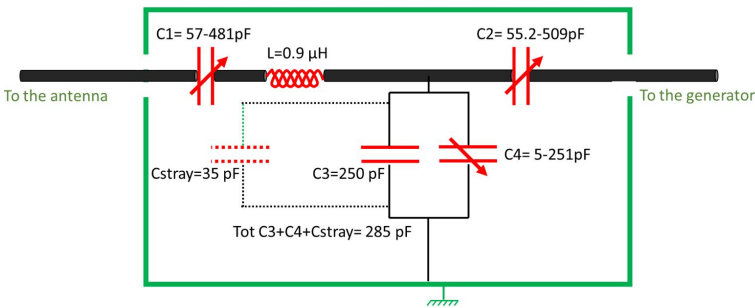
Figure 2.9 – Electrical components of the matching box.
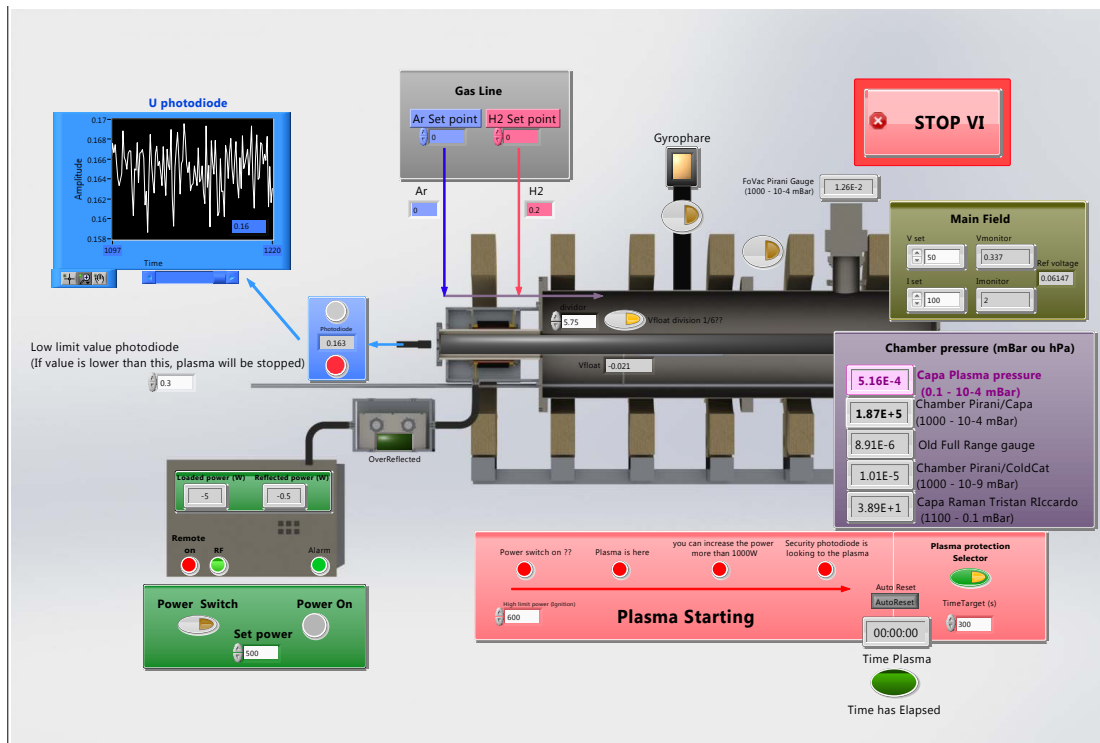
Figure 2.10 – Labview interface to control RAID parameters such as the RF power, the aperture of the gas flow controllers and the current flowing in the coils.

the system automatically modifies the values of C1 and C2 so that the load impedance at the end of the RF line is close to 50 Ohm.

Control and acquisition of the main plasma parameters with LabVIEW and NI modules.

The control of RAID machine parameters (magnetic field, pressure gauge and delivered RF power) is performed by a NI USB-6343 module from National Instruments. The user interface is developed in LabVIEW, as shown in Fig. 2.10. With some analog inputs, the operator can have a quick access to the pressure in the chamber, the gas flow, the power delivered to the antenna, the current flowing in coils, and the intensity of the visible light emitted by the plasma in the visible light (see below). Analog outputs are used to adjust the different parameters to achieve a plasma discharge with an arbitrary combination of parameters. Another important role of LabVIEW is to verify the presence of the plasma in the vessel. A plasma shutdown can occur due to different factors such as the development of a plasma instability, a sudden variation of gas pressure or a failure in current supply to current coils. If the RF power generator continues to deliver the power to the antenna when no plasma is present, a huge amount of power is dissipated in the antenna. If this power is not dissipated into the plasma, the high current can burn the antenna capacitors. To avoid capacitor failure, a safety system consisting of a photodiode monitoring the plasma light is employed. When the light detected by the

photodiode is below a threshold, the power generators shuts down.

Control of the probe positioner

On the same NI USB-6343 module, two counter signals are used to control two stepper motors enabling the positioning of different probes inside the RAID vessel. One moves the probe along the axial direction, and the other along the radial direction. Before any test, the probe is sent to the home position, set by two mechanical end-switches. The positions of these two switches give the absolute zero (axial and radial) of the probe. The position of the probe is calculated by counting the number of steps performed by the motor.

2.1.4   Considerations on hydrogen and deuterium plasmas

The capability of the birdcage antenna to sustain hydrogen and deuterium plasma discharges makes it interesting for fusion applications. Hydrogen and deuterium plasmas deserve a particular attention because their chemistry and dynamics is quite different from atomic gases. We discuss here the case for hydrogen but the same applies for deuterium.
Owing to the molecular nature of hydrogen, a pure hydrogen plasma can contain different atomic and molecular species, such as neutral atoms and molecules (H and H_2) and positive and negative ions (H^+, H_2^+, H_3^+, H^-) and the electrons. In a low temperature hydrogen plasma, each species is significant in the plasma mixture and therefore the equilibrium properties of the plasma are determined by all interactions between the multiple plasma components. Moreover, the hydrogen molecule shows a number of electronic, vibrational and rotational states [120], which can strongly affect the overall plasma chemistry. For example, the cross section of the dissociative attachment reaction, described in Sec. 1.2.1, is highly dependent on the vibrational state [78] and therefore the negative ion rate production. Fusion plasma, however, are made of a mixture of H^+ and electrons and the other species do not play an important role in plasma equilibrium.
To determine the total density of the dominant hydrogen positive ion species, one can compare the microwave interferometry and LP measurements along the same line of sight [93], but there is no diagnostic able to measure the ratio of the different species. We will further discuss the numerical simulations of the plasma transport in the RAID scenario in Sec. 7. A typical hydrogen plasma in RAID in shown in Fig. 2.2. The plasma consists of a bright and uniform column from the antenna region (center) to the target (shown in the bottom-right).
Although deuterium has very similar atomic cross sections to hydrogen, the isotopic effect leads to considerable difference in the molecular vibrational state of the molecule and in global plasma transport. Indeed, the dissociative attachment cross section for D_2 shows a significant difference compared to H_2 [81]. Deuterium plasma discharges show larger electron densities compared to hydrogen when the same source parameters are used. This is evident in D^- extraction experiments, which are always characterized by higher co-extracted currents compared to hydrogen plasmas [131]. In this thesis, we investigate the isotopic effect in helicon plasmas, which has been poorly described so far.

2.1.5 Overview of Plasma Diagnostics

The purpose of this section is to present a short overview of all the diagnostics, which can be installed on RAID. The specific hardware and the techniques will be discussed in detail in the next chapters.

RAID is equipped with several glass and plexiglass windows along the vacuum vessel: one circular 10 cm diameter whose center is 20 cm from the left side of the vessel, a 40 cm long horizontal antenna in the center and a 15 cm high and 6 cm wide vertical window downstream at the axial position $z = 83$ cm (see Fig. 2.3). Many laser-based diagnostics discussed in this thesis are located at this axial location.

In Fig. 2.2, a 2-axis system can move axially and radially inside the plasma column holding either a LP or a B-dot probe. The origin of the z-axis corresponds to the leftmost position of the two-axis system, 5 cm from the left flange of the chamber vessel. The rightmost position of the 2-axis system is at $z = 1.3$ m, where the water cooled target is located. Additionally, a radially moving LP can be installed on the top at $z = 83$ cm and at $z = 53$ cm. Another LP can be installed to measure the plasma in the antenna region and can be displaced along the axis. This LP however suffers a non negligible RF noise due to the proximity to the high voltage antenna legs, more details on the LPS are in chapter 3.

As in many basic plasma physics devices, each diagnostic can measure only one or a few plasma parameters, thus, multiple diagnostics are needed to have a complete comprehension of the whole plasma dynamics. Owing to the high plasma density which can be achieved in RAID, LPs, which are commonly considered as simple and robust diagnostics, showed limited application in RAID. Therefore, other microwave-based and laser-based diagnostics were employed such as the microwave interferometry, the CRDS, the LP laser photodetachment and the Thomson Scattering.

The positive ion density and the electron temperature are measured with LPs with spatial resolution of the order of a few mm and temporal resolution of the order of the period of the voltage sweep, which is about 0.1 s. LPs suffer strong heating for an electron density larger than a few 10^{18} m^{-3}, which is achieved in argon gas with a relatively low RF power ($\sim$ 600 W), and in hydrogen or deuterium with about 3000 W RF power. This limits the use of LPs to the edge of the plasma column and for low RF powers.

To measure the electron density profile at high powers we use a 100 GHz microwave interferometer (described in chapter 3) and a LP which quickly passes through the plasma along the same line of integration as the interferometer. The interferometer is a robust and reliable way to measure plasma line integrated density, however it lacks in terms of spatial resolution along the chord.

To measure the electron density and temperature in high density plasmas, such as in the core of an argon discharge, a Thomson scattering diagnostic was developed, described in chapter 6. The system is able to measure electron density down to 10^{18} m^{-3} and electron temperature down to about 2 eV. The spatial resolution is of the order of a few mm and the temporal resolution of the order of the laser pulse duration, which is a few ns.

Negative ions in plasmas could be theoretically detected by LPs by measuring the shape of the

second derivative of the IV probe characteristic. This technique is used when the electronegativity of plasma is about 1 or more [111]. However, in the case of low temperature hydrogen plasmas, the electronegativity is of the order of $\sim 10\%$, and the negative ion density is too small compared to the typical noise on the IV curves. Therefore, the measurements of negative ions in such plasmas requires other dedicated techniques.

RAID can be equipped with Cavity-Ring Down Spectroscopy (described in Sec. 4.1), which measures the line integrated density of negative ions by photodetachment. It is a direct and non invasive technique, however, the sensitivity of the optical cavity to particle bombardment and the non local nature of the technique requires the use of complementary methods to detect negative ions. One of these is the LP laser photodetachment (described in Sec. 4.2), which has a spatial resolution of the order of a few mm but requires the use of LPs which could affect plasma parameters. The combined use of the two diagnostics, however, is employed to determine the absolute volume distribution of negative ions.

The propagation of helicon waves is measured by a B-dot probe on the two axis system with a spatial resolution, along the axial direction, of less than 1 cm, which is sufficient to measure the parallel wavelength, but not the radial wavelength which is expected to be of the order of a few mm. The design of a smaller and actively cooled B-dot probe is envisaged. This would allow a more precise mapping and the study of finer modes of helicon propagation.

The temperature and the density of ion species, such as H^+, H_2^+ and H_3^+ is determined by OES measurements interpreted by a collisional radiative code. The temperature of molecular species is estimated by the analysis of rovibrational levels.

The density of H is not currently measured in RAID, but the development of a TALIF system is envisaged, which would also allow to determine the temperature of H by Doppler effect.

2.1.6 Basic Plasma Studies in RAID

The high versatility of RAID in terms of accessible ports and related diagnostics allows a variety of basic plasma physics studies, beyond the main use for negative ions for fusion. First of all, RAID is a linear steady-state helicon plasma device: this simplifies the use of many diagnostics and makes the plasma highly reproducible. Unlike toroidal devices, linear plasma devices are more easily accessible for diagnostics and plasma transport can be relatively easily modeled. The production of impurities is a major issues in many linear plasma devices, where cathodes or filaments are employed. Since helicon sources do not have any electrode inside the source, these can produce high densities in hydrogen and helium making them attractive for experiments relevant to fusion. The magnetic field can be relatively easily shaped to study different magnetic geometries, for example, a divergent magnetic field is interesting for space thruster investigations (see Sec. 8.2).

RAID can produce high power helicon plasmas, up to 10 kW, as one of the few device in the world [117], in hydrogen and in steady state regime. RAID currently operates with a single helicon antenna but the use of a double birdcage antenna configuration to achieve high powers and more homogeneous plasmas is under investigation (see Sec. 8.2). High power helicon plasma is a novel area of research offering the possibility to study not fully understood

phenomena such as the neutral depletion which might also be a factor limiting the power deposited by the helicon wave [97, 92]. In high power helicon plasmas, the electron pressure can be comparable to the neutral pressure, so that neutrals could be expelled from the plasma core and therefore no further ionization can be achieved.

2.2 First evidence of negative ions in RAID

An optical emission spectroscopy campaign performed in RAID in 2017 gave the first hints of the presence of negative hydrogen ions in RAID plasma [94]. The first Balmer lines α, β, γ and the Fulcher-α were measured with a $f/2$ spectrometer for both H_2 and D_2 plasmas. The radiance profiles were Abel inverted to obtain the absolute emissivity profiles. The absolute line emissivities were then interpreted with the collisional-radiative code YACORA [147] to estimate the degree of dissociation, the density profiles of atomic and molecular species and of the ions, including H^- and D^-. YACORA solves the rate equations for 40 states of H, taking into account the excitation and de-excitation by electron collision, the spontaneous emission, the recombination of H^+, the dissociation of H_2 and the mutual neutralization of H^- with the positive ions. Three body reactions are also taken into account. However, the opacity is neglected because of the low pressure (0.3 Pa). Fig. 2.11 shows in (a) the degree of dissociation, in (b) the degree of ionization, in (c) the density of H^+ and in (d) the density of H^-. The degree of dissociation is defined as:

$$D_d = \frac{\frac{n_H}{n_{H_2}}}{\frac{n_H}{n_{H_2}} + 2}.$$ (2.7)

The degree of ionization is defined as:

$$D_i = \frac{n_e}{n_H + n_{H_2}}.$$ (2.8)

The dissociation is quite flat in the center of the plasma column around 20% and the ionization is peaked at the center reaching about 0.7%. Also n_{H^+} is narrow peaked at the center reaching $2 \times 10^{17}\,\mathrm{m}^{-3}$. The most interesting plot is that of the density of the negative ions H^-, showing an off-axis peak at $\sim 4\,\mathrm{cm}$, where the density reaches $2 \times 10^{16}\,\mathrm{m}^{-3}$. Moreover, measurements of the density of H^- and D^- showed a linear increasing trend with power, as shown in Fig. 2.12, suggesting that high power helicon plasma sources may produce densities of negative ions high enough for fusion related applications.

These measurements were the first evidence of the presence of volume produced negative ions in RAID and partially motivated the present thesis. The design of the laser based diagnostics discussed in Sec. 4.1 and Sec. 4.2, namely the Cavity Ring-Down Spectroscopy and the LP laser photodetachement, were driven by this very first evidence of negative ions.
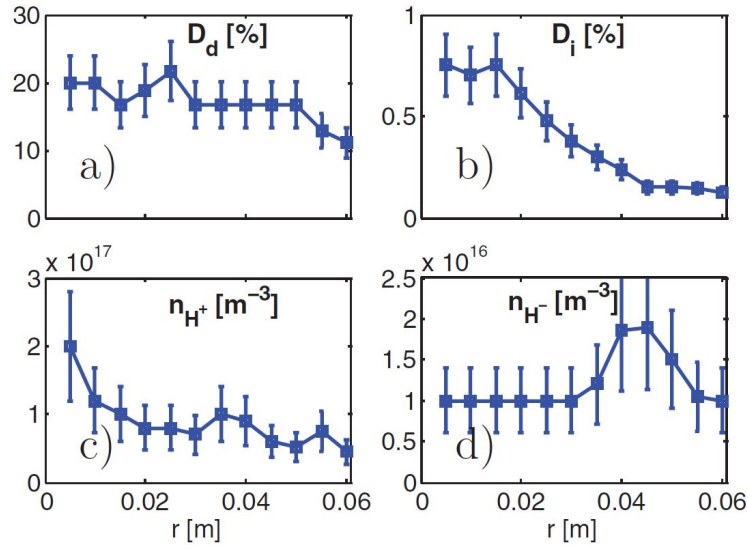
Figure 2.11 – (a) degree of dissociation, (b) degree of ionization, (c) density of H^+ and (d) density of H^-, estimated by YACORA for an input power of 3 kW in hydrogen in RAID (from [94]).
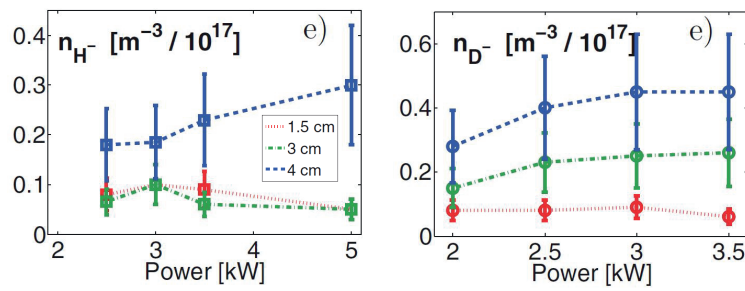
Figure 2.12 – Power scan in hydrogen and deuterium for the radial position 1.5, 3 and 4 cm (from [94]).

3 Characterization of the RAID plasma

The goal of this chapter is to characterize the RAID plasma column as a base for further more detailed investigations. The knowledge of plasma parameters is fundamental to understand how the source works. This is achieved by standard plasma diagnostics such as Langmuir Probes (LPs) and microwave interferometry. We show the LP theory and how LPs are implemented in RAID to measure the main plasma parameters. LPs can be used in RAID despite the not negligible magnetization and the high power operations. LP measurements are usually calibrated with a microwave interferometer to determine the absolute electron density. We provide steady state 3D profiles of electron temperature, electron density, floating potential and plasma potential and typical plasma fluctuations measured by LPs in I_{sat}. We also compare plasma density profiles produced by the Birdcage antenna with a conventional Half-Helix antenna.

3.1 Langmuir Probes

The Langmuir Probe is an electrostatic probe which measures the main plasma parameters such as the floating and plasma potential, the electron temperature and the electron density. In this standard implementation, LP consists of a small conducting tip, cylindrical, spherical or planar [28], which collects electrons and/or ions when biased at different voltages. The LP works like an electrostatic filter for the plasma particles, selecting the energy of particle from which plasma parameters can be calculated.

LPs are one of the most employed devices in plasma physics owing to its simplicity of construction and installation, the relatively simple data interpretation, and the low cost. The most simple kind of LP is the uncompensated probe whose implementation is straightforward but it has to be used carefully since it can be easily influenced by RF field sustaining the plasma discharge. In the following section we will describe how uncompensated LPs are employed to determine the time-averaged and time-resolved plasma parameters in RAID.

3.1.1 Classical theory of Langmuir Probes

The collection of plasma particles by a LP depends on the transport of electrons and ions across the plasma sheath, which is the region where quasi-neutrality is not satisfied. A LP can be biased at different potentials to select the kind of collected particles. The current I_{pr} collected by a probe biased at the potential V_{pr}, in a collisionless isotropic plasma (no magnetic field), is described by the following equation [133]:

$$I_{pr}(V_{pr}) = I_{sat}\left[1 - \alpha(V_{pr} - V_{fl}) - \exp\left(\frac{V_{pr} - V_{fl}}{T_e}\right)\right],$$ (3.1)

where V_{fl} is the floating potential, I_{sat} the ion saturation current and α is an empirical parameter which takes into account the expansion of the sheath [137, 54]. The sheath expansion consists in the increase of the collection area of the probe when it is biased at negative potentials. I_{sat} is given by:

$$I_{sat} = 0.61 e n_i A_{eff}\sqrt{\frac{k_b T_e}{m_i}},$$ (3.2)

where e is the electron charge, n_i is the ion density, A_{eff} the effective collection area of the probe, k_b the Boltzmann constant, m_i the ion mass and T_e the electron temperature. Also we are considering the ion temperature $T_i = 0$. A reasonable estimate of the electron temperature can be obtained by measuring only the floating and the plasma potential. In the floating regime, a zero net current is drawn by the probe, so that the electron flux is equal to the ion flux to the probe; by equating the two fluxes we obtain:

$$V_p - V_f = \frac{kT_e}{2q_e}\ln\left(\frac{m_i}{2\pi m_e}\right),$$ (3.3)

where V_p is the plasma potential. For a hydrogen plasma, Eq. 3.3 gives:

$$\frac{kT_e}{q_e} \approx \frac{V_p - V_f}{2.8}.$$ (3.4)

This is a practical and widely employed way to obtain the electron temperature in a cold plasma. In such a plasma, typical electron temperatures range from 2 to 5 eV, also suggested by particle balance considerations [89]. The estimate of the electron temperature can also be performed by fitting the exponential part of the IV curve and by subtracting the ion current. In the case of RAID, rather than using the just presented classical theory of LPs to interpret IV curves, we employ a recent theory described in Ref. [62]. This theory includes the sheath expansion described by the empirical factor α in Eq. 3.1.

In the following section we show the analysis of a typical IV curve measured in RAID using the
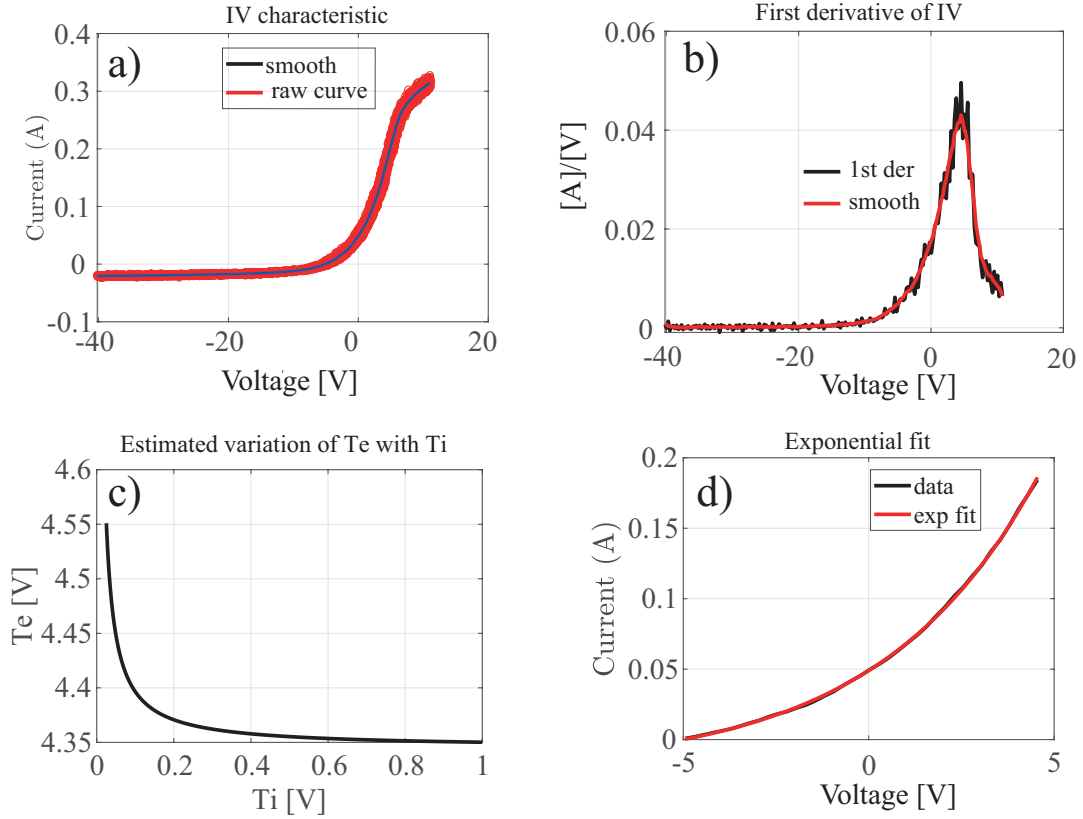
Figure 3.1 – Procedure of analysis of a IV characteristic. (a) raw IV characteristic with smoothing for a H_2 plasma and 2.5 kW RF power in the plasma core at 75 cm from the center of the antenna. (b) First derivative and smoothing to determine the plasma potential. (c) Variation of T_e when T_i is varied. (d) Exponential fit of the electron branch to determine the electron temperature T_e.

theory described in Ref. [62].

3.1.2 IV curves analysis and interpretation

We discuss here the analysis procedure of a typical IV characteristic in RAID. The analysis of experimental IV characteristics in RAID is performed by the method described in [62], which shows the solution for a one-dimensional problem of LPs in a collisionless, isothermal plasma. Fig. 3.1 (a) shows an IV characteristic for a H_2 plasma in the center of the plasma column and 2.5 kW RF power. The analysis of IV characteristics requires a smoothing (average on 5 or 7 points usually) since even a small noise in the raw curve would lead to huge fluctuations of the derivative. The technique is to apply a moving average until data points show a monotonic trend. When required, the current points are excluded by the calculation, for example for large electron current, above the plasma potential, where the effect of RF and B field is more important. As a next step, the first derivative, Fig. 3.1 (b), is computed. Fig. 3.1 (b) shows

both the first derivative of the smoothed IV characteristics, which reaches its maximum close to the plasma potential V_p. The first derivative is smoothed as well to more precisely find the position of V_p. The floating potential computed by finding the zero crossing point of the IV curve, where the electron current is equal to the ion current. Only the portion of the IV curve between V_f and V_p is analyzed. According to the model in [62], the electron and the ion current at the probe surface are given by:

$$J_e = q u_{the} n_0 e^{-\frac{1}{2}} e^{\frac{V_a - V_p}{T_e}},$$

(3.5)

$$J_i = -q u_{thi} n_0 \sqrt{U_i(V_a)} e^{\frac{U_i(V_a)}{2} - \frac{V_a - V_p}{T_i}},$$

(3.6)

with V_a (the applied voltage) in the range $[V_f, V_p]$, u_{the} the electron thermal velocity, u_{thi} the ion thermal velocity, n_0 the electron density respectively. In this equation, U_i is a function of the ion temperature. Since the ion contribution to the total current is rapidly negligible above the floating potential, a small error results by assuming constant ion contribution in the range $[V_f, V_p]$, which is equal to the ion current at the floating potential. Fig. 3.1(c) shows the effect of varying the ion temperature in the estimate of the electron temperature. Therefore, according to Eq. 3.5:

$$J_i(V_f) = -J_e(V_f) = q u_{the} n_0 e^{-\frac{1}{2}} e^{\frac{V_f - V_0}{T_e}}.$$

(3.7)

By exponentially fitting the IV curve in the interval $[V_f, V_p]$, the electron temperature T_e, and the electron density n_0 can be obtained (see Fig. 3.1(d)).

This procedure is employed to determine the plasma characteristic for this thesis, except for the LP photodetachment experiments described in Sec. 4.2, where a more detailed technique based on the analysis of the EEDF is employed. When not specified, the method described in this paragraph has been used, which allows a fast and quite good estimate of plasma properties. Although the estimate of n_0 is not accurate, maybe due to the electron magnetization (see Sec. 3.1.1), the method is still accurate to determine V_f, V_p and T_e. More reliable measurements of the electron density were performed by the Thomson scattering technique, described in Sec. 6.

We have so far discussed the analysis of time-averaged plasma parameters. The measurement of the fast variation of local plasma parameters would require to perform IV sweep above a few kHz. However, at these frequencies, capacitive effects due to cable stray capacitance can considerably distort the shape of the IV curve leading to unreliable results. Close to the floating potential, the sheath acts like a resistor with resistance R_{sheath} [54]:

$$R_{sheath} \approx 1.27 \times 10^{15} \frac{\sqrt{T_e[\text{eV}] m_i / m_e}}{A_{probe}[\text{m}^2] n_e[\text{m}^{-3}]}.$$

(3.8)

The sheath resistance, together with the cable capacitance C, which is of the order of 100 pF/m for conventional BNC cables, acts like a RC low-pass filters. The simplest way to measure plasma fluctuations is to record I_{sat} time traces, this is detailed in Sec. 3.4. Provided that capacity effects are not so important as to distort the IV characteristics, the usual way to measure high frequency oscillations of plasma parameters is to measure $I(t)$ for a fixed bias, then change to another bias, and build up the $I(V)$ curve, taking account of the RF phase [73]. Although RAID can generate high density plasmas making LP unreliable in certain regimes (for example in the center of the plasma column when the RF power is higher than 5 kW), due to high thermal fluxes on the tip, it can still be used to obtain I_{sat} profiles (which, can be assumed proportional to the electron density, according to Eq. 3.2, if we consider the plasma quasi neutral) and to study plasma density fluctuations.

We have so far considered a collisionless, isotropic plasma. A factor perturbing the accuracy of LP in RAID is the presence of the magnetic field, which cannot be avoided, since this is required for the propagation of helicon waves. The effect of the magnetic field in described in Sec. 3.1.3.

3.1.3 Effect of the magnetic field

The IV curves measured by LPs can be affected by the presence of a magnetic field [54]. The electron collection is no longer isotropic when the plasma is immersed in a magnetic field since electrons and ions move preferentially along the magnetic field lines. A particle with electric charge q and mass m, moving with a velocity v in a magnetic field of intensity B, has a circular trajectory of radius r_L know as *Larmor radius*, given by:

$$r_L = \frac{mv_\perp}{|q|B},$$
(3.9)

where $v_\perp$ is the component of the velocity v perpendicular to the magnetic field.

To quantify the effect of the magnetic field on electron collection, one has to compare the Larmor radii of electrons, r_L^e, and of ions, r_L^i, to the typical dimension of the probe, r_p, for example the diameter in the case of a cylindrical LP tip. The ratio r_p/r_L is usually used to quantify the magnetization of the system under investigation. When $r_p/r_L^{(e,i)} \gg 1$, electrons and ions are strongly magnetized and the electron and ion fluxes strongly depend on the orientation of the magnetic field with respect to the probe. In typical low temperature laboratory plasmas, where $T_i \ll T_e$ and $r_L^i \gg r_p$, the effect of the magnetic field on the ion saturation current can be neglected. If also $r_L^e \gg r_p$ the effect of the magnetic field can be ignored. If $r_p/r_L^e \approx 1$, the electron current collected is affected by the presence of the magnetic field, resulting in inaccurate estimate of the electron density. However, the IV characteristic close to the floating potential can still be used to measure the electron temperature.

In the case of RAID, the ratio r_p/r_L^e approaches 1 for magnetic field $B > 200\,\text{G}$, meaning that the estimate of T_e is not accurate for certain combination of T_e and magnetic field. For example, Fig. 3.2 shows measurements of IV curves performed on RAID with a L-shaped LP clearly
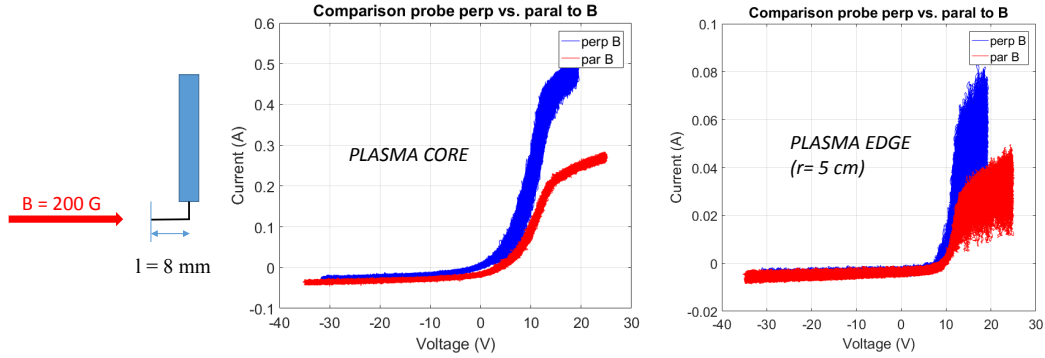
Figure 3.2 – IV curves when the Langmuir probe tip ($r_p = 0.2$ mm) is parallel (red) or perpendicular (blue) to magnetic field lines ($B = 200$ G), showing the influence of the magnetic field on electron collection. The probe is L-shaped and is 8 mm long and was located in the center of the plasma column in the core and on the plasma edge.

illustrating the effect of the magnetic field on electron collection depending on the orientation of the probe tip. When the tip is parallel to the magnetic field (red curve), the collected current is strongly reduced. The measurements are performed in the plasma center and at the edge and show that even in the plasma core, where the electron temperature is the highest (about 5 eV), the electron magnetization cannot be neglected. The ion saturation current however seems less affected by the magnetic field and can be used to determine the ion density. All LP measurements reported in this thesis are performed with the LP tip perpendicular to magnetic field lines for which a free streaming of plasma along field lines can be assumed.

3.1.4   Other phenomena affecting the shape of the IV characteristics

There are other factors that may distort the shape of the IV characteristic, apart from the electron magnetization. These are: the RF pickup, the probe heating, the presence of the mixture of ion species and non-Maxwellian electron distribution.

A LP immersed in a plasma sustained by a RF discharge can be affected by its time oscillating electric field. In this case we will talk about a *RF pickup* to define the effect of the external RF field on the LP. The effect of the RF pickup is in general to distort the IV characteristic. The so called "compensated probes"[55] picks up the RF sustaining the plasma discharge and use it as a reference to subtract it from the IV curves.

Another phenomenon that could affect the IV curve is particle bombardment. Since RAID can produce a high density plasma, a strongly negatively polarized LP tip is subject to high ion bombardment. If on the one hand this helps removing surface impurities, on the other hand, this can lead to ion sputtering resulting in the surrounding ceramic stick covered with a thin layer of conductive material, which can cause parasitic currents. In the electron saturation region of the IV curve, since the electrons have a higher mobility compared to ions, electron currents are typically ten times larger than ion currents. Owing to the low gas pressure, the only

way to cool down is by radiation or by heat transfer along the wire. Besides thermal damage, if the surface temperature of the tip is sufficiently high, it can emit electrons by thermionic emission; the emitted electrons can, in turn, affect the IV characteristic. A glowing tip is a clear signature of overheating, and IV are not considered reliable in this case.

Another phenomena is the presence of ions with different masses and same charges. The ion saturation current, in the case of a hydrogen plasma, is the sum of the current due to H^+, H_2^+ and H_3^+, and the single ion current contribution to the total ion saturation current cannot be separated. We will see, in 3D numerical simulations reported in Sec. 7, that the core of RAID plasma is mostly populated by H^+ (about 90 %) and the remaining ion population is shared between H_2^+ and H_3^+, whereas on the edge, H_3^+ is the most abundant species. The assumption of a pure proton plasma is clearly not satisfied on the edge of the RAID plasma column. The ion saturation current should be a factor $\sqrt{3}$ lower if we consider a pure hydrogen plasma. In general, when the electron temperature is low ($T_e \lesssim 2\,\mathrm{eV}$) and the neutral pressure is high, the H_3^+ ion is the most abundant species in a hydrogen plasma.

Another factor which might affect the shape of the IV curve is the presence of a non Maxwellian distribution of electrons or many Maxwellian distributions, namely many different electron populations. To detect different electron populations with different temperatures the IV characteristic should have a very low value of noise, which is not easy in most plasma devices, RAID included. The fits of the exponential part of the IV characteristic in RAID barely shows the presence of a hot and a cold electron population, as we will see in Sec. 4.2. Since the power deposition process of the helicon wave plasma is not localized, and the plasma density is high (leading to high collisionality) this probably enhances the thermalization of plasma electrons. In other kinds of plasma sources such as the ECR sources, since the electron heating has a narrow peak close to the resonance frequency, the heating is localized and a hot electron population is present [29]. In the case of RAID, we expect a hot electron population in the antenna region since strong electric fields and currents are generated close to the antenna legs.

3.1.5   Langmuir Probes available in RAID

To characterize the plasma in 3D, a LP, dubbed *axial probe*, measures plasma parameters at different axial and radial locations along the plasma column. This LP can be displaced along the z direction in the interval $[0-1200]\,\mathrm{mm}$ (see Fig. 3.4). The rotation axis of the axial probe is at the bottom left part of the chamber vacuum vessel and can rotate up to the wall covering a total angle of $120°$ (see Fig. 3.3(a)). The probe ceramic stick length is 17.6 cm and the center of the tip passes though the mechanical axis of the vessel (and the center of the plasma column), to measure radial profiles. Fig. 3.3(a) shows the cross section of the RAID chamber vessel at the axial position $z = 0.83\,\mathrm{m}$, looking from the antenna side (z axis direction pointing into the page). The axial movement is performed by a steel rod sliding along vacuum tight passages kept at an intermediate pressure (about 1 mbar) between the atmospheric pressure and the vessel pressure by differential pumping.

This system is employed to perform local measurements of the plasma properties. When the

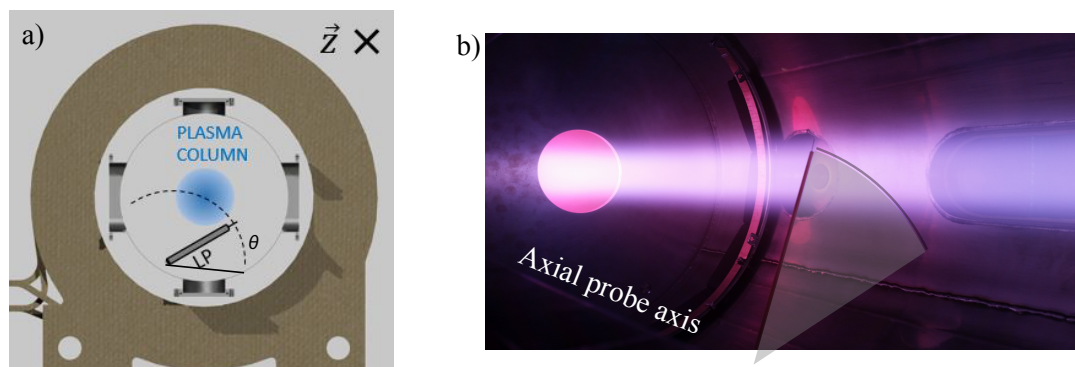Figure 3.3 – (a) Cross section of RAID vacuum vessel at axial position $z = 0.83\,\text{m}$. The dashed line shows the trajectory of the center of the tip of the axial probe passing through the center of the plasma column. (b) Picture of the axial LP inside RAID vessel showing the movable axis and the trajectory of the probe.
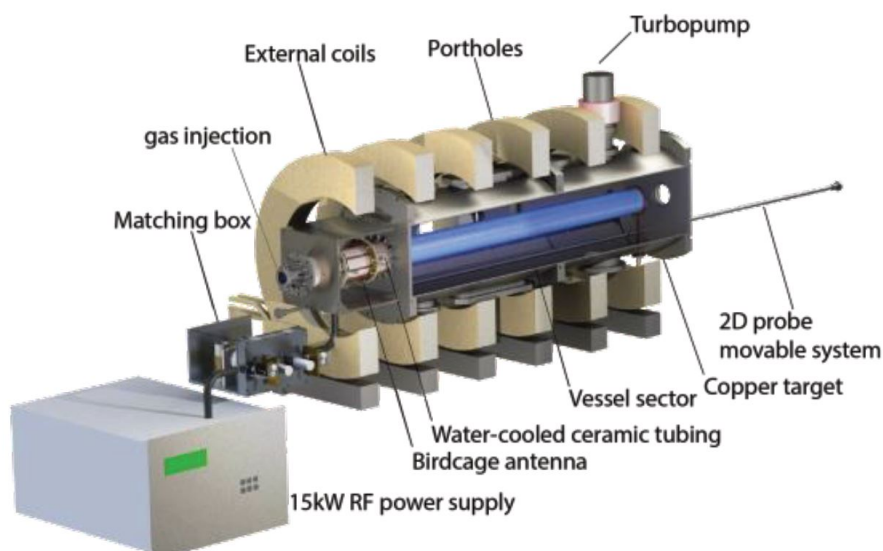
Figure 3.4 – Longitudinal cut of RAID showing the 2D probe movable system.
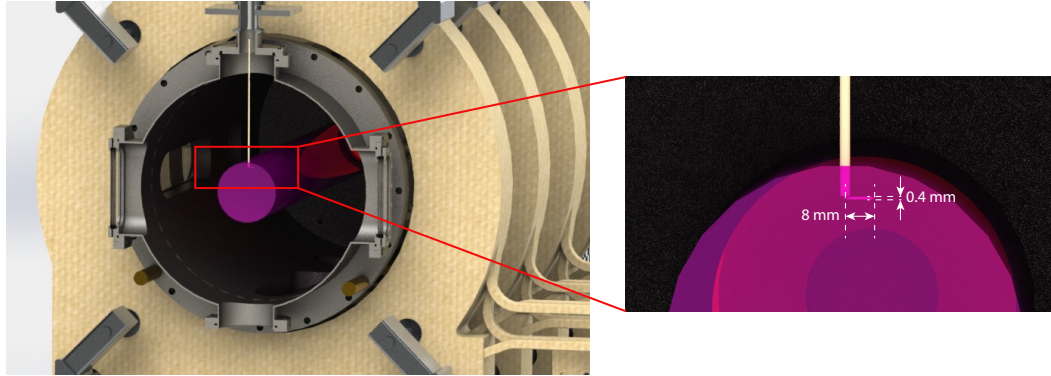
Figure 3.5 – Cross section of RAID showing the position of the vertical LP and the dimension of the L-shaped tip. The probe tip can be located from the center of the column to the radial position $r = 10\,\mathrm{cm}$.

plasma density is too high, it can rapidly pass though the center to minimize the thermal flux hitting the LP tip. The longitudinal cut of RAID in Fig. 3.4 shows the location of the 2D probe movable axis system.

RAID can also be equipped with a second LP, sliding from the top of the vessel, at the axial position $z = 83\,\mathrm{cm}$ (see Fig. 3.5): it is a L-shaped probe (8 mm long and 0.2 mm diameter) employed for laser photodetachment measurements of negative ions described in Sec. 4.2. This probe can slide from the center of the plasma column to the radial position $r = 10\,\mathrm{cm}$. Another LP can measure the plasma in the antenna region, moving co-axially with the mechanical axis of the vessel; this LP is used to study how the antenna couples to the plasma (see Sec. 3.6.2).

3.2   Microwave interferometry

Owing to the high plasma density regimes that can be achieved in RAID, LPs cannot withstand thermal fluxes in the plasma core, therefore, non invasive diagnostics are required. Microwave beams are, for example, one of the tools to investigate high density plasmas in magnetic confinement experiments, as well as in basic plasma devices [63, 34, 75, 42, 41, 141]. A common way to employ microwave beams is by performing microwave interferometry, consisting of measuring the phase shift due to the index of refraction of the plasma [75]. Microwave interferometry is considered as the best performing diagnostic to measure the electron density in a wide range of plasma regime for a number of reasons. First, this technique relies on a relatively simple theory compared to LP, making data straightforward to interpret. The probing microwaves weakly interact with the plasma, therefore the measurement is intrinsically non-invasive. Second, microwaves are not affected by the radiofrequency sustaining

the plasma discharge, the electron temperature distribution, the ion mass and the plasma electronegativity. All these aspects make diagnostics with microwave beams, also known as *mm-wave diagnostics* [63], an attractive technique, usually considered as the reference point and the ultimately cross check technique for electron density measurement [118].

Because of the magnetic field needed in fusion experiments, the frequency of microwaves is usually in the range of 50 - 200 GHz, corresponding to a wavelength of 6 - 1.5 mm. Depending on the plasma properties and the probing wavelength, the probing waves can be transmitted, scattered of reflected by the plasma.

3.2.1 mm-wave theory

Microwave interferometry in plasma deals with the propagation of microwave beams propagating in free space, this is usually included in the description of *quasi-optical systems.* In optical systems, the dimensions of lenses, mirrors and aperture is such that one can consider the radiation wavelength $\lambda \rightarrow 0$. Such systems can be satisfactorily described by the propagation of bundles of parallel rays. This is the domain of geometrical optics. In the opposite case, the diffraction limit, λ is comparable to the system size, the diffraction effects dominate the propagation and a description of the near field is required. Quasi-optics describes systems located in the range between the two aforementioned regimes. In the quasi-optic regime, beams of radiation are well described by Gaussian beam propagation [56]. Microwave and mm-wave propagation are usually Gaussian beam produced by feed horns (with conical or rectangular cross section, for example), with the beam waist located inside them. A collimated beam of transverse dimension D and wavelength λ diverges by an amount comparable to its initial size in a distance D^2/λ. Therefore, typical horns of 1 cm size and with a radiation wavelength of $\lambda = 1\,\mathrm{mm}$ diverge in $\sim 10\,\mathrm{cm}$, comparable to the size of the RAID vacuum vessel diameter. Therefore, microwave beams employed to probe the plasma have to be described by the propagation of Gaussian beams. We provide in the following section a brief theoretical description of the propagation of gaussian beams.

Gaussian beam propagation

The electric (or magnetic) field component ψ of an electromagnetic wave propagating in free space satisfies the Helmoltz equation:

$$(\nabla^2 + k^2)\psi = 0, \tag{3.10}$$

where k is the wave number. If we consider the z axis as the propagation direction, we assume a linearly polarized wave and without considering the time dependent part of the field ($\propto e^{i\omega t}$),

the component of the electric field can be written as:

$$E(\mathbf{r}) = u(\mathbf{r})e^{-ikz}, \tag{3.11}$$

where $u(\mathbf{r})$ is a scalar function describing the non-plane wave part of the beam. If we substitute $E(\mathbf{r})$ in Eq. 3.10, we obtain the equation for the electromagnetic wave in free space. Since we will study Gaussian beams emitted by conical horns, the cylindrical coordinates (r, ϕ, z) are the most suitable. In this reference frame the wave equation can be written as [56]:

$$\left[\frac{\partial^2 u}{\partial r^2} + \frac{1}{r}\frac{\partial u}{\partial r} + \frac{1}{r}\frac{\partial^2 u}{\partial \phi^2} + \frac{\partial^2 u}{\partial z^2} - 2ik\frac{\partial u}{\partial z} \right] e^{ikz} = 0. \tag{3.12}$$

A number of simplifications are possible. The third term on the left hand side is equal to zero because of the cylindrical symmetry. Moreover for the case under investigation, the paraxial approximation can be used since the variation of the wave amplitude along the propagation direction over a wavelength is small and also much smaller than the variation along the perpendicular direction. Under the paraxial approximation, the wave equation 3.12 can be written as:

$$\left[\frac{\partial^2 u}{\partial r^2} + \frac{1}{r}\frac{\partial u}{\partial r} - 2ik\frac{\partial u}{\partial z} \right] e^{ikz} = 0. \tag{3.13}$$

Eq. 3.13 can be solved using the ansatz:

$$u(r, z) = A(z)e^{\left(\frac{-ikr^2}{2q(z)} \right)}, \tag{3.14}$$

where $A(z)$ and $q(z)$ are complex functions. The final solution for the electron field $E(r, z)$ can be written as:

$$E(r, z) = E(z)\exp\left[-\frac{r^2}{w^2(z)} - i\left(kz + \frac{\pi r^2}{\lambda R(z)} \right) \right]. \tag{3.15}$$

The electric field decreases exponentially from the beam axis. $w(r)$ is the characteristic beam radius, which depends on the axial position. The beam diameter w and the radius of curvature R of the beam front depend on the axial position by the following equations:

$$w(z) = w_0\sqrt{1 + \left(\frac{\lambda z}{\pi w_0^2} \right)^2}, \qquad R = z + \frac{1}{z}\left(\frac{\pi w_0^2}{\lambda} \right)^2, \tag{3.16}$$

where w_0 is the minimum beam radius, called *beam waist*. λ, the wavelength defines a characteristic length, called *Rayleigh length* $z_R = \pi w_0^2 / \lambda$, which is the characteristic length over which the beam diameter is $\sqrt{2}$ the beam waist.

Gaussian beams well describe the propagation of mm-wave beams which are commonly used to measure plasma properties. In the next section, we will show how a microwave beam is affected by the presence of a plasma and how is used to deduce plasma properties.

Basics of interferometry

We begin by defining the following quantities:

$$X = \left(\frac{\omega_p}{\omega}\right)^2 \propto n_e, \qquad Y = \frac{\omega_c}{\omega} \propto B_0, \tag{3.17}$$

where ω_p is the plasma frequency and ω_c is the cyclotron frequency. We also define:

$$S = 1 - \frac{X}{1 - Y^2}, \qquad D = -\frac{XY}{1 - Y^2}, \qquad P = 1 - X. \tag{3.18}$$

It can be demonstrated that the dispersion relation of waves in the cold plasma limit is given by [63]:

$$\begin{bmatrix} S - N^2 \cos^2\theta & -iD & N^2 \sin\theta\cos\theta \\ iD & S - N^2 & 0 \\ N^2 \sin\theta\cos\theta & 0 & P - N^2 \sin^2\theta \end{bmatrix} \begin{bmatrix} E_x \\ E_y \\ E_z \end{bmatrix} = 0, \tag{3.19}$$

where $N = kc/\omega$ is the refractive index and θ the angle between the wave vector and the magnetic field. In the non magnetized plasma limit, the off-axis terms in the coefficient matrix are zero and the dispersion relation does not depend on the propagation direction, and the refractive index is given by:

$$N^2 = 1 - X. \tag{3.20}$$

When the probing frequency is much lower than the plasma frequency, the previous equation can be approximated to $N \approx 1 - \frac{1}{2}(n_e/n_c)$ and the expression of the phase shift $\Delta\phi$ with and without the plasma is given by:

$$\Delta\phi = \int_{\Delta l} N\frac{\omega}{c} dl = \frac{e^2}{2\omega c \epsilon_0 m_e} \int n_e(l) dl. \tag{3.21}$$
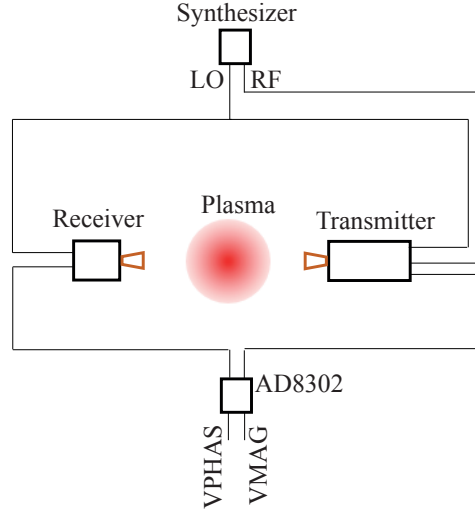
Figure 3.6 – Schematic of the interferometer connections showing the synthesizer producing the reference local oscillator (LO) signal and the probing signal RF. The circuit AD8302 compares the wave probing the plasma with the reference wave, giving a signal proportional to the phase shift, VPHAS, as output.

The plasma line-integrated density $\int n_e dl$ is measured by comparing the delay of the probing wave and a reference wave. Therefore, the line integrated electron density can be estimated by measuring the phase delay. In practice, the phase shift is measured by comparing the phase of the wave which has passed through the plasma with a reference wave. In Sec. 3.2.2, we describe the experimental interferometric system implemented for RAID.

3.2.2 The RAID interferometric system

We describe in this section the hardware and the basic principles of the microwave interferometer system in RAID. The experimental setup was originally developed for the basic plasma physics device TORPEX (TORoidal Plasma EXperiment) at the Swiss Plasma Center [46, 76] and has been adapted and optimized for RAID geometry. The system is quite compact and can be easily displaced and adapted to different plasma devices. The interferometer is commonly known as a single pass *heterodyne interferometer* [75]. The term "heterodyne" refers to the use of two frequencies: a "probing frequency" and a "local oscillator".
A schematic of the mw interferometer setup used in RAID is shown in Fig. 3.6. The setup is made of a Synthesizer, producing the microwave signals, a transmitter, a receiver (WR-10, Virginia Diodes) and the AD8302 circuit [1] which measures the phase shift. Both the transmitter and the receiver operate in the 75-110 GHz frequency range, which is a reasonable compromise between the expected electron density regimes, the divergence of the beam due to its gaussian-like behaviour and the precision in measuring the phase shift of the AD8302 circuit. The transmitter and the receiver are equipped with conical horns mounted on adapters from rectangular to circular cross sections. The synthesizer, shown on the top of Fig. 3.6 can deliver

two signals: in our setup we choose as the local oscillator output frequency $f_{LO}^{synth.} = 8.43\,\text{GHz}$ and as probing radio frequency $f_{RF}^{synth.} = 8.375\,\text{GHz}$.

Both the transmitter and the receiver multiply by a factor 12 the two frequencies, so that the LO frequency at the transmitter and receiver is $f_{LO} = 101.6\,\text{GHz}$ and the RF frequency at the transmitter is $f_{RF} = 100.5\,\text{GHz}$, this is the microwave frequency which is used to probe the plasma. Then, the transmitter mixes the LO and the RF signal; mathematically it performs the multiplication of the two waves so that the output signal has $2 f_{RF}$ high and a $f_{RF} - f_{LO}$ low frequency components. The $2 f_{RF}$ signal is filtered out and only the low frequency component, which is $f_{RF} - f_{LO} = 55\,\text{MHz}$, is delivered to the AD8302 circuit. The receiver mixes the LO signal and the probing RF wave passed through the plasma, whose phase is delayed by the presence of plasma electrons, and the low frequency component is delivered to the AD8302 circuit. This circuit then compares the two low frequency signals and produces in turn a signal VPHAS, proportional to the phase difference and a signal VMAG proportional to the logarithm of the ratio of the amplitudes [1]. The output voltage for VPHAS goes from 0 V to 1.8 V and a slope of 10 mV/DEG with a phase reversion at 0 DEG. The output voltage for VMAG is also in the range 0 V to 1.8 V linearly from -30 to 30 dB, corresponding to a slope of 30 mV/dB. More details on the electronics and the evaluation of error can be found in Ref. [76].

The major technical challenges for the use of the microwave interferometry in RAID in these frequencies are the mechanical vibrations, the time stability of the signal and the focusing of microwaves. At 100 GHz, corresponding to 3 mm wavelength in vacuum, this means that even mechanical vibrations of a fraction of a mm can compromise the measurement of the mw phase. This is problematic considering that the vacuum pumps can produce considerable vibrations. Therefore, the entire system has to be mechanically isolated from the vessel. Even the high frequency cables are sensitive to positioning, and any displacement can modify the value of the detected phase at the circuit.

In RAID, since the center of the plasma column is 23 cm away from the window port from which microwaves are launched, the size of the probing beam would be comparable to the diameter of the plasma column, by computing the beam diameter w using Eq. 3.16. This would not allow to accurately measure different parts of the plasma column. The need to focus the microwave beam is indeed evident.

Focusing the mw beam with a teflon lens

To reconstruct radial profiles of the electron density, focusing of the microwave beam is required. This is obtained by focusing elements such as elliptically shaped mirrors or lenses for microwaves [88]. To focus the mw beam in the center of the plasma column we have designed and tested a teflon lens. The advantage to use such a system is that plastic lenses are easy to machine and the whole system can be easily translated in the vertical direction to scan the entire plasma diameter. The role of the lens is to transform the wave front curvature of the mw beam from positive to negative so that the beam converges after the lens. A lens made of two spherical concave surfaces is not good enough to correctly focus a microwave beam

because of spherical aberration. To calculate the optimal shape of the lens surface one has to apply the Fermat principle, stating that the trajectory of a ray minimizes the time of travel, or that the phase of two adjacent rays has to be the same. To convert a spherical wavefront to a planar wavefront the lens surface has to be a hyperbola whose profile y_h is given by [88]:

$$y_h^2 = 2fz(n-1) + z^2(n^2-1), \tag{3.22}$$

where z is the position along the optical axis, n is the refractive index of the lens and f the wave frequency. Fig. 3.7 shows the path of the microwave beam along the cross section of
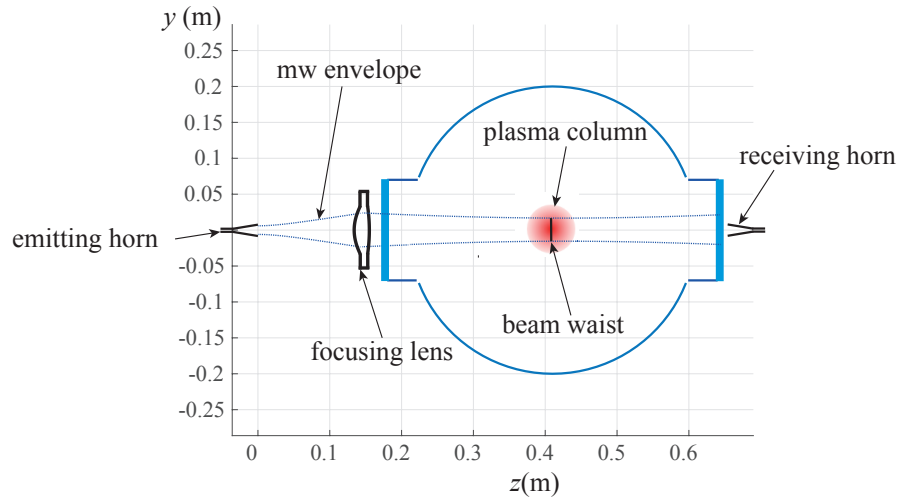
Figure 3.7 – Interferometry setup in RAID showing the envelope of the 100 GHz probing microwave beam, which is focused by a lens to the center of the plasma column.

RAID. The microwave beam exits from the transmitting horn on the left and diverges in air up to the lens where it is focused towards the center of the plasma column. The beam waist in the center of the column is $\sim 2\,\text{cm}$, which is sufficiently small to provide satisfactory resolution to measure a few radial positions in the plasma column but not to accurately reconstruct the entire radial density profile by Abel inversion.

The role of the lens is to transform the curved wavefront of the emitted beam into a plane wavefront passing through the middle of the lens and then the other side surface modifies the wavefront with a opposite curvature.

The lens is installed on a holder at a fixed distance from the transmitter (13 cm) and can be vertically displaced on a manual translation stage, as shown in Fig. 3.8. The lens is supported on two moving stages with the perpendicular axis to finely adjust the axis of the lens with the microwave beam. The transmitter is elevated with respect to the lens axis to avoid reflections, which could interfere with the probing beam. The receiver, which is located in the opposite position of the vessel, can be either fixed or vertically displaced on an automatic translation stage. By measuring the profile of the scattered beam, one can deduce some plasma features,

Figure 3.8 – Picture of the microwave interferometer setup showing the transmitter and the teflon lens to focus the probing microwave beam, for a typical hydrogen plasma column.

which are discussed more in detail in Sec. 3.5.

3.2.3 Interpretation of interferometer signals
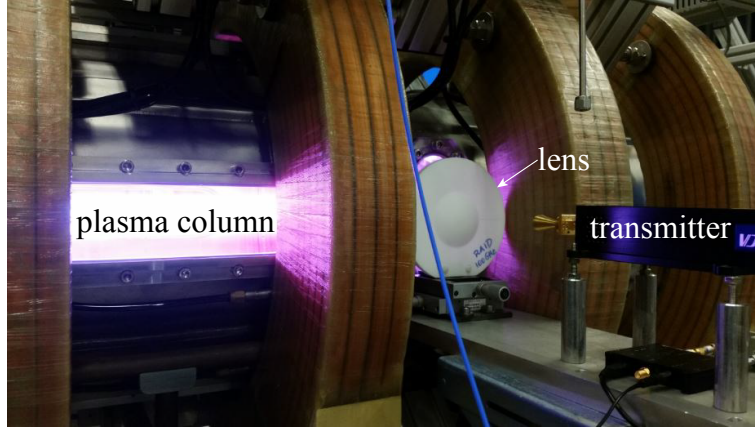
The measurement of the line-integrated electron density relies on the ability to detect the small variation of wave phases. Since the phase measurement is extremely sensitive to vibrations and drifts, the technique consists of recording the phase signal during a few seconds before and after the plasma shut down. The signals are usually recorded with a sampling frequency of 250 kS/s which guarantees a sufficient temporal resolution and a wide enough temporal window to study the stability of the apparatus.

Fig. 3.9 shows the phase signal ϕ during (red highlighted area) and after an argon plasma discharge for different RF powers. Plasma is turned off at $t = 0\,$s and the phase signal performs fast oscillations (of the order of 0.1 ms) before it stabilizes to a constant value, namely ϕ_{bkg}. The phase shift $\Delta\phi$, due to the plasma, is calculated by $\Delta\phi = \phi_p - \langle\phi_{bkg}\rangle$ where ϕ_p is the phase during the plasma discharge and $\langle\phi_{bkg}\rangle$ is the average value of the phase when there is no plasma, the "phase background".

An ambiguity which might arise in the interpretation of the phase shift is the phase change direction [75]. This occurs when the phase is $\phi = 0, \pi, 2\pi$ and so forth, because at these points the interferometer is close to a phase jump of the signal. A priori, it is impossible to compute the number of phase inversions which occurred just by a single value of the phase. However, by slowly ramping up the RF power one can track the phase and remove the ambiguity.

Let's consider the case at 1000 W power in Fig. 3.9: when plasma is on, the phase signal is constant at $\approx 1\,$V, then, when the plasma is turned off, the signal drops to 0V and then stabilizes to about 1.3 V. The total signal accumulated due to the phase shift is 2.3 V, corresponding to 75 deg, from which we can deduce the line integrated density $\int_l n_e(l)\,dl$. By increasing the RF power, ϕ_p increases, then, the phase is reversed and the signal decreases again. In this way, the RF power we can count the number of phase reversions and evaluate the total phase shift.
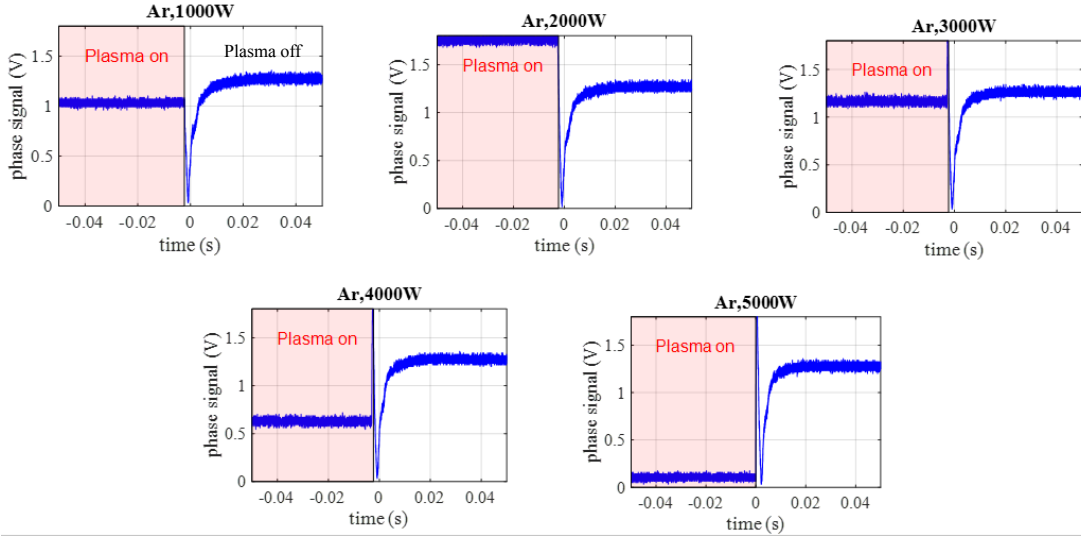
Figure 3.9 – Variation of the phase signal of the interferometer when the plasma is shut down for different RF powers, showing the inversion of the phase signal.

The phase after the plasma is turned off does not vary much from one plasma shot to another, meaning that the entire system was rigid enough. When there is no plasma, the noise of the phase signal is of the order of 0.1 V, corresponding to a minimum detectable plasma density, on the typical size of the plasma column ($\approx 6\,\text{cm}$), of $10^{17}\,\text{m}^{-3}$.

When the plasma is on, the fast temporal variation on the phase signal reflects the plasma density fluctuations along the beam path. Although this would be in principle a non invasive technique to measure plasma density fluctuations, the interpretation of the scattered wave is not straightforward and requires numerical modeling the mm-wave beam scattering [32].

Since RAID radial electron density profiles cannot be usually approximated by a flat square profile, the line-integrated measurements with the interferometer only provides an averaged value over an arbitrary average length. To determine the absolute density profiles, the mmw-interferometer is coupled with LPs. This technique is detailed in Sec. 3.3.2.

3.3 Plasma steady-state profiles

The results presented in the next paragraphs are obtained with the source operating in *standard conditions*, i.e. 0.3 Pa of gas pressure and magnetic field peak of 200 G in the vessel (see Sec. 2.1 for more details), and 3 kW of RF power. The choice of this power is motivated by the reasonable compromise between the interest to study the source in high power regime and the possibility of using LPs.

The axial probe is used to measure 3D profiles of I_{sat} current and considering the profiles with cylindrical symmetry. I_{sat} profiles provide a rough measurement of n_e profiles, since $I_{sat} \propto n_e \sqrt{T_e}$. In a very first approximation, we can neglect the temperature gradients and suppose I_{sat} proportional to the ion density. Fig. 3.10 shows radial profiles of I_{sat} at different
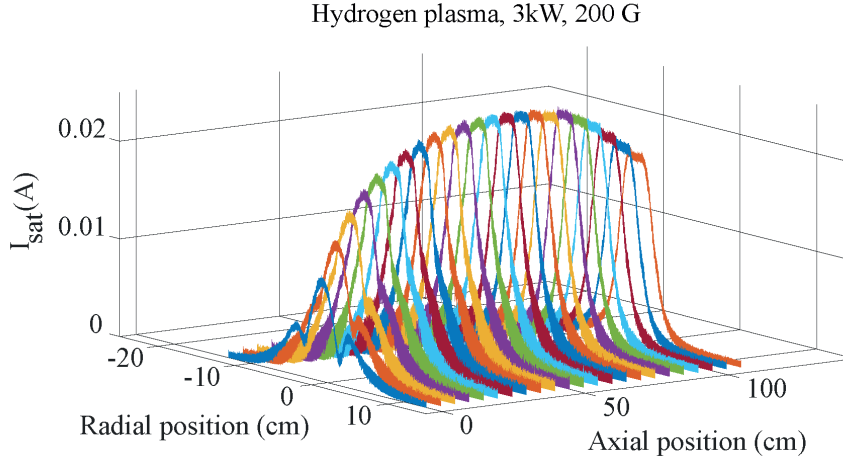
Figure 3.10 – I_{sat} radial profiles at different axial locations measured with the axial LP in ion saturation. The maximum density is reached at the axial position $z \approx 50$ cm. I_{sat} profiles are peaked along the plasma column.

axial positions for a hydrogen plasma at 3 kW RF power and 200 G magnetic field in the center of the vessel. The axial position axis covers the full axial range of the axial probe. Due to the high thermal fluxes, the LP is rapidly scanned through the plasma (<1s in plasma) to avoid probe damage. We remark that plasma density profiles are centrally peaked. This suggests that helicon waves deposit their power in a narrow region around the axis of the plasma. The axial magnetic field also helps to confine the plasma in the radial direction. The maximum value is also quite homogeneous along the axis of the vessel peaking downstream at about 50 cm. This I_{sat} profile has also been observed in other helicon devices, and can be explained by simple particle and energy balance [35]. This a crucial feature of the helicon waves, able to deposit their energy far from the antenna region and therefore sustaining elongated plasmas. The lower plasma density in front of antenna region might be also due to the proximity of the chamber wall absorbing plasma. The I_{sat} profiles in front of the antenna (up to ~ 20 cm) show two small side peaks close to the central one. This might be due to a residual inductive plasma generated close to the antenna legs which then expands in the vessel region, or perhaps to the effect of the change of radial boundary conditions for the helicon wave when passing from the antenna region to the vessel. The decrease of the peak height in the downstream region might be due to the presence of the target absorbing plasma particles. Unfortunately, no measurements close to the target are available, because of the limited axial range of the axial probe.

Fig. 3.11 shows 2D mapping of $V_{floating}$ and I_{sat} in the plasma column for a hydrogen plasma. $V_{floating}$ shows two mimima at about $V_{floating} \sim 15$ V in front of the antenna, probably because of hot electrons accelerated by the high electric fields close to the antenna legs. For $r > 4$ cm, outside the typical size of the plasma column, $V_{floating}$ is quite flat and its value is ~ 7 V. The I_{sat} mapping are also helpful to have an idea of the spatial distribution of plasma. A major advantage of measuring I_{sat} profiles is the spatial resolution. However, the electron

temperature is required to accurately determine relative radial plasma density profiles. IV characteristics are obtained by sweeping the probe voltage to then allowing to extract values of n_e, T_e, V_p ad V_f.

Fig. 3.12 shows the T_e, n_e, V_f and V_p radial profiles in three locations of the plasma column: at $z = 0$ cm (left column), at $z = 50$ cm (central column) and at $z = 110$ cm (right column). The square data points are the results of the LP characteristics analysis with the method previously described, whereas the asterisks indicate the data obtained with a four parameter fit. The two analysis methods show a good agreement between each other. It is interesting to extend the electron temperature measurements in other axial locations of the plasma column. This was done only one since the procedure was not automatized at the time of the experimental campaign. Fig. 3.13 shows the electron temperature measurements along the plasma column. Every data point is obtained by a IV curve analysis according to the method described in Sec. 3.1.2. T_e radial profiles are centrally peaked reaching $T_e \approx 8$ eV in front of the antenna and monotonically decreasing downstream to 4 eV. T_e radially drops to 2 eV in a radial distance of ~ 3cm, suggesting that electron heating is concentrated around the axis of the plasma column. Fig. 3.14 compares the axial profiles of T_e and I_{sat} in the center of the plasma column, showing the approximate monotonic decrease of T_e and the I_{sat} peaking far from the antenna.

The I_{sat} and T_e 3D profiles show that RAID can efficiently generate elongated and quite homogeneous hydrogen plasma columns, in steady state regime with 0.3 Pa gas pressure, the pressure relevant for NBIs application for ITER [67]. These features are promising for the development of a negative ion source extracting a constant current over the plasma length [53].

The plasma transport also depends on the electric field in the plasma which in turn is caused by the plasma potential gradient. It is therefore instructive to show axial and radial V_{plasma} profiles. Fig. 3.15 shows the V_{plasma} axial profile along the center of the plasma column (on the top) and the V_{plasma} radial profiles (on the bottom), at the axial position $z = 0.83$ m. We remark that the the axial plasma potential is quite flat at 12 V suggesting that axial electric fields are weak. The radial profile has a ~ 10 cm plateau in the center of the column, decreasing monotonically to zero at the walls of the vessel.

3.3.1 Dependence of radial profiles with injected RF power

It is crucial to study how plasma profiles depend upon the discharge parameters such as the RF power, the magnetic field and the gas pressure. The radial profiles are a direct way to visualize the response of the plasma to input parameters. These measurements were performed with the L-shaped Langmuir probe (tip of 0.2 mm diameter and 8 mm long) movable in the vertical direction. Fig. 3.16 we show the radial profiles of n_e, T_e, V_f and V_p for a hydrogen plasma at 0.3 Pa pressure and different powers at the axial location $z = 0.83$ cm, 1 m from the center of the antenna. At this position, the plasma is only sustained by the helicon regime since the inductive effect of the antenna is negligible in the downstream region.

We are interested to study plasma profiles at this axial location since this is the location that will be investigated with negative ion diagnostics in Sec. 4.
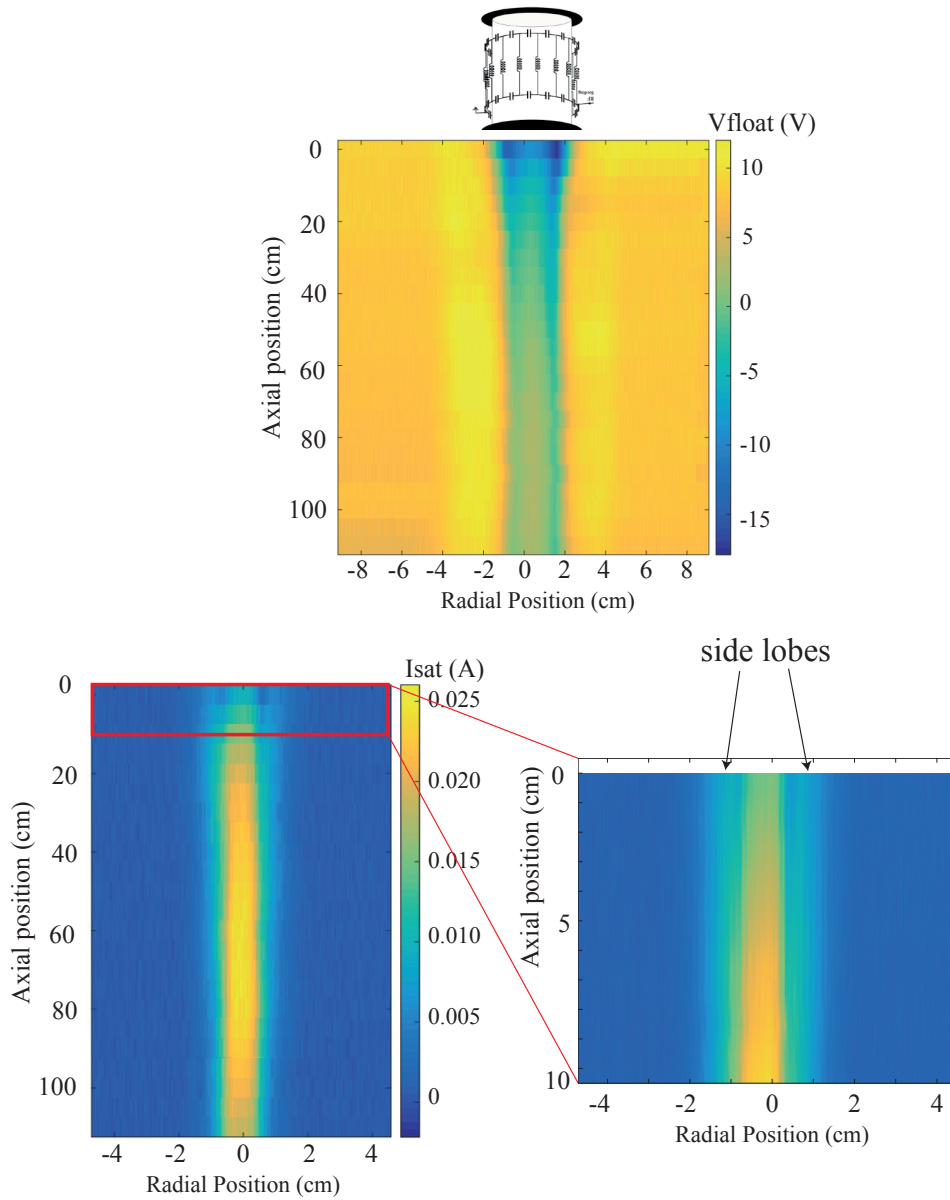
Figure 3.11 – on the top: 2D mapping of the $V_{floating}$ profile and position of the antenna. On the bottom-left: 2D mapping of I_{sat}. On the the bottom-right: zoom of the first 10 cm in the vacuum vessel showing two side lobes for a hydrogen plasma with 0.3 Pa gas pressure, 3 kW power and 200 G peak field.
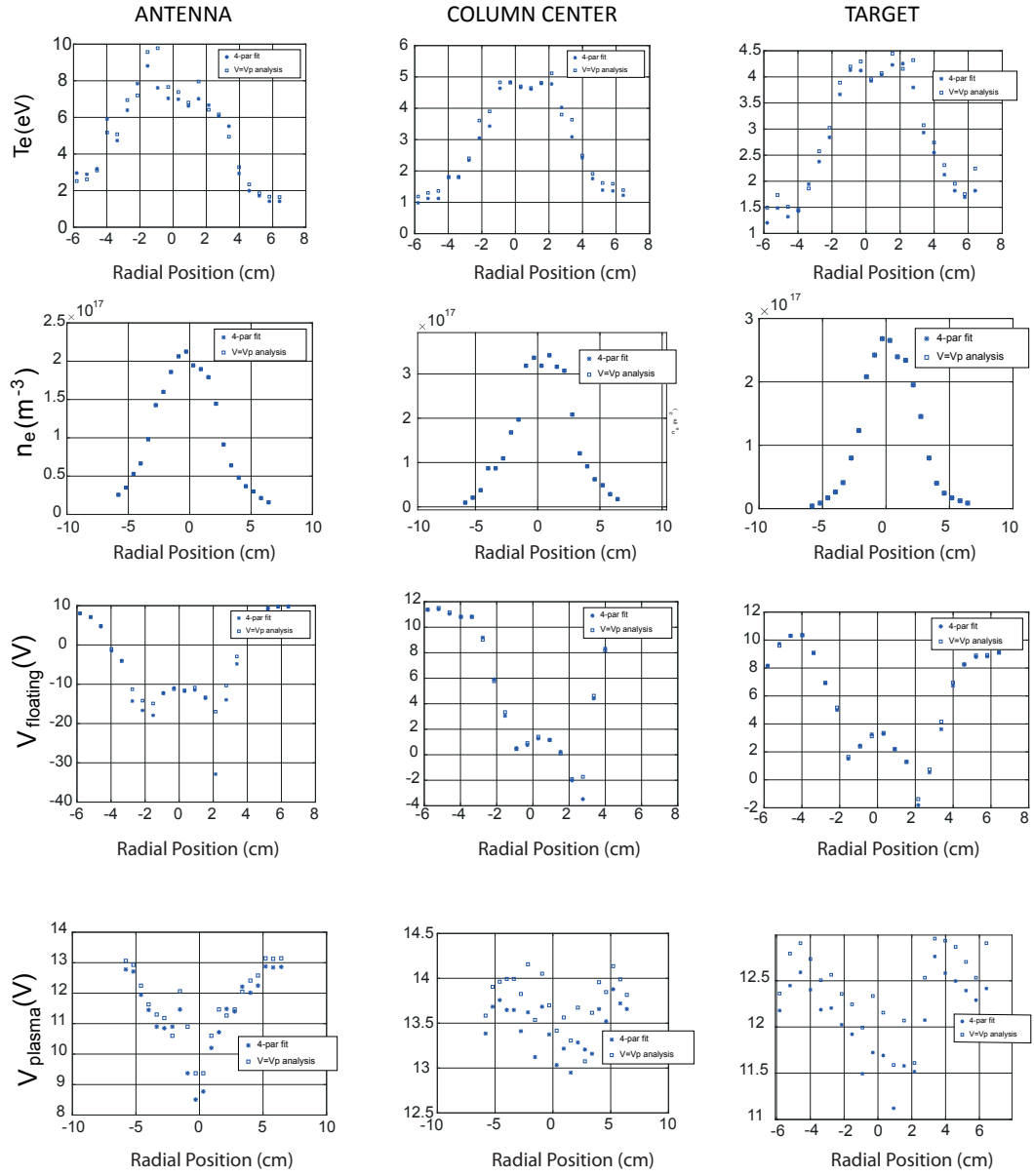
Figure 3.12 – T_e, n_e, V_f and V_p radial profile in three different axial locations in the plasma column: close to the antenna (left column), in the center (central column) and close to the target (right column).
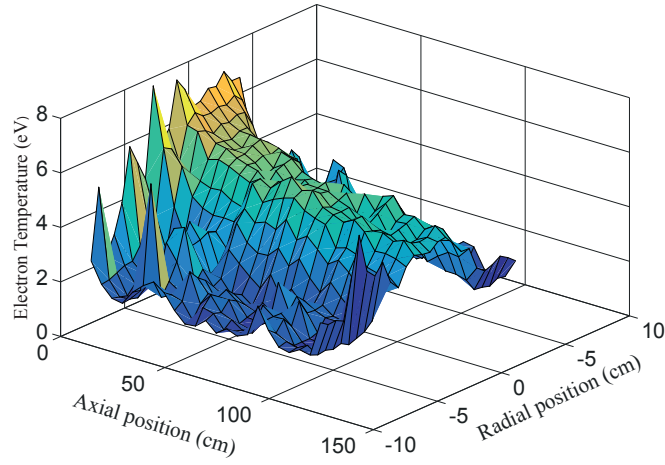
Figure 3.13 – Electron temperature profile for a 3kW H_2 plasma showing hotter electrons close to the antenna (on the left) and the electron cooling in the radial and downstream direction.
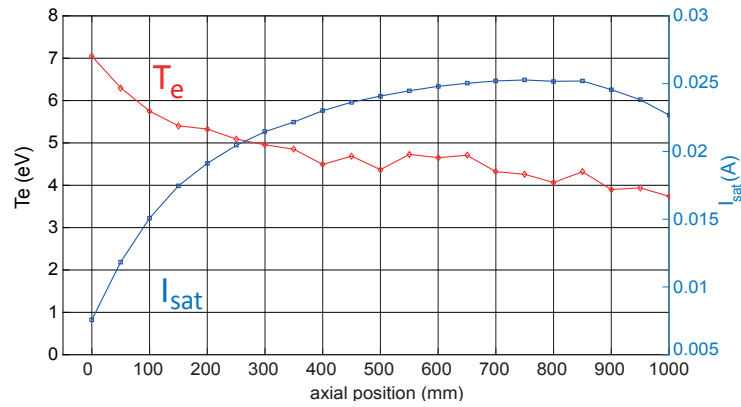
Figure 3.14 – Axial profiles of T_e and I_{sat} in the center of the plasma column.
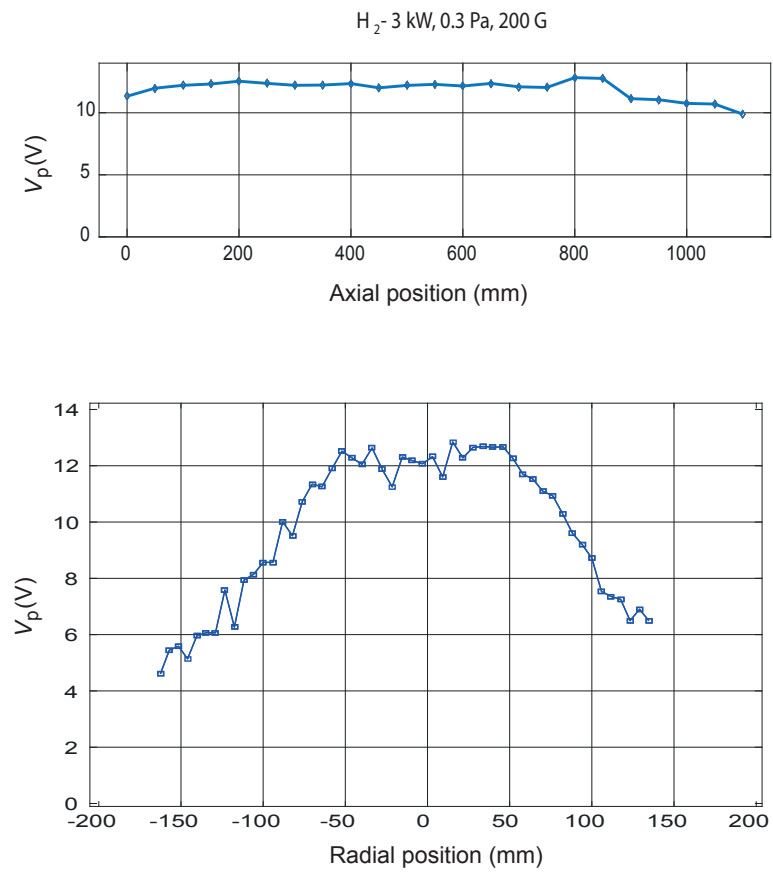
Figure 3.15 – Axial (top) and radial (bottom) profile of V_{plasma}.
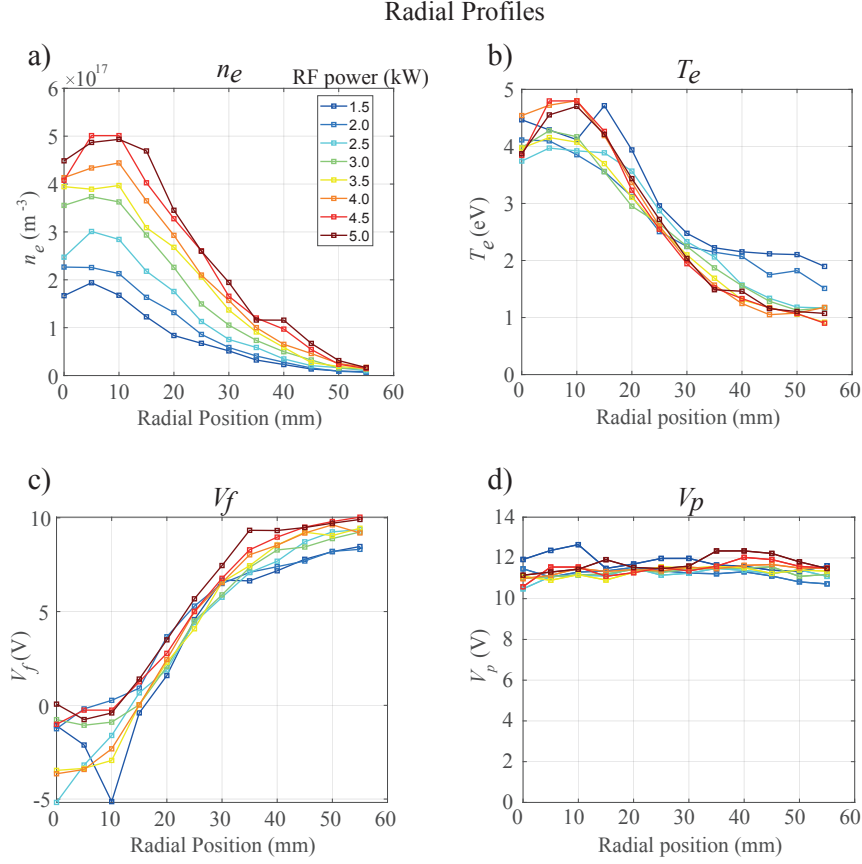
Radial Profiles

Figure 3.16 – Radial profiles of n_e, T_e, V_f and V_p for a hydrogen plasma at 0.3 Pa pressure and different powers at the axial position $z = 0.83$ cm. Error bars, which are typically the 20% of the point value, are not shown for clearness.

Fig. 3.16(a) shows the electron density strongly increasing with RF power, demonstrating efficient ionization. The monotonic increase of electron density with power is expected from power balance considerations [89]. Electron density profiles are centrally peaked and there are no sign of saturation with RF power, such as, for example, due to neutral depletion. The electron density drops by one order of magnitude from the center of the plasma column to 5 cm radial position. Beyond this location the signal to noise ratio is too low to extract plasma parameters. The absolute value of the electron density measured only by LP is underestimated due to partial electron magnetization. We will show in Sec. 3.3.2 how to more accurately estimate of n_e by microwave interferometry.

Fig. 3.16(b) shows the electron temperature profiles. We remark that they are only weakly dependent on the RF power. This can be explained by simple particle balance considerations: at this plasma regime, the electron temperature is independent of the plasma density and therefore the input power [89]. This is a common behaviour of helicon plasma devices, and cold plasmas in general [132]. The peaked temperature profile is favorable for the volume production of H^- since it provides a central hot region to rovibrationally excite the H_2 molecules

and a colder region at the edge where low-energy electrons can produce H^- by dissociative attachment.

Fig. 3.16 (c) shows the V_f profiles. The decrease close to the center is mostly due to the higher core temperatures. Fig. 3.16 (d) shows the plasma potential profiles. We remark that it is quite flat along the radial direction, this means that the radial electric field is weak and the transport in this region is only determined by the magnetic field and the collisions.

3.3.2 Combining Langmuir Probes with microwave interferometry

Microwave interferometry alone could in principle be used to determine the absolute electron density profile when the transverse size of the probing beam is much smaller that the typical size of the plasma. In this case, by considering the system to be cylindrical symmetric, one could deduce the radial density profile by calculating the Abel transform [140]. The mw beam measuring the RAID plasmas, however, has a beam waist of 2 cm, which is not negligible compared to the diameter of the plasma column. To obtain the absolute electron density profile we use the microwave interferometer with the beam passing through the center of plasma column and the axial LP tip passing through the center of the plasma column as well and considering the plasma with cylindrical symmetry. When the probe is operated in ion saturation regime, the absolute electron density n_e is given by [28]:

$$n_e = \frac{I_{sat}}{e A_{eff}} \sqrt{\frac{2\pi m_i}{k T_e}}, \tag{3.23}$$

where A_{eff} is the effective collection area of the probe, which is not straightforward to estimate. Even though A_{eff} is not known, a probe in I_{sat} regime can be used to measure normalized electron density profiles n_e^{norm}, if the T_e profile is known. The absolute electron density profiles can be written as $n_{abs} = n_e^{peak} n_e^{norm}$, therefore Eq. 3.21 becomes:

$$\Delta\phi = \frac{e^2}{2\omega c \epsilon_0 m_e} n_e^{peak} \int n_e^{norm} dl. \tag{3.24}$$

By integrating the normalized density profile, one can deduce n_e^{peak} and then obtain the absolute radial profiles n_{abs}. Fig. 3.17 (a) shows the radial electron density profile of a H_2 plasma, 0.3 Pa, 200 G, using the technique already described. The shape of the profiles is quite reliable since it takes into account the T_e profile measured by the IV sweep. We remark that the peak density profiles are about four times larger compared to those in Fig. 3.16(a). This confirms that LPs largely underestimate the absolute electron density in these regimes and other techniques are required to obtain more reliable data. In the case of argon plasmas, LPs suffer a very strong heating when the IV sweeps are performed. Radial T_e profiles in argon show a peak at $\sim 4\,\text{eV}$ and $\sim 2\,\text{eV}$ at $r = 5\,\text{mm}$ but the profile is very distorted, therefore we do not take it into account. In this plasma regime, the LP is biased at I_{sat} and rapidly
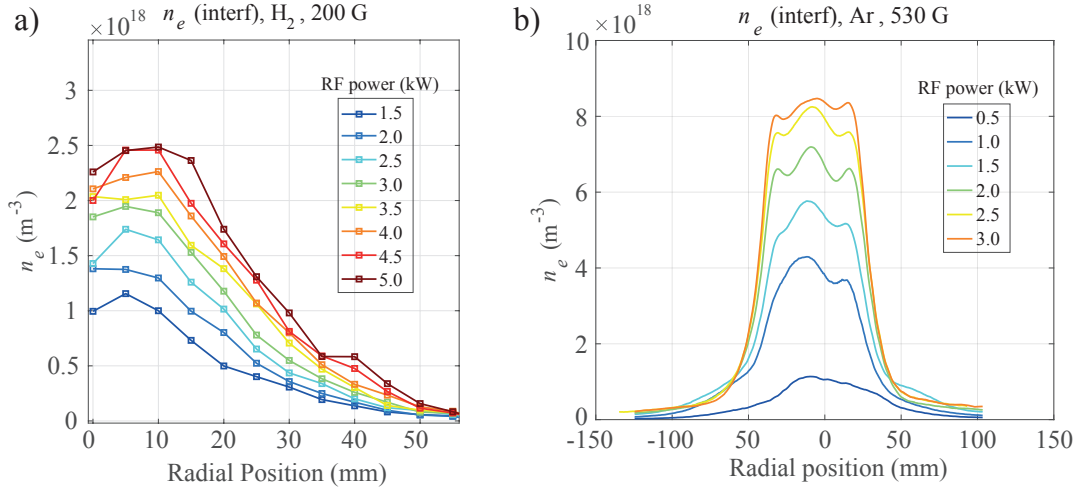
Figure 3.17 – (a) Radial electron density profile of a H_2 plasma, at 200 G, and (b) for an Ar plasma, at 530 G, for different RF powers. The gas pressure in both cases was 0.3 Pa. The profiles are obtained with LP and calibrated with microwave interferometry.

passes through the center of the plasma column. The I_{sat} profiles are then calibrated using microwave interferometer data and considering a uniform electron temperature along the radius. Fig. 3.17 (b) shows radial n_e profiles for a argon plasma with 530 G magnetic field on axis and different RF powers. We remark the rapid jump in electron density from 0.5 to 1.0 kW RF power: this might be due to the complete transition from the inductive to the helicon regime. The central part shows multiple peaks, in particular the case at 2 kW shows an almost symmetrical triple peak profile. In the visible light, a brighter zone, in the literature known as the *blue core* appears [136]. In this condition, the helicon wave is efficiently depositing its power into the plasma. We also remark that argon profiles are characterized by a sharper radial density gradient compared to H_2, therefore plasma fluctuations induced by density gradients might be even more important in this case. The non perfect radial symmetry of the profile for argon is not trivial to explain and might be due to a combination of effects such as the mechanism of power deposition of the helicon waves, plasma turbulence and neutral depletion. A more direct and local technique to measure n_e and T_e in Ar plasmas is the Thomson Scattering, which is discussed in Sec. 6.

By combining the n_e and T_e radial profiles along the plasma column with interferometric measurements, it is then also possible to obtain 3D n_e profiles, by fitting I_{sat} radial profiles along the plasma column. I_{sat} radial profiles exhibit two small side peaks near the antenna, which then smoothly disappear moving towards the downstream region. The I_{sat} radial profiles are fitted by the sum of the three following Gaussian-like functions:
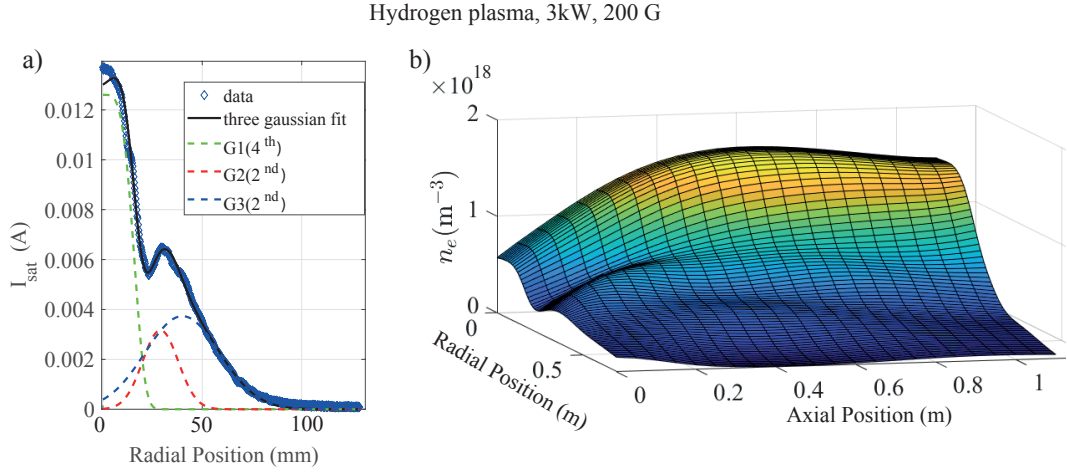
Figure 3.18 – (a) 3 Gaussian fit of the I_{sat} profile in front of the antenna region. (b) 2D n_e interpolated axisymmetric profile for a H_2 obtained with LP and calibrated with microwave interferometry.

$$G_1(r,z) = a_1(z)e^{-\left(\frac{r}{w_1(z)}\right)^4}, \tag{3.25}$$

$$G_2(r,z) = a_2(z)e^{-\left(\frac{r-r_2(z)}{w_2(z)}\right)^2}, \tag{3.26}$$

$$G_3(r,z) = a_3(z)e^{-\left(\frac{r-r_3^0}{w_3(z)}\right)^2}. \tag{3.27}$$

where $a_1(z)$, $a_2(z)$, $a_3(z)$, $w_1(z)$, $w_2(z)$, $w_3(z)$ and $r_2(z)$ are model functions fitting the peaks' amplitude, width and position along the axial direction and r_3^0 is a constant. The total function $G = G_1 + G_2 + G_3$ is a quite good modeling of the I_{sat} 3D profiles since its displacement with respect to the experimental data is comparable to the typical I_{sat} noise. The evolution of the T_e profiles along the plasma column is less regular compared to I_{sat} profiles and it is modeled by the following function:

$$T_e(r,z) = T_e^0(z)e^{-\left(\frac{r}{w(z)}\right)^2}. \tag{3.28}$$

By combining $G(r,z)$, $T_e(r,z)$ and the microwave interferometry data, we can obtain the full 3D axisymmetric profile in Fig. 3.18(b). The electron density on axis increases from $0.5 \times 10^{18}\,\text{m}^{-3}$ in front of the birdcage antenna to $1.6 \times 10^{18}\,\text{m}^{-3}$ at 50 cm away from it and it is quite homogeneous ($\pm 5\,\%$) over 60 cm. The good axial homogeneity in the downstream region is particularly interesting for elongated negative ion sources, required for photoneutralization schemes [127] also briefly discussed in Sec. 8.3. The 3D model function of T_e and n_e are also useful to numerical models, discussed in Sec. 7. By combining the n_e and the T_e mapping in the plasma column it is straightforward to determine the electron pressure mapping since
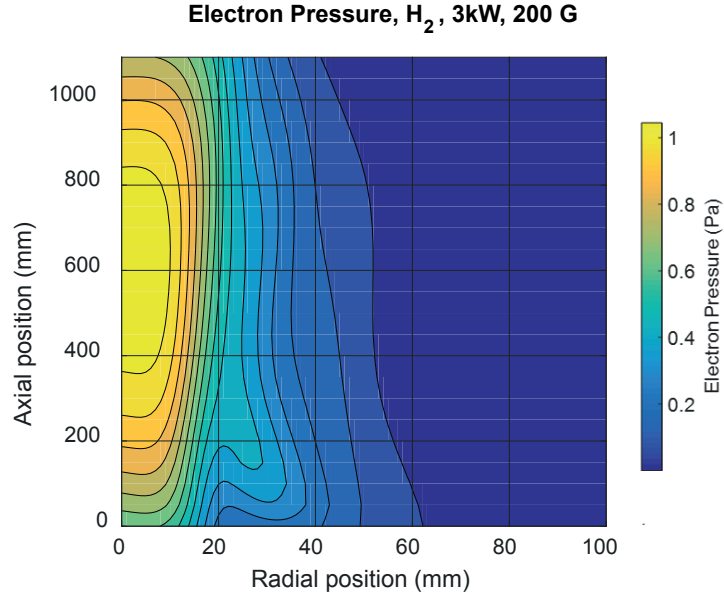
Figure 3.19 – Electron pressure 3D profiles calculated by the n_e and the T_e 3D mapping.

$p_e = k_b n_e T_e$. Fig. 3.19 shows p_e in the plasma volume. We remark that p_e in the center reaches 1 Pa, comparable to the neutral pressure. This means that the neutral depletion may be not negligible for this plasma regime.

3.3.3 EEPF for electrons and isotopic effect

The electron energy probability function (EEPF) might help to better understand the heating mechanism of plasma electrons and can be obtained by the Druyvesteyn formula [43]. The procedure employed to analyse the IV characteristic is to calculate their second derivative by a Savitzky-Golay filter, using second order polynomials [29]. To measure electron populations with different temperatures, IV characteristics with low noise are needed. This was not possible to achieve with the data acquisition system in RAID since the sweep modules often exhibit noise and RF disturbances. To measure clear IV sweeps, a dedicated system developed by Dr. S. Béchu of Centre de Recherche Plasmas-Matériaux-Nanostructures (Grenoble, France), was installed in RAID. The measurements shown in this paragraph where performed during Langmuir Probe laser photodetachment experimental campaigns, which are described in details in Sec. 4.2. The measurements were performed on the edge of the plasma column ($r > 40$ mm) where the electron current is tolerable for the system. Fig. 3.20 shows EEPF (Electron Energy Particle Function) for two RF powers, 1500 W and 5000 W and for two radial locations: $r = 40$ mm and $r = 65$ mm. Measurements at larger radial position were not performed because of the lengthy procedure and because we were mostly interested to the region where negative ions are most efficiently produced.

We can see the presence of a "cold" and a "hot" electron population, which are determined
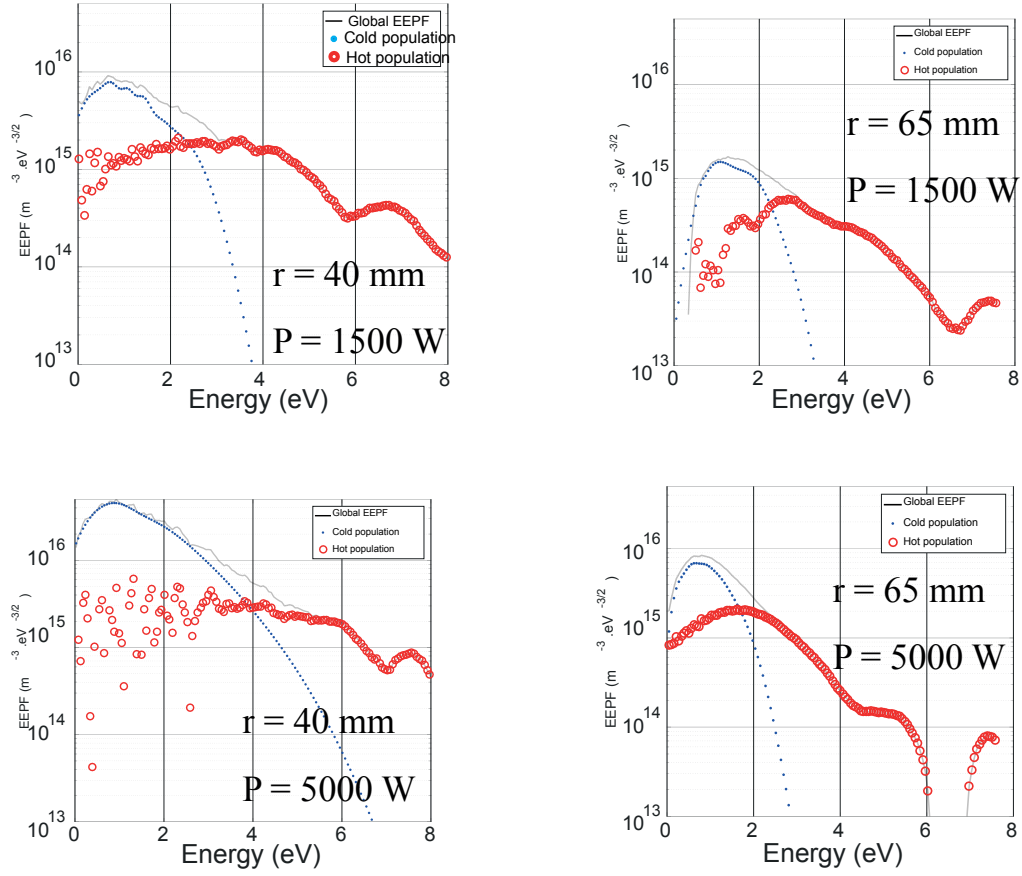
Figure 3.20 – Electron energy probability functions at the radial position $r = 40$ mm (left column) and at $r = 65$ mm (right column) for 1500 W (top row) and for 5000 W (bottom row) for a hydrogen plasma, showing the points which are considered belonging to a "cold" population (in blue) and to a "hot population" (in red).

by linear fitting with several Maxwellian distributions. The large oscillations above 6 eV are due to measurement uncertainties. Indeed, in this region, where the electron temperature is typically 1-2 eV, when the probe is biased at 5 it is strongly repulsive and very few electrons are collected.

The EEPF can be integrated numerically to obtain the electron density and the effective electron temperature, according to the electron distribution function considered. Fig. 3.21 shows the cold (blue squares) and hot (red squares) electron populations as a function of the RF power for a hydrogen plasma (left column) and for a deuterium plasma (on the right). The violet stars are for the total electron density. We remark that for the same RF power, the electron density in deuterium is about two times that in hydrogen, showing an important isotopic effect at the edge of the plasma column.

Since the LP can be affected by the presence of the magnetic field and other phenomena previously discussed (see Sec. 3.1.2), we investigated H_2 and D_2 plasmas with the interfero-
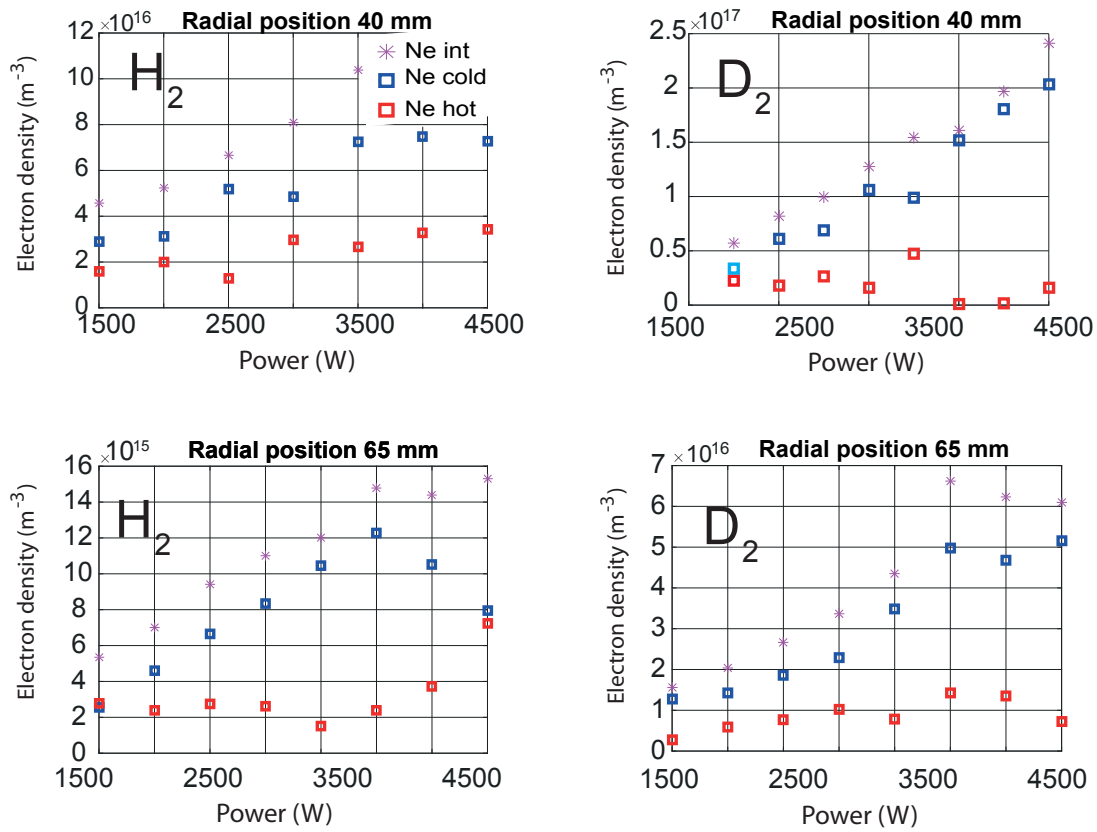
Figure 3.21 – Cold (blue squares) and hot (red squares) electron populations as a function of the RF power for a hydrogen plasma (left column) and for a deuterium plasma (on the right). For the same power, the electron density in deuterium is about two times that in hydrogen.

microwave phase shift H_2 and D_2 200 G
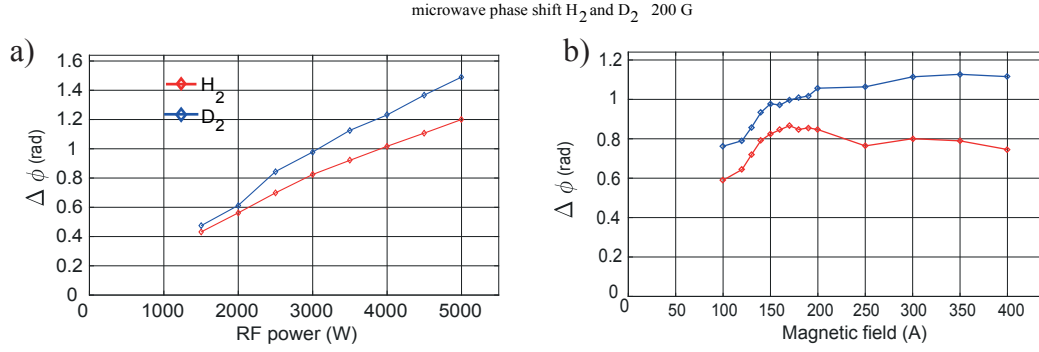
Figure 3.22 – (a) Line integrated density (through the plasma diameter) as a function of RF power for a hydrogen and a deuterium plasma with $B = 200\,G$ at the center. (b) Line-integrated electron density as a function of magnetic field (coil current) for a hydrogen and a deuterium plasma with 3 kW RF power. The gas pressure in both cases was 0.3 Pa. The line-integrated electron density is 20 % higher in deuterium suggesting that the Birdcage antenna has a better coupling in deuterium discharges.

metric system alone, which is only sensitive to the electron density. The mw modules are located at the axial position $z = 83\,cm$ and the probing mw beam was directed towards the center of the plasma column. Fig. 3.21 (a) shows the measured phase shift $\Delta\phi$ of a microwave beam when passing though the plasma diameter, which is proportional to the line integrated electron density $\int n_e dl$, for a hydrogen and a deuterium plasma as a function of the RF power, 200 G magnetic field and 0.3 gas pressure. Despite the non local measurement, the higher electron density (about 20% more) in the case of D_2 plasma is evident. A similar difference in density also appears in Fig. 3.21(b), showing $\Delta\phi$ as a function of the external magnetic field. A monotonic increase is measured up to 150 A coil current, corresponding to 200 G, and then a saturation is observed. For every magnetic field, $\Delta\phi$ is about 20-30% higher in the case of deuterium. By changing the measurement position of the microwave beam, one can measure the line integrated electron density along the radius. Fig. 3.23 shows the radial profiles of $\Delta\phi$ for different RF powers for hydrogen and deuterium. Unfortunately, the poor spatial resolution of the probing mw beam is $\sim 1.5\,cm$, which is not sufficient to perform an Abel inversion to calculate the radial n_e profiles. Nevertheless, we remark 20 % more in the case of deuterium also here. The measurements in D_2 at power > 4.5 kW were not reliable because of strong fluctuations resulting in ambiguity on the phase measurement.

To summarize, these interferometric tests suggest that the Birdcage antenna has a better coupling in deuterium discharges than in hydrogen.

Figure 3.23 – Radial profiles of the line integrated electron density for a hydrogen plasma (on the left) and for a deuterium plasma (on the right) for different RF powers, 200 G magnetic field and 0.3 Pa gas pressure.

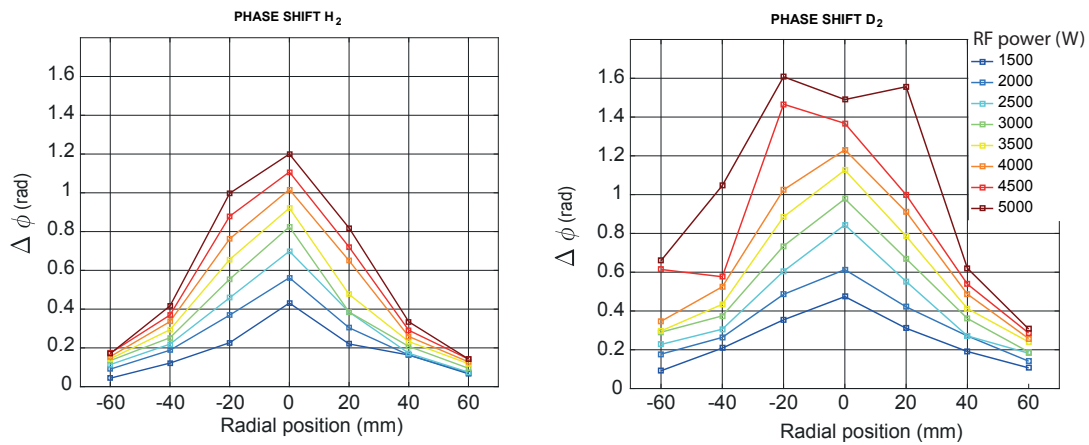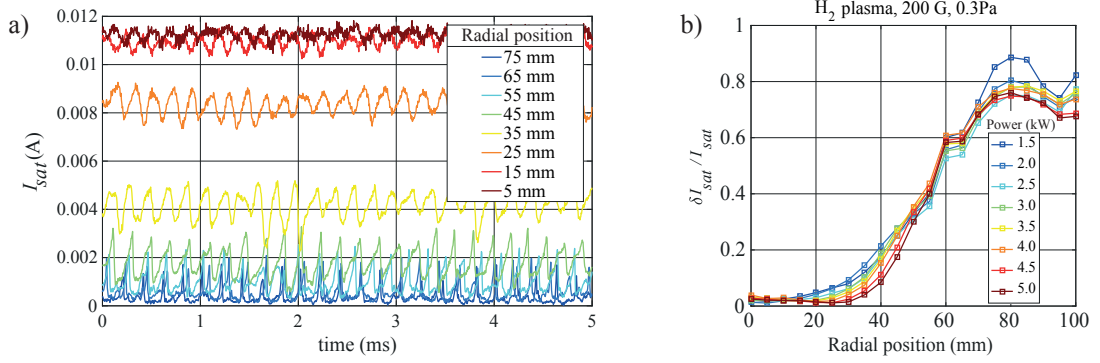Figure 3.24 – (a) Time traces of I_{sat} showing the local fluctuations of plasma density from the center to the edge of a H_2 plasma column. (b) Normalized amplitude of plasma density fluctuations along the radial direction.

3.4 Plasma Oscillations

So far we have studied equilibrium plasma profiles, namely time averaged plasma profiles. The IV curves considered in previous sections to extract plasma parameters are usually obtained over many periods of the IV sweep, which is of the order of 0.1 Hz. Therefore, all plasma oscillatory phenomena, such as MHD modes and microinstabilities, which have characteristic frequencies larger than a few kHz, cannot be distinguished. To measure the local fluctuation of electron density one should in principle bias the probe above the plasma potential. However IV curves are usually distorted by the RF in this region.

To avoid these problem, a LP can be negatively biased, in the ion saturation regime, and the measured fluctuations are still proportional to the plasma density and much less affected by thermal heating. Since $n_i \propto I_{sat}/\sqrt{T_e}$, this leads to $\frac{\delta n_i}{n_i} = \frac{\delta I_{sat}}{I_{sat}} + \frac{1}{2}\frac{\delta T_e}{T_e}$. However, since $\frac{\delta T_e}{T_e} \ll \frac{\delta I_{sat}}{I_{sat}}$, we neglect the contribution of the electron temperature variation in the interpretation. Fig. 3.24(a) shows the I_{sat} time traces of LPs at different radial positions (from close to the plasma center, at $r = 5$ mm, to the edge, at $r = 75$ mm), over 5 ms for a hydrogen plasma in standard conditions and 3.5 kW power. The probe is negatively biased at -27 V in ion saturation mode. We remark that high amplitude plasma density fluctuations are mostly localized at the edge of the column. Also, the narrow peaks of I_{sat} at $r > 55$ mm suggest that there might be small scale density structures such as blobs or filaments on the plasma edge which could be generated by turbulent effects. The presence of turbulence at the edge of plasmas is typical of SOL (Scrape-Off Layer) in tokamaks and even in smaller toroidal plasma experiments [9], and it is triggered by sharp density gradients.

To understand the nature of the plasma density fluctuations with respect to the background density, it is more convenient to plot the amplitude of the fluctuation over the background local density. In Fig. 3.24(b) we plot $\delta I_{sat}/I_{sat}$, where δI_{sat} is the standard variation of I_{sat}, along the radial direction for a H_2 plasma in standard condition and different RF powers. We note that plasma density oscillations are within 20% for $r < 40$ mm increasing up to almost 100% on at $r \sim 80$ mm. This suggests that the entire plasma column is subject to important
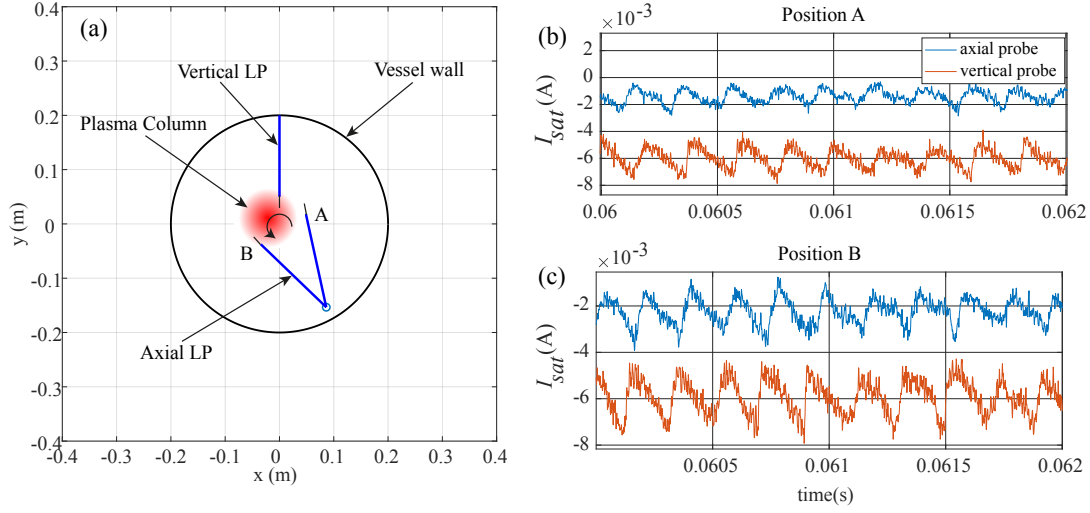
Figure 3.25 – (a) Setup with two LPs to study the dynamics of the plasma column in the transverse plane. (b) Time traces of I_{sat} measured by the vertical LP and the axial LP at the location A and B showing the phase shift of the two I_{sat} signals, suggesting the propagation of a plasma along the azimuthal direction.

displacements at peripheral radial locations. Also, the shape of the profile is only weakly dependent on the RF power, and thus the density, suggesting that the characteristic radial gradients of the plasma density are invariant with power. In other words, plasma density profiles scale proportionally with power. This is confirmed by looking at n_e profiles in Fig. 3.16 (a) evolving linearly with power.

Tests with two LPs to measure plasma waves fluctuations

By using two LPs one can study the space-time nature of plasma fluctuations by measuring the phase shift between two I_{sat} time traces measured in two close positions. If the two tips are separated by a distance Δx and the two signals have a phase difference of $\Delta\phi$, the wavenumber is $k = \Delta\phi / \Delta x$, from which the wavelength of the perturbation λ can be deduced $\lambda = 2\pi / k$. We expect that radial density and electric field gradients trigger a global azimuthal movement of the plasma column due to the $\vec{E} \times \vec{B}$ drift and $\nabla p \times \vec{B}$ diamagnetic drift [34]. To investigate the dynamic of the column in the tangential direction we have employed two LPs, the axial probe and a radial LP, both at the axial position $z = 83$ cm, as shown in Fig. 3.25 (a). The axial probe can be located at different radial positions by rotating around its axis. The vertical LP can be automatically displaced along the vertical direction. The tip of the vertical LP is fixed at $r = 5$ cm whereas the axial LP is also at $r = 5$ cm in position A and position B. In this way, we can study the plasma evolution along a chord at a certain radial distance from the center. In A, the tip of the axial LP and the tip of the vertical LP form an angle of about 80 deg. When the axial probe is in position B the axial LP and the vertical LP tips form an angle of 135 deg. In Fig. 3.25(b) and 3.25(c) we show the I_{sat} for the two probes and the positions A and B, in a
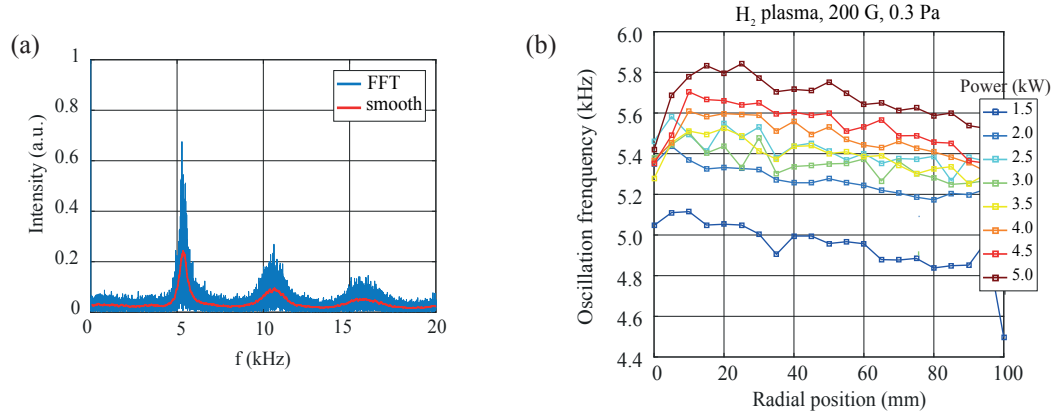
Figure 3.26 – (a) Fourier transform of I_{sat} showing the first harmonic at 5 kHz, a frequency characteristic of drift-interchange modes. (b) Oscillation frequency along the radius for different RF powers, suggesting the rigid rotation of the entire plasma column.

temporal window of 2 ms. We remark that the shape of the oscillations is similar suggesting that the dynamic is similar in every point of the plasma. In Fig. 3.25(b) we see that the peaks of the axial probe I_{sat} precede those of the vertical probe of about a quarter of period. In Fig. 3.25(c) the two signals are almost in phase opposition. This general behaviour suggests that the plasma column is rigidly moving counterclockwise. The force driving this rotation is either the $\vec{E} \times \vec{B}$ or the diamagnetic drift, or a combination of both. The measurements of azimuthal modes with higher azimuthal number would require an array of multiple radial LPs. Perhaps the axis of the plasma column is displaced by a few cm with respect to the mechanical axis of the chamber vessel and globally rotates in the azimuthal direction. Even though we are interested in the steady state profiles, we should always take into account the fact that the plasma performs these oscillations.

To further investigate the origin of these plasma density fluctuations, we show in Fig. 3.26(a) the FFT (Fast Fourier Transform) of a typical I_{sat} temporal trace, like that in Fig. 3.24. We see the first harmonic at ~ 5kHz which is a frequency typical of plasma MHD (Magneto Hydro Dynamics) fluctuations in cold plasma devices [9]. In general experiments in plasmas, electrostatic fluctuations associated with drift/interchange modes are in the range of a few tens of kHz. Fourier based technique are largely employed to study such fluctuations [54].

Fig. 3.26(b) shows the frequency of the plasma density fluctuations as a function of the radial position and for different RF powers. We remark that the frequency decreases by only a few percent up to 10 cm from the center. This suggests, as a confirmation of the previous discussion, that we are dealing with the rigid rotation of the entire plasma column. The decrease in frequency might be due to a shear effect making the plasma on the edge rotating a bit slower than that at the center. To reconstruct the transverse structure of the RAID plasma column, the development of a full tomographic system moving on an automatic arc-rail is currently underway. X-ray tomography is used in Tokamak research to study plasma fluctuations in the plasma core [52], where the electron temperature is several hundreds of keV.

In the case of RAID, because of the much lower electron temperatures, the radiation emitted from the plasma is mostly located in the visible range.

3.5   Scattering of microwaves by a magnetized plasma column

Turbulent structures are present in both tokamaks and in simple magnetized torus experiments [99, 9]. In these magnetic configurations, the SoL is usually characterized by turbulent structures, called filaments and blobs [99]. Linear plasma devices, such as RAID, also show plasma instabilities. One of these is the *flute instability* which arises due to radial pressure gradients $kT\nabla n_e$ [34]. The rapid change in density in the radial direction induces drift waves on the surfaces of the plasma cylinder which in turn make the entire structure rotate in the azimuthal direction. We believe that this might be one of the main mechanisms producing the rotation of the plasma column. We can therefore expect that the propagation of a mw beam injected transverse to the plasma column is affected by the dynamics of the plasma column. Unlike tokamaks, where plasma profiles could be irregular and where a large variety of turbulence is present, linear plasma devices show a more symmetric cross section and a smaller variety of instabilities. This makes it much simpler to study and model numerically the scattering of a mw beam from plasma structures. The measurements reported in this section were performed in the framework of a study aimed to investigate a possible use of microwave beams to measure edge turbulence in tokamaks [32].

The scattering of a mw beam by a plasma column is expected to spread the power due to refraction and could be used to determine the plasma density distribution [149]. The idea is to use the setup shown in Fig. 3.7 and study how the transmission of mw is affected by the properties of the plasma column. We can study the effect of varying the plasma density and shape, which can be achieved by changing the RF power and the magnetic field. The cross section of the plasma column regularly displaces in the azimuthal direction and temporally affects the propagation of the mw beam. The mw beam in this setup has the electric field $\vec{E}$ perpendicular to $\vec{B}$, corresponding to X-mode propagation. Even for the highest magnetic field achievable in RAID (800G), the expression for the refractive index N for unmagnetized plasma in Eq. 3.20 is accurate within 0.1 %.

We measure the power deposition along the vertical axis by displacing the receiver module on an automatic rail. The receiver is moved back and forth to double check possible plasma asymmetries. By measuring VMAG along the vertical direction, we detect the scattered mw profiles and also signal fluctuations due to plasma refraction of mw rays. In the most peripheral locations, the amplitude of these fluctuations is comparable to the average signal suggesting that the plasma column completely diffracts the mw beam on the edge. To understand the power deposition profiles it is more convenient to average out these fluctuations. Fig. 3.27 (a) and (b) respectively show the intensity of the microwave beam along the vertical position measured by the receiver for Ar plasma in the absence and in the presence of the blue core regime. In Fig. 3.27 (a) the black curve shows the intensity profile without plasma (in vacuum). The other profiles are obtained in the presence of a 3 kW RF power, 0.3 Pa and
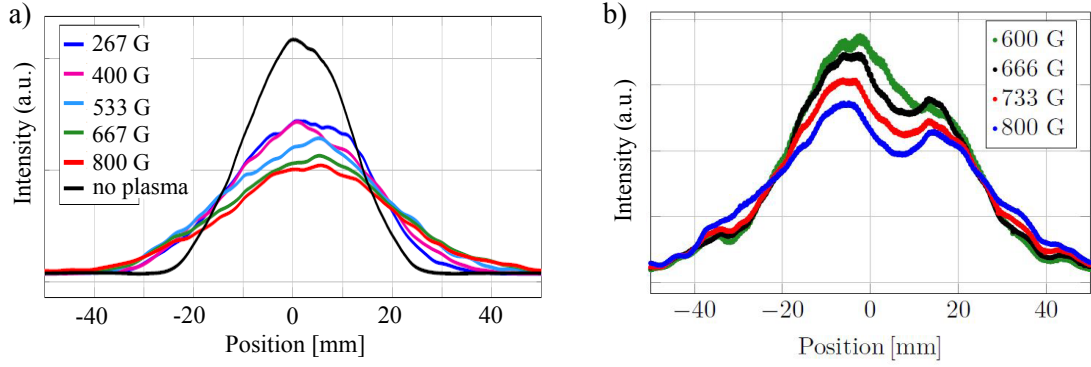
Figure 3.27 – Intensity profile of a mw beam scattered by an argon plasma column for (a) 3 kW RF power for different magnetic fields (no blue core) (b) 2kW RF power (blue core regime) showing the effect of the dense core region scattering the mw beam to the sides.

varying magnetic fields. By increasing the magnetic field, the plasma column shrinks (and the density increases) and the intensity profile of mw tends to broaden. In Fig. 3.27 (b) the argon plasma is at 2 kW RF power, the blue core is visible and its presence is also confirmed by LP measurements in Fig. 3.17. The intensity profiles show a clear hole at about the center, whose depth increases with the magnetic field. This effect is very likely due to the effect of the central denser region, which scatters the mw beam to the sides. This technique could be helpful to study high density plasmas even though the interpretation of the scattered beam is not straightforward and requires numerical modeling, which is briefly described in Sec. 3.5.1.

3.5.1 Simulation of mw propagation in plasma

To verify the correct focusing of the microwave beam by the lens and to better understand how plasma affects the propagation of the probing microwave beam, numerical simulations are very helpful. The COMSOL model of electromagnetism can be employed to calculate the wave field propagation in materials with arbitrary refractive index. Since a full 3D model would require several weeks of computation time and would not add any additional relevant physics, we opted for a 2D model, which is enough to visualize the beam propagation patterns. In Fig. 3.28 the simulation of a typical mw beam used to probe RAID plasma is shown. This is a cross section of RAID at the axial position $z = 0.83\,\mathrm{m}$ when the interferometric setup and other laser-based diagnostics are usually installed. The blue area represents the domain of the simulation. The granularity of the mesh is such that $\frac{\lambda}{9} < mesh\,size < \frac{\lambda}{4}$, where λ is the wavelength in free space, this was a good compromise between the resolution of the wavefield and the computational time. We consider the propagation of the fundamental mode in the rectangular waveguide (see the zoom inset in Fig. 3.28), whose electric field is described by $E_y(x) = E_0 \sin\left(\frac{\pi x}{a}\right)$, where x is the direction of the axis (perpendicular to the page), E_0 is the peak electric field and a is the width of the waveguide. The wave propagates in free space up to the first surface of the lens where the curve wavefront is transformed into a planar wave front. Then, when exiting the lens from the second surface it is focused again so that the
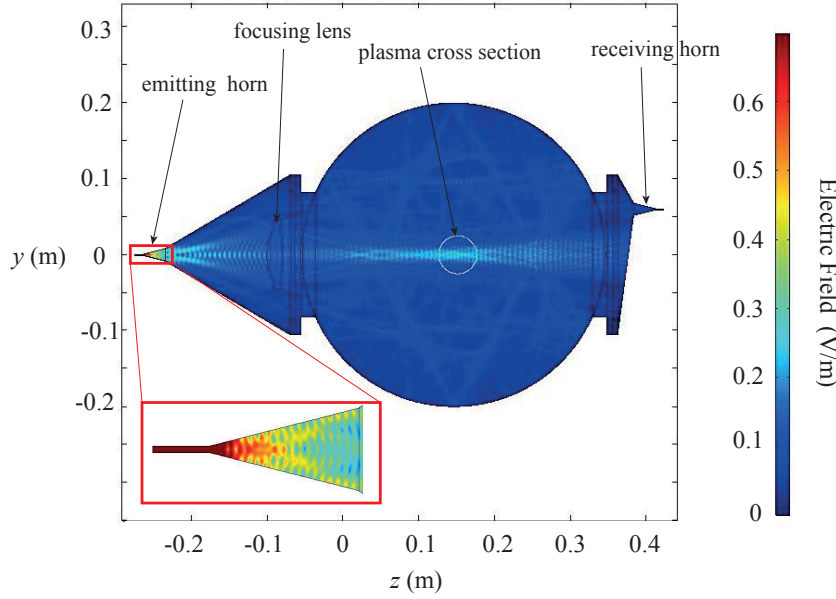
Figure 3.28 – Simulation of the propagation of a microwave beam employed to perform microwave interferometry in RAID. The horn on the left emits a microwave beam which is focused to the high density core (up to $10^{19}\,\mathrm{m}^{-3}$). The phase and the amplitude of the scattered wave is then measured by the receiving horn on the right.

beam waist is approximately in the center of the plasma column. This simulation verifies that the lens is properly focusing the beam. The central white circle represents the FWHM of the plasma profiles with $n_e^{peak} = 10^{19}\,\mathrm{m}^{-3}$. The wave is then measured by the receiving horn. We confirmed that the presence of the plasma column makes the beam spread more than in free space and that an axial displacement of the column makes the entire beam deviate far from the propagation axis.

3.6 Comparison of plasma profiles produced by a Birdcage and a Half-Helix antenna

The RF power transfer efficiency is a crucial feature of plasma sources and determines how much of the delivered power from the power generator is effectively used to ionize the gas. Currently, Inductively Coupled Plasmas (ICPs) are the most common radiofrequency low pressure plasma sources for fusion where a high degree of ionization and dissociation are required. The understanding of coupling efficiency with hydrogen and deuterium plasmas is under investigation [38]. For the next generation of tokamaks, whose design will be driven by RAMI requirements [130], the power efficiency of the drivers will represent an important issue and it is high desirable to be optimized. Helicon plasmas are very attractive in terms of coupling efficiency because when the helicon regime is achieved, a high electron density

Figure 3.29 – Right handed half helix antenna installed on the ceramic tube.

can be obtained with a few kW power. The coupling efficiency of a helicon antenna in a Nagoya geometry was previously investigated [25] giving promising results also in terms of the dissociation degree. In this section, we compare the plasma coupling efficiency of a conventional type of helicon antenna, named Half-Helix (HH) antenna with the BirdCage (BC) antenna. It is instructive to understand the pros and cons of the BC with a HH, in RAID magnetic field geometry. The HH antennas are Nagoya antennas (two straight legs) but with twisted legs, to better match the helicon wave field. There are two kinds of HH antennas according to what azimuthal helicon mode number m they can excite: the *right-helical*, exciting the mode number $m = +1$, and the *left-helical*, exciting the mode number $m = -1$ [125]. It is experimentally observed that the right helical antenna couples better to the plasma, although the exact reason is still under debate [97]. To study the efficiency in sustaining the plasma discharge we will measure the plasma characteristics both in the antenna and in the vessel region, employing the techniques described in Sec. 3.

3.6.1 The Half-Helix antenna

The installation of the BC antenna was described in Sec. 2.1.2; we herein present some short detail on the setup with the HH. The HH antenna, whose length and diameter is very similar to the BC, was installed in the same axial location on the BC in the ceramic tube, and it is depicted in Fig. 3.29. It is made of two copper rings linked by two half-twisted copper bars making a half rotation. The antenna is connected to the same matching box as the BC and is operated at 13.56 MHz. Water cooling is also used similarly to the BC antenna. To compare the behaviour of the two antennas, we perform LP measurements both in the antenna region with a LP movable along the axis and in the downstream region with the axial LP calibrated with the mw-interferometer. All the tests were performed in Ar since plasma ignition is easier and electron densities are larger compared to H_2.

Figure 3.30 – I_{sat} profiles along the axis of the antenna region in Ar in inductive regime (no magnetic field) with 0.3 Pa gas pressure for the BC in (a) and the HH in (b).

3.6.2 Measurements in plasma with the Birdcage and the Half Helix antenna

We show here the measurements performed in the antenna region both in inductive and helicon regime, then we show the radial downstream profiles of plasma density and then we investigate the effect of varying the magnetic field in the antenna region. The experimental results reported here were performed in the framework of a project dedicated to the investigation of the RF Coupling efficiency of the HH and the BC in different magnetic geometries in RAID [82].

Measurements in the antenna region

To start with, it is interesting to measure the power coupling to the plasma when the BC and the HH are operated without magnetic field, therefore in the purely inductive regime. Because of the high RF noise, it was impossible to obtain reliable IV curves from which it would have been possible to estimate the electron temperature and the plasma potential, therefore the following results only show I_{sat} profiles. The high electron temperature close to the antenna shown in Fig. 3.13 suggests that there might be hot electrons ($T_e \gtrsim 8\,\text{eV}$) in the antenna region. In Fig. 3.30(a) and (b) we show the I_{sat} profiles along the axis of the antenna region in argon in the inductive regime and different RF powers for the BC and for the HH. The dark grey area in the center corresponds to the antenna length, the lighter dark area marks where the vacuum vessel starts. We remark that the axial LP can enter inside the vessel by 5 cm, to bridge the range which is not sampled by the axial probe. The axial position of 5 cm corresponds to the edge of the ceramic foam which bounds the column on the left. Plasma is mostly produced in the antenna region as expected and diffuses smoothly in both directions. If we suppose that the electron temperature is the same for both antennas, the BC achieves a slightly higher density compared to the HH, but the two profiles are quite similar.
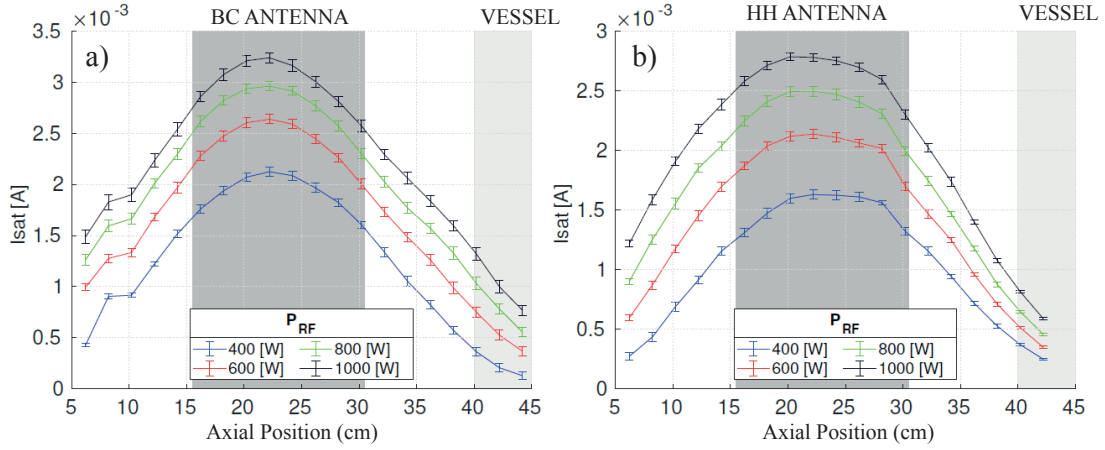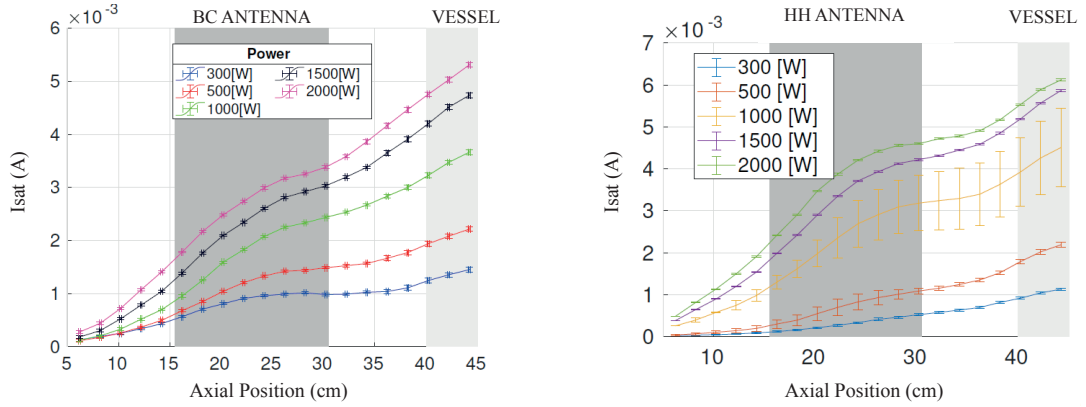
Figure 3.31 – I_{sat} profiles along the axis of the antenna region in Ar in helicon regime with 0.3 Pa gas pressure for the BC in (a) and the HH in (b). The magnetic field in the center of the antenna region is about 60 G (RAID standard conditions).

When the magnetic field is turned on, the helicon regime can also be excited. Fig. 3.31(a) and (b) shows the I_{sat} profiles along the antenna axis for both antennas in the presence of an axial magnetic field and different RF powers. The magnetic field on axis is that for RAID standard conditions as shown in Fig. 2.4. Instead of the I_{sat} decaying toward the vessel region, a monotonic increase is observed. This increase of density far from the antenna can only be explained by the achievement of the helicon regime. The small bump in the center of the antenna region might be due a residual inductive regime superposed on the helicon regime. However, the only direct approach to confirm the propagation of a helicon wave, would be to perform measurements in the antenna region. Unfortunately this is technically hard because of the limited access and the not negligible size of a magnetic probe compared to the plasma volume in the antenna region.

Radial downstream profiles

In the helicon regime it is also interesting to compare the radial plasma profile in the vessel region with the BC and the HH. In Fig. 3.32 (a) and (b) we plot the radial profiles in two different configurations of the magnetic field and for two powers, 800 and 1000 W. The profiles are obtained by rapidly passing the axial probe in I_{sat} through the center of the plasma column as previously described. The blue and the red profiles are respectively for the BC and the HH with the same direction of the magnetic field pointing towards the target. In this situation the helicity of the HH antenna has the same direction as the magnetic field and the mode $m = +1$ is coupled. The black profile marked by "HH-inv" is for the HH when the magnetic field is directed towards the antenna. In this last case, the the mode $m = -1$ is coupled. In the case at 800 W power we see that the HH profile is a bit higher than the HH-inv profile, in the core region, as expected from the better coupling of the $m = +1$ mode, and the BC profiles higher than both. In the case at 1000 W, the HH profile shows important oscillations, whose top
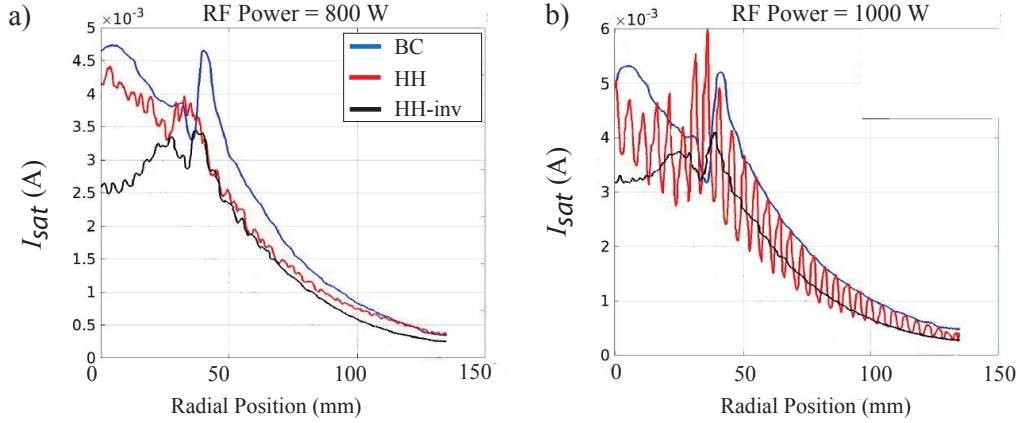
Figure 3.32 – Radial I_{sat} profiles at the exit of the antenna region (axial position $z = 50\,\text{mm}$) with the BC antenna, and the HH antenna in $m = +1$ mode (HH) and in $m = -1$ mode (HH).

convolution are almost entirely coincident with the BC profile. This might mean that the HH antenna tries to couple to a stable regime which is achieved by the BC. It is interesting to note that these oscillations appear by just slightly increasing the RF power, suggesting the presence of narrow transition zones in the parameter space. The results of these tests is that the BC antenna couples to the plasma better than the how the HH antenna does. This is another element to justify the use of BC antenna to efficiently produce helicon plasmas. It is expected that a twisted BC antenna would couple even better than the current BC with parallel legs [61]. This is because the RF field generated by the twisted antenna rotates both in time and along the longitudinal axis. However, experiments and full wave numerical simulations are required to confirm this.

3.7 Conclusions

We have characterized the RAID plasma column by means of LPs and a mw interferometer showing that the BirdCage (BC) antenna efficiently produces high density peaked plasma discharges both in hydrogen and argon. By combining LPs and mw-interferometry, it was possible to estimate the electron density in the plasma core, where LPs suffer strong heating. Plasma temperature profiles are also centrally peaked, and quite uniform along the column, suggesting that the power deposition is mostly concentrated along the plasma axis. Preliminary measurements of plasma density fluctuations show that the plasma column exhibits an approximate azimuthal rigid rotation with a few kHz frequency, however the exact mechanisms triggering this motion should be further investigated. We have finally compared the BC antenna with a conventional antenna Half-Helix by measuring plasma profiles, showing that the BC produces a plasma with much less density fluctuations, suggesting a better RF coupling of the BC than the conventional HH antenna.

4 Laser-based diagnostics for negative ions

The measurement of the density of negative ions produced in a hydrogen and deuterium helicon plasma source for fusion is one of the core topics of this thesis. To understand the viability of helicon plasmas as sources of negative ions for future NBIs, one has to know if negative ions can be efficiently produced. The measurement of negative ions in plasmas can be performed by direct techniques such as Cavity-Ring Down Spectroscopy (CRDS) and LP laser photodetachement, or by an indirect technique, using Optical Emission Spectroscopy (OES) supported by collisional radiative codes. These techniques are routinely employed in negative ion sources for fusion [19, 36, 45], but have been rarely employed in helicon plasma devices. In this chapter, we will focus on CRDS and LP laser photodetachment and we will discuss their implementation in RAID including the technical challenges, the experimental results and how these could drive the future development of helicon sources for fusion. The chapter is organized as follows: in Sec. 4.1 [1] we will detail the most direct and non invasive technique, the CRDS. We will present the design of the experimental setup and the technical challenges due to the interaction of the high finesse optical cavity with the plasma. In Sec. 4.2 [2] we will show how LP probe photodetachment can measure the spatial distribution of negative ions and how this can be combined with CRDS to compute the absolute density of H^- and D^- in the plasma column.

4.1 Cavity Ring-Down Spectroscopy

In a Cavity Ring-Down spectroscopy system, a light pulse bounces multiple times between two high reflectivity (HR) mirrors to measure the medium absorbance. It was introduced by O'Keefe in 1988 to measure absorption spectra [101]. The main features of CRDS are that it is very sensitive, directly measures the number density of the species of interest, and is independent of the intensity of the light source. The main element of a CRDS system is the optical cavity made of two very HR mirrors between which the light undergoes multiple reflections, thus multiplying the interaction length of the light with the absorbing medium.

---

[1]Part of the work presented in this section is published in [3, 4]

[2]Part of the work presented in this section is published in [4]
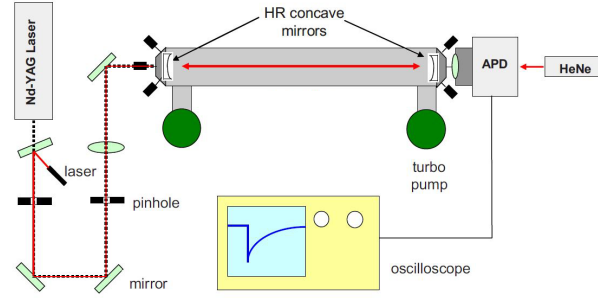
Figure 4.1 – Typical CRDS setup to measure H^- and D^- densities in negative ion sources for fusion (from [106]).

CRDS can be applied as a plasma diagnostic to measure the number density of different plasma species. In fusion, it is particularly interesting for the detection of H^- and D^- in negative ion sources [19, 100]. A typical scheme of a CRDS for fusion is shown in Fig. 4.1. To detect H^- and D^- densities, the employed light source is usually a pulsed Nd:YAG laser whose photon energy (E = 1.2 eV, corresponding to a wavelength of λ = 1064 nm) is large enough to strip the weakly bound electron of H^- ($E_{binding}$ = 0.75 eV) by photodetachment,

$$h\nu + H^- \rightarrow H + e. \tag{4.1}$$

The light reflected back and forth inside the cavity is lost both because of the transmission of the mirrors and the presence of an absorbing medium along the line of sight (LOS) of the laser. The signal leaking through the cavity consists of a train of pulses whose intensity $I(t)$ shows an exponential decay

$$I(t) = I_0 e^{-t/\tau}, \tag{4.2}$$

where I_0 is the initial intensity and τ can be expressed as:

$$\tau = \frac{L}{c(1 - R + \alpha d)} \tag{4.3}$$

where L is the cavity length, c is the speed of light, R is the reflectivity of the mirrors, and the absorption coefficient is given by $\alpha = \bar{n}_{H^-} \sigma_{H^-}$ where σ_{H^-} is the interaction cross section ($\sigma_{H^-} = 3.5 \times 10^{-21} m^2$ at a wavelength of 1064 nm) and $\bar{n}_{H^-}$ is the H^- line-integrated density. d is the path length of the laser beam in the absorbing medium and is usually the parameter more affected by uncertainty. Equation 4.3 can be used to obtain the line-average of density

$\bar{n}_{H^-}$ as:

$$\bar{n}_{H^-} = \frac{1}{\sigma_{H^-}} \frac{L}{cd} \left(\frac{1}{\tau} - \frac{1}{\tau_0} \right), \tag{4.4}$$

where τ_0 and τ are the values of the decay time in the absence and presence of absorbing medium (H^-/D^-), respectively.

Optical Cavity Stability and modes

To produce a stable cavity, the following equation has to be satisfied [115]:

$$0 \leq g_1 g_2 \leq 1, \tag{4.5}$$

where $g_1 = 1 - L/r_1$ and $g_2 = 1 - L/r_2$, (where r_1 and r_2 are the radii of curvature of the two mirrors [115]. To guarantee the confinement of the light inside the optical cavity, therefore to make the cavity stable, two confocal mirrors are usually employed. In our case, we use two symmetrical concentric mirrors, so we have a symmetrical resonator. In this case, the condition of stability is given by: $0 \leq \frac{d}{-R} \leq 2$ [115], where the radius of curvature R, has to be $R < 0$ for a concave mirror. Another feature that should be taken into account is that the optical cavity, which is basically a resonator, can sustain a large variety of modes. Along the axial direction, for example, the spectrum of possible frequencies ν_q is:

$$\nu_q = q \frac{c}{2L}, \tag{4.6}$$

where q is an integer number and c the speed of light. In the transverse direction, the Transverse Electromagnetic Mode (TEM) can exist, which in a cylindrical symmetric system are described by Laguerre polynomials. The light in the optical cavity of the CRDS is therefore distributed in a variety of resonance modes. It can be demonstrated [87] that the output spectral density is given by:

$$I_0(\omega) = \frac{T^2 e^{-\alpha L}}{(1-R)^2 + 4R \sin^2(kL - \theta)} I_i(\omega), \tag{4.7}$$

where T and R are the transmissivity and the reflectivity of the mirrors, L is the cavity length, $k = \omega/c$ is the wave vector of the light, θ is the phase shift per reflection of the mirrors (usually is π) and $I_i(\omega)$ the input spectral intensity. Therefore, the cavity acts as a frequency selector. We have to remark that the spectral selectivity of the cavity does not depend on the intensity of $I_i(\omega)$.
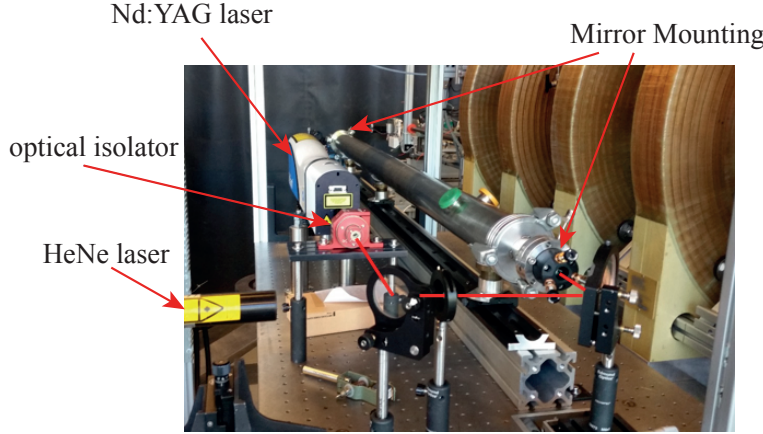
Figure 4.2 – Picture of the testbench employed to measure the reflectivity of the HR mirrors.

4.1.1 Characterization of the HR mirrors and the laser

The results reported in Sec. 4.1.1, 4.1.2, 4.1.3 and 4.1.4, published in [3], were obtained in April-May 2018 during the first successful experimental campaign after more than one year of solving technical issues on the experimental setup and testing several HR mirrors. The main problem was that the first pair of mirrors tested on RAID showed a rapid degradation of reflectivity when exposed to plasma. Despite the countermeasures to limit plasma exposure, such as the use of mechanical shutter and the gas flushing in front of the mirrors, the first pair of mirrors lasted no more than a few minutes in a plasma. It was not possible to restore the initial reflectivity by cleaning the surface, suggesting an irreversible degradation of the HR coating. Other HR mirrors with satisfactory performance were finally provided by another supplier [102] and these were used for the tests described in the next sections (see in the Appendix for more details on HR mirrors).

Since the reflectivity is the crucial parameter for the minimum detectable negative ion density, we tested the HR mirrors on a dedicated testbench. This is to isolate the mirrors from any source of noise coming from mechanical vibrations and to avoid direct exposure to plasma. These tests are necessary to check the nominal reflectivity measured by the supplier on these specific mirrors, which is 99.997% at 1064 nm [102] (the technical note on the company website guarantees, for this type of mirrors, a reflectivity larger than 99.994% at 1064 nm). A picture of the testbench experimental setup is shown in Fig. 4.2. The setup is made of two Layertech HR mirrors with radius of curvature $r = 1$ m. The testbench consists of a 1.8 m tube where the HR mirrors are installed at the extremities. The HR mirrors can be finely tilted by means of three micrometric screws on the mirror mounting to perform the alignment of the laser beam inside the optical cavity. The laser pulses are delivered by a commercial Nd:YAG laser, which is installed on the same optical testbench. The Nd:YAG laser beam has a diameter of 6 mm (FWHM), divergence $\lesssim 0.7$ mrad, and FWHM pulse duration of $\Delta t \approx 5$ ns. This last parameter determines the minimum length $L_{min} = c\Delta t/2 = 0.75$ m of the cavity to avoid overlapping of subsequent pulses, which may result in multiple cavity modes and then
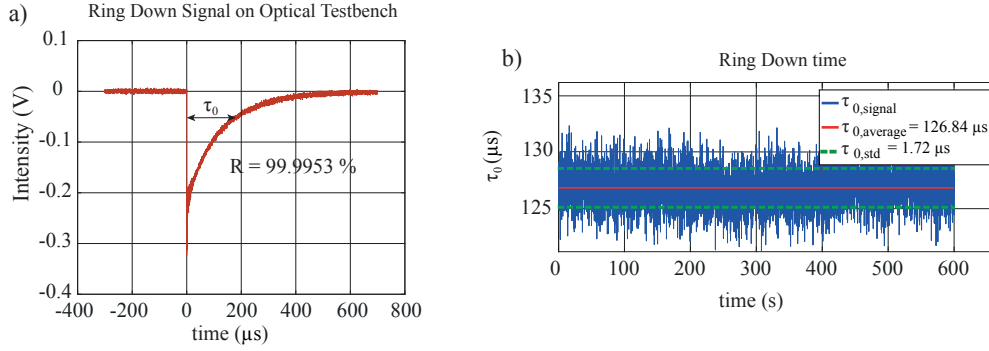
Figure 4.3 – (a) A typical decay signal measured on a 1.8 m long cavity employed to check the nominal reflectivity of the mirrors. (b) Ring-Down decay time during 10 min of laser shots at 10 Hz, showing the stability of the signal.

in a non-exponential decay of the measured light intensity. In front of the laser exit is located an optical isolator to avoid the back reflected light from the planar external surface of the HR mirrors. The alignment is done using a He:Ne visible laser collinear with the trajectory of the Nd:YAG laser. To check the entrance spot of the laser pulse into the cavity, we monitored the mirrors with a webcam sensitive in the infrared region of the spectrum.

The laser light transmitted through the far-side mirror is collected by using a photodiode detector after having been focused by a lens. The detector consists of an avalanche photodiode of 3 mm diameter. The photodiode is coupled to a transimpedance amplifier 4000 V/A and 40 MHz bandwidth and internal amplification 75[112]. The signal is then acquired by a waveform recorder LeCroy 755Zi with 10 MS/s sampling rate and 14 bit digitization in a time window of 1 ms. The laser is pulsed at a frequency of 10 Hz, i.e. 10 ring down signals per second; this was found to be a good trade-off between the temporal fluctuation of τ_0 and the data acquisition rate. Fig. 4.3(a) shows a typical ring down signal after having optimized the mirror alignment. τ_0 denotes the ring down time, namely the e-folding time to reduce the intensity by a factor $1/e$. The signal reflects the convolution of the multiple reflections and shows a characteristic exponential decay. The transient undershoot at $t = 0$ s might be due to the very first reflections in the cavity selecting the main modes. The intrinsic noise of the signal comes from thermal electronic noise of the detector. Fig. 4.3(b) shows the ring-down decay time during 10 min of laser shots. The average over 6000 laser pulses is 126.84 μs, with a standard deviation $\sigma_{\tau_0} = 1.72\,\mu$s. This corresponds to a mirror reflectivity of 99.9953%, above the nominal reflectivity, but below the company measurement report [102]. We also remark that the τ_0 is stable during the entire time interval. This is crucial since the temporal drift of the cavity could be difficult to decouple in the presence of the plasma.

Once we verified that the decay time was satisfactory, we studied the operating regime of the laser and, in particular, how laser parameters should be optimized to minimize τ_0 time fluctuations. Fig. 4.4 shows the standard deviation of the ring-down signal, σ_{τ_0}, as a function of (a) the laser pulse energy, (b) the sampling rate of the oscilloscope, (c) the laser repetition frequency. In Fig. 4.4 (a), σ_{τ_0} slightly decreases with the laser pulse energy. Perhaps, when
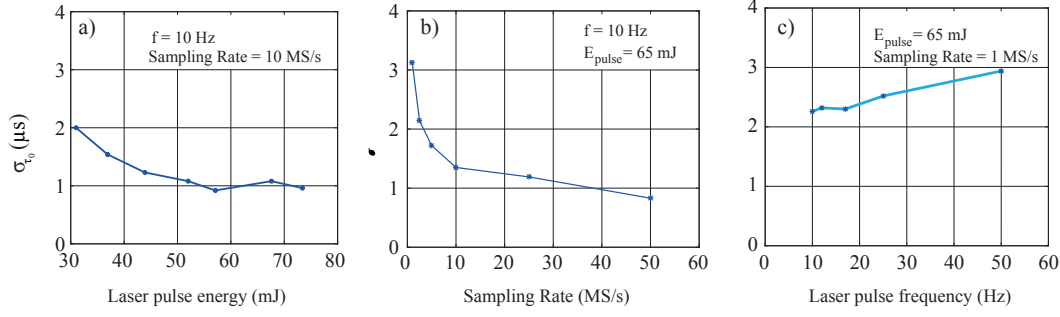
Figure 4.4 – Standard deviation of the decay time, σ_{τ_0}, as a function of (a) the laser pulse energy, (b) the Sampling Rate of the oscilloscope, (c) the laser pulse frequency.

more power is injected in the cavity, the signal to noise ratio is higher and therefore the exponential fit of the decay signal is more precise. Since the laser pulse energy shows non-negligible time fluctuations, we collect 50 laser shots and we average. The typical standard deviation of the pulse energy is about $4-7\%$. In Fig. 4.4 (b), σ_{τ_0} decreases with the sampling rate, in particular in the interval 1-10 MS/s. This might be due to the higher number of points collected with higher sampling rates and therefore to more precise exponential fits. In Fig. 4.4 (c), σ_{τ_0} slightly increases with the laser pulse frequency. This is probably due to the fact that at higher frequencies, the energy spreading of laser pulses is larger. Moreover, at 50 Hz, the oscilloscope is not able to record each ring down signal due to the limited speed of data saving in the hard disk. As a reasonable compromise, we operate the laser at 65 mJ energy per pulse, 10 Hz repetition rate and 10 MS/s. These parameters were employed in the CRDS tests described in the following paragraphs.

With these preliminary tests, we have therefore demonstrated the suitable reflectivity of HR mirrors and the temporal stability of the optical cavity. In the next section we discuss the system implementation in RAID.

4.1.2 CRDS experimental setup in RAID

To install the CRDS system in RAID, we must take into account both physics and technical constraints. The measurement position of the CRDS diagnostic is based on past OES measurements [94], which revealed a significant volume production of H^-/D^-. Their radial distribution is shown in Fig. 4.5 for a H_2 plasma and suggests that negative ions are distributed on a radial shell $\sim 1\,cm$ thick and located around $r \approx 4\,cm$. At this radial location we expect a higher density of negative ions off-axis, since the electron temperature drops to 1-2 eV, which is favorable for the dissociative attachment. We then decided to explore this radial shell by CRDS. Fig. 4.6 shows the arrangement of the optical cavity of the CRDS setup in RAID and its positioning with respect to the expected position of the negative ion ring (in blue) on the background plasma electron (the red region).

In Fig. 4.7 shows a picture of the experimental setup of the CRDS in RAID, from the laser

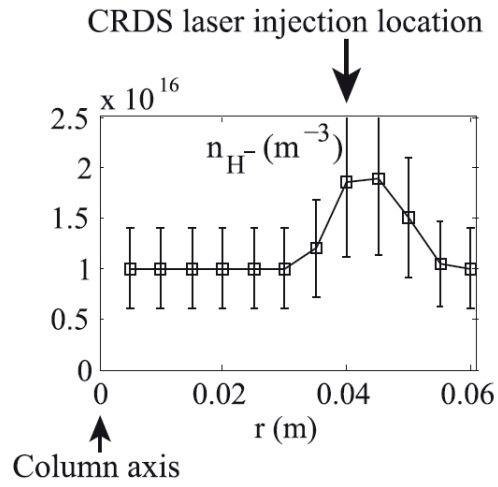CRDS laser injection location

Figure 4.5 – Radial distribution of n_{H^-} as measured by OES [94] at 1.0 m from the RF antenna: the density is peaked off-axis.
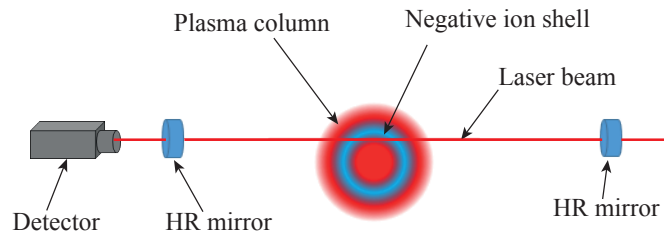

Figure 4.6 – Schematic drawing showing the position of the laser beam in the CRDS optical cavity in RAID. The blue ring shows the region where the highest density of H^- is expected with respect to the background electrons, in red.
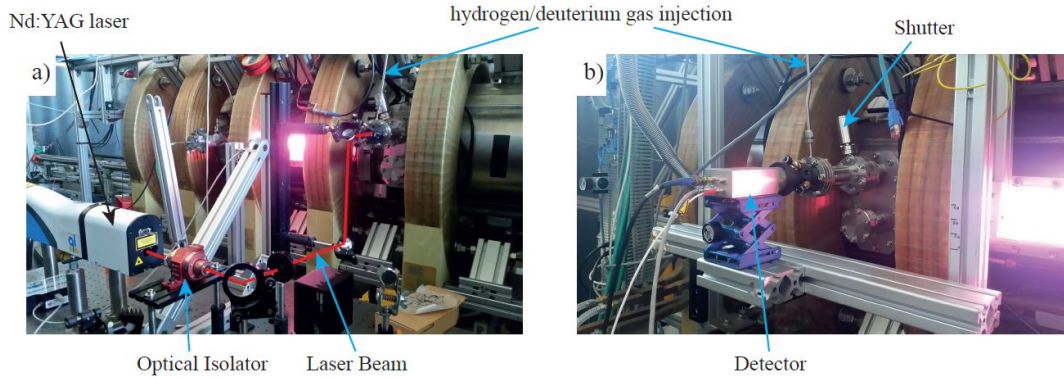
Figure 4.7 – Photo of the CRDS experimental setup in RAID: (a) injection side of the laser: the laser beam passes through the optical isolator, is reflected by three mirrors and injected inside the optical cavity. (b) detection side: the detector collects the light leaking the optical cavity.

injection side, in Fig. 4.7(a) the laser beam (in red) passes through the optical insulator, it is reflected by three mirrors and it is finally injected into the cavity. Approximately, 4% of the impinging laser energy enters the cavity. From the detection side, in Fig. 4.7(b), the detector measures the light leaking from the cavity. The detector objective is connected to the mirror mounting with a conical adapter. Fig. 4.8 (a) and (b) show a schematic of the CRDS experimental setup installed on RAID. The optical cavity is 91 cm long, enough to avoid overlapping of the laser pulses inside the cavity, which may result in multiple cavity modes and then in a non-exponential decay of the measured ring down signal. The HR mirrors are positioned on a vacuum tight mirror mountings on two tube extensions. This is also to minimize the solid angle of exposure of the mirrors to the plasma. The reflectivity of the mirrors must be kept as high as possible, this indeed determines the minimum detectable density, together with the intrinsic electronic noise of the ring-down signal. To limit the exposure time of the mirrors to the plasma, a mechanical shutter in each extension is closed when the CRDS is not operational (see Fig. 4.7(b)). Moreover, to reduce the effect of incoming energetic particles impacting on the mirror HR coating, the feeding hydrogen gas is flushed in front of the HR mirrors. During all CRDS experiments hydrogen, deuterium and helium gases are always flushed in front of the mirrors. Only Ar, which is needed to facilitate the plasma ignition, is injected into the vacuum vessel, from the back flange of the helicon antenna.

4.1.3 Tests in vacuum and gas

A typical decay signal in H_2 gas (in the absence of a plasma) measured at the detector is shown in Fig. 4.9(a). The initial transient peak at $t = 0\,\mathrm{s}$ corresponds to the instant at which a laser pulse strikes the mirror in front of the detector for the first time. After a few reflections, the transverse modes are damped and only the Gaussian mode survives in the optical cavity. The calculation of τ_0 is performed by an exponential fit [in red in Fig. 4.9(a)] after the first $2\,\mu$s of

Figure 4.8 – (a) Side view of RAID: the laser beam is steered and enters the optical cavity perpendicular to the RAID axis. (b) Transverse section of RAID in the CRDS plane: the line-of-sight of the laser beam (s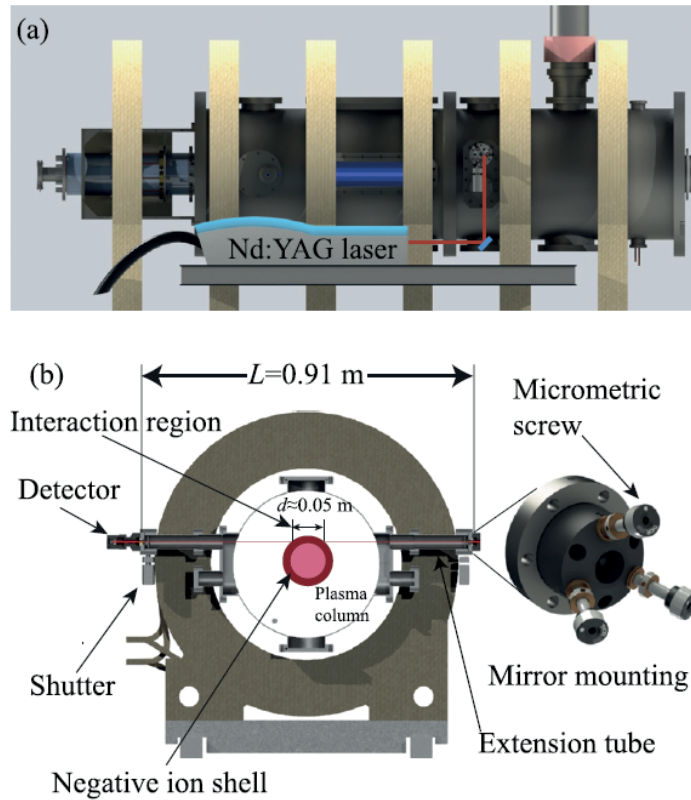chematically shown in red) is 4 cm displaced from the plasma column center so that it traverses the negative ion shell (as expected from OES measurements [94]).
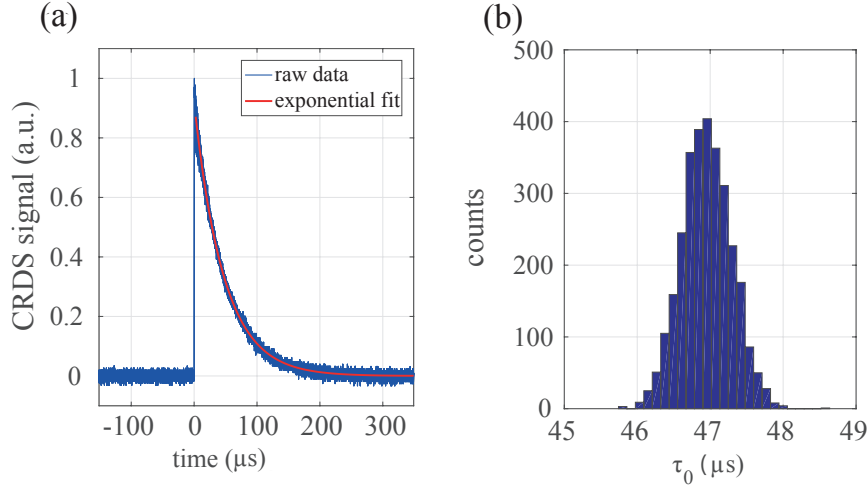
Figure 4.9 – (a) A typical decay signal measured in H_2 gas: the laser pulse (pulse energy 65 mJ) strikes the detector at $t = 0$s. The decay constant τ_0 is calculated from the exponential fit (red continuous line). (b) The histogram shows the distribution of τ_0 over 3000 laser shots. The standard deviation σ_{τ_0} of the distribution determines the sensitivity of the CRDS diagnostic.

the signal, to exclude transient undamped modes. An average τ_0 of $46.95\,\mu s$ with a standard deviation σ_{τ_0} of $0.34\,\mu s$ is found (baseline noise of 0.7%) for 3000 shots, as shown in Fig. 4.9(b). This corresponds to a reflectivity R = 99.9935%, which is slightly smaller (0.0005%) than the one measured on the testbench. The reason for this loss of reflectivity might be due to dust deposition on mirrors' surfaces during the installation on RAID. The error on the exponential fit is of the order of 0.1%. The time fluctuation of τ_0, being much bigger than the error on the fit, can be used to estimate the lowest detectable density for a single measurement of H^-/D^- in RAID, and results in $\bar{n}_{min} = (1-R)\frac{1}{\sigma_{D^-}d}\frac{\sigma_{\tau_0}}{\tau_0} \sim 2.7 \times 10^{15}\,m^{-3}$. This lower limit can be decreased by a factor $\sqrt{N}$ by averaging over N CRDS signals.

The alignment of the laser beam with the axis of the optical cavity is crucial (see the Appendix for more details). If the beam enters misaligned with respect to the optical cavity the ring down time can vary strongly. Thus, HR mirrors were aligned to stabilize the τ_0 level. These effects, combined with mechanical vibrations associated to the rotary-pumps, the vessel water cooling and thermal effects due to the plasma, render CRDS a challenging diagnostic in this scenario. To check if the gas flushing induced a mechanical stress on the optical cavity (H_2/D_2 are flushed through the mirror mountings) the temporal behavior of τ_0 for different pressure conditions was studied. Fig. 4.10 shows the τ_0 evolution in vacuum, in H_2 gas at 0.35 Pa, and in a mixture of H_2 + Ar gas at 0.74 Pa. As shown, τ_0 remains stable during the entire phase. This is a proof that perturbation due to the gas flushing can be neglected during different gas injection phases. τ_0 in these tests is slightly less than in vacuum (by $\sim 2.0\,\mu s$). This is maybe due to a loss of alignment or dust deposition on mirrors caused by gas flushing.
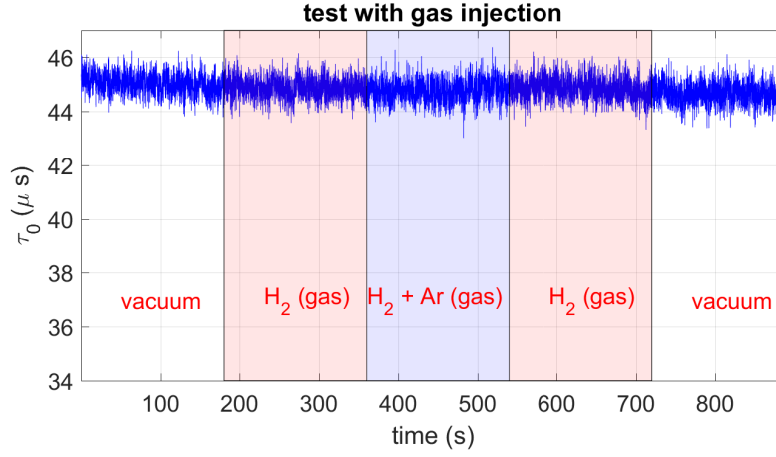
Figure 4.10 – The picture shows the trend of τ_0 during different phase of gas injections demonstrating that the optical cavity is not perturbed by different gas flushing.

4.1.4 First tests in deuterium plasmas

First measurements in plasmas were performed with D_2 plasmas at a constant pressure of 0.3 Pa and a magnetic field of 200 G, since D_2 is directly relevant to NBI applications, and also to compare with past OES measurements [94]. The technique consists in measuring τ before, during, and after a plasma discharge. A typical τ measurement in a D_2 plasma at 5 kW RF power and with an argon plasma at 700 W RF power are shown in Fig. 4.11(a) and 4.11(b), respectively. The entire time range for the deuterium is divided into four intervals marked by the letters A, B, C and D. The RF power in argon was limited to 700 W to avoid sputter damage of the HR mirror coating. In Fig. 4.11(a), during the first 300 s (interval A) only D_2 gas is present and the RF power is off. Argon gas is injected to facilitate plasma ignition a few seconds before it. At $t = 300$ s the plasma discharge is initiated and the argon gas flow is progressively decreased. This transient time when there is a mixture of D_2 and Ar plasma lasts about 50 s (interval B). During this period (50 s), the τ_D decrease is due to the combination of D^- absorption and a thermal effect on the cavity. After $t = 350$ s, only D_2 is injected and maintained stable for about 150 s (interval C). Then, the plasma is turned off at $t = 500$ s when τ_D exhibits a jump from $34.8\,\mu$s to $37.1\,\mu$s between two consecutive acquisitions (see zoom box at $t = 500$ s in Fig. 4.11(a)) due to the sudden disappearance of D^-. Finally, τ_D tends to restore to its value before the plasma discharge (interval D).

To demonstrate that mostly hydrogen gas is present at the end of interval C, optical emission spectroscopy measurements during plasma ignition, shown in Fig. 4.12, were performed. We monitored the intensity of a bright Ar emission line at 811 nm and the H_α emission line at 656 nm. After the plasma ignition starting from an injected RF power of approximately 700 W (during the phase indicated by the blue shaded area in Fig. 4.11(b)), the Ar line is the most intense in the emission spectrum. Approximately 50 s after the ignition, when the Ar flow rate has been progressively reduced to zero and the injected RF power increased to the nominal value, the intensity of the Ar line drops below the detection level, while the H_α line dominates.
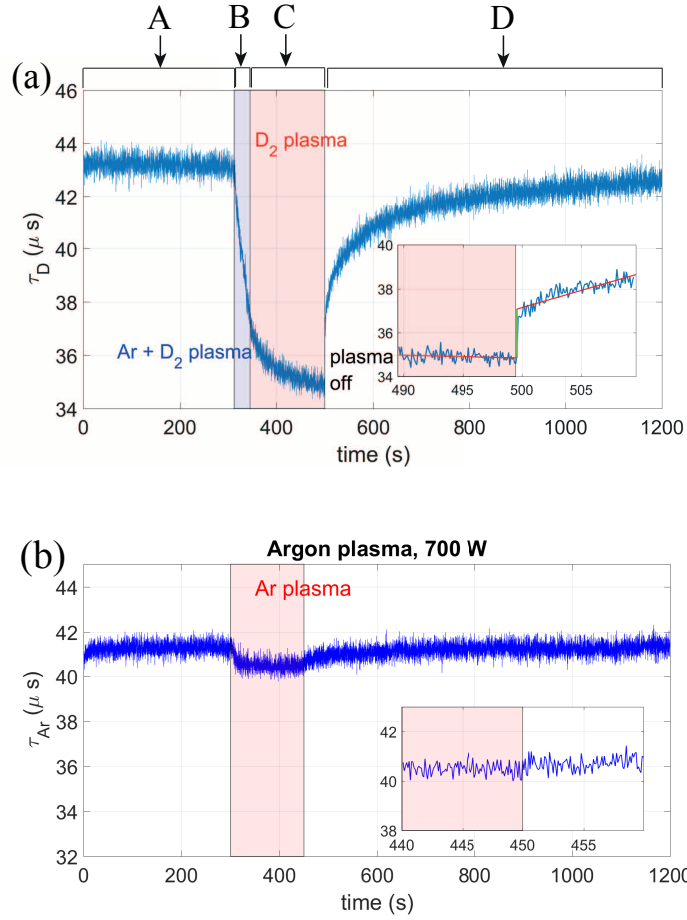
Figure 4.11 – The time evolution of τ before, during and after the plasma discharge for a D_2 plasma (a) and for an Ar plasma (b) at a pressure of 0.3 Pa. The red area identifies when the plasma is on. The box inset is a zoom around the instant when the plasma is turned off ($t = 500\,$s for D_2, and $t = 450\,$s for Ar). The D_2 exhibits a jump due to D^- disappearance (see zoombox in (a)), while no jump is observed for the Ar plasma (see zoombox in (b)).
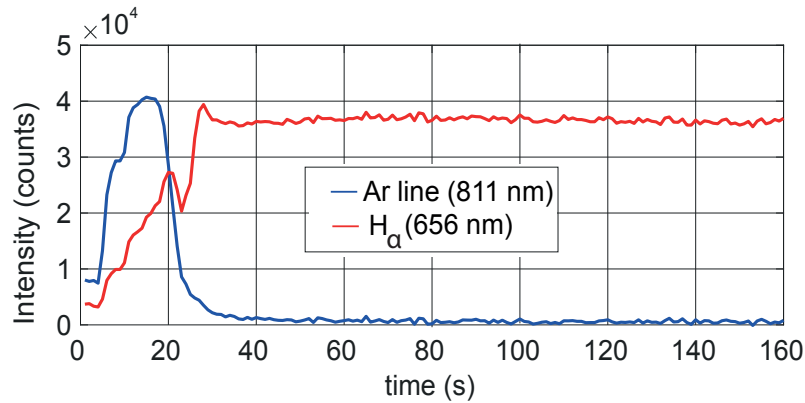
Figure 4.12 – Intensity of the 811 nm Ar line and H_α during plasma ignition, showing a pure hydrogen discharge ~50 s after the RF power ignition.

This confirms that for $t > 50\,$s, the discharge is sustained by a predominant hydrogen plasma. During the transient, the power of the discharge is increased while the system automatically matches the impedance to minimize the reflected RF power.

A few considerations will be presented below to discuss how D^- ions are lost at the plasma shutdown in Fig. 4.11(a). For this purpose we will consider the case of H^- for which cross sections of relevant destruction mechanisms are readily available. However, similar estimates remain valid for the D^- case. In the energy range of RAID plasmas, the typical H^- temperature is $\sim 0.1\,$eV. At this energy the processes that play the most important role in H^- destruction are mutual neutralization (MN) and associative detachment (AD) [6], respectively described by the Eqs. 4.8 and 4.9:

$$H^- + H^+ \rightarrow H + H \quad \text{(MN)}, \tag{4.8}$$

$$H^- + H \rightarrow H_2 + e \quad \text{(AD)}. \tag{4.9}$$

An estimate of the characteristic loss times of H^- for MN and AD processes are given by: $t_{MN} \sim 1/(n_{H^+}\sigma_{MN}v_{MN})$ and $t_{AD} \sim 1/(n_H\sigma_{AD}v_{AD})$ where v_{MN} and v_{AD} are the center of mass velocities and n_H is H density. The cross section for the MN, σ_{MN}, at 0.1 eV is about $2 \times 10^{-13}\,\text{cm}^2$[6]. The cross section for the AD, σ_{AD}, at the same energy[6], is two orders of magnitude smaller than σ_{MN}. However, the H density in the H^- shell is about two or three orders of magnitude higher than n_{H^-} as shown by OES measurements [94]. For both MN and AD processes, the estimate of the characteristic loss time $t_{MN,AD}$ of H^- is of the order of $\sim 0.1\,$ms which is much less that the time between two consecutive CRDS acquisitions (100 ms).

As one can clearly see in Fig. 4.11(a), together with the rapid jump due to the plasma extinction, a slower variation can be observed, lasting some minutes after the plasma is turned off. τ_D takes more than ten minutes to recover to its initial value before the plasma discharge. Even during the plasma D_2 discharge, τ_D is observed to drift. These long period drifts are most likely due to thermal effects causing a distortion of the optical cavity, observed at $t = 500\,$s in Fig. 4.11(a).

To verify that the sudden jump is due to the disappearance of negative ions, a test with an argon plasma, not contributing to laser absorption, was performed. No jump occurred when the argon plasma was turned off (see zoom box in Fig. 4.11(b)), confirming that the jump seen in D_2 plasma is due to the disappearance of negative ions produced in this plasma. A gradual drop $\delta\tau_{Ar}$ of about 0.5 μs, at the limit of the sensitivity, is observed when the argon plasma is turned on. This is probably due to a loss of alignment caused by the thermal expansion of the cavity. When the argon plasma is turned off, τ_{Ar} recovers slowly to its pre-discharge value after some minutes. Thus, the fast dynamics of τ that characterizes the plasma extinction (of the order of 100 μs), with respect to the slow drift of optical cavity thermal expansion, can be taken as a signature of the negative ion disappearance in H_2 and D_2 plasmas. By making a

linear fit of τ_D a few seconds before and after the τ_D jump (see Fig.4.11(a)), the D^- density can be calculated. The error on the calculation of $\bar{n}_{D^-}$ is estimated using the errors on the coefficients of the linear fit. An average density $\bar{n}_{D^-}$ of $(3.05 \pm 0.09) \times 10^{16}\,\mathrm{m}^{-3}$, on a 5 cm path length, is deduced; this value is comparable to the results of OES in hydrogen in Fig. 4.5.

To summarize this initial phase of the CRDS development, we installed and successfully employed a CRDS diagnostic on the RAID device to measure D^- density providing results in agreement with previous OES measurements. We showed that D^- is produced in the volume of a steady state helicon plasma discharge with a average density of $\bar{n}_{D^-} = (3.05 \pm 0.09) \times 10^{16}\,\mathrm{m}^{-3}$ computed over a path length of 5 cm. The filling gas pressure was 0.3 Pa, which is the operational pressure of negative ion sources for fusion and, the RF input power was 5 kW. Various technical aspects were investigated during this preliminary measurement campaign, such as the implementation of the experimental setup and the thermal effects on the optical cavity caused by the presence of a plasma. The dependence of the ring down time on the precise mirror alignment in the presence of mechanical vibrations and thermal distortion due to the plasma, combined with a critical sensitivity to mirror reflectivity, make CRDS a challenging diagnostic in RAID. Despite these technical challenges, we were able to successfully perform first measurements of negative ion density in helicon plasmas and routinely use CRDS diagnostics on RAID.

Once the reliability of the technique was established, we performed extensive scans in RF power and pressure, which are reported in Sec. 4.1.5.

4.1.5   Characterization at different RF powers, gas pressures and magnetic fields

The results described in this paragraph were published in [4] and belong to the second successful experimental campaign performed in October 2018. The purpose of these tests was to perform parametric scans in RF power, magnetic field and gas pressure, to investigate the behaviour of the source at higher powers (up to 8 kW) and to optimize the CRDS technique. Moreover, unlike in Sec. 4.1.4 where we only investigated D_2 plasmas, here we also study the H_2 plasmas and we use shorter acquisition time, since the time behaviour of the optical cavity was already studied in Sec. 4.1.4.

CRDS measurements are performed employing the technique described below, which was already introduced in Sec. 4.1.4 and reviewed here for clarity. Fig. 4.13 shows τ, the ring down time, as a function of time, before, during, and after a H_2 plasma discharge with 5 kW RF power. The laser is pulsed at 10 Hz so that the temporal resolution is of the order of 0.1 s. The plasma discharge starts at $t \cong 30\,\mathrm{s}$ in the presence of a mixture of H_2 and Ar gas (see Fig. 4.13); the Ar gas is added to facilitate plasma ignition [3]. The drop of τ just after plasma ignition is due to a combination of the absorption of the laser pulse by negative ions and the thermal stress of the optical cavity. Just after plasma ignition, Ar is removed in a few seconds and RF power is increased meanwhile. In the plateau where $\tau \cong 37\,\mu\mathrm{s}$, the plasma consists of H_2 pure gas and it is steady state. The discharge is then terminated at $t \cong 80\,\mathrm{s}$ causing the sudden increase of τ. To determine the line-integrated negative ion density $\bar{n}_-$, τ is linearly fitted 10 s
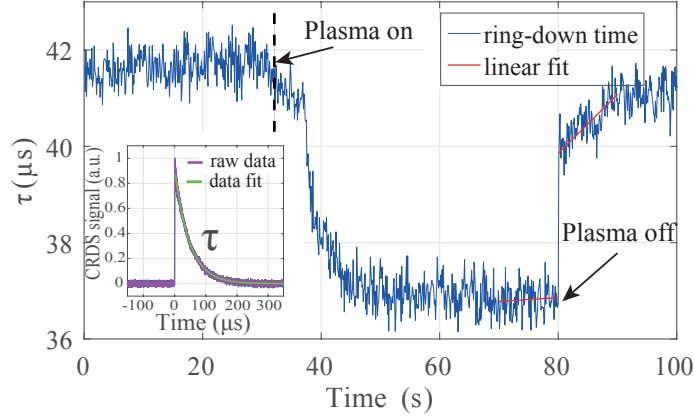
Figure 4.13 – Ring-down time τ before, during, and after a plasma discharge for a H_2 plasma at 5 kW RF power. The plasma discharge starts at $t \cong 30\,$s and it is stabilized after a few seconds. Plasma is terminated at $t = 80\,$s causing the jump of τ due to the disappearance of H^- ions. The linear fit of τ before and after the plasma termination is used to accurately determine the value of n_{H^-} as described in the main text. The jump is used to evaluate the line-averaged H^- density. The inset shows a fit used to calculate the ring-down time for each data point τ.

before and after the τ sudden increase, so that accurate values of τ just before and after the jump can be estimated. The τ after the plasma shut down does not recover immediately to the pre-discharge value since the optical cavity was deformed by thermal stress during the plasma discharge. After a few tens of seconds, the complete recovery to the pre-discharge value is observed.

Having established the reliability of the CRDS technique, power scans were performed. Fig. 4.14 shows measurements with H_2 and D_2 plasma for different RF powers and gas pressures. H^- and D^- line-integrated density increases with RF power for both plasmas. For power larger than 4 kW, however, the growth rate is reduced for H^-. Note that these values are obtained in CW operation on RAID, so the production of negative ions is in a stationary regime. The data in H_2 are up to 8 kW of power and four gas pressures: 0.2 Pa, 0.3 Pa, 0.4 Pa and 0.5 Pa. The data in D^- are shown up to 5 kW at 0.3 Pa because at the time of the experiments the impedance matching system was not calibrated for powers larger than 5 kW and we were mostly interested in the pressure relevant for application for NBI, namely 0.3 Pa. We remark that RAID operation at 0.2 Pa is possible, but this results in a reduced performance of negative ion production. For these experimental investigations we chose to operate at 0.3 Pa as a compromise between a good signal-to-noise ratio and the low pressure requirements for the NBI applications. The line-integrated negative ion density appears to increase with fill pressure, but this is not helpful, given the low pressure requirements for NBI applications. The magnetic field has an effect on the electron density transport and equilibrium distribution and therefore on the negative ion equilibrium profile. Fig. 4.15 shows the line integrated H^- density with varying external magnetic field in the range $B = [133, 530]\,$G by changing the
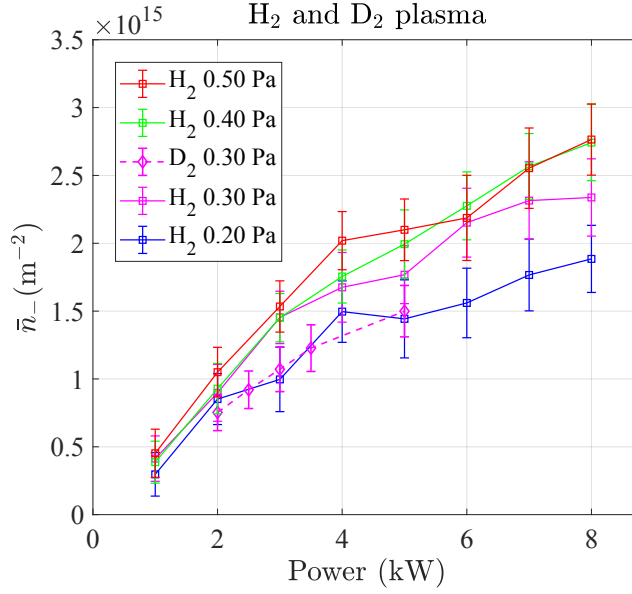
Figure 4.14 – Line-integrated negative ion density as a function of RF power at different pressures for H_2 and D_2 plasmas, demonstrating the steady-state production of negative ions up to 8 kW of RF power.

current in the vessel coils. $\bar{n}_{H^-}$ looks to be saturated with magnetic field at any power. This is in agreement with similar tests performed in a high power helicon device and using laser photodetachment technique [117] showing a low field peak at $\sim 200\,G$ and a fairly flat trend with increasing magnetic field. However, the magnetic field might considerably affect the negative ion radial profile and laser photodetachment measurements are needed to have spatially resolved H^- density profiles, these will be described in Sec. 4.2.

4.1.6 Attempts to explore different measurement positions by displacing the plasma column

We have so far investigated negative ions at a fixed measurements position, however we are also interested to the overall radial n_{H^-} profile. The reconstruction of a profile with radial symmetry, requires measurements at many radial positions. This can be done in theory, in CRDS, by changing different flanges for every measurement position. However, since the alignment is a time consuming procedure and this would require breaking the vacuum for every new flange installation, we preferred to move the position of the plasma column.

The technique consists in bending the plasma column vertically by means of a vertical magnetic field component. For this, a magnetic coil is installed on the top of RAID device, as shown in Fig. 4.16. The vertical field coil has 14.75 cm internal radius, 19.25 cm external radius and is 12.5 cm high and its center is 1 m from the axis of RAID coils and 1.2 m from the antenna. It was not possible to install the coil above the CRDS flange because of lack of space. The coil,
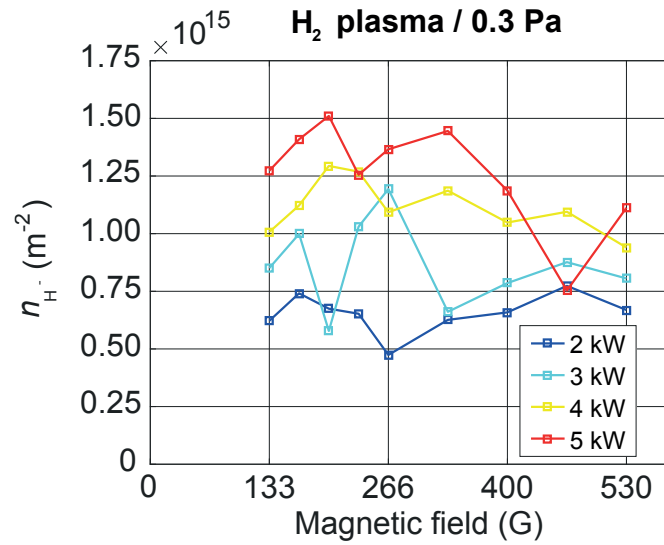
Figure 4.15 – Line-integrated negative ion density as a function of the magnetic field and different RF powers for a H_2 plasma and 0.3 Pa gas pressure.
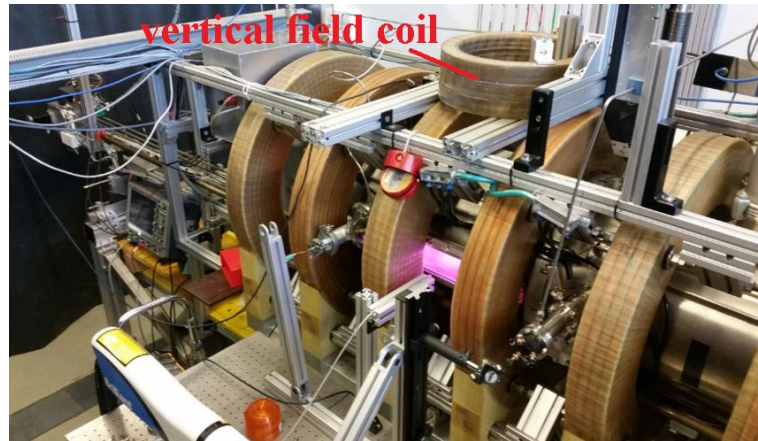
Figure 4.16 – Picture showing the location of the vertical field coil used to displace the plasma column along the vertical direction.

Figure 4.17 – Vertical displacement of the plasma column by the vertical field coil. From left to right, the vertical magnetic field, at the CRDS axial position, is 0, 5 and 10 G. The red line shows the position of the laser beam.
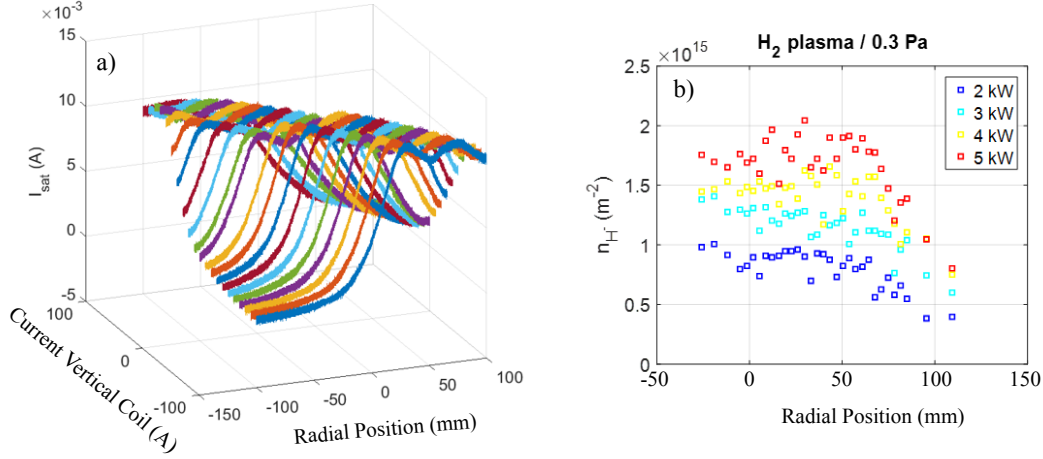
Figure 4.18 – (a) I_{sat} radial profiles as a function of the current in the upper coil, displacing the plasma column along the vertical direction. (b) Line-integrated H$^-$ density (unity of m^{-2}) as a function of the relative position of the CRDS LOS with respect to the center of the plasma column.

when it is not water-cooled (as in the present situation), can sustain a current up to 100 A, corresponding to a vertical component of magnetic field of ~ 10 G in the center of the vessel at the CRDS position. This value of magnetic field is enough to bend the plasma column by $\sim$ 11 cm with respect to the on-axis position. The effect of the vertical magnetic field upon the plasma column is shown in Fig. 4.17 using a visible light image. The vertical field results in the vertical displacement of the plasma column. The vertical displacement of the plasma column is also measured by the LP in ion saturation mode. Fig. 4.18 (a) shows radial I_{sat} profiles for different values of the current circulating in the upper coil. The impact parameter at zero vertical magnetic field is 4 cm. The current in the vertical coil is varied from -100 A to 100 A corresponding to a measurement position range from -2.5 cm (plasma column axis bent down) to 11 cm. The direction of current in the coils is changed by manually inverting the polarity of the coil. The I_{sat} profiles in Fig. 4.18(a) are therefore used to determine the vertical displacement of the plasma column and thus the impact parameter of the CRDS LoS (Line of Sight). For every position, the CRDS measurement is repeated for four values of RF powers: 2, 3, 4 and 5 kW (see Fig. 4.18(b)). For $r < 50$ mm, $\bar{n}_{H^-}$ is quite flat, and then it drops to half at the radial position 50 mm, indicating that we are exiting the region richer in negative ions.
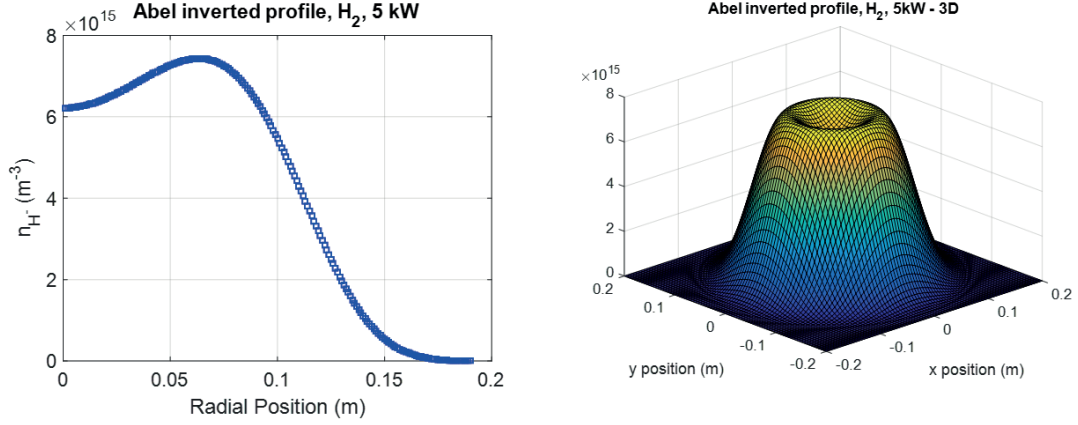
Figure 4.19 – (a) Abel inverted n_H^- radial profile. (b) 3D view of the Abel inverted profile showing a H$^-$ depletion in the plasma center.

By considering the cylindrical symmetry of the H$^-$ density profile, the absolute H$^-$ radial density profile can be calculated by Abel inversion [140] using:

$$n_{\text{H}^-}(r) = -\frac{1}{\pi} \int_r^R \frac{d\bar{n}_{\text{H}^-}}{dy} \frac{1}{(y^2 - r^2)^{1/2}} dy. \tag{4.10}$$

Fig. 4.19(a) shows the Abel inverted profile of 5kW experimental data in Fig. 4.18. The presence of an off-axis peak at $r \sim 6$ cm is clearly visible. Fig. 4.19 (b) shows a 3D view of the Abel inverted H$^-$ density profile highlighting the presence of a central depletion.

The technique just described assumes that the plasma column cross section is not deformed by the presence of the vertical magnetic field, but is just shifted along the vertical direction. This might not be completely true in this case since the vertical component of the magnetic field considerably affects the vertical transport and thus the equilibrium cross section of the plasma column along the vertical direction. This is partially observed in the I_{sat} vertical profiles in Fig. 4.18 showing a non negligible broadening and flattening at high vertical magnetic fields. Spatially resolved measurements by LP laser photodetachment, discussed in Sec. 4.2, are then used to determine a more accurate shape of the H$^-$ profile.

4.2 Langmuir Probe Laser Photodetachment (LPLP)

CRDS at a fixed measurement position is not sufficient to determine the local negative ion density since the CRDS signal results from the interaction of the laser beam along the whole path intersecting the plasma. Moving the laser beam across the plasma column would allow to Abel invert the data to reconstruct the n_- radial profile by assuming cylindrical symmetry. However, this method is impracticable due to the lengthy alignment procedure. Although measurements performed by vertically shifting the plasma column by an external vertical magnetic field in Fig. 4.1.6 show the presence of a hollow H$^-$ density profile, the cross section

of the plasma column might be too deformed. LPLP can alternatively be used to obtain relative negative ion profiles with a spatial precision comparable to the laser beam diameter. In the next paragraph we briefly review the purposes of LP laser photodetachment.

4.2.1   Theory of LPLP

A full review of LPLP can be found in [12, 17], here we briefly review the basic purposes of LPLP. Since the extra electron of H^- or D^- is weakly bound to the atom, a laser pulse can photodetach a large number of negative ions in plasma, which in turn release photodetached electrons. A laser requires a relatively low energy flux ($\sim 10\,\mathrm{mJ/cm^2}$) to photoneutralize all H^- or D^- ion along its path [12]. Moreover, since the laser pulses are very short $\sim 5\,\mathrm{ns}$, the photodetachment process happens on a time scale much shorter than that of the plasma evolution, allowing to temporally resolve the negative ion density.
Langmuir Probes (LPs) can be employed to measure both the photodetached electrons and the local plasma density [12]. The LP probe is coaxial with the axis of the laser beam and biased at a potential higher than the local plasma potential. With such a bias, the LP draws a current I_{dc}, proportional to the local electron density n_e. The laser pulse causes a very fast increase of the detected current over a few ns, I_{pd}, proportional of the number of photodetached electrons. The negative ion density n_- can then be estimated by:

$$\frac{n_-}{n_e} = \frac{I_{pd}}{I_{dc}},$$

(4.11)

Eq. (4.11) can be applied provided that the following criteria are satisfied [12]:

1. The laser wavelength is suitable to photodetach the electrons of the negative ions.

2. The laser pulse energy is sufficiently large to photodetach all negative ions in the target volume.

3. The laser beam must have a minimum diameter from which the amplitude of the signal does not increase with beam diameter.

4. The probe bias must be above the plasma potential.

In the following we discuss how these criteria are implemented on the RAID LPLP diagnostic.

4.2.2   LPLP system on RAID

Fig. 4.20 shows a schematic drawing of the LPLP experimental setup in RAID. Unlike the CRDS setup, the laser beam measurement position is not constrained by the position of the HR mirrors but can be vertically displaced along the window. The blue ring in Fig. 4.20 shows the region where the highest density of negative ions is expected with respect to the background
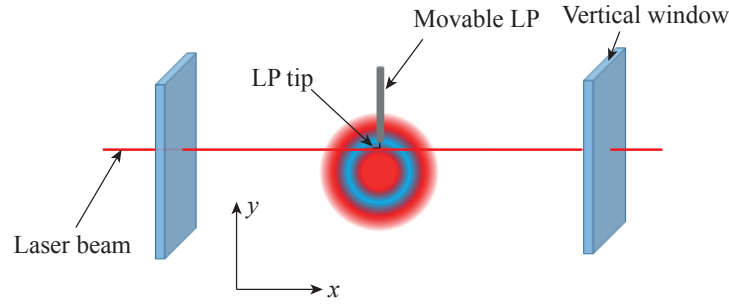
Figure 4.20 – Schematic drawing showing the position of the laser beam and the LP tip with respect to the the plasma column. The blue ring shows the region where the highest density of H^- is expected with respect to the background electrons, in red.

electrons, marked by the red region. Fig. 4.21(a) shows a picture of the experimental setup of the LP laser photodetachment on RAID. The laser pulses are produced by the same Nd:YAG laser described in Sec. 4.1.2 and injected into the vacuum vessel by an optical beam path similar to that used for CRDS but with varying injection position. To detect the photodetached electrons, a LP moving in the vertical direction is employed (see Fig. 4.21(a) and (b)). The probe is displaced by a stepper motor and the vacuum is maintained by a bellow. The probe tip is L-shaped co-axially aligned with the direction of the laser beam. The probe is biased at $V_{bias} = 26$ V above the plasma potential (shown in Fig. 4.23) which is $V_{plasma} = 12\,(\pm 1)$ V for $r < 0.06$ m, for both H_2 and D_2 plasmas, and independent of gas pressure. Fig. 4.21(b) shows a picture of the ceramic stick of the LP probe inside the vessel, at its most external radial position ($r_{max} = 10$ cm).

To measure at different radial locations in the plasma column, the LP and the laser measurement position have to be simultaneously displaced. This requires to align the laser beam and the LP tip at each measurement position. This is done by vertically displacing the last reflecting laser beam injection mirror and the LP by the same distance. The correct alignment is obtained by detecting the laser beam spot after the exit window by flash paper. Fig. 4.22(a) shows the shadow of the LP tip on the beam spot when the system is well aligned. Fig. 4.22(b) shows the cross section of RAID at the LP laser photodetachment axial position. The length of the vertical windows allows measurement of the cross section plasma column up to $r_{max} = 7$ cm. A schematic of the circuit to measure the photodetachment signal is shown in Fig. 4.23. To filter out the DC component of the signal collected when the probe bias is at V_{bias} from the fast transient due to the photodetachment, an AC-coupling circuit, consisting of a high pass filter, was initially used. However, to avoid the distortion of the signal due to the bandwidth of the circuit, we finally employed an AC toroidal current transformer (FTC-016, 10:1) with 2.5 V/A sensitivity and upper cut-off frequency at 1.17 GHz. Signals are acquired by an oscilloscope mounted on the top of RAID (see Fig. 4.21 (a)), to minimize the length of the cable to avoid parasitic capacitance effects. Photodetachment signals are usually acquired in a few microseconds temporal window with a sampling rate of 10 GS/s. Signals are triggered by a photodiode sensitive to the laser wavelength (not shown here) detecting the passage of the
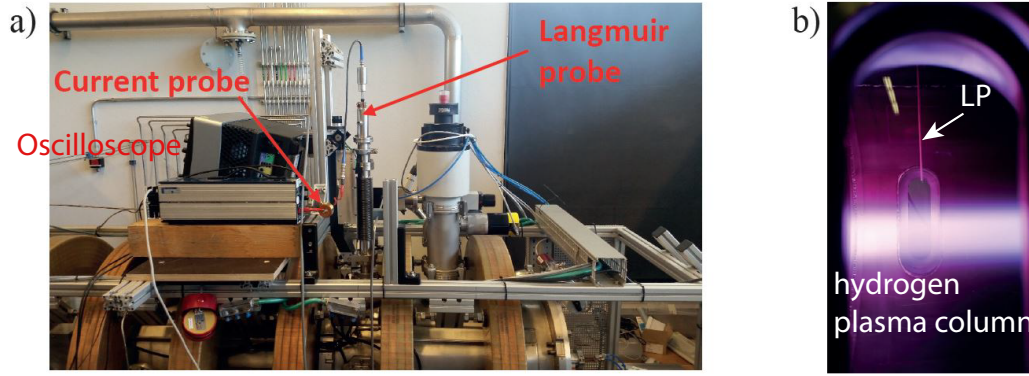
Figure 4.21 – (a) Experimental setup for LPLP measurements in RAID showing the positioning of the LP, of the current probe and of the oscilloscope. (b) Picture of the interior of the vessel showing a hydrogen plasma column and the location of the Langmuir Probe for photodetachment measurements.

laser pulse before entering the vessel. The noise level on the single LPLP signal is such that averaging over several hundred acquisitions is usually required.

4.2.3 Tests with laser pulse energy

To verify that the lase pulse has enough energy to photodetach all electrons from negative ions, one has to check that the photodetachment measurements are in agreement with the theoretical photodetachment fraction $\Delta n_-/n_-$ [12, 119]:

$$\Delta n_-/n_- = 1 - \exp\left(-\frac{\sigma}{h\nu}\frac{E}{S}\right) \tag{4.12}$$

where E is the energy of the laser pulse, h is the Planck constant, σ the photodetachment cross section and ν the laser frequency. Fig 4.24 shows photodetachment signals in a deuterium plasma with 0.3 Pa gas pressure and with the LP tip located at $r = 55\,$mm and different laser pulse energy. Each laser pulse energy is the average over 50 pulses, the typical standard deviation is of the order of 5% and is measured with a power meter prior to each measurement in plasma. The amplitude of the photodetachement current is indicated by the double arrow. These photodetachment signals were measured with a capacitive circuit at the beginning of the experimental campaign which was subsequently replaced with a toroidal current transformer previously discussed. The laser is shot at $t = 0\,$s and the rapid overshoot (FWHM$\sim 0.2\,\mu$s) is due to photodetached electrons. Laser pulse energy is increased from 35.6 to 74.7 mJ and no significant variation of the shape is seen. In Fig. 4.24 (b), the blue solid line shows the theoretical normalized photodetachment current and, the red square points, the experimental data of the photodetachment current, normalized to the photodetachment current at the largest laser pulse energy (74.7 mJ). These results show that the photodetachment current is
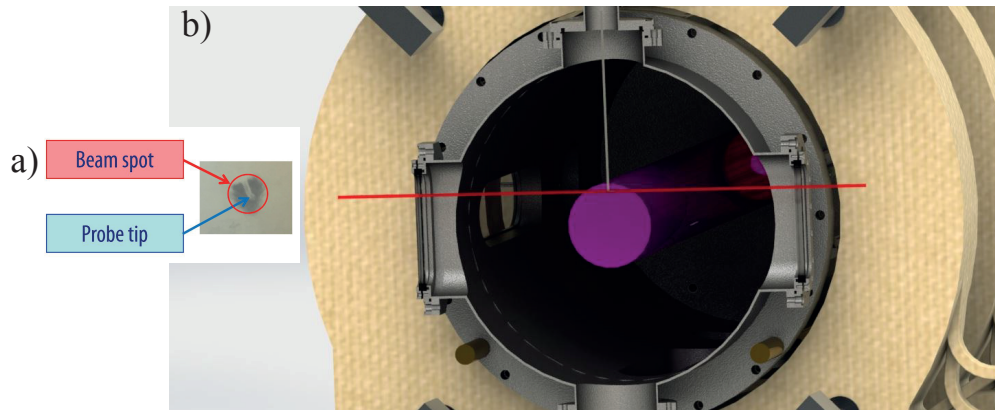
Figure 4.22 – (a) Shadow of the probe tip on the laser beam spot showing the correct coaxial alignment. The flat part on the spot is due to the edge of the ceramic holder (b) SolidWorks drawing of the cross section of RAID showing the laser beam impinging on the LP tip immersed in the plasma column.
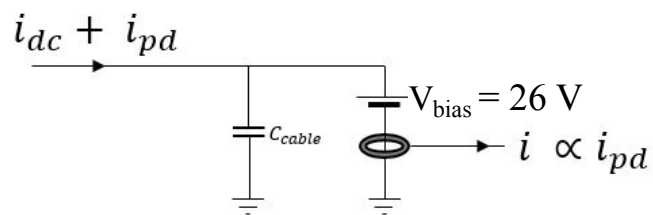
Figure 4.23 – (a) Schematic of the electrical circuit to measure the photodetachment current i_{pd}.
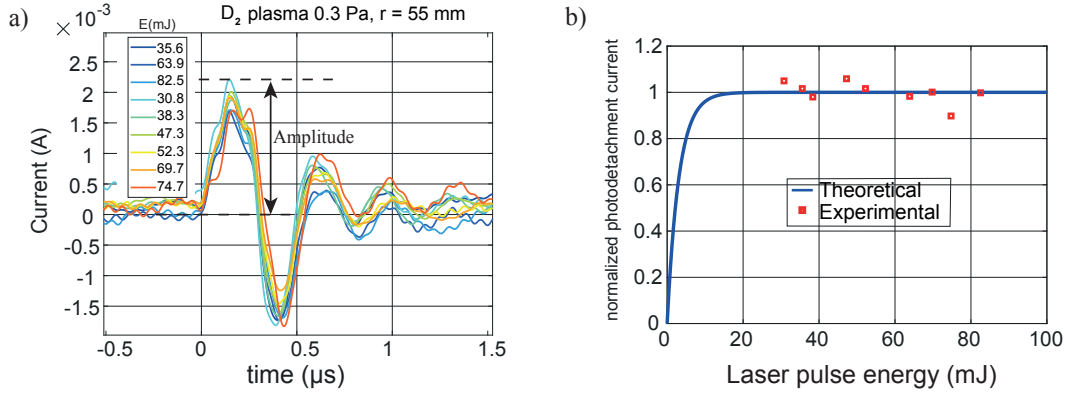
Figure 4.24 – (a) Photodetachment signals for a deuterium plasma with 0.3 Pa gas pressure and with the LP tip at $r = 55$ mm and different laser pulse energies. (b) Theoretical normalized photodetachment current in blue, and experimental data, normalized to the photodetachment current at the largest laser pulse energy (74.7 mJ). These tests demonstrate that laser pulse photodetaches all D^- in the interaction region.

saturated for $E \approx 35.6$ mJ. All following measurements are obtained with a pulse energy of 50 mJ. Photodetachment signals reported by other authors show an approximate flat overshoot and a small (or even absent) undershoot before recovering to the pre-pulse value [119, 117]. The photodetachment signals measured in RAID, such as that in Fig. 4.24 however, show a large undershoot. This effect is discussed in the next section.

4.2.4 Testing the LPLP system on H_2 and D_2 plasmas

In this section we present the results of the photodetachment campaign performed in RAID in June-July 2018 and published in [4]. A typical photodetachment signal is shown in Fig. 4.25. The laser pulse strikes the LP tip at $t = 0$ s causing the overshoot (increase of the collected electron current) whose amplitude is indicated by the vertical arrow for the 5 kW case. The subsequent undershoot and the lack of "plateau" has been reported by other authors such as by P. Devynck et al. [40], M. Bacal [12] and S. Aleiferis [6]. This effect is partly due to the motion of ions caused by the thermal motion of the electrons [49]. The large undershoot and the double peak might also be an effect of the magnetized electrons. Ions are however not magnetized for the magnetic fields employed for these tests (200 G). Numerical simulations using a particle-in-cell code are presently under way to fully model the temporal dynamics of the observed photodetachment signal (see also Sec. 4.3). If the laser pulse strikes the probe when there is no plasma, no variation of the signal is detected. The amplitude increases with RF power confirming the trend observed during CRDS tests.

To radially characterize the plasma, the LP is moved in the vertical direction. For each position, a new alignment laser beam-probe is needed, such as that depicted in Fig. 4.22(a). Fig. 4.26 summarizes the results obtained with laser photodetachment while varying the RF power. The left and the right columns show the results for H_2 and D_2 plasmas respectively. The gas filling
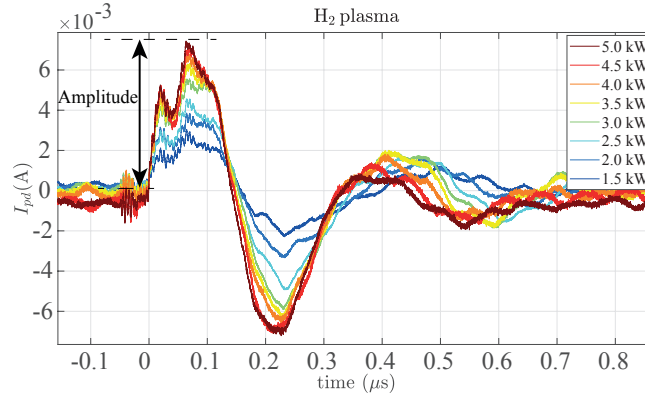
Figure 4.25 – Typical photodetachment signals for a H_2 plasma. The laser strikes the LP tip at $t = 0\,s$ causing the overshoot whose amplitude is indicated by the arrow.

pressure is 0.3 Pa.

In Fig. 4.26(a), the amplitudes of the photodetachment signals are shown. On average, a weaker signal is measured in the case of D_2. As suggested by Eq. 4.11, the shape of the curve is due to a combination of the negative ion density and the electron temperature. Fig. 4.26(b) shows the electron current I_{dc} when the probe is biased at $V_{bias} = 26\,V$, above the plasma potential. On average, more electrons are collected in the case of D_2 suggesting that the electron density is higher in these plasmas. It was not possible to perform measurements for $r < 0.04\,m$ because I_{dc} was too high and risked damaging the system. Moreover, the window height limited the LOS of the laser to $r < 0.065\,m$.

Fig. 4.26(c) shows the ratios n_{H^-}/n_e and n_{D^-}/n_e, given by Eq. 4.11. Although the electrons are magnetized, the electron transport coefficient is the same both for the photodetached electrons and for the electrons collected by the probe when biased above V_{plasma}. This is justified because the background electrons have an energy of about $\sim 1.5\,eV$ in this region of the plasma column and the photodetached electrons are released into the plasma at $\sim 0.45\,eV$. Since the two energies are of the same order of magnitude, we expect that the transport coefficients should be very similar. Therefore, the effect of the transport coefficients tend to cancel out in the ratio. We note the strong difference between the two plasmas. At $r = 0.06\,m$, n_{H^-}/n_e reaches 0.3, while n_{D^-}/n_e reaches about 0.05. Also, the profile ratios are only weakly dependent on power, as shown in Fig. 4.26(c). The independence of the ratio n_-/n_e might be an advantage for negative ion extraction because it makes the negative ion yield in the source easier to tune. The reason for this difference between n_{H^-}/n_e and n_{D^-}/n_e is mainly due to the higher electron density measured in D_2 plasma, as shown in Fig. 4.26(d). At 5 kW power and $r = 0.04\,m$ (where the fixed LOS of CRDS is located) n_e reaches $\sim 1.3 \times 10^{17}\,m^{-3}$ in H_2 and $\sim 2.9 \times 10^{17}\,m^{-3}$ in D_2. Although the absolute value of n_e might be unreliable because of electron magnetization, this data completes the set of quantities that can be obtained only relying on the LP laser photodetachment technique. The higher density in D_2 is also measured by microwave interferometry at the edge, at the measurement position $r = 0.04\,m$, revealing a
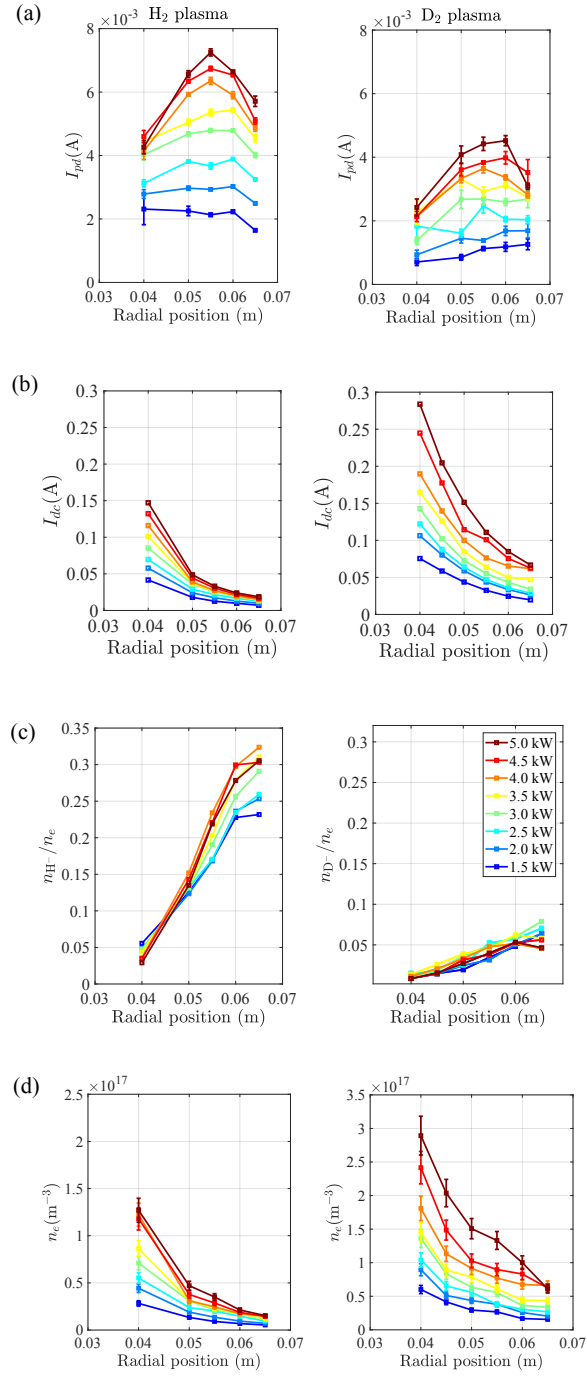
Figure 4.26 – Results of the laser photodetachment measurements for H_2 (left column) and D_2 (right column) plasmas at 0.3 Pa: (a) Photodetachment amplitudes I_{pd}; (b) Electron current I_{dc} collected when the probe is biased at $V_{\text{bias}} = 26\text{V}$, above the plasma potential; (c) Ratio n_-/n_e; and (d) electron density n_e. On the edge of the plasma column, hydrogen plasmas have lower electron density and a higher ratio n_-/n_e.
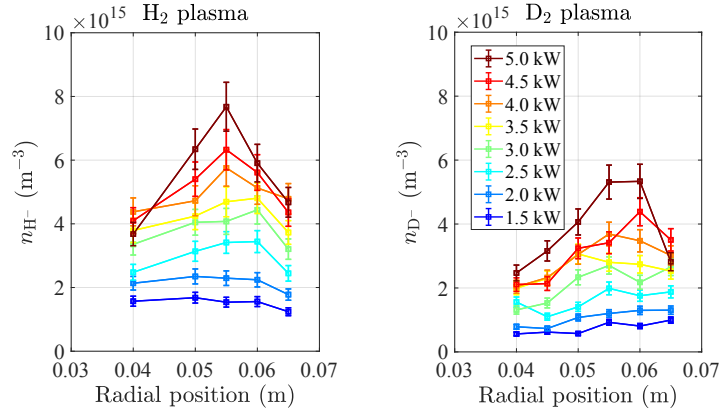
Figure 4.27 – Radial profiles of negative ion density obtained with laser photodetachment and measuring the electron density via IV curves. These data are not calibrated with CRDS.

line-integrated density a factor 2 higher in the case of deuterium.

The n_e profiles are obtained from the analysis of IV curves measured with the same LP used for laser photodetachment. The electron energy distribution function (EEDF) is calculated using the Druyvesteyn formula [43] and the second derivative of the measured electron current is calculated with a Savitzky-Golay filter to obtain the floating and plasma potential. An effective electron temperature T_e and the total electron density are then obtained by numerically integrating the EEDF. More details on the analysis can be found in [29]. The data shown in Fig. 4.26(a), (b) and (d) can be used to calculate the negative ion density, shown in Fig. 4.27. The negative ion density peaks at $r \sim 0.055\,\mathrm{m}$ and H$^-$ and D$^-$ are distributed in a shell-like shape, as also measured by OES [94]. The peak density of H$^-$ is $7.7 \times 10^{15}\,\mathrm{m}^{-3}$ which is a factor ~ 2.5 lower compared to $2.0 \times 10^{16}\,\mathrm{m}^{-3}$ measured via OES [94]. The disagreement between OES and laser photodetachment might be due to an incorrect estimate of n_e via LPs. For completeness we also show the temperature profiles in Fig. 4.28. T_e decreases weakly along the radial direction down to $1\,\mathrm{eV}$ at $r = 0.065\,\mathrm{m}$ and $5\,\mathrm{kW}$ of power for both H$_2$ and D$_2$. Moreover, a general decrease of T_e is observed for increasing RF power. The T_e values in the edge are in the range where the DA cross section peaks, depending on the rovibrational state of H$_2(v)$ and D$_2(v)$. Thus, the T_e profiles show that the electron cooling on the edge, caused by the magnetic field needed to sustain the helicon discharge, is also effective to reach a favorable electron temperature for DA process.

4.2.5 CRDS combining with LPLP to extract absolute negative ion density profiles

In this section, we focus only on the data at 0.3 Pa. Since this is the pressure relevant to present NBIs systems, such as the system designed for ITER, although lower pressure may be more relevant for future systems [67]. The measurement of n_e via LPs in a plasma with magnetized electrons, might lead to error on the final estimate of negative ion density, n_-,
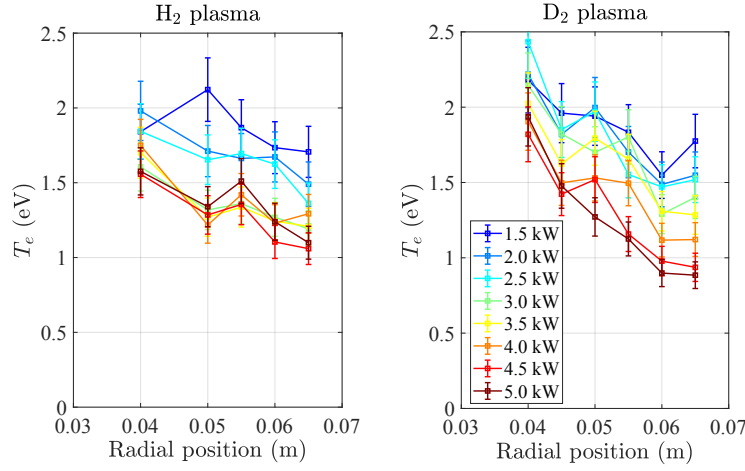
Figure 4.28 – Electron temperature profiles for different RF powers in the range of measurements. The low value of electron temperature is favorable for the production of negative ions by dissociative attachment (DA).

when n_- is deduced from Eq. 4.11 and one should compare the n_e deduced by microwave interferometry. To overcome this problem, we can use the line-integrated negative ion density measured using CRDS for absolute calibration. The negative ion density profiles obtained with laser photodetachment in Fig. 4.27(a) and Fig. 4.27(b) are interpolated using Gaussian normalized to maximum data value. Thus, they can be still used to extract the width and the position of the negative ion shell. Fig. 4.29(a) and (b) show the relative n_- profiles with the normalized Gaussian fits, the positions of CRDS line-of-sight and of the vessel wall. The region at $r < 0.04\,\text{m}$ is not taken into account for the estimate of the absolute n_- profile since CRDS does not sample this region. We define $F(x, y)$ as the normalized n_- profile, where x and y are coordinates in the plane transverse to the plasma column axis, shown in Fig. 4.20. $F(x, y)$ is a form factor, thus providing the shape of the negative ion density profile. The absolute negative ion density $n_-(x, y)$, shown in Fig. 4.20, can be written as:

$$n_-(x, y) = n_-^{peak} F(x, y), \tag{4.13}$$

where n_-^{peak} is the negative ion peak density. CRDS measures the integral of Eq. 4.13 along the line of sight at the measurement position $y = y_{CRDS}$, which is:

$$\bar{n}_-^{CRDS} = n_-^{peak} \int_{x_1}^{x_2} F(x, y_{CRDS})\, dx, \tag{4.14}$$

where x_1 and x_2 are the integration limits along the line of sight. From Eq. 4.14 one can deduce n_-^{peak} which, inserted in Eq. 4.13, provides the absolute negative ion density profile.
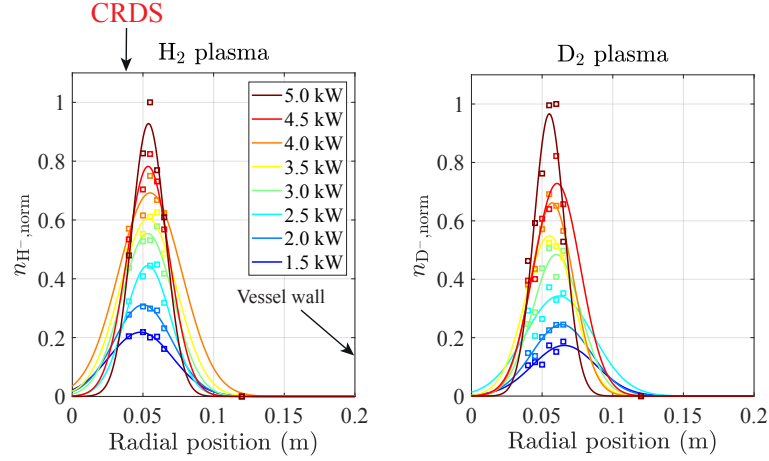
Figure 4.29 – Gaussian fits of the relative n_- profiles measured with laser photodetachment. The position of CRDS line-of-sight to calibrate n_- absolute profiles and the vessel wall position is indicated.

The results of this procedure are summarized by Fig. 4.30 showing n_{H^-} and n_{D^-} profiles. Only 2, 3 and 5 kW RF powers are shown for clarity. The peak value obtained at 5 kW for H_2 is $1.9 (\pm 0.3) \times 10^{16} \, m^{-3}$, close to the value measured by OES [94], which was $3.0 (\pm 0.8) \times 10^{16} \, m^{-3}$. For D^- the peak value for 5 kW results in $1.8 (\pm 0.3) \times 10^{16} \, m^{-3}$, a bit low compared to $4.5 (\pm 2.0) \times 10^{16} \, m^{-3}$ measured with OES. In Fig. 4.31, we plot the peak value of n_- for increasing powers, showing a linear trend. The isotope effect seems to result in a slightly higher negative ion density for the case of hydrogen, but this is comparable to the error bar. Furthermore, in Fig. 4.32 we plot the negative ion density with electron density measured by the LP at $r = 0.055 \, m$, close to n_- peak values. n_- increases almost linearly with n_e and higher values may be attained by increasing the RF power. The lower ratio n_-/n_e in the case of deuterium is clearly visible. This suggests that the co-extracted electrons might be a more important issue for D^- extraction. The isotopic effect in negative ion and electron density has been investigated by some authors [128, 26, 51] and it is due to a combination of different phenomena which we briefly explain in the following text. Calculations and experiments show that n_e is higher in deuterium than hydrogen plasmas and is mostly due to ion transport. Positive ions are indeed mostly lost by transport to the walls where they are neutralized. For deuterium, the transport of positive ions is a factor $1/\sqrt{2}$ smaller than hydrogen because of the mass difference. This might explain in part the higher n_e in deuterium [128]. Concerning the isotope effect on the negative ion density, the lower negative ion density in deuterium might be due to the higher degree of dissociation in deuterium leading to increased V-t cooling (cooling of $D_2(v)$ in collision with D) and then less efficient D^- production [128]. For a better understanding of the processes, modeling is envisaged, however, cross sections for deuterium are nor easily available like for hydrogen.
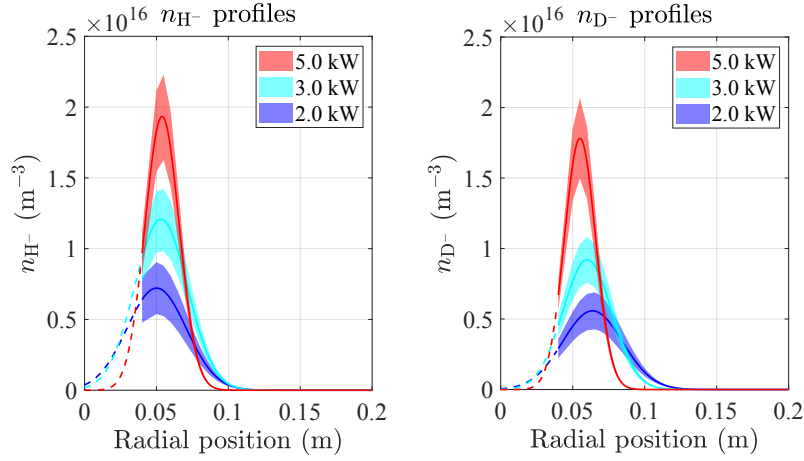
Figure 4.30 – n_{H^-} and n_{D^-} radial profiles for different powers obtained using the relative negative ion profiles measured with laser photodetachment and calibrated with CRDS line-integrated measurements.
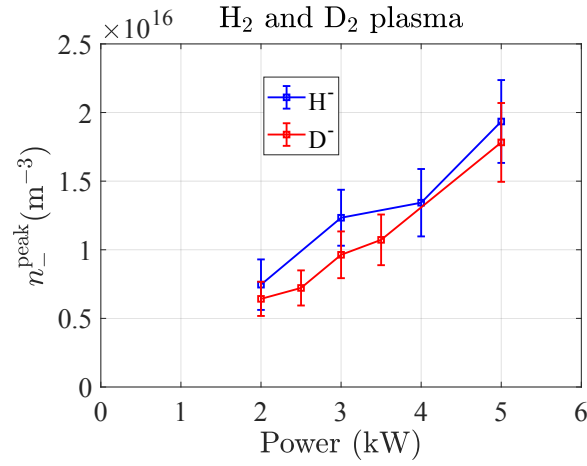
Figure 4.31 – Peak negative ion density as a function of RF power at 0.3 Pa. n_- increases with power and higher density is observed in the case of H^-.
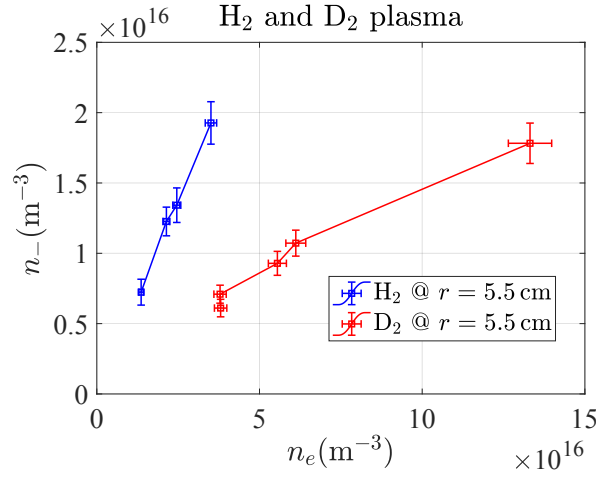
Figure 4.32 – Negative ion density vs. electron density in hydrogen and deuterium plasmas.

4.3 Conclusions and Outlook

Langmuir probe laser photodetachement is a powerful technique to measure plasma electronegativity. The theory of LP laser photodetachment used so far, however, depends on many assumptions and neglects the presence of the magnetic field. Numerical modeling of the interaction probe-plasma could help the interpretation of experimental data [103], such as the interpretation of the photodetachment signals in Fig. 4.25 and Fig. 4.24. In the framework of a collaboration with Dr. F. Taccogna of Centro Nazionale delle Ricerche (Italy) and Dr. N. Oudini of Laboratoire des plasmas de décharges (Algeria), preliminary simulations of the interaction biased probe - plasma have started. Fig. 4.33 shows the perturbation induced by the LP probe used for the laser photodetachment measurements (diameter 0.4 mm, length 8 mm) in RAID plasma. The size of the simulation domain is $1\,\text{cm} \times 1\,\text{cm}$ and it is perpendicular to the probe tip axis and passing through the middle of the tip. The input plasma parameters are those for a H_2 plasma at $r = 40\,\text{mm}$, 0.3 Pa, $B = 100\text{G}$ and 5 kW power for which, according to the OES [94], it has the following features: $T_e = 2.16\,\text{eV}$, $n_e = 1.59 \times 10^{17}\,\text{m}^{-3}$, $n_H = 1.70 \times 10^{19}\,\text{m}^{-3}$, $n_{H^+} = 1.30 \times 10^{17}\,\text{m}^{-3}$, $n_{H_2^+} = 1.40 \times 10^{16}\,\text{m}^{-3}$, $n_{H_3^+} = 3.00 \times 10^{16}\,\text{m}^{-3}$, $n_{H^-} = 3.00 \times 10^{16}\,\text{m}^{-3}$. The plasma potential is set uniform and constant at +12 V in the entire simulation domain. The probe tip is then biased at +26 V (14 V above the plasma potential) and it starts to drain the surrounding plasma electrons. This creates important plasma fluctuations close to the tip; the n_e mapping in Fig. 4.33 after the probe biasing and before the laser pulse. We remark that the tip biasing creates a local depletion of n_e which is elongated in the direction of the magnetic field, suggesting that the electron collection is not isotropic. Therefore the assumption taken to describe the photodetachment signals in the previous paragraph may be not very accurate. The next step of the simulation is to observe a damping of plasma oscillations and then the shot of a laser pulse, which photodetaches the H^-, will be simulated.

The measurements performed with CRDS and LP-assisted photodetachment show that H^- and D^- are produced both in hydrogen and deuterium helicon plasmas in steady state regime
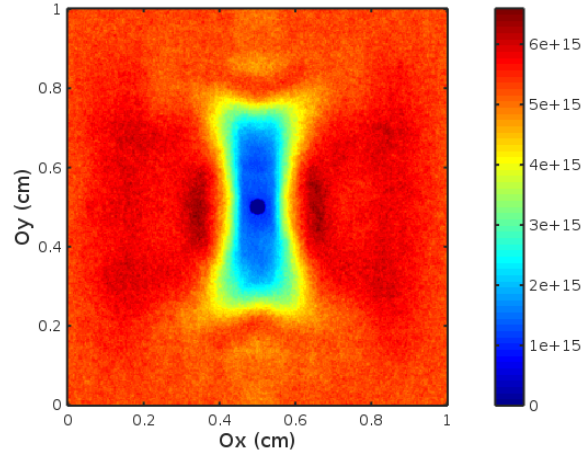
Figure 4.33 – PiC simulation showing the electron density mapping for a LP biased at -27V in a plasma region of size $1 \times 1\,cm$. The axis of the probe is perpendicular to the plane. The magnetic field is directed in the vertical direction. The probe causes a density depletion which is elongated in the direction of the magnetic field.

with significant densities in volume production mode, without using caesium and with a few kWs RF power. The measurements were performed at a gas fill pressure of 0.3 Pa, relevant to NBIs of ITER. Future NBIs may require lower pressures, and future studies at those pressures will be required [67]. We showed that LP-assisted photodetachment is not sufficient alone to obtain reliable measurements because the electrons collected by the LPs magnetized making IV sweeps not reliable to the estimate of n_e. Thus, to extract the absolute negative ion density profile, LP-assisted laser photodetachment is employed in combination with line-integrated measurements of CRDS. The LP-assisted laser photodetachment is used to measure the relative negative ion density profile showing that it is peaked off-axis. The line-integrated measurement performed by CRDS is then used to obtain the absolute negative ion density profile. Taking into account the peak negative ion density at 5 kW RF power, H$^-$ density reaches $1.9\,(\pm 0.3) \times 10^{16}\,\mathrm{m}^{-3}$, close to $3.0\,(\pm 0.3) \times 10^{16}\,\mathrm{m}^{-3}$ measured with OES. However, D$^-$ reaches $1.8 \times 10^{16}\,\mathrm{m}^{-3}$ quite low compared to $4.5\,(\pm 2.0) \times 10^{16}\,\mathrm{m}^{-3}$ measured with OES. The reason for this disagreement in the D$_2$ case is under investigation. Although the absolute H$^-$ and D$^-$ densities appear to be comparable, the ratio n_-/n_e is about 6 times lower in deuterium than hydrogen. This suggests that the co-extracted electrons might be a more important issue for deuterium, if the current magnetic geometry is employed. The ratio n_{H^-}/n_e is comparable to the value obtained in ICP (Inductively Coupled Plasma) sources, with moderate source conditioning, close to the extraction grid, at 0.4 Pa pressure and 55 kW power, using the same technique [36]. However, a comparable n_{H^-}/n_e does not necessarily imply that the extracted negative ion current from a hypothetical helicon source will be comparable to ICP. The magnetic field employed for these experiments (200G) is approximately larger of a factor of two compared to the magnetic filter field of ICP sources leading to different transport of the relevant species.

We believe that these experimental investigations add relevant data on the volume production of H^- and D^- in hydrogen and deuterium helicon plasmas. However, the design of a source based on a helicon plasma requires the investigation of different magnetic field geometries and the compatibility with an extractor and an acceleration system. Thus, a next step with the current system is the characterization of negative ions along the plasma column and the study of different magnetic geometries, such as the expanding magnetic field, with the diagnostics mentioned in this chapter. In parallel with this, 3D numerical simulations, described in Sec. 7, could be an important tool to predict the negative ion production as a function of source parameters.

5 Helicon Wave Field Diagnostic with a B-dot probe

The purpose of this chapter is to investigate the propagation of helicon waves in RAID plasmas. Although the production of an elongated plasma column and the observation of the Ar blue core are signatures of the propagation of a helicon wave, a direct verification was required. We have therefore performed experimental campaigns to characterize the structure of the helicon waves produced by the birdcage antenna. This is achieved by measuring the time-varying magnetic field in plasmas by means of a magnetic B-dot probe. We describe herein some relevant features of the theory of the helicon wave propagation, the calibration of B-dot probe, the measurements of longitudinal waves, the effect of changing plasma parameters and we finally present a comparison with numerical simulations.

5.1 The B-dot probe: basics

The B-dot probe measures the local variation of the magnetic field. The probe is made of a small coil of wire which, in the presence of a time varying magnetic field, produces a signal described by the Faraday's law [114]:

$$V = -\frac{d\Phi_B}{dt},$$
(5.1)

where V is the voltage that can be measured out of the wire, and Φ_B is the magnetic flux though a surface S. In general, Φ_B is defined as:

$$\Phi_B = \int\int_S \mathbf{B}(\mathbf{r}, t) \cdot d\mathbf{A},$$
(5.2)

where $\mathbf{B}$ is the time varying magnetic field and $d\mathbf{A}$ the element of the surface area. Provided that the size of the coil is much smaller than the variation length of the magnetic field, the
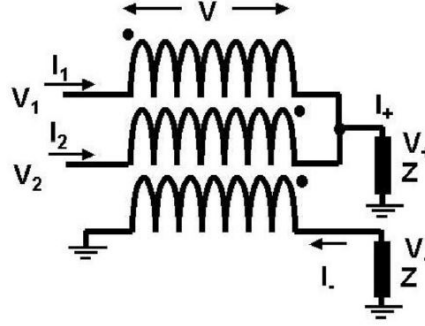
Figure 5.1 – Schematic circuit of a hybrid combiner.

previous equation can be written as:

$$V = -A_{eff}\frac{dB}{dt},\tag{5.3}$$

where A_{eff} is the effective area of the coil and B is the component of the magnetic field perpendicular to the surface of the coil. Usually, the B-dot probe is made of many loops around the probe bulk, to maximize the signal. If the B-dot probe is made of n loops and they form an angle θ with respect to the magnetic field direction, the previous equation becomes:

$$V = -nA\frac{dB}{dt}\cos\theta.\tag{5.4}$$

Assuming a harmonic variation of the magnetic field, i.e. $\propto e^{i\omega t}$, the amplitude of the measured voltage is:

$$V = -inA\omega B\cos\theta.\tag{5.5}$$

The hybrid combiner

We have so far described only the *inductive* part of the measured voltage. Since the probe is immersed in a plasma, it is also affected by a *capacitive* coupling due to the potential difference between the probe and the plasma. While the sign of V_{ind} (inductive part of the voltage) is dependent on the orientation of the probe with respect to the magnetic field, V_{cap}, the capacitive part, does not change sign. To eliminate V_{cap}, we have used a method based on a *hybrid combiner* [22]. A hybrid combiner is an electrical circuit (shown in Fig. 5.1) which provides two output signals $V_+ = V_{cap}$ and $V_+ = V_{ind}$, the latter is that which we are interested to know. According to the scheme in Fig. 5.1, one can verify that $V_1 - V = V_+$ and $V_2 + V = V_+$. Since $V_- = V$, we obtain: $V_- = \frac{V_1-V_2}{2} = V_{ind}$.

5.1.1 Design and mounting of the B-dot probe in RAID

The main technical challenge in building a B-dot probe suitable for RAID is to make it operational at temperature close to 1000 K, which is the typical gas temperature [94]. At such temperatures, the coil has to be isolated with a ceramic shielding. The probe head, shown in Fig. 5.2(a) is made of alumina (Al_2O_3), and it is the support for the three coils on three perpendicular planes. Copper wires coated with a heat-resistant ceramic are wound on the ceramic head (see Fig. 5.2(b)). Each wire is 50 cm long and makes 3 loops around the ceramic head. The two wires are twisted together to reduce the stray magnetic pickup. The head is then fixed on the top of a stainless non-magnetic steel rod (see Fig. 5.2(c)) shielding the signal delivered to the measurement from the surrounding plasma. The head is covered with kapton foil to tighten the wires on the head ceramic bulk. The head and the rod are then covered with a ceramic tube shielding the probe against thermal fluxes (see Fig. 5.2(d)). The rod is screwed on an aluminium box and wires are soldered to BNC cables. The box can be mounted on the movable 2-axis system for LPs, which allows displacement at different radial locations in the plasma column. Fig. 5.3 shows the two axis system with the possible mounting positions of the B-dot and the LP. B-dot probes are shifted by an angle of 6° to avoid reciprocal plasma shadowing. The positioning system is partially automatized to measure the helicon wave amplitude and the local plasma properties. At each location, the three components of the helicon wave are recorded and then the LP performs sweeps at the same position to measure n_e, T_e, V_f and V_p. By fixing the angular position, the system performs a scan along the axial direction.

5.1.2 Calibration of the B-dot probe

To accurately measure the absolute value of the time-varying magnetic fields and to know the relative response of the three axes of the B-dot probe, a calibration system is required. The technique consists of measuring the three signals in the presence of an external time varying magnetic field of known intensity. For this, a dedicated calibration testbed was developed. The calibration system consists of a birdcage antenna fed with a RF current pulsed at 13.56 MHz, shown in Fig. 5.4(a), which generates a quite uniform magnetic field over its cross section [77]. The transverse cut of the antenna in Fig. 5.4(a) shows the computed magnetic field intensity at the time of the RF peak. The computation of the magnetic field is performed by Faraday's law considering the mutual impedances between the legs. To perform the calibration, the head of the ceramic probe is placed in the center of the antenna and oriented along the three perpendicular axes. For each position, the B-dot signals from the three axes are measured for different external RF feeding powers (and therefore magnetic field intensities), and a calibration curve for each axis is obtained (see Fig. 5.4(b)). The calibration of the three axis resulted in the three axis responses with coefficients which not differ more than 5% between each other, meaning that the three coils winding are very similar each other. The average absolute calibration coefficient resulted in 0.25 mT/V. The measurements shown in the next paragraph are sometimes not absolutely calibrated since part of the measurements
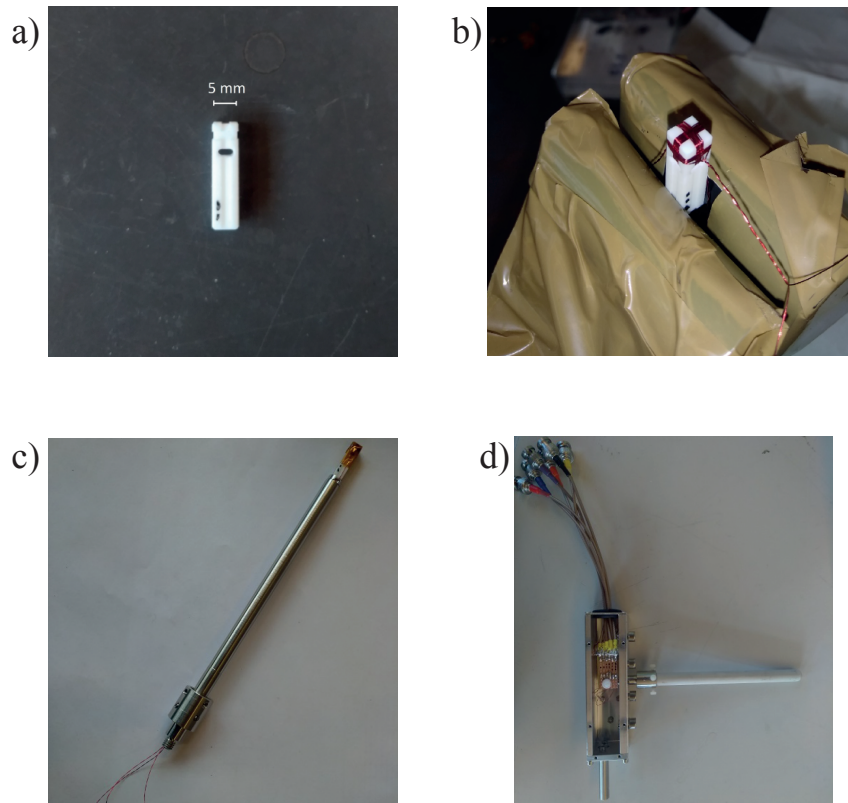
Figure 5.2 – Mounting of the B-dot probe for RAID. (a) Ceramic bulk head of the probe. (b) Winding of copper wires of the probe head. (c) Mounting of the ceramic head on the steel rod. (d) Insertion of the ceramic cup and installing of the moving support with BNC cables.
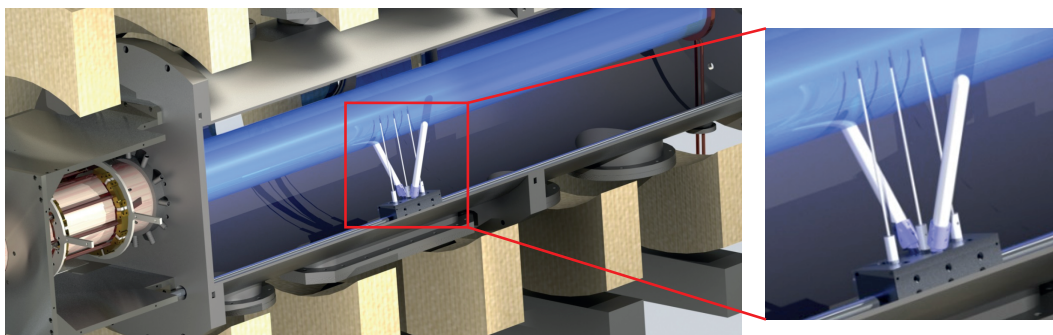
Figure 5.3 – Cross section of RAID along the axial direction showing the locations where the B-dot and LPs can be installed on the 2-axis system. LPs and the B-dot are shifted in angle to avoid reciprocal plasma shadowing.
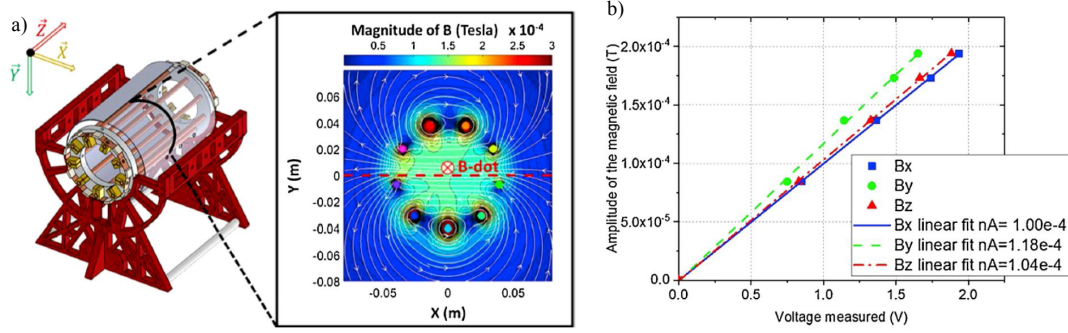
Figure 5.4 – (a) Calibration test bench for the B-dot probe. The transverse cut shows the magnetic field intensity generated by the birdcage antenna. (b) Calibration of the three coils of the B-dot probe, showing the linear trend of the three signals.

were performed in a preliminary campaign prior to full development of the calibration system. In this case, the y axis only reports the value of the signal measured by the oscilloscope.

5.2 First evidence of helicon waves in RAID plasmas

In this section, we discuss preliminary B-dot measurements. At first, we show in Fig. 5.5, the time varying magnetic field components at a fixed position, $z = 500$ mm and $z = 40$ mm, as shown in the photo in Fig. 5.6, in a time range of 300 ns. This measurement was performed in a H_2 plasma, 3 kW RF power, external DC magnetic field of 200 G and 0.3 Pa gas pressure. The first important feature that we remark is that this signal oscillates at a frequency of 13.56 MHz, as we expect from the theory of the helicon wave; the antenna exciting frequency is therefore directly transferred to the plasma without dispersion into other modes. Moreover, the signal is sinusoidal, indicating that large non-linear effects are not present.

In Fig. 5.5, the RF signal (black curve) is measured by a small one turn coil located close to the birdcage antenna. It is used as a "reference signal" to trigger the oscilloscope to evaluate the phase of the three components of the oscillating magnetic field. When the probe is moved in the axial direction, the RF signal does not move but the B_x, B_y and B_z are time shifted proportionally to the displacement along the axial direction. The B_x, B_y and B_z oscillating signals are obtained by averaging over 50 cycles. The B_x and the B_y components are phase shifted by $\pi/2$, since the the helicon wave has, in general, an elliptical polarization. The B_z component is much weaker compared to the other components but it also oscillates sinusoidally. The effect of the plasma on the ceramic cap can be observed also in visible light, as shown in the picture in Fig. 5.6. The surface of the ceramic cap is glowing, especially on the side oriented toward the antenna. Plasma shadowing is instead observed in the downstream direction. This may suggest that, for these particular plasma parameters, particles are mostly transported from the antenna region to the target. The diameter of the ceramic cap (1 cm) may be quite invasive for the plasma and could locally modify the propagation of the helicon wave.
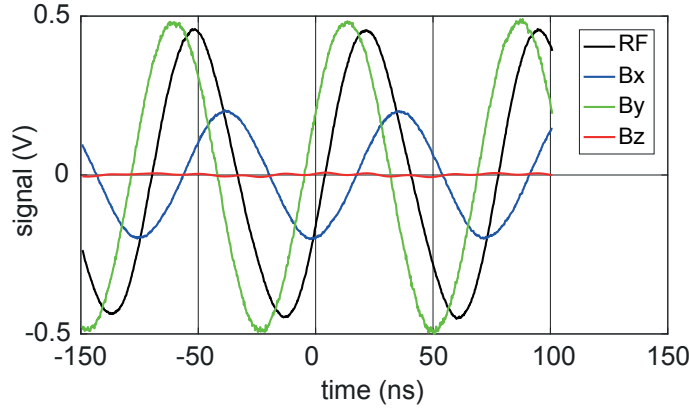
Figure 5.5 – Time varying components of the magnetic field measured by the B-dot probe. The black curve is the RF pickup signal measured by a coil close to the antenna used as a reference to evaluate the phase of the magnetic field components.
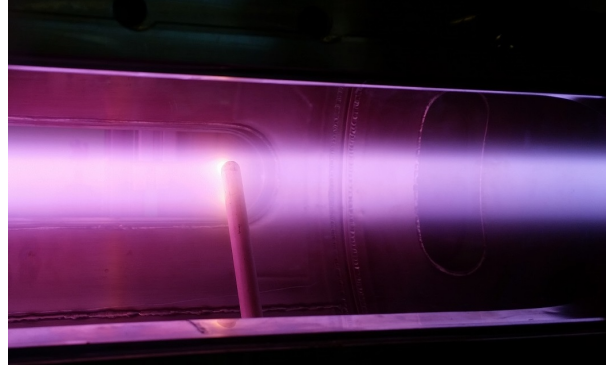
Figure 5.6 – Picture of the B-dot probe measuring the helicon wave propagating in the RAID plasma column. The ceramic cap shielding the three small coils is hit by plasma particles making its surface glow.

The two axis system, allows moving the probe along the axial direction. By measuring the phase and amplitude of each magnetic field component along the axial direction, the structure of the helicon wave can be reconstructed. Fig. 5.7 shows the B_x and B_y components at $t = 0$ ns (solid lines) at $t = 10$ ns (dashed lines). The axial displacement of the wave during this period is evident. The helical structure and the time rotation of the helicon wave is clear when its components are plotted in 3D space. Fig. 5.8 shows the transverse components B_x and B_y along the z axis at times: $t = 0, 20, 40$ and 60 ns. From this data one could extract the k_z and the phase velocity. The time difference between two pictures corresponds approximately to a quarter of a period, so the entire sequence represents a full rotation of the helicon wave. The DC external magnetic field $\vec{B}_0$ points towards the antenna and the rotation is clockwise with respect to $\vec{B}_0$. By carefully analyzing the polarity of the signal, this was found to be in agreement with the expected rotation direction [77].

To reconstruct the propagation of the full helicon wave front, we have performed B-dot
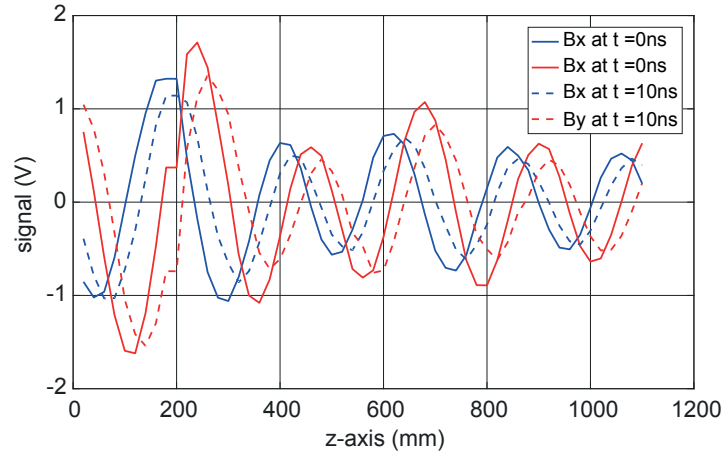
Figure 5.7 – Transverse components of the helicon wave along the axial direction at $t = 0$ ns and $t = 10$ ns.
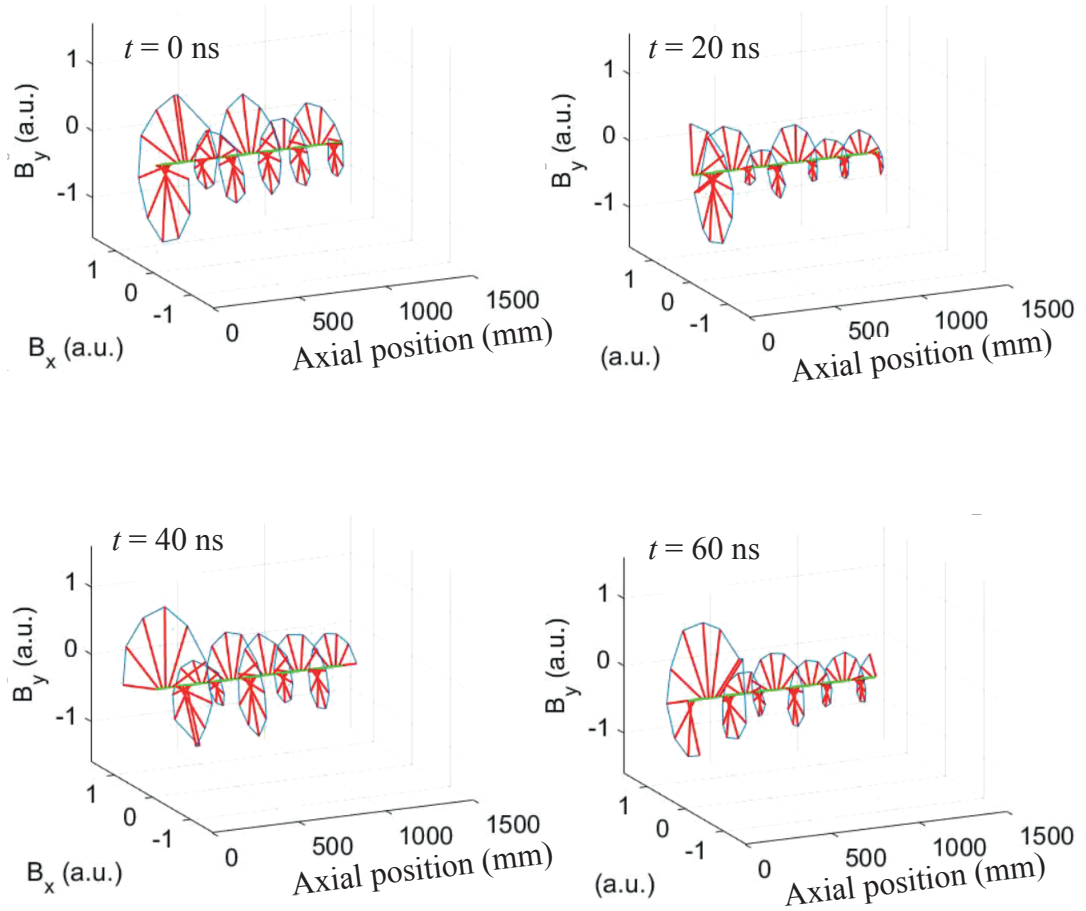
Figure 5.8 – Transverse component of the helicon wave (red lines) along the z axis (green line) at four times: t=0, 20, 40 and 60 ns, showing the helical structure and the rotation over one period. The time difference between two pictures corresponds to a quarter of period.

123
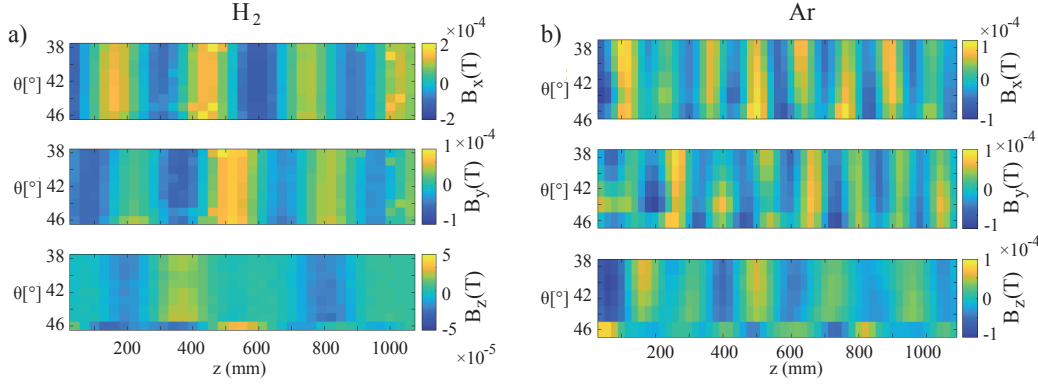
Figure 5.9 – 2D mapping of the helicon wave inside the plasma column for: (a) H_2 plasma, 2 kW RF power, 200 G magnetic field and 0.4 Pa of gas pressure; (b) Ar plasma, 1.5 kW RF power, 200 G magnetic field and 0.3 Pa of gas pressure.

measurements at low RF powers at different radial positions. 2D colormaps are a suitable tool to visualise the spatial structure of the helicon wave. Fig. 5.9 shows the intensity of the helicon wave at fixed instant for a H_2 plasma, in (a), and for an argon plasma in (b). The vertical coordinate is the angular position of the axial probe; $\theta = 42°$ corresponds to B-dot probe on the mechanical axis. The first remarkable feature between (a) and (b) is the difference in wavelength. The wavelength is not set by the length of the antenna [31], but also by the electron density, since n_e in Ar is three-four times higher than in H_2, for the same parameters. In general, the wavelength is defined by the dielectric tensor of the plasma, which mainly depends on B_0 and n_e. The question is: can we excite any wavelength with a given antenna length? It seems that this is possible with the birdcage antenna. From the plots in Fig. 5.9(a) and (b) we measured an axial wavelength of $\lambda_z \sim 14$ cm for Ar and $\lambda_z \sim 30$ cm for H_2. Also here, the B_x and B_y are phase shifted by $\pi/2$, as previously observed in Fig. 5.7. We remark that the B_z shows a phase inversion at the radial position $\theta = 42°$. The phase inversion of the B_z is expected from helicon wave theory to be at the center of the plasma. The disagreement in the position of the center in the measurements may be due to a misalignment of the two-axis system.

5.2.1 Helicon wavelength measurements

Accurate measurements of the axial wavelength can be used to draw some preliminary considerations on the helicon wave dispersion in our scenario. We performed wavelength measurements in H_2 and Ar varying the RF power and the DC magnetic field B_0. Full measurements of the helicon wave for varying RF power and magnetic field are reported in the Appendix. The peak electron density was measured by LP calibrated with interferometry and then checked with Thomson Scattering measurements. We have to point out that the effect of the electron density on the axial wavelength λ_z can be easily quantified since the external DC magnetic field does not depend on plasma density. However, by changing the B_0 field, n_e also changes,
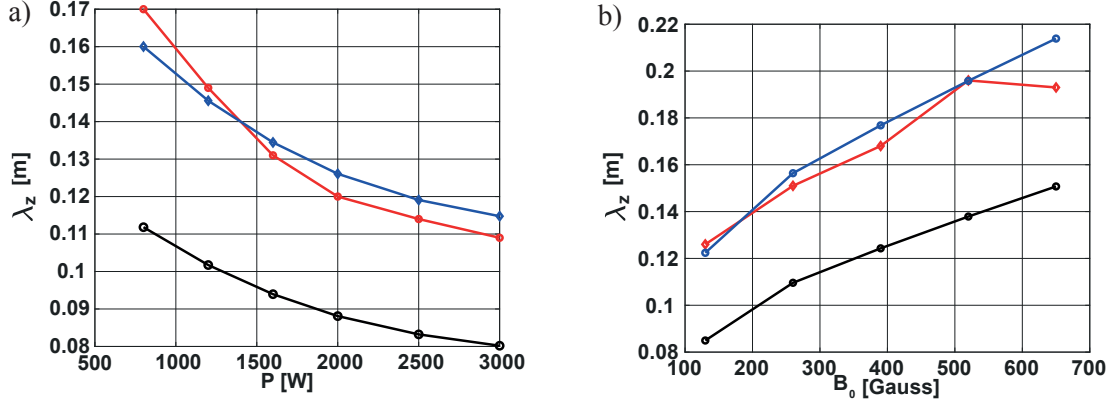
Figure 5.10 – (a) The red curve is is the measured parallel wavelength. The black curve is the theoretical minimum wavelength ($k_{perp} = 0$), according to the helicon dispersion relation. The blue curve is analogous to the red one but with n_e lowered by a factor 1.5. (b) The red curve is the measured parallel wavelength as a function of the DC magnetic field. The black curve is the theoretical minimum wavelength ($k_{perp} = 0$), according to the helicon dispersion relation. The blue curve is analogous to the red one but with n_e lowered by a factor 2.

since the plasma column is compressed, therefore the effect of B_0 on λ_z is corrected by taking into account the dependence $n_e = n_e(B_0)$. According to Eq. 1.26, and disregarding the transverse wavenumber, we can find a simple proportionality relation between the parallel wavelength λ_z and n_0 and B_0:

$$\frac{(2\pi)^2}{k_z^2} = \lambda_z^2 = \frac{(2\pi)^2}{\mu_0 e \omega} \frac{B_0}{n_0} \implies \lambda_z \propto \sqrt{\frac{B_0}{n_0}}. \tag{5.6}$$

Fig. 5.10(a) and (b) respectively show the measured λ_z (red curve) as a function of the RF power and the static B_0 field. The experimental results are also compared to the theoretical λ_z calculated from the dispersion relation (Eq. 5.6). The measured wavelengths have the same trend as the theoretical values but they differ by a factor of two from the absolute value. This discrepancy could be explained in two ways. The first is due to the fact that the electron density is not radially uniform but is clearly peaked. Therefore, instead of considering the central n_e, an effective electron density should be taken. By reducing the electron density in the dispersion relation by a factor 1.5, the calculated λ_z seems in very good agreement with the measured λ_z, as shown by the black curve in Fig. 5.10(a) and (b). The second remark is that the measurement of a longitudinal wavelength higher than the minimal theoretical values may be due to the fact that the propagation of the helicon wave is not purely longitudinal but also the transverse wavenumber k_{perp} should be taken into account to correctly describe the propagation.

The theoretical perpendicular wavelength λ_{perp} for both roots of the dispersion relation is shown in Fig. 5.11. We see a root in the 6-11 cm range and another in the 0.1-0.5 cm range.
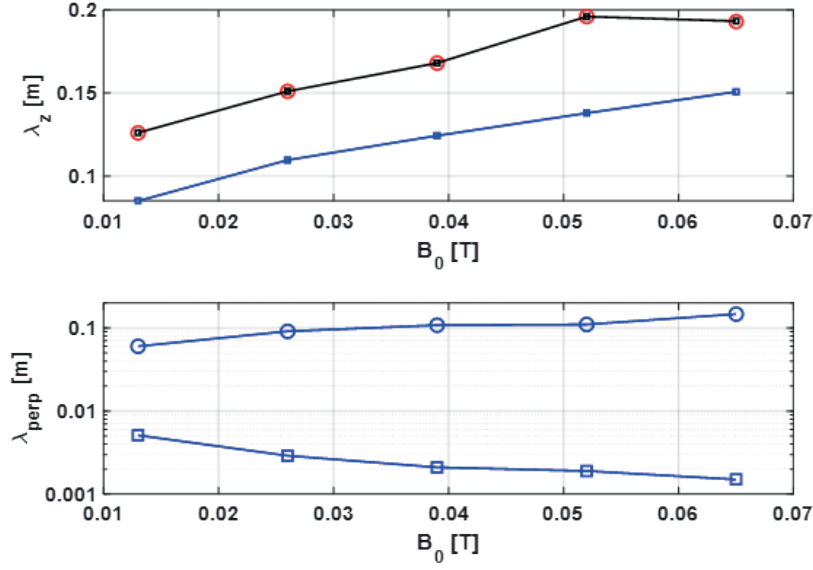
Figure 5.11 – Top figure: red open dots are the measured λ_z as a function of B_0. The blue curve is the theoretical λ_z for $k_p = 0$ (minimum λ_z). Bottom figure: Perpendicular wavelengths obtained from the two roots of the dispersion relation.

Since the plasma column has a typical n_e FWHM diameter of $\sim 6\,\mathrm{cm}$ (see Fig. 3.12), only the second root should be considered. Such a small mm-wavelength, however, cannot be resolved by the current B-dot probe. The production of a smaller and less invasive B-dot probe is envisaged for future measurements. The possible existence of k_{perp} is an important question in the theory of helicon waves. It would be interesting to investigate this further using purpose-built B-dot probes in RAID.

5.3   Simulation of helicon wave propagation

Numerical simulations of the propagation of the helicon wave are a useful tool to understand the structure of the wave and to compare it to experimental results. The model developed for this thesis is based on the resolution of Maxwell's equations in a dielectric medium that simulates the plasma. We therefore model an existing background plasma and a helicon wave propagating through it. The wave equations are solved in COMSOL multiphysics via the PDE (Partial Differential Equation) module.

5.3.1 Description of the helicon wave model

Helicon Wave equations

Let us consider Maxwell's equations without free charges and zero currents, i.e. a dielectric description:

$$\begin{cases} \nabla \times \vec{E} = -\dfrac{\partial \vec{B}}{\partial t}, \\[2mm] \nabla \times \vec{H} = \dfrac{\partial \vec{D}}{\partial t}, \end{cases} \tag{5.7}$$

where $\vec{D} = \bar{\bar{\epsilon}} \cdot \vec{E} = \epsilon_0 \bar{\bar{\chi}} \cdot \vec{E}$ and $\vec{B} = \bar{\bar{\mu}} \cdot \vec{H} = \mu \vec{H}$, and $\bar{\bar{\chi}}$ is the electric permittivity tensor and $\bar{\bar{\mu}}$ the magnetic permeability tensor. We consider time harmonic variation of the fields, namely that any physical quantity $\vec{X}(\vec{r}, t)$, is described by:

$$\vec{X}(\vec{r}, t) = \vec{X}(\vec{r})\, e^{-i\omega t}. \tag{5.8}$$

Eqs. 5.7 can then be written as:

$$\begin{cases} \nabla \times \vec{E} = i\omega \vec{B} = i\omega \mu \vec{H}, \\[2mm] \nabla \times \vec{H} = -i\omega \vec{D}. \end{cases} \tag{5.9}$$

By combining the two Eqs. 5.9 we obtain the following expression for the electric field $\vec{E}$:

$$\nabla \times \nabla \times \vec{E} = k_0^2 \bar{\bar{\chi}} \vec{E}. \tag{5.10}$$

By manipulating the double curl, Eq. 5.10 can be written as:

$$\nabla^2 \vec{E} = \vec{\nabla}(\vec{\nabla} \cdot \vec{E}) - k_0^2 \bar{\bar{\chi}} \vec{E}. \tag{5.11}$$

Eq. 5.11 can be written in the form of a continuity equation: $\vec{\nabla} \cdot \vec{\Gamma} = S$ where $\vec{\Gamma}$ is the flux term and S is the source term. This is done by imposing:

$$\begin{cases} \vec{\Gamma}_{x,y,z} = \overrightarrow{\nabla E}, \\[2mm] S_{x,y,z} = \left[\vec{\nabla}(\vec{\nabla} \cdot \vec{E})\right]_{x,y,z} - \left[k_0^2 \bar{\bar{\chi}} \vec{E}\right]_{x,y,z}. \end{cases} \tag{5.12}$$

This is the form of the equations needed for the PDE module of COMSOL. Since we do not consider free charges $\vec{\nabla} \cdot \vec{E} = 0$, and the source terms is simply: $S_{x,y,z} = -\left[k_0^2 \bar{\bar{\chi}} \vec{E}\right]_{x,y,z}$. Then, by

introducing the source terms $S_{x,y,z} = -\left[k_0^2 \bar{\bar{\chi}} \vec{E} \right]_{x,y,z}$, and the dielectric properties of the plasma medium, the PDEs are solved in the 3D space to compute the electric field associated with the helicon wave.

The conductivity tensor $\bar{\bar{\sigma}}$ for the medium in the frame of time harmonic dependence can be written as: $\bar{\bar{\sigma}} = i\omega\epsilon_0(\mathbb{1} - \bar{\bar{\chi}})$. In the next paragraph we describe the structure of the plasma tensor for RAID plasma.

Plasma Dielectric Tensor

If we consider a uniform plasma of density n_0, magnetized by a static B_0 field aligned with the z direction, the conductivity tensor $\bar{\bar{\sigma}}$ and then $\bar{\bar{\epsilon}}$, can be obtained by linearizing the momentum conservation equation for the electrons:

$$m_e n_0 \frac{\partial \vec{v}_e}{\partial t} = -q n_0 \vec{E} - q n_0 \vec{v}_e \times \vec{B}_0 - m_e n_0 \nu \vec{v}_e = -i\omega m_e n_0 \vec{v}_e, \tag{5.13}$$

where $\vec{v}_e$ is the electron fluid velocity and ν is the collision frequency electron-neutrals. It can be shown that for low values of ω with respect to the plasma frequency ω_{pe} the displacement current can be neglected. The electrical permittivity tensor, in the limit $\frac{\omega}{\omega_{pe}} \ll 1$ can then be written as:

$$\frac{\bar{\bar{\epsilon}}}{\epsilon_0} = \bar{\bar{\chi}} = \begin{bmatrix} \mu & -\tau & 0 \\ \tau & \mu & 0 \\ 0 & 0 & \mu + \tau^2 \end{bmatrix}, \tag{5.14}$$

where:

$$\begin{cases} \tau = \frac{\omega_{pe}}{\Gamma}, \\ \mu = 1 + \frac{1}{\chi_0}, \\ \Gamma = \nu - i\omega, \\ \chi_0 = \frac{i\omega_{pe}^2}{\omega\Gamma(1+\tau^2)}, \\ \omega_{pe} = \sqrt{\frac{n_e e^2}{\epsilon_0 m_e}}. \end{cases} \tag{5.15}$$

ω_{pe}, the plasma electron frequency, can be negative with this definition, as B_0 must be taken with its sign. ν, the electron-neutral collision frequency is estimated to be 10^7 Hz for this range of gas pressure and has an important effect of the wave damping.

5.3.2 Model geometry and current sources

Since the helicon wave has in general three arbitrary electric field (and/or magnetic field) components, no cylindrical symmetry can be assumed and a full 3D model is required. Fig. 5.12 shows the geometry of the model. The simulation space is made of many concentric cylinders; the outermost cylinders are the one on the left, surrounding the antenna, and the one on the right corresponding to RAID vessel walls. The inner long cylinder in the RAID vessel corresponds to the volume where plasma is considered. The six wire loops around the simulation volumes are simulated the six copper coils surrounding the antenna tube and the vacuum vessel. The DC magnetic field is calculated by solving Ampère's equation for magnetic vector potential $\vec{A}$, defined by: $\vec{B} = \vec{\nabla} \times \vec{A}$:

$$-\vec{\nabla}^2 \vec{A} = \mu_0 \vec{j}, \tag{5.16}$$

where $\vec{j}$ is the current of currents flowing into the coils. The current flowing through the coils is that for RAID standard conditions, i.e. -40 A in the antenna coil and 150 A in the others. Moreover, we have considered the Coulomb Gauge for $\vec{A}$, namely $\vec{\nabla} \cdot \vec{A} = 0$. The magnetic field is calculated in a large volume surrounding the helicon simulation volume (a cylinder of diameter 3 m and 4 m long, coaxial and centered with respect to the vacuum vessel) to minimize edge effects. Although the plasma is a diamagnetic medium, the reduction effect of the DC magnetic field is so small that it is neglected. The magnetic permeability of the alumina tube and of the vacuum vessel are considered equal to that of the vacuum μ_0. The static magnetic field $\vec{B}$ is then inserted as input in the helicon wave propagation model described in Sec. 5.3, for the dielectric tensor describing the plasma medium. As a first step, we have verified the possibility for a RAID-like plasma to sustain the propagation of helicon waves. We consider an existing plasma characterized by a dielectric tensor $\bar{\bar{\epsilon}}$ of the form described in Sec. 5.3 and we study how the antenna RF field couples to this plasma. From the theory of birdcage presented in Sec. 2.1.2, we know that when the birdcage antenna is fed by a RF current, a sinusoidal current distribution is established along the legs.
Fig. 5.13 (a) and (b) respectively show the position of edge current sources located either in edges linking the legs (where capacitors are located) and the leg edge sources. The amplitude of the current flowing in the n-th leg is given by:

$$I_z = I_0 \sin(k_m n), \tag{5.17}$$

where $k_m = \frac{2\pi}{N}$ is the wave mode number m. The current flowing along one edge of the
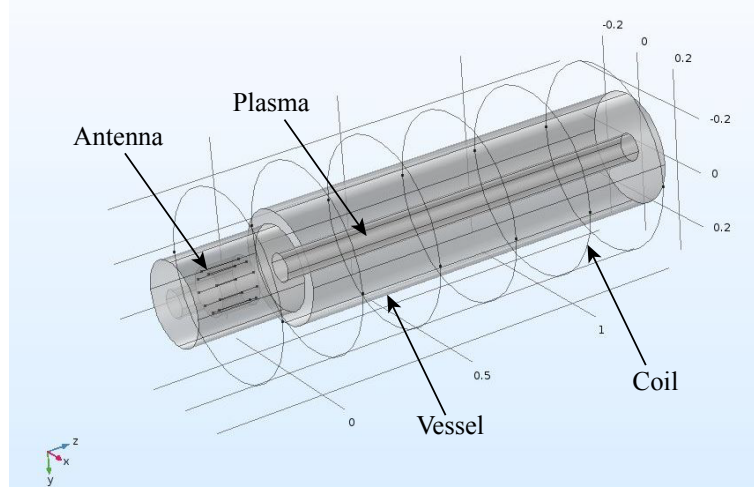
Figure 5.12 – Geometry of the model for the simulation of the propagation of helicon waves in RAID plasma. The plasma is located in the internal long thin tube which passes across the vessel and the antenna region. The outer external cylinders are connected to the ground. The circular loops around the cylindrical simulation volume correspond to the current circulating in the coils producing the DC magnetic field.

antenna (like that in Fig. 5.13 (a)) is expressed by the two transverse components:

$$
\begin{cases}
I_x = \pm \dfrac{1}{2} \dfrac{I_0}{\sin(k_m)} \cos\left(k_m\left(n+\dfrac{1}{2}\right)\right) \cos\left(\dfrac{x}{D_{ant}}\right), \\
I_y = \pm \dfrac{1}{2} \dfrac{I_0}{\sin(k_m)} \cos\left(k_m\left(n+\dfrac{1}{2}\right)\right) \sin\left(\dfrac{x}{D_{ant}}\right),
\end{cases}
\tag{5.18}
$$

where the sign depends on the position of the antenna edge. N is the number of legs ($N = 9$), and I_0 the peak current in legs and D_{ant} is the antenna diameter. As boundary conditions, the vessel walls are connected to the ground.

5.3.3 Structure of the helicon wave and comparison with experimental results

The plasma volume dielectric tensor is computed by introducing a typical electron density mapping in standard condition and a 3 kW power. Fig. 5.14 shows the propagation of the electric field component of the helicon wave along the axis of the plasma column. The field rotates clockwise by moving towards the target, meaning that it is a right handed wave. This is expected since the birdcage antenna excites the $m = +1$ mode. The wave shows two large peaks in the antenna region due to the proximity of the high electric field produced by the antenna legs. The wave looks linearly polarized close to the target. This may results from the the superposition of a propagating and a backreflected wave, with two circular opposite polarization. By solving the wave equations at different instants of time, the rotation of the entire structure is evident, like in the experimental measurements in Fig. 5.7 (not shown here).
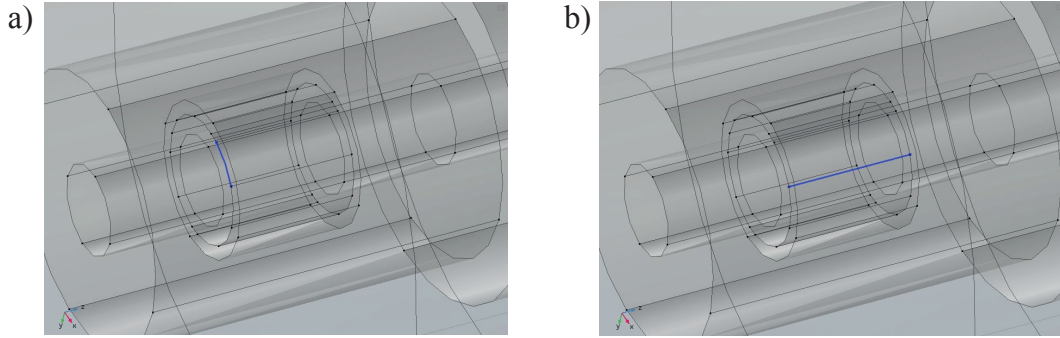
Figure 5.13 – Zoomed view of the antenna geometry showing the legs and edge connections (highlighted in blue). These correspond to the current edge sources term of the model: (a) Antenna edges (along which the capacitors are connected); and (b) the Antenna legs.
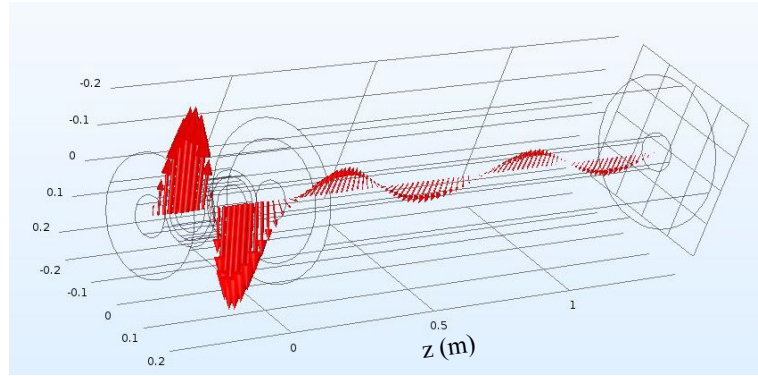
Figure 5.14 – Propagation of the electric field vector of the helicon wave along the axis of the plasma column for a typical H_2 plasma, showing the right-handed helicon structure of the helicon wave across the plasma column.

The knowledge of the entire structure of the plasma column is sufficient to perform some quantitative comparison with experimental results. We made simulations of the helicon propagation for the plasma parameters investigated experimentally. For each simulation, the axial wavelength was estimated and compared to the experimental results, as shown in Fig. 5.15. We remark that calculated wavelengths in H_2 are much larger compared to Ar, in agreement with experimental results. For each position, the helicon magnetic field is averaged over a few thousand RF periods and the longitudinal wavelength is computed for B_x and B_y. The increase of λ_z with B_0 predicted by the proportionality predicted in Eq. 5.6 is verified. Also a good agreement with the absolute values of the axial wavelength is found. These preliminary results suggest that these kind of simulations may be a versatile and powerful tool for these scenarios. Indeed, the simulation parameters can be easily varied for different devices, provided that a detailed mapping of the electron density is available.
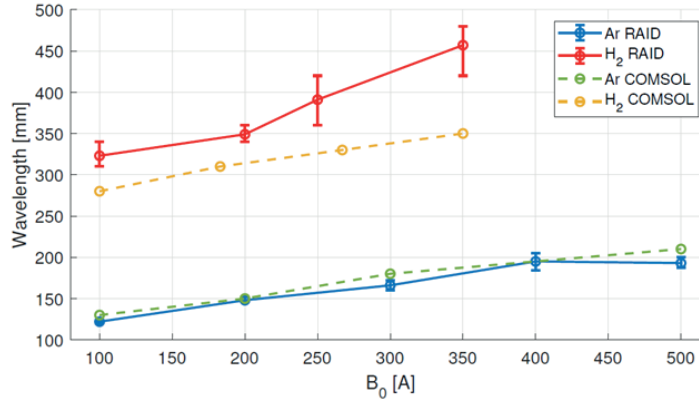
Figure 5.15 – Comparison between the helicon wavelength measured by the B-dot probe (solid line) and the wavelength computed by COMSOL simulations for H_2 and Ar plasmas.

5.4 Discussion and Conclusion

The objective of this chapter was to demonstrate the propagation of helicon waves in the RAID plasma and to initiate the study of the physics of the helicon waves produced by the birdcage antenna. A B-dot probe installed on the 2-axis moving system was used to measure the spatial and temporal structure of helicon waves propagating in RAID's plasma in different conditions of RF power, magnetic field and pressures. A preliminary characterization of helicon waves was successfully accomplished. We demonstrated the propagation of helicon waves in Ar, H_2, and we analyzed their 3D structure and the axial wavelength. The behaviour of helicon waves is found to be in agreement with the simple dispersion relation for the axial wavelength. Finally, numerical simulations were performed in COMSOL multiphysics of the helicon wave, using RAID plasma profiles from experimental measurements. These showed that the birdcage antenna launches right-hand polarized waves and that its wavelength in H_2 and Ar are in very good agreement with experimental results.

There remains a large scope to technically improve the B-dot moving system. The current system in RAID does not allow a complete transverse mapping over the whole azimuthal cross section. A ring of variable radius supporting an array of B-dot probes such as, for example, that in [142] could be very helpful to study the azimuthal modes and therefore the full 3D structure. Also, a smaller less-invasive probe is necessary to spatially resolve the radial wavelength and make comparison with the full dispersion relation in Eq. 1.26 possible. Certainly, a wide spectrum of physics should be investigated. For example, it would be very interesting to study the propagation of helicon waves in high power helicon plasmas and the power deposition mechanisms, which are not fully understood yet. From the simulation side, we have supposed the presence of a preformed plasma, without giving any hint on how it is produced. A self consistent model would require the coupling of the helicon wave propagation with the plasma, but this is beyond of the scope of this preliminary work.

6 Application of Thomson Scattering to helicon plasma sources

In this chapter we will discuss a Thomson Scattering (TS) system, developed in the framework of a collaboration with the AWAKE (Advanced WAKefield Experiment) project at CERN, for the plasma acceleration of particles using GeV/m electric fields in plasmas. [1] The possibility of performing precise electron density and temperature measurements in a high power helicon plasma is a crucial issue for AWAKE. RAID produces a helicon plasma column with characteristics similar to that of the AWAKE helicon source, and is therefore an optimal testbed for application to the AWAKE device. Presented here are details of the TS diagnostic and the first tests in RAID, and the expectations for the system when employed on the AWAKE device. The other advantage of having a TS system in RAID is that it was necessary to investigate high power discharges, especially in argon plasma, which cannot be measured with LP alone and to compare to previous LP and mw-interferometry measurements. We will start by describing the mechanical implementation of the TS in RAID, and its relative and absolute calibration. Then we will show time resolved measurements and radial profiles in different conditions of input parameters and we compare them to interferometric data. Finally, we discuss the feasibility of employing the TS setup for RAID in AWAKE, including physics and technical constraints.

6.1   Motivation: The AWAKE project

The next generation of particle accelerators for high energy physics will be based on more efficient methods of acceleration, beyond conventional RF accelerating cavities. One way to achieve the gigaelectron volt (GeV) energies required for particle physics research, is to use the strong microelectric fields, called "plasma wakefield" which can be generated by plasma density fluctuations [134]. In AWAKE, proton bunches will be used to drive wakefields where electron bunches are subsequently accelerated to the target energies. Electrons can thus be linearly accelerated in a few meters up to multi-GeV energies [2]. The AWAKE project is

---

[1] Part of the the work presented in this chapter is currently submitted for publication in "Journal of Plasma Physics".

Figure 6.1 – Prototype of the helicon plasma cell developed by the AWAKE collaboration at CERN. The pulsed Ar plasma discharge is produced by three twisted helicon antennas.

therefore a crucial step for the development of compact and efficient particle accelerators [11].

A challenging goal for the development of the AWAKE plasma source is the achievement of an electron density near $10^{21}\,\mathrm{m}^{-3}$, with high homogeneity (better than 0.2 %) over a 10 m plasma cell [10]. Such a stringent plasma density uniformity is required for wakefield acceleration and electron bunch focussing [110]. Moreover, the electron temperature has to be kept below a few eV, since high electron temperatures tend to destroy the accelerating structure of the wakefield. A Rb vapor source was already successfully employed to achieve the acceleration of electrons in the plasma wakefield generated by proton bunches [2]. This kind of source, however, requires a laser pulse to ionize the gas. Helicon plasma cells are a promising candidate to generate the plasmas needed for AWAKE. Their main advantage is that they can produce elongated and centrally peaked plasma columns with high density (maximum achieved steady state density is $\sim 10^{20}\,\mathrm{m}^{-3}$) and few eV of electron temperature. The target density for AWAKE is $7 \times 10^{20}\,\mathrm{m}^{-3}$ and it is suggested that helicon plasmas could reach such a target density. Still, some limitations due to neutral pumping, preventing high central electron densities, have to be fully investigated [27]. A prototype helicon plasma cell currently under study at CERN is shown in Fig. 6.1. Plasma discharges are produced in argon gas using three twisted helicon antennas. Research is currently under way to determine if such a set up could fulfill the requirements for plasma wakefield acceleration.

Thomson Scattering (TS) is a well established technique to measure electron density and temperature in plasmas, including those sustained by helicon waves [21, 20, 24, 124]. It is routinely used in Tokamak research to obtain electron density and temperature profiles in the plasma core where the density reaches about $2 \times 10^{20}\,\mathrm{m}^{-3}$ and the temperature several keV [109, 107]. In this work, we tested a TS diagnostic in the RAID helicon plasma produced by an antenna in a birdcage geometry on RAID [61]. Helicon devices such as RAID can sustain plasma discharges up to $n_e \approx 10^{19}\,\mathrm{m}^{-3}$ and low electron and ion temperatures with a few kW power as we discussed in Sec. 3 and Sec. 4. In these regimes Langmuir Probes (LPs) suffer strong heating and, moreover, electrons are strongly affected by magnetic fields making measurements unreliable.

In the Rb vapor source for AWAKE, the electron density was indirectly estimated by measuring the Rb gas pressure and considering the ionization of all Rb atoms in the laser beam volume [110]. The only way to directly measure plasma density in such high density regimes is to employ active or passive spectroscopic techniques which are far less invasive, such as TS. The advantages of TS diagnostics are: (1) measurements of local quantities; (2) time resolution of the order of the laser pulse duration; (3) interpretation of the signal reflects the velocity distribution of the particles without requiring any collisional-radiative code. The TS scattering signal is proportional to the number of the electrons scattering the electromagnetic pulse, therefore high density plasmas are well adapted. This makes argon plasma suitable to test the TS diagnostic since high degrees of ionization can be easily achieved with a few kW power on helicon devices. RAID represents a suitable testbench for a TS diagnostic for the AWAKE project, since helicon plasma columns in Ar can be easily produced at relative high densities ($10^{19} - 10^{20}\,\mathrm{m^{-3}}$).

In the following section, we describe the design of the TS experimental setup, the relative calibration of the polychromators, the absolute Raman calibration in nitrogen gas, and the precautions to mitigate the problem of undesired "stray light". Sec. 6.4 presents the measurements performed in steady-state argon plasma discharges. Sec. 6.6 discusses the physics and technical challenges of the implementation of the present TS system in AWAKE scenarios. In Sec. 6.7 we conclude with a summary and possible improvements.

6.2 Theory of Thomson Scattering

The Thomson Scattering (TS) diagnostic is based on the analysis of the scattering emission spectra of plasma when excited by an electromagnetic wave. Although a detailed description of TS can be found in [75, 144, 48], we provide a brief introduction here.
An electromagnetic wave impinging on a charged particle makes it oscillate in the direction of the incident electric field $\vec{E}_i$. The accelerated charged particle subsequently emits electromagnetic radiation in all directions. From the quantum point of view, the process consists in the scattering of incident photons in all directions. Considering a photon of frequency ω_i impinging on a particle of mass m, the radiation scattering is considered Thomson Scattering when the rest mass of the target particle is much larger that the incident photon mass ($h\omega_i \ll mc^2$). By using the dipole approximation in the non-relativistic limit, the scattered electric field $\vec{E}_s$ is given by [75]:

$$\vec{E}_s = \frac{r_e}{R} [\hat{s} \times (\hat{s} \times \vec{E}_i)], \tag{6.1}$$

where $\hat{s}$ is the unitary vector in the direction of the scattered radiation, R is the distance from

135

the charge and r_e is the classical electron radius:

$$r_e = \frac{e^2}{4\pi\epsilon_0 m_e c^2} = 2.82 \cdot 10^{-15}\,\text{m}.$$

(6.2)

The power scattered per unit of solid angle $\frac{dP}{d\Omega}$, is:

$$\frac{dP}{d\Omega} = r_e^2 \sin^2\phi c\epsilon_0 \mid E_i \mid^2,$$

(6.3)

where ϕ is the angle between the $\hat{s}$ and $\vec{E}_i$. The proportionality factor between $\frac{dP}{d\Omega}$ and the incident power per unit area $c\epsilon_0 \mid E_i \mid^2$, $r_e^2 \sin^2\phi$, is called *TS differential cross section*. By integrating Eq. 6.3 over all the solid angle, we obtain the *total TS cross section σ_{TS}*:

$$\sigma_{TS} = \frac{8\pi}{3} r_e^2 = 6.65 \cdot 10^{-29}\,\text{m}^2.$$

(6.4)

From the experimental point of view, the tiny value of σ_{TS} requires the use of powerful incident radiation and sometimes makes it difficult to discern the TS photons from the background radiation photons, as we will discuss in Sec. 6.3.4. We have so far considered the radiation scattered by a single electron. Since plasmas are composed of many electrons, we have to consider the cumulative effect of plasma electrons on the scattered radiation. In a plasma, microelectric fields are screened on a distance comparable to the Debye length λ_D:

$$\lambda_D = \sqrt{\frac{\epsilon_0 T_e}{n_e e^2}}.$$

(6.5)

Plasma electrons inside a volume of the order of the Debye sphere are correlated with each other. When the incident radiation has a wavelength λ_i much smaller than the λ_D, the scattering is incoherent, otherwise it is coherent. The degree of correlation in the scattering is usually described by a parameter α, defined as [144]:

$$\alpha = \frac{\lambda_i}{4\pi\lambda_D \sin(\theta/2)},$$

(6.6)

where θ is the angle between the direction of the incident and the scattered radiation. The scattering is incoherent when $\alpha \ll 1$. In this condition, the emission spectrum can be expressed by the Selden formula [123]:

$$S(\epsilon,\theta) = c(\beta) A^{-1}(\epsilon,\theta) \exp(-2\beta B(\epsilon,\theta)),$$

(6.7)

with:

$$\epsilon = \frac{\lambda_s - \lambda_i}{\lambda_i}, \tag{6.8}$$

$$\beta = \frac{m_e c^2}{2 k_b T_e}, \tag{6.9}$$

$$A(\epsilon, \theta) = (1 + \epsilon)^3 [2(1 - \cos\theta)(1 + \epsilon) + \epsilon^2]^{1/2}, \tag{6.10}$$

$$B(\epsilon, \theta) = \{1 + \frac{\epsilon^2}{[2(1 - \cos\theta)(1 + \epsilon)]}\} - 1, \tag{6.11}$$

$$c(\beta) = \left(\frac{\beta}{\pi}\right)\left(1 - \frac{15}{16}\beta^{-1} + \frac{345}{512}\beta^{-2}\right). \tag{6.12}$$

where λ_s is the wavelength of the scattered radiation. The Selden formula is used to deduce n_e and T_e for TS measurements in RAID. For the RAID plasma regime, the scattering is incoherent and the shape of the spectrum depends only on T_e. n_e is obtained by absolute calibration with Raman anti-stokes lines (see Sec. 6.3.3).

If the scattering is (partially) coherent, as expected for AWAKE application of TS, the scattering spectrum will depend on both T_e and n_e. This is discussed in Sec. 6.6.

6.3 A Thomson Scattering system for RAID

Argon plasmas are more suitable to test the TS diagnostic, since a larger number of photons is scattered, due to the higher densities compared to other gases. Moreover, high-Z gases are preferred for plasma acceleration, to minimize the background plasma motion [143]. Testing the TS in RAID can help assessing the possibility of using this technique for AWAKE in terms of accuracy, spatial resolution and the technical design of a TS diagnostic. A major difference between RAID and AWAKE is that, while RAID produces a steady state plasma column, AWAKE is a pulsed plasma device where discharges last a few ms [27], thus this does not require to synchronise the TS laser to the plasma pulse. The vacuum flight tubes for the laser beam used for the TS system shown in Fig. 6.2 are installed at a distance of 1.1 m from the center of the antenna. At their extremities, windows tilted at the Brewster angle are installed. The TS probing photons are produced by a Q-switched Nd:YAG Lambda Laser of 1064 nm wavelength, 0.8 J pulse energy, 6 ns pulse duration and 10 Hz repetition rate. The laser beam exits the laser head with a diameter of 8 mm, a divergence < 0.5 mrad and a pointing stability < 50 μrad. The alignment of the Nd:YAG laser beam is performed with a He-Ne laser (632 nm) collinear with the Nd:YAG.

Fig. 6.3 shows the positioning of the laser beam path in the RAID vessel. The trajectory of the Nd:YAG beam is checked with flash paper for fine adjustments. The location and mounting of the present laser on the optical bench is the same as for the Nd:YAG laser employed for CRDS and LPLP measurements in Sec. 4. The laser is mounted on an optical table close to
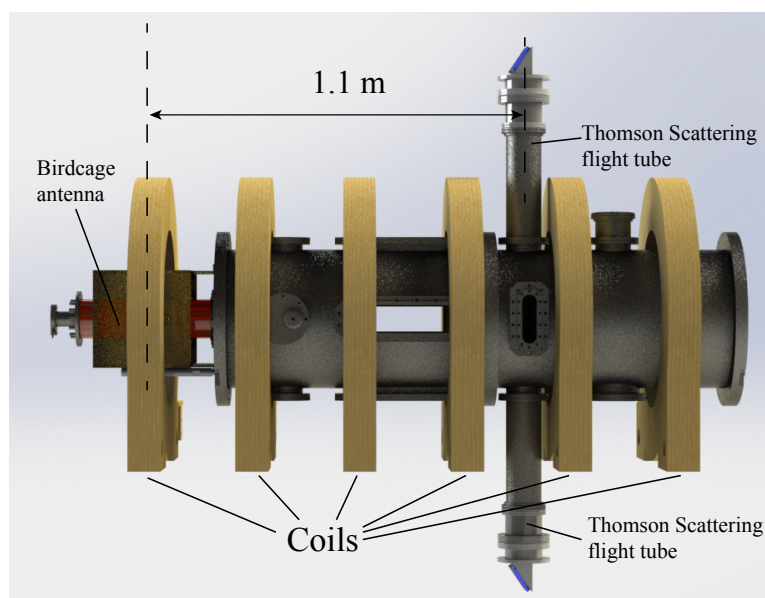
Figure 6.2 – Schematic of the RAID showing the position of the Thomson Scattering vacuum flight tubes with respect to the antenna position.
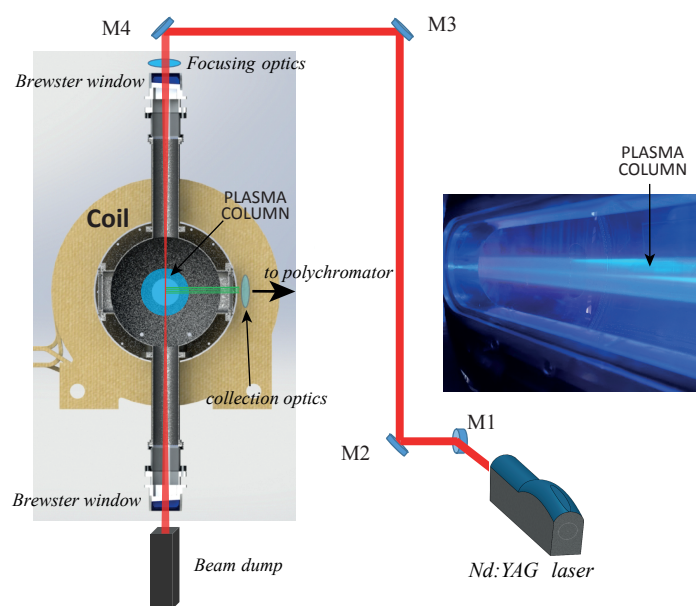
Figure 6.3 – Laser path and optical arrangement of the Thomson Scattering diagnostics in RAID (not to scale). Before entering the vacuum vessel, the beam is focused by lenses and passes through a window tilted at the Brewster angle to minimize back reflections. On the right, a picture of a typical argon plasma in RAID is shown.

the vessel and the frame supporting the laser beam path is free standing from the vacuum vessel. This minimizes mechanical vibrations caused by pumping and cooling systems. The laser beam is directed to the vessel by the mirror M1, then vertically directed by M2 and finally it enters vertically from the top of the vessel after having been steered by mirrors M3 and M4. Before entering the vessel, the laser beam is focused so that its diameter is $\sim 1\,mm$ at the measurement position. This is to increase the density of photons in the interaction volume. After the beam waist, the beam expands, exits from the bottom window and is collected in the beam dump, made of multiple tilted glass plates. The vacuum flight tubes on the top and bottom of the cylindrical vessel are 50 cm long and 11 cm of diameter.

The light collection optics consists of camera lenses (f/10) pointing towards the center of the vessel to the plasma column and the line of sight is perpendicular to the laser beam. The collection lenses image an array of four 1 mm diameter glass optical fibers in the plasma column. The diameter of each light spot is 4 mm at the center of the plasma column. The intersection of the laser beam and the line of sight of the fibers defines the photon collection volume and thus the volume resolution of the system. The vertical spatial resolution with 4 fibers is then 16 mm. If fewer fibers are used, the spatial resolution increases but the signal-to-noise ratio decreases. The length of the optical fibers is 10 m so that the signal is delivered outside the laser interlock area. The scattered light is sent to a polychromator, described in Sec. 6.3.1, where it is analyzed.

To accurately estimate the electron temperature and density, two kinds of calibrations are required: (1) a relative calibration of the spectral transmissivity of the polychromator's filters (see Sec. 6.3.1) and, (2) an absolute calibration using Raman anti-Stokes lines of nitrogen (See sec. 6.3.3), performed *in situ*, namely when the entire setup is installed on the plasma device.

6.3.1 Calibration of the polychromators

The Thomson scattered photons are emitted in a spectrum whose width increases with the electron temperature, and whose peak is located at a lower wavelength with respect to the exciting radiation. The scattered power P_s per unit of solid angle $d\Omega$ and frequency ω by a laser beam of power P_1 can be expressed by [144]:

$$P_s d\Omega d\omega = \frac{P_1 n_e L e^4}{2\pi m_e^2 c^4} d\Omega d\omega |\hat{s} \times (\hat{s} \times \hat{e})|^2 S(\vec{k}, \omega),\qquad(6.13)$$

where L is the interaction length between the laser beam and the solid angle viewed by the optical fibers, $\hat{s}$ is the unit vector pointing from the interaction volume to the detector, $\hat{e}$ is the unit laser electric field vector, c is the speed of light, m_e is the electron mass and $S(\vec{k}, \omega)$ is the spectral density function, depending on electron density and temperature [74]. If the TS is incoherent (see Sec. 6.6 for more details), the number of scattered photons is proportional to the electron density.

To analyze the spectrum, we employed one of the polychromators developed for the divertor TS diagnostic on TCV (Tokamak à Configuration Variable) [8]. The technique is based on
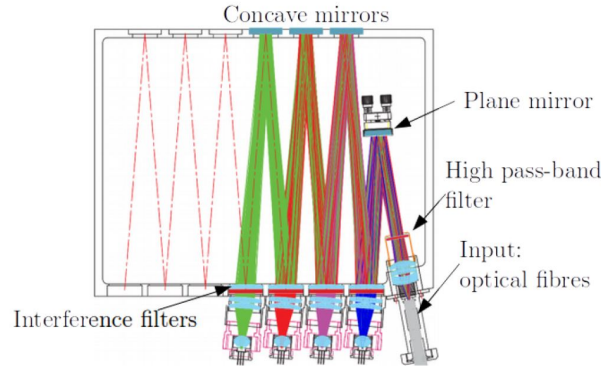
Figure 6.4 – Schematic of the polychromator. The TS light entering the polychromators is measured by four APDs detectors in a well defined spectral-range selected by filters.
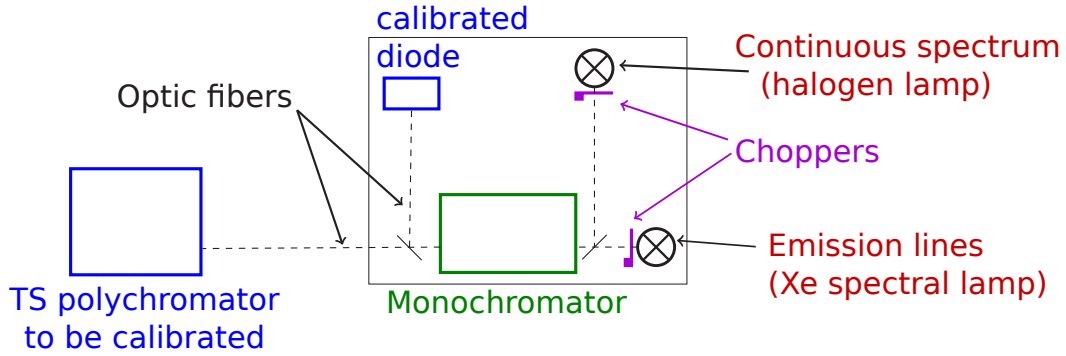
Figure 6.5 – Schematic of the spectral calibration system for the polychromator.

the fast collection of light during ~ 2 s plasma shots [65, 109]. The polychromator collects Thomson scattered photons in a few spectral intervals and consists of a set of interference filters and avalanche photodiodes (APDs). When the light enters the TS polychromator, shown in Fig. 6.4, it performs multiple reflections and it is collected by four APDs, through different filters each one selecting a different spectral bandwidth. A schematic of the polychromator spectral calibration setup is shown in Fig. 6.5. The light used to calibrate the polychromator is produced by two sources: a halogen lamp emitting a continuous spectrum and a xenon spectral lamp for the wavelength calibration. The monochromator box, consisting of a movable diffraction grating, selects a narrow wavelength interval, typically $\delta\lambda = 0.15$ nm. The spectral transmissivity of each filter is measured by sweeping the monochromator wavelength over a wide portion of the spectrum. At the same time, the intensity of the light is measured by a calibrated diode. The monochromator output light is then transported via a fiber bundle to the polychromator to be calibrated. The measured transmissivity of the polychromator filters is shown in Fig. 6.6 (a). Filters are located in the blue-shifted part of the spectrum, where APDs have higher quantum efficiency, however, in other TS setups, like that on DIII-D, the red-shifted part of the spectrum is sampled as well [95].
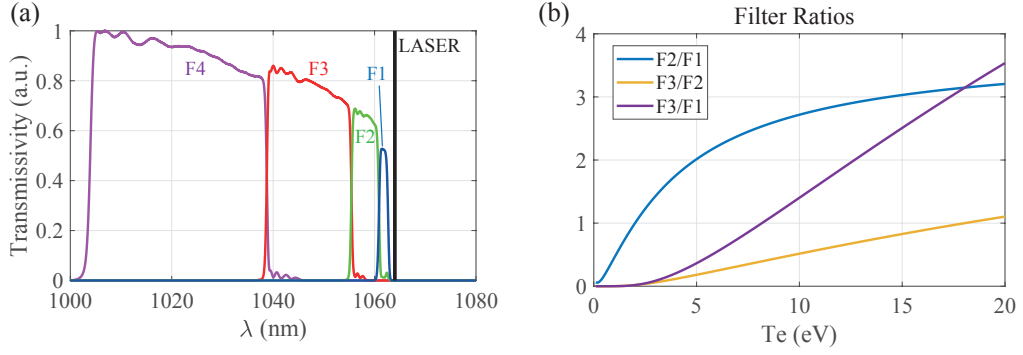
Figure 6.6 – (a) Transmission characteristics for the four bandpass filters (F1, F2, F3 and F4) of the TS polychromator. The laser wavelength at 1064 nm, indicated by the black line, is scattered as a spectrum and collected by the filters. (b) Polychromator calibration curve calculated using $S(k,\omega)$ used to determine T_e. Only three ratios are shown for clarity. In the present setup only the ratio F2/F1 is used since filters F3 and F4 collect negligible light when $T_e < 5$ eV.

Since for RAID plasmas the electron temperature is below 5 eV (see discussion in Sec. 3), only two filters close to 1064 nm collect photons. Therefore, the estimate of the electron temperature is based on the ratio between the light intensity collected by filters F1 and F2 (so the filters F3 and F4 are actually redundant for RAID plasma regimes). The response function of the polychromator used for the present experiment is shown in Fig. 6.6(b). One issue regarding the proximity of these filters to the laser wavelength is their residual sensitivity around the laser wavelength. Although the transmissivity of F1 and F2 decays respectively by 4 and 5 orders of magnitude at 1064 nm compared to the peak transmissivity, the amount of 1064 nm photons collected by F2 is comparable to TS photons. These laser photons collected by the filters represent a sort of filter leakage and are subtracted in data analysis.

6.3.2 Signal acquisition

The polychromator output can be either 4 HF (high frequency) channels, or 4 integrated channels. Typical HF signals measured by the APDs of the polychromator for the first channel (CH1) and the second channel (CH2) are shown in Fig. 6.7(a). The oscilloscope acquisition is triggered by the laser pulse, which is shot at $t = 0$ ns. The trigger signal is produced by a photodiode sensitive to the laser wavelength detecting the passage of the laser pulse in front of it along the optical path. The peak is then recorded by the oscilloscope at $t \sim 620$ ns, corresponding to the travel time of the light along the optical fibers and the electronic acquisition. We remark that the noise level on CH2 is comparable to the signal in the presence of a plasma. This is due to the non negligible residual sensitivity of filter F2 at the laser wavelength. The HF signals were only checked at the beginning of the experimental campaign and were not used for data analysis. For the estimate of the electron density and temperature we are interested in the integrated values of these HF signals. The integration is performed by an
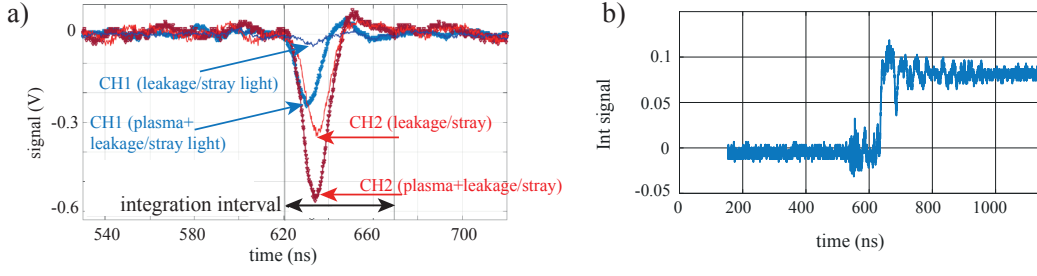
Figure 6.7 – (a) High frequency signals. (b) Example of an integrated signal .

electronic module which integrates the HF signal in a time interval covering the entire large HF undershoot and the small overshoot. The time integration range is shown by the horizontal arrow in Fig. 6.7(a). The integration range is manually optimized prior to the experimental campaign and is not changed afterwards. A typical integrated signal is shown in Fig. 6.7(b), the signal is proportional to the integral of the HF signal. Due to the non negligible oscillations caused maybe by current ringing, the integrated signal is averaged over $t > 620$ ns in the entire time acquisition range.

6.3.3 Absolute calibration with Raman anti-Stokes lines

As described in 6.3.1, the T_e measurements only require the relative calibration of the spectral channels. To determine n_e, however, one has to know the absolute transmission efficiency of the entire system such as the optics, the polychromators and the emission volume. Therefore, an absolute in-situ calibration is needed for every plasma measurement. The rotational anti-Stokes lines of nitrogen are routinely used for the absolute calibration, as commonly done for TS in large fusion devices [85, 121]. The anti-Stokes part of the nitrogen spectrum is composed of narrow lines, mostly located in the region of the spectrum covered by filters F1 and F2, as shown in Fig. 6.8(a). Since broad band filters are used to detect the Raman signal, we use an "effective" cross section, σ_{eff}^{RAM}, given by the integral of the discrete lines weighted by the local filter transmissivity [48]:

$$\sigma_{eff}^{RAM} = \sum_{n=1}^{N} \tau(\lambda_n)\sigma_{N_2}^{RAM}(\lambda_n), \tag{6.14}$$

where $\tau(\lambda_n)$ is the transmissivity at the wavelength of the n-th Raman line and $\sigma_{N_2}^{RAM}$ the Raman scattering cross section for N_2. A Raman calibration is performed by filling the vacuum chamber with nitrogen with 4 different gas pressures in the interval 20 - 70 mbar. This range is low enough to avoid laser-induced breakdown in the gas which occurs at ~ 100 mbar. Fig. 6.8(b) shows the results for the Raman calibration for F1 and F2. Each data point is averaged over 700 laser shots. The typical error on the determination of the slope is a few percent. The offset does not affect the estimate of n_e, since the Raman calibration factor only
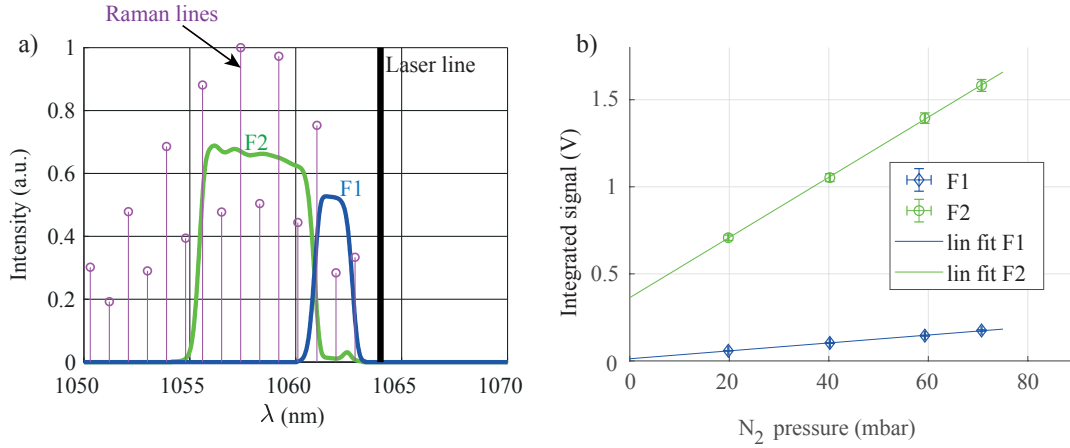
Figure 6.8 – (a) Location of the anti-Stokes Raman lines with respect to the filters' transmissivity (b) Raman calibration data obtained with filter 1 and filter 2, and linear fits of the experimental data. Each data point is averaged over 700 laser pulses.

depends on the slope. The large difference of vertical offsets between the two filters (0.37 V for F2, 0.01 V for F1), is due to the much higher level of leakage photons collected by F2. Thus, we opted to use F1 for all the Raman calibrations, since less affected by leakage light.

Since the wavelength resolution of the spectrometer employed to calibrate the filters is 0.15 nm wide, this may result in a shift of the filter F1 and F2 with respect to the Raman lines. In the case of F1, which is used for the Raman calibration, this would result in a systematic error < 8.5%. Since this cannot be known *a priori*, we do not consider this error in the data analysis for clarity.

6.3.4 Mitigation of stray light and leakage photons

One of the major challenges of TS diagnostics is the mitigation of the "stray light", which is unwanted errant laser photons collected by the filters together with Thomson scattered photons. With 0.8 J at 1064 nm, there are 4.3×10^{18} photons emitted per laser pulse. Only a small fraction of these photons is detected by the system. The number of detected photons N_{det} is approximately given by:

$$N_{det} = \frac{1}{2} N_{pulse} \sigma_{TS} n_e L \Delta\Omega \eta, \tag{6.15}$$

where σ_{TS} is Thomson scattering total cross section, n_e is the electron density, L is the length of the scattering volume, $\Delta\Omega$ is the fractional collection solid angle, η is the efficiency of transmission of the different optical components and the factor 0.5 is due to the fact that the RAID's polychromator detects only the blue-shifted photons. For our system we expect $\sim 10^5$ scattered photons. Because of this relatively small number, the stray light coming from the laser is the main factor limiting the signal-to-noise ratio (SNR). These photons come both

from internal reflections in the vacuum vessel and the flight tubes and also from the laser path outside the vessel. These are usually distinguished by the leakage photons through the filters at the laser line. To mitigate the noise due to stray light photons, the interior of the vacuum chamber in front of the collection optics was covered with Aktar Spectral Black foil [2] reducing the stray light by about 50%. The residual leakage light signal was subsequently subtracted in data analysis. The widespread solution to drastically limit the amount of stray photons is to install "light baffles" in the vacuum flight tubes [30]. A couple of beam diaphragms are currently being built for the upgrade of the TS system in RAID, and their mechanical design is shown in Fig. 6.21. These prevent the diffusion of stray photons in the vacuum vessel. One possibility to reduce the stray leakage photons through the filters at the laser line would be to shift the position of sensitivity regions of filters F1 and F2 far from the laser wavelength. This would in turn increase the SNR of the system. This could be done by tilting the filters a few degrees, since the transmissivity depends on the angle of incidence of light of filters. Otherwise, new filters with higher rejection at the laser wavelength should be employed. The drawback of these approaches is that this would require a re-design of the polychromator optics.

6.4   Testing the Thomson Scattering system in argon plasmas

We will start by describing Ar tests. In Sec. 6.5 the experiments with other gases such as He, H_2 and D_2 are described. For the preliminary tests, to find the highest possible signal-to-noise ratio, we employed all the available optical fibers (4 fibers) and directed them to the plasma center, where n_e peaks and therefore the highest yield of laser photons is expected. Fig. 6.9 shows time-resolved measurements of electron density and temperature during a 100 s plasma discharge in Ar with 5 kW RF power and 665 G magnetic field on axis, and the laser pulsed at 10 Hz. A Matlab routine based on a robust non-linear least-square fitting [109], is used to obtain n_e and T_e, together with the error bar. The typical relative error for a single shot is 25.2% on T_e and 17.6% on n_e. For magnetic fields above 530 G, the typical "blue core" [122], which we will discuss later on, is observed in visible light, resulting in a narrow peaked brighter region in the plasma center. The average values of n_e and T_e during the steady state plasma discharge are $n_e = 1.10 \times 10^{19}\,\mathrm{m}^{-3}$ and $T_e = 2.3\,\mathrm{eV}$, and we remark that n_e and T_e are stable during the plasma discharge. Error bars could be reduced by averaging over many laser pulses. Once verified that the signal-to-noise was tolerable, we performed a scan in RF power and magnetic field. Fig. 6.10 shows the electron density and temperature when increasing the RF power and for different magnetic fields. n_e increases with the RF power from $5 \times 10^{18}\,\mathrm{m}^{-3}$ to $1.1 \times 10^{19}\,\mathrm{m}^{-3}$ for 665 G of the main magnetic field. T_e, however, is only weakly dependent on RF power as expected by particle balance considerations [89]. To improve the volume resolution of the system we employed only two optical fibers, resulting in a spatial resolution of 8 mm. The collection optics were mounted on a translation stage fixed on a vessel flange, and the plasma column was scanned by moving the translation stage with 10 mm steps in the

---

[2]www.acktar.com, last access 21.01.2020
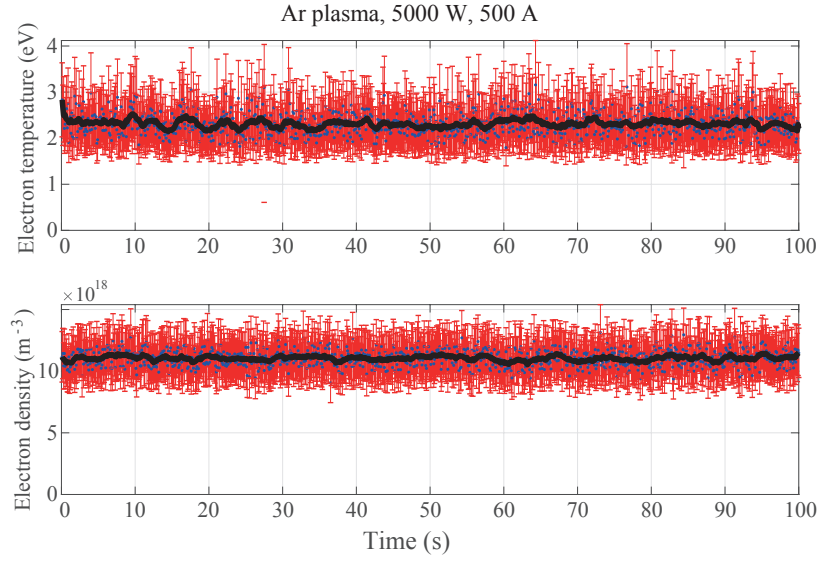
Figure 6.9 – Time resolved T_e and n_e in the plasma column center (spatial resolution of 16 mm) over 100 s, corresponding to 1000 laser shots. The blue spots are the measurements for each laser pulse, the red lines are the error bars on the single measurements and the black line is the moving average over 15 laser pulses.
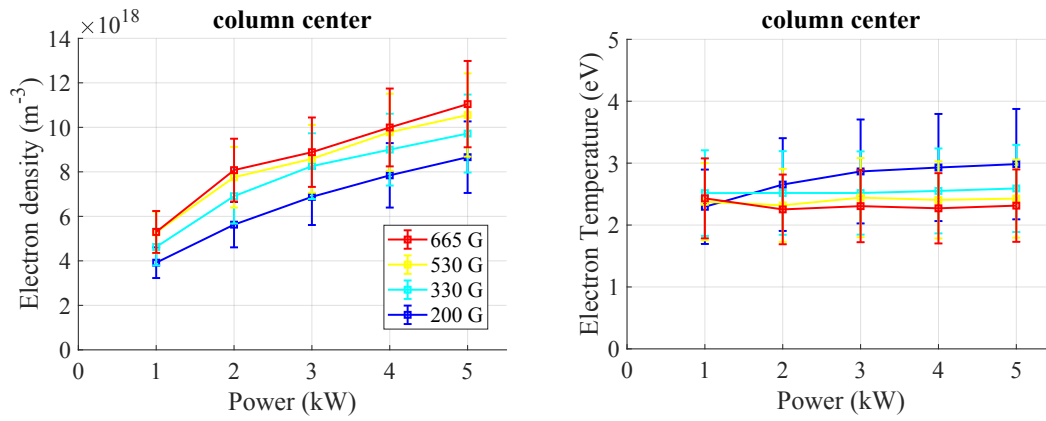
Figure 6.10 – Electron density and temperature as a function of RF power for different magnetic fields in the center of the plasma column measured by TS diagnostic. The spatial resolution is 16 mm along the vertical direction.

vertical direction. For each position, a Raman calibration was performed (and stray + leakage light measurements); this required filling the vessel with nitrogen and then pumping to the base pressure for plasma measurements.

Fig. 6.11 shows the radial electron density and temperature profiles of the plasma from -50 mm (below the center) to 40 mm above the center. These measurements were performed from 1 to 5 kW of power in 1 kW steps, and for four values of magnetic fields. Electron density profiles show a hollow profile when the magnetic field is $\lesssim 500\,\text{G}$, while the small peak at B = 665 G at 5 kW is the effect of the presence of the blue core. Electron temperature profiles are always quite flat and lie between 2 and 3 eV. The electron temperature profiles measured in RAID look comparable to measurements performed in proto-MPEX by double Langmuir probes and a Thomson Scattering system, showing a roughly flat T_e profile in the center of the plasma column [113, 58]. The double peak profile for n_e and T_e in Fig. 6.11 for low magnetic fields, $B = 200\,\text{G}$ and $B = 330\,\text{G}$, may be a hint of neutral depletion. The presence of hollow profiles consequently triggered the development of a LIF system in RAID with the aim of measuring the absolute density of a metastable state of neutral helium atoms. Another process which could be invoked to justify the double peak may be the power dissipation mechanism of the helicon waves along the plasma column. Evidence of the propagation of a helicon wave was measured in RAID by a B-dot probe [77]. Numerical simulations are currently underway to investigate how the helicon wave power produced by the birdcage antenna is transferred to the plasma, depending on gas pressure, electron density and boundary conditions.

The measurements performed in RAID demonstrate that the current TS set up can be successfully employed to measure n_e down to $4 \times 10^{18}\,\text{m}^{-3}$ and T_e down to 2 eV in a plasma column sustained by helicon waves. In Sec. 6.6, we discuss the physics and technical constraints of a TS diagnostic in AWAKE concerning the scattering regime and a first schematic design.

6.4.1 Cross check of TS results with mw-interferometry

To cross check the TS results for n_e we employed a combination of a LP and microwave interferometer which we have already detailed in Sec. 3 and we briefly review here. The interferometric set up is shown in Fig. 6.12: a microwave transmitter injects a microwave beam though the center of the plasma column and the receiver measures the phase shift due the presence of plasma. This is used to obtain the measurement of the line-integrated electron density. In parallel, the LP is used to measure plasma I_{sat} radial profile to estimate the approximate n_e FWHM of the plasma column. The LP tip (8 mm length and 0.4 mm diameter) rapidly passes (< 1 s) through the center of the plasma, measuring I_{sat}, which is approximately proportional to the electron density. Indeed, owing to the high electron density, the LP cannot measure current-voltage (I/V) characteristics, due to excessive thermal flux.

Fig. 6.13 shows the I_{sat} profiles when the probe is biased at $V_{bias} = -27\,\text{V}$ for different RF powers and magnetic fields. Note the effect of the magnetic field steepening and shrinking the plasma column, which is also visible in TS n_e profiles in Fig. 6.11. We also remark that the relative magnitude of the I_{sat} plateaux compared between different powers appears consistent
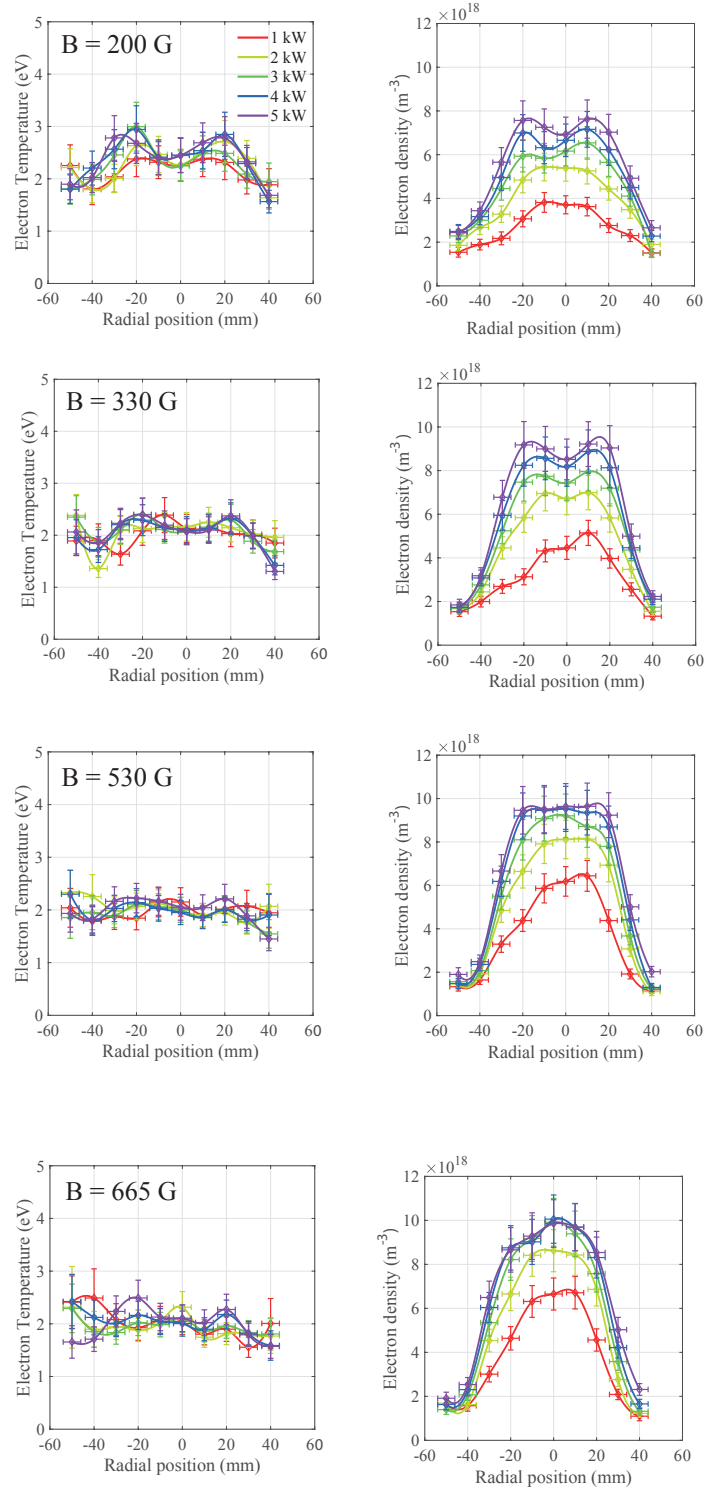
Figure 6.11 – Electron temperature (left column) and density profiles (right column) in a steady state Ar plasma at 0.3 Pa measured by the Thomson Scattering diagnostic (spatial resolution 8 mm). Starting from the top row B = 200, 330, 530 and 665 G. Data points are interpolated with cubic splines.
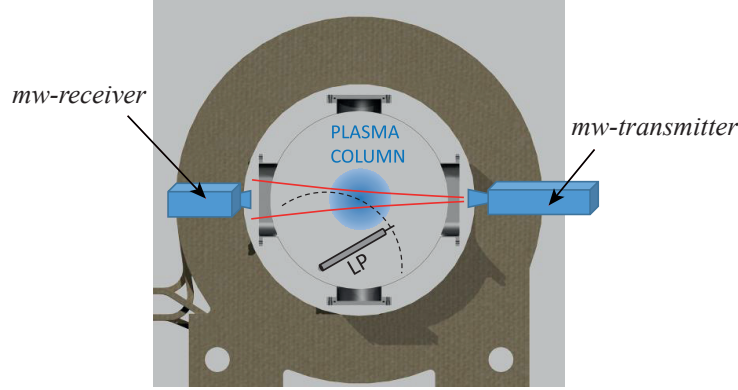
Figure 6.12 – Schematic showing the microwave interferometer (mw) modules and the LP. The mw-transmitter shines a microwave beam through the center of the plasma column (the red lines show the mw beam envelope). The LP describes an arc passing through the center of the column to determine the plasma column density radial profile.
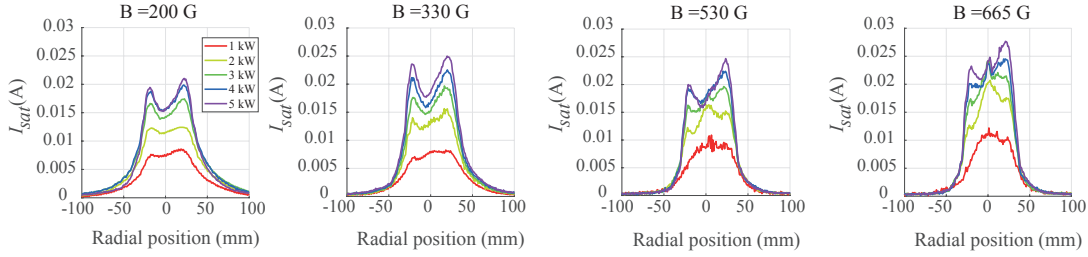
Figure 6.13 – I_{sat} radial profile of the Ar plasma column when the LP is biased at -27 V. By increasing the magnetic field, the plasma column becomes sharper. These profiles are used to estimate the FWHM of the column and so the length over which the line integrated density measured by the interferometer is averaged.

with the TS measurements in Fig. 6.11. The FWHM in the radial direction of the plasma column is estimated by using these profiles. This, in turn, determines the length over which the line integrated density by the microwave interferometry is averaged. We note that the shape of the TS n_e profiles look like LP I_{sat} profiles, the difference in shape might be due to the convolution effect of the TS measurements over 8 mm. The presence of hollow profiles of n_e and T_e might be due to a combination of different effects such as the local topology of the helicon wave depositing its energy into the plasma and the neutral depletion preventing further ionization in the plasma core. Fig. 6.14 compares the results for $\langle n_e \rangle$ measured by microwave interferometry and TS with same plasma conditions in the center of the plasma column. The two techniques result in comparable values of electron density, within ~ 20%. The comparison of T_e with LP would require to perform I/V sweeps, but this is not possible in this plasma due to the high density and the non negligible electron magnetization.
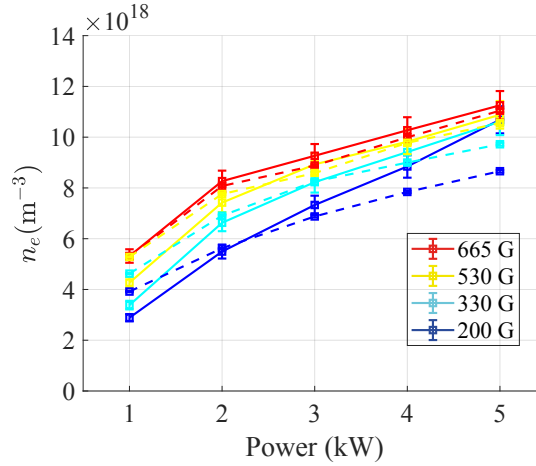
Figure 6.14 – Line-averaged n_e measured by interferometry (solid lines) and n_e measured by TS (dashed lines) from Fig. 6.10, in the center of the plasma column.

6.5 Effect of gas pressure and other gases (hydrogen, deuterium and helium)

Fig. 6.15 shows the electron density (left column) and electron temperature (right column) measured by Thomson scattering for Ar and He as a function of gas pressure for 3kW RF power and 200 G magnetic field. The electron density in argon peaks at ~ 0.7 Pa. By increasing the gas pressure, more gas is available for ionization, but, the helicon wave damping also increases. This may justify the presence of this peak. The electron temperature decreases monotonically due to an increase of collisions with neutral gas molecules requiring lower T_e to maintain ionization [89]. TS was also an opportunity to cross check the measurements of electron density and temperature in H_2 and D_2 in the center of the plasma column. Fig. 6.16 shows the electron density (on the left) and the electron temperature (on the right) as a function of the RF power, in standard conditions. n_e increases linearly with power up to 8kW the highest power reached by the birdcage antenna with the "conventional" capacitors. Operation of the birdcage antenna at larger powers (up to 10 kW) needed more robust mica capacitors. Electron density measurements with TS are, at least for H_2, in good agreement with LP-interferometric measurements shown in Fig. 3.12. Electron temperature values measured with TS, are $\sim 30\,\%$ less that those estimated with LP. TS measures in H_2 and D_2 plasma are however in general characterized by large error bars due to the poor signal-to-noise ratio.

Finally, Fig. 6.17 compares the electron density and temperature in the center of the plasma column for different plasma species (H_2, D_2, He and Ar) with 5 kW RF power, 200 G magnetic field and 0.3 Pa gas pressure. Despite the large error bars for H_2, D_2 and He, we remark that Ar reaches the highest density, and He the highest electron temperature.
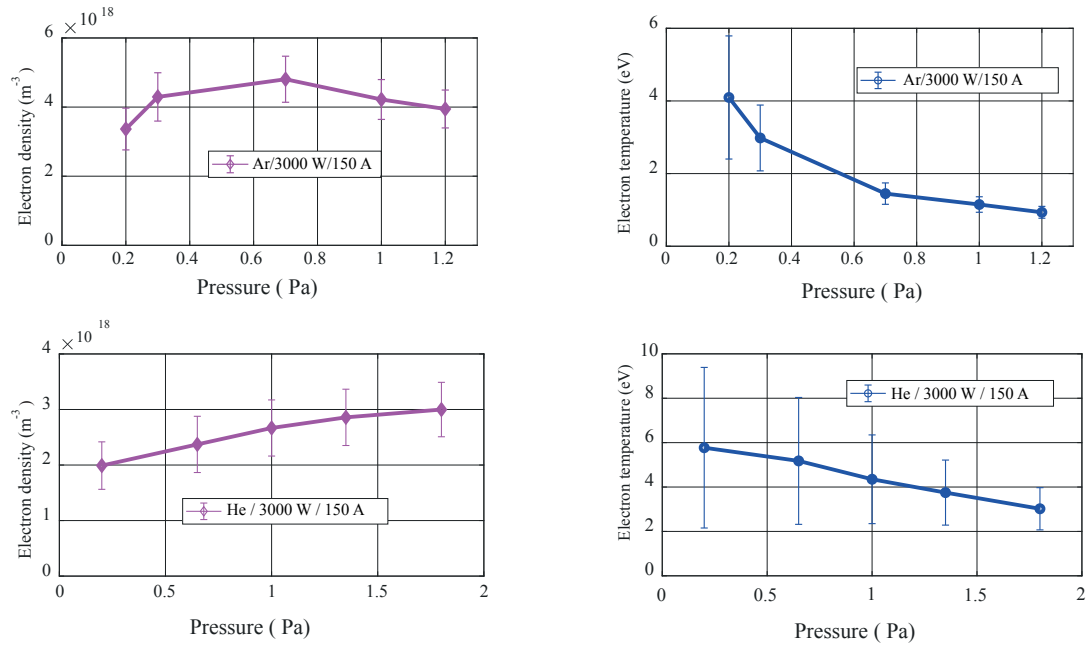
Figure 6.15 – Electron density (left column) and electron temperature (right column) measured by Thomson scattering for Ar and He as a function of gas pressure.
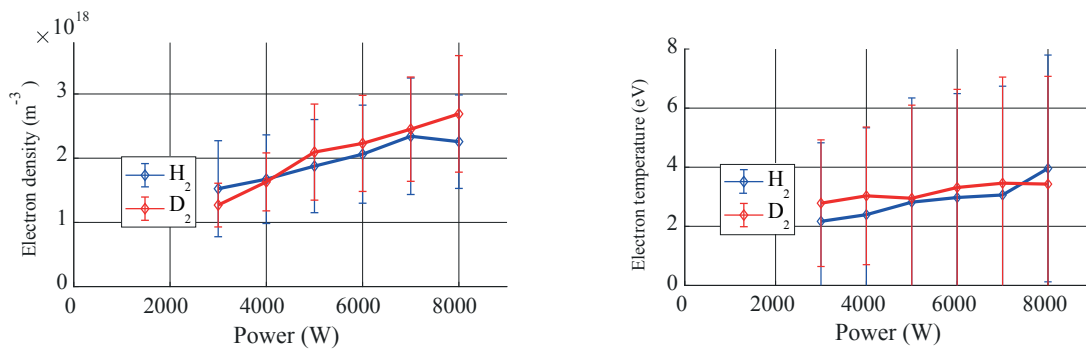
Figure 6.16 – Electron density and electron temperature measured by Thomson scattering for H_2 and D_2 as a function of RF power.
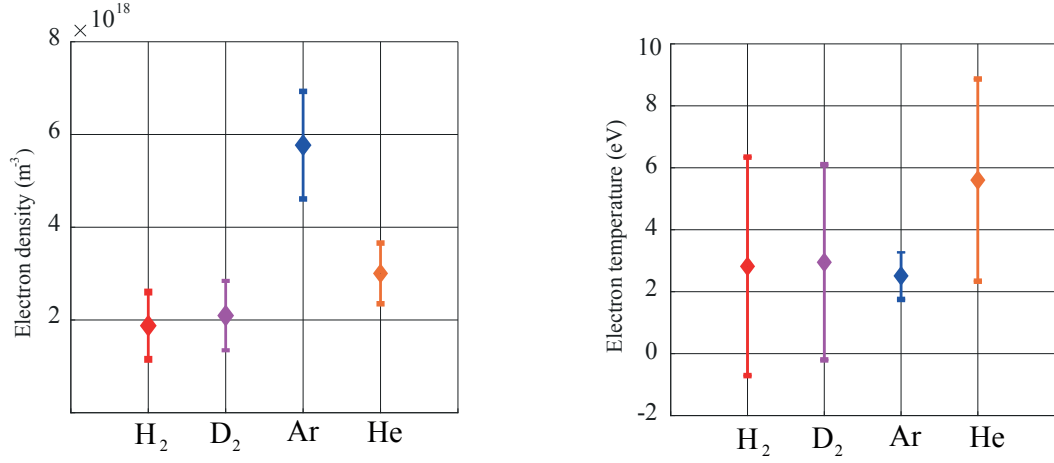
Figure 6.17 – Comparison of the electron density and electron temperature measured by Thomson scattering in the plasma center for different gases: H_2, D_2, Ar and He, for 5 kW power and 0.3 Pa gas pressure.

6.6 Consideration of a Thomson Scattering system in AWAKE

In this section, we study the TS in AWAKE, including physics and technical constraints. One main issue concerning the application of the TS apparatus developed on RAID to AWAKE is the range of validity of the incoherent scattering theory assumed for the RAID measurements. This is discussed in the following with a brief review of TS theory in coherent and incoherent regimes.

TS describes the interaction of plasma free electrons with low energy photons ($h\nu \ll m_e c^2$). As described in Sec. 6.2, when the wavelength of the exciting radiation is comparable to the Debye length, all electrons in the sphere will oscillate coherently in phase, and the scattering will be coherent. In the opposite case, the electrons oscillate independently and the scattering is incoherent. In this case, T_e can be estimated by the width of the distribution of scattered photons. Otherwise, the shape of the electron spectral distribution function $S(k,\omega)$ has to be known to determine T_e and n_e. The parameter α, also known as the *Salpeter parameter* [116], determines whether the scattering regime is incoherent ($\alpha \ll 1$) or coherent ($\alpha \gtrsim 1$):

$$\alpha = \frac{\lambda_L}{4\pi \lambda_D \sin\frac{\theta}{2}}, \tag{6.16}$$

In Fig. 6.18, we show the α parameter for $\lambda = 1064\,\text{nm}$ (Nd:YAG laser wavelength) and $\theta = 90°$ as a function of n_e and T_e. There are two expected working regimes for AWAKE: the high density regime when $n_e = 7 \times 10^{20}\,\text{m}^{-3}$, and the low density regime, for which $n_e = 2 \times 10^{20}\,\text{m}^{-3}$. They are indicated in Fig. 6.18. The electron temperature can vary typically between 1.5 and 2.5 eV, according to global particle and power balance simulations [27]. If we assume $T_e = 2\,\text{eV}$
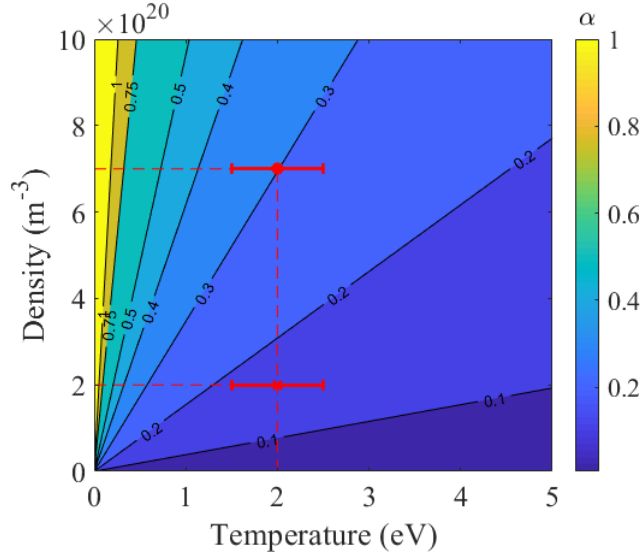
Figure 6.18 – The α parameter for $T_e = 2\,(\pm 0.5)$ eV and two n_e regimes with theta = 90 degrees. The target regime for AWAKE density is $n_e = 7 \times 10^{20}\,\mathrm{m}^{-3}$ (red dot) resulting in $\alpha = 0.30$. The lower density regime is at $n_e = 2 \times 10^{20}\,\mathrm{m}^{-3}$ (red cross) resulting in $\alpha = 0.16$. For this last regime the current system can be employed with a 3.5% error for n_e estimate.

as an average value, α is 0.30 and 0.16 for the high and low density regime, respectively. This suggests that collective effects begin to appear in the TS spectrum and thus the coherent scattering has to be taken into account to correctly estimate n_e and T_e. When α increases, emission spectra are deformed with respect to the Gaussian emission spectra previously described, and this has to be taken into account in the estimate of the error. Because of the very different masses between electrons and ions, Salpeter [116] demonstrated that the expression for the spectral density function $S(\vec{k}, \omega)$ can be separated into an a electron term and an ion term:

$$S(\vec{k},\omega)\,d\omega = \Gamma_\alpha\,dx_e + Z\left(\frac{\alpha^2}{1+\alpha^2}\right)\Gamma_\beta(x_i)\,dx_i, \qquad (6.17)$$

where:

$$x_e = \frac{\omega}{kv_e}, x_i = \frac{\omega}{kv_i}, \tag{6.18}$$

$$\Gamma_\alpha(x_e) = \frac{e^{-x_e^2}}{|1 + \alpha^2 W(x_e)|^2 \pi^{1/2}}, \tag{6.19}$$

$$\Gamma_\beta(x_i) = \frac{e^{-x_i^2}}{|1 + \beta^2 W(x_i)|^2 \pi^{1/2}}, \tag{6.20}$$

$$\beta^2 = Z \frac{\alpha^2}{1 + \alpha^2} \frac{T_e}{T_i}, \tag{6.21}$$

$$W(x) = 1 - 2xe^{-x^2} \int_0^2 e^{P^2} dP - i\pi^{1/2} xe^{-x^2}, \tag{6.22}$$

and ω is the frequency shift with respect to λ_L, x can be x_e or x_i, Z is the atomic number, v_e

and v_i are the thermal electron and ion speeds, respectively. $\Gamma_\alpha(x_e)$, known as the "electron feature", only depends on the α parameter. $\Gamma_\beta(x_i)$, the "ion feature", depends both on ion and electron temperature. When $\alpha \ll 1$ the spectral density function almost coincides with the electron one. In the transition region ($0.1 < \alpha < 1$) the shape of the spectrum depends both on electron and ions. The total contribution to the scattered photons is given by integrating Eq. 6.17 over ω. As α increases, $\Gamma_\alpha(x_e)$ flattens and two satellite peaks start to appear when $\alpha > 1$. At the same time the central peak due to ion contribution $\Gamma_\beta(x_i)$ increases [96]. The total spectral density function is then given by:

$$\int_\omega S(\vec{k}, \omega) \frac{d\omega}{2\pi} = S_e(\vec{k}) + S_i(\vec{k}); \tag{6.23}$$

where:

$$S_e(\vec{k}) = \frac{1}{1 + \alpha}; \qquad S_i(\vec{k}) = \frac{Z\alpha^4}{(1 + \alpha^2)\left[(1 + \alpha^2 + Z\left(\frac{T_e}{T_i}\right)\alpha^2\right]}. \tag{6.24}$$

Since the ion spectral function is very narrow compared to the electron one, $S_i(\vec{k}, \omega)$ has a very weak influence on the width of the total spectral function which is then dominated by the electron contribution. In the transition range ($0.1 < \alpha < 1$), the electron spectral function is no longer a Gaussian distribution. In Ref. [30] of a TS system in a tokamak, authors estimate that for $\alpha < 0.8$ a 20% error is made by neglecting the collective effect when fitting the data.

For application in AWAKE, we want to study the effect of varying the α parameter on the measured ratio F_2/F_1. Fig. 6.19 (a) shows the evolution of the electron emission spectrum when α is varied from 0 to 1, when $T_e = 2$ eV. As α increases, S_e flattens and broadens and more light is collected by filter 2. Fig. 6.19 (b) shows the ratios as a function of the electron temperature for different values of α. For a given value of the ratio, the "real" temperature decreases as α increases. Thus, the current TS system overestimates the temperature measurements. Concerning the error on the electron density, we tend to underestimate it since the integrated emission spectrum decreases. In Ref. [74] it is stated that the quantity of scattered photons decreases by a factor $\frac{1}{1+\alpha^2}$. In the case of RAID, $\alpha = 0.03$, resulting in an error on T_e due to the coherent scattering $< 0.2\%$, so, negligible compared to the typical error on the
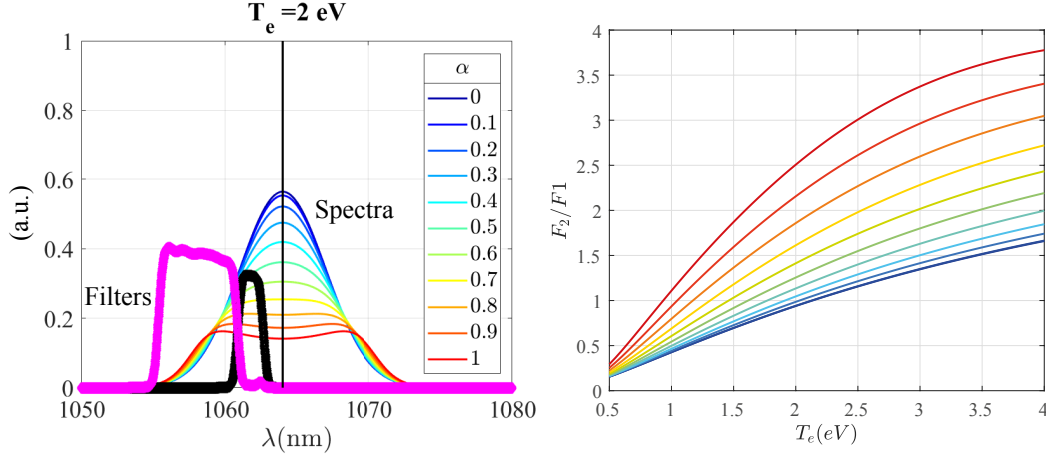
Figure 6.19 – (a) Broadening of the electron emission spectrum due to the increasing effect of the coherent regime, for a fixed electron temperature of 2 eV. (b) Ratio of filter signals as a function of electron temperature by varying the α parameter.

Scenario	$n_e(\times 10^{20}\mathrm{m}^{-3})$	T_e (eV)	α	$(\delta T_e/T_e)_{coher.}$	$\delta(n_e/n_e)_{coher}$	$\delta(\Delta n_e)/\Delta n_e$
RAID	0.11	2.3	0.03	0.2%	0.09%	0.12%
AWAKE low	2.0	2	0.16	1%	2.5%	3.5%
AWAKE high	7.0	2	0.30	3.3%	10.9%	15%

Table 6.1 – Estimates of errors due to the partially coherent scattering regimes in different scenarios.

single measurement. For the low density AWAKE regime, for which $\alpha = 0.16$, the contribution to the total error due to the partially coherent scattering regime would be $\sim 1\%$ on T_e and $\sim 2.5\%$ on n_e. Therefore, when comparing two density points, this results in $\sim 3.5\%$ base uncertainty. For the high density AWAKE regime, for which $\alpha = 0.30$, this value increases to $\sim 15\%$. Tab. 6.1 summarizes the discussed scenarios showing the contribution to the error coming from the partially coherent scattering regime.

6.7   Future development of the Thomson Scattering system

To reduce the coherent emission, one possibility is to decrease the laser wavelength, which in turn decreases α. The laser used on RAID can operate with 4ω (266nm), 10 Hz repetition rate and 90 mJ energy per pulse. At this wavelength, the "worst condition" for AWAKE makes α drop to 0.1. In this scattering regime, S_e is 99.7% of the total emission spectrum.
Concerning the practical implementation of the polychromator system, this would require, firstly, more narrow bandwidth filters than those for 1064 nm. Fig. 6.20 shows the emission spectrum for laser wavelength of 266 nm. The spectrum width at $T_e = 1$ eV is about 1 nm, thus filters with a much narrower bandwidth are required. To increase the accuracy of the
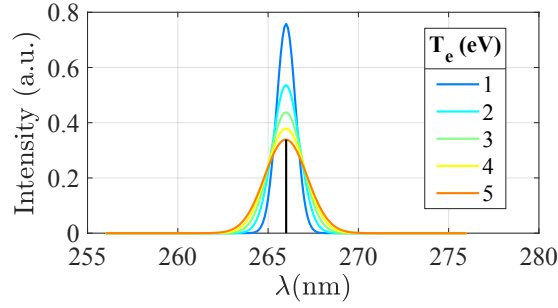
Figure 6.20 – Emission spectrum for $\lambda_L = 266\,\mathrm{nm}$ (black line) and different electron temperatures showing that for these parameters, a filter widths of the order of half nm are required.

measurements more than two filters should be used. Although reducing the wavelength to 266 nm would be very effective to minimize α, the practical implementation is cumbersome since it requires the use of ultraviolet filters and grating which are not easily available and expensive. An alternative way to measure T_e and n_e would consist of measuring the entire scattered spectrum, to deduce the scattering regime. A Thomson scattering diagnostic with a ICCD camera was successfully installed in a linear steady state plasmas [86]. To upgrade the current TS system in RAID, a system based on a high resolution grating and a high resolution CCD camera for acquisition is envisaged. The measurement of the entire spectrum would also allow to detect the presence of electron populations with different temperatures. Since CCD cameras are much more sensitive in the visible regime, a frequency-doubled YAG would be required. The use of a CCD camera to measure the entire spectrum is currently envisaged for the next improvement step for the TS in RAID.

In parallel with this, the design and machining of laser beam diaphragms to reduce the level of stray light, is currently under way. Fig. 6.21 shows the design of the two laser beam array of diaphragms and their positioning in TS extension tubes. Similar sets of diaphragms should also be considered for the TS on AWAKE.

6.8 Preliminary design of a Thomson Scattering system in AWAKE

A preliminary schematic design of a TS diagnostic for AWAKE is shown in Fig. 6.22. The laser beam is injected along the axis to perform multiple measurements along the entire plasma axis. This requires a lens system able to position the laser beam waist along the axis. The collection optics could be installed on a translation stage to perform axial scans. The already existing two view ports could be used to compare the density at two axial positions. In the case of a helicon cell with a length comparable to the Rb vapor source ($\sim 10\,\mathrm{m}$), the positioning of the laser beam waist may be more difficult, requiring remote controlled focusing. The experience acquired with RAID suggests that diaphragms are necessary to strongly reduce the level of stray light caused by multiple reflection in the vessel. Therefore, two sets of five diaphragms at each side of the plasma cell are envisaged. Moreover, to avoid stray light diffusion from the laser beam path outside the cell, the laser beam path should be enclosed. The current

155
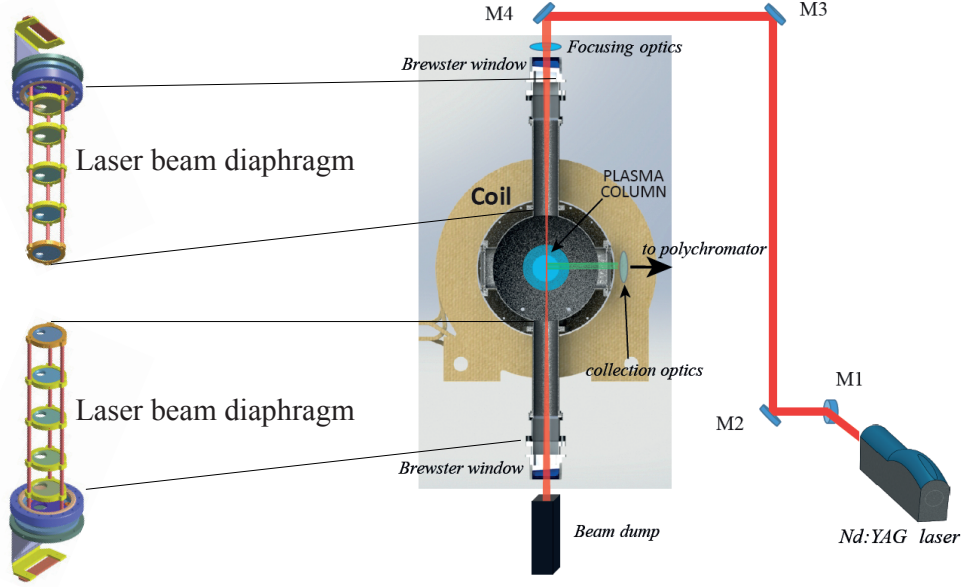
Figure 6.21 – Schematic of the couple of array of beam diaphragms to reduce the stray light designed for the upgrade of the TS system on RAID.

TS system in RAID based on polychromators allows to detect an electron temperature down to ~ 1.5 eV; lower temperature would be difficult to detect because of the emission spectrum would be too narrow compared to filters. If this would be the case for AWAKE, more narrow filters would be required. Alternatively, a different system to acquire the scattered light should be implemented.

As a further improvement step, the knowledge of the shape of the entire electron emission spectrum would allow a measurement of n_e and T_e. If the AWAKE plasma discharge pulse is reproducible one could rely on statistics and collect a sufficient number of photons to have a S_e with an acceptable signal-to-noise ratio. This would require to phase lock the laser with the plasma discharge pulse. By doing some technical adaptations, the current system could in principle be used in AWAKE to perform TS measurements with a contribution to the error coming from the partially coherent scattering regime of ~ 1% on T_e and ~ 2.5% on n_e at a single measurement location.

6.9 Conclusions

We have installed and successfully tested a Thomson Scattering diagnostic on RAID, as a testbench for AWAKE. We verified that the current system measures electron temperature down to 2 eV and the electron density down to $4 \times 10^{18}\,\mathrm{m}^{-3}$. The present TS diagnostic requires a relative calibration of polychromator filters to measure T_e and a *in-situ* Raman calibration to determine n_e. The results in RAID show an electron density $n_e = 1.10 \times 10^{19}\,\mathrm{m}^{-3}$ and electron temperature of $T_e = 2.3\,\mathrm{eV}$ in the center of an Ar plasma discharge with 5 kW RF
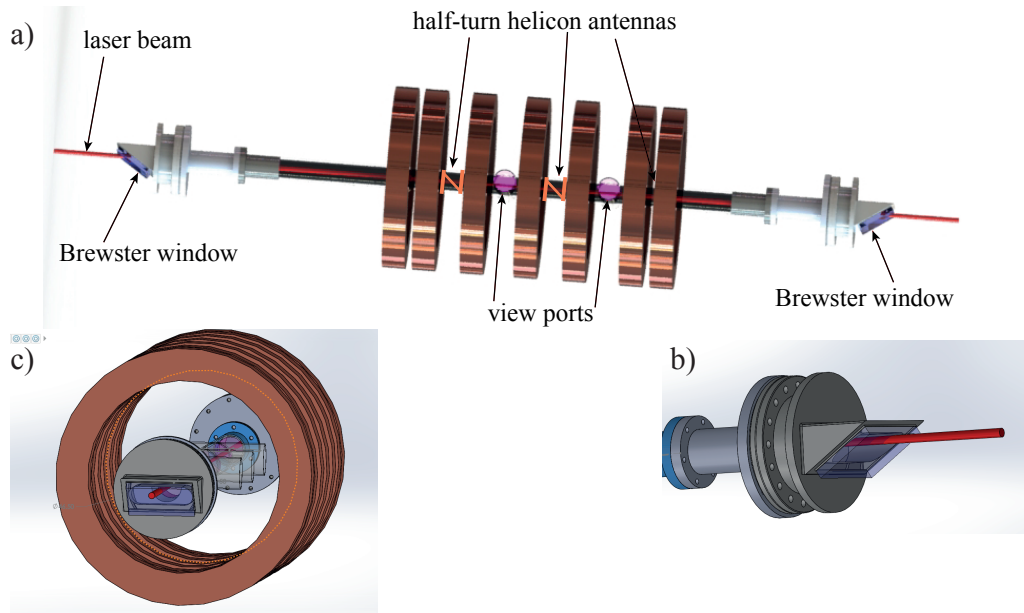
Figure 6.22 – Schematic design of a Thomson scattering diagnostic for AWAKE helicon source: (a) Side view of the AWAKE helicon cell showing the position of the three helicon antennas and the viewports for TS light collection. (b) View along the axis showing the distance between the vacuum tube and the coils. (c) Detail of the Brewster window.

power. Microwave interferometry and LP measurements are used to cross-check TS results, showing good agreement. We performed radial profiles measurements, showing the effect of the magnetic field.

We presented some preliminary calculations to apply the current TS diagnostic for AWAKE plasma regimes. In AWAKE, the α parameter, determining the scattering regime, lies in a transition region where the coherent contribution to the scattering signal cannot be neglected. Finally, we outlined a preliminary schematic design of a TS diagnostic for the AWAKE helicon plasma cell.

7 Hydrogen plasma modeling

Numerical simulations of plasma chemistry and transport are an important tool to understand fundamental plasma processes and to cross check with experimental results. As in many other basic plasma devices, we have initiated a model describing plasma transport in RAID. This is motivated by the fact that plasma diagnostics are usually lengthy to set up, not all plasma species are easy to measure, and numerical simulations can contribute to make predictions and drive source optimization. In this chapter, we develop a model describing the transport in RAID hydrogen plasmas, based on the solution of the transport equations of a complete set of plasma hydrogen species in a cold magnetized plasma column. The cylindrical symmetry of RAID is also particularly advantageous in simplifying the model in terms of formulation and computational time. The model is developed using the PDE (Partial Differential Equation) module of COMSOL Multiphysics and is able to calculate the equilibrium profiles of the different plasma species including hydrogen ions and neutrals. We describe the mathematical formulations, the plasma reactions, the boundary conditions and we compare the calculations to experimental results, including the negative ions profiles.

7.1   Hydrogen plasma transport model for RAID

A major motivation for the development of the transport plasma model is to verify the presence of the negative ion ring measured with laser-based diagnostics, discussed in Sec. 4. In the literature, some authors developed 0D models to predict the volume H^- density by simple balance equations in hydrogen plasma such as in [57, 14, 37]. These formulations try to explain the H^- density by correlation with a few plasma parameters such as the electron and the neutral density. These so-called *global* models are used to predict the H^- production and optimize the negative ion sources for fusion. Nowadays these models contain a detailed set of chemical reactions in hydrogen plasmas [70, 148]. Although very exhaustive in including many reactions describing the hydrogen plasma chemistry, these approaches do not take into account the transport and the source geometry. On the other hand, there are complex self-consistent 3D models which consider the transport of all plasma species together with chemistry. An important effort is indeed devoted to model the transport and the extraction of

negative ions in RF sources for fusion [50, 64]. These numerical simulations consider large plasma volumes and rely on sophisticated PIC models including turbulence, making them highly computationally demanding.

In the case of RAID, we decided to adopt a compromise between the requirement to model the plasma transport still being able to perform simulations with a desktop PC in a reasonable time. In Sec. 7.1.1, we provide the mathematical description of the RAID hydrogen plasma model. The plasma is described as a collisional magnetized fluid and transport equations are solved for heavy species. The goal of this model is to predict the equilibrium profiles of different plasma species such as H^+, H_2^+, H_3^+, H^- and H, which are difficult to measure, and to study the effect of changing the input parameters for the source optimization. The electron density n_e, electron temperature T_e, ion temperature T_i, neutral temperature T and the molecular hydrogen density n_{H_2} and the radial plasma potential are the input parameters. The model takes into account the chemical reactions occurring in a hydrogen plasma and the transport of different plasma species in the magnetic field produced by RAID in standard conditions. The main advantage of this approach is that by introducing the volume profiles of n_e and T_e, available from experimental measurements, a power deposition profile regulating the ionization is not required.

7.1.1 Description of the transport model

In kinetic theory, the Boltzmann transport equation usually describes the evolution of the velocity distribution function $f(\vec{r}, \vec{v}, t)$ of plasma particles with mass m [34]:

$$\frac{\partial f}{\partial t} + \vec{v} \cdot \nabla_{\vec{r}} f + \frac{\vec{F}}{m} \cdot \nabla_{\vec{v}} f = \left. \frac{\partial f}{\partial t} \right|_c , \tag{7.1}$$

where $\vec{v}$ is the particle velocity, $\vec{F}$ is the force acting on the plasma particle, $\left. \frac{\partial f}{\partial t} \right|_c$ is the time rate of change of f due to collisions, and $\nabla_{\vec{r}}$ and $\nabla_{\vec{v}}$ are the gradient in the x, y, z space and in the velocity space, respectively. In the absence of collisions, the collision term is set to zero and the equation is called *Vlasov equation*.

The direct resolution of Eq. 7.1 is usually computationally complex. To simplify the description of the system, we assume that the particles of a certain species are in thermodynamic equilibrium and therefore the distribution function f is described by a Maxwellian distribution. In RAID, this is supported by the fact that the plasma particle collisionality assures the thermodynamic equilibrium and the plasma dynamics can be satisfactory described by a fluid approach. The fluid model can be applied provided that the collision mfp (mean free path) is smaller than the typical size of the device. Typical RAID plasma parameters are summarized in Tab. 7.1. Since the plasma is magnetized, the step-size for ion-H_2 collision, in the direction transverse to the magnetic field, is approximately of the order of the Larmor radius, about 1 mm for the ions, much smaller that the vessel radius ($R = 0.2$ m). Along the axial direction, however, because of the free-streaming along the magnetic field, the step-size for ion-H_2

Parameter	Value
f_{ci}	$\approx 300\,\text{kHz}$ ($B = 20\,\text{mT}$)
f_{ce}	$\approx 560\,\text{MHz}$
$\nu_{i\text{H}_2} \approx n_i \sigma_{i,\text{H}_2} v_{th,i}$	$\lesssim 4\,\text{kHz}$
$\nu_{e\text{H}_2} \approx n_i \sigma_{e,\text{H}_2} v_{th,e}$	$\approx 1\,\text{MHz}$
$\nu_{ee} = e^4 ln\Lambda n_e Z^2 / [3(2\pi)^{3/2} \epsilon_0^2 \sqrt{m_e} T_e^{3/2}]$	$\approx 80\,\text{kHz}$
$\lambda_{mfp,\text{H}_2} = v_{th,i}/\nu_{i\text{H}_2}$	$\sim 0.1\,\text{m}$
$\rho_i = v_{th,i}/(2\pi f_{ci})$	$\lesssim 1\,\text{mm}$
$\rho_e = v_{th,e}/(2\pi f_{ce})$	$\lesssim 0.25\,\text{mm}$

Table 7.1 – RAID plasma parameters.

collision is given by $v_{th,i}/\nu_{i,\text{H}_2} \sim 10\,\text{cm}$, also smaller that the RAID length (2 m).

By integrating Eq. 7.1 over the velocity space dv^3, the continuity equation is obtained:

$$\frac{\partial n_s}{\partial t} + \nabla \cdot (n_s \vec{u}) = S_s - L_s, \tag{7.2}$$

where $\vec{u}$ is the fluid element velocity, S_s the source term and L_s the loss term, which, in our scenario, depend of the chemical reactions occurring in the plasma. Eq. 7.2 is also known as the *zeroth* moment of Boltzmann equation. We now consider that the force acting on charged particles is the Lorentz force $\vec{F} = q(\vec{E} + \vec{v} \times \vec{B})$, where $\vec{E}$ and $\vec{B}$ are the electric and magnetic fields. By multiplying Eq. 7.2 by $m\vec{u}$ and integrating over the velocity space, we obtain the momentum conservation equation (or fluid equation of motion):

$$mn\left[\frac{\partial \vec{u}}{\partial t} + (\vec{u} \cdot \nabla)\vec{u}\right] = qn(\vec{E} + \vec{u} \times \vec{B}) - \nabla \cdot \bar{\bar{P}} + P_{ij}, \tag{7.3}$$

where $\bar{\bar{P}}$ is the species' pressure tensor and P_{ij} the change of momentum due to collisions. A number of assumptions can be considered in the case of RAID plasma. First, we consider the system to be in steady-state, therefore the acceleration term vanishes. We also neglect the inertia i.e. $\frac{|mn(\vec{u}\cdot\nabla)\vec{u}|}{|qn(\vec{E}+\vec{u}\times\vec{B})|} \ll 1$. Second, we assume that the collisional term P_{ij} can be written as: $-mn\nu_s\vec{u}$, where ν_s is the momentum transfer collision frequency. Third, we neglect the the viscosity and the temperature gradients so that the pressure tensor can be expressed as follows: $\nabla \cdot \bar{\bar{P}} = \nabla p = kT\nabla n$.

Defining the particle flux as $\vec{\Gamma} = n\vec{u}$, the momentum conservation equation reads:

$$-m_s\nu_s\vec{\Gamma} + q_s n_s\vec{E} + q_s\vec{\Gamma} \times \vec{B} - k_b T_s\overrightarrow{\nabla n} = 0. \tag{7.4}$$

In the following, it is useful to define the cyclotron frequencies $\omega_{c,x}$, $\omega_{c,y}$, $\omega_{c,z}$, associated with each space direction:

$$\omega_{c,x} = \frac{q_s B_x}{m_s}, \qquad \omega_{c,y} = \frac{q_s B_y}{m_s}, \qquad \omega_{c,z} = \frac{q_s B_z}{m_s}, \qquad (7.5)$$

and also $\omega_{c,r}$ as: $\omega_{c,r}^2 = \omega_{c,x}^2 + \omega_{c,y}^2$. By rearranging Eq. 7.4, it can be shown that $\vec{\Gamma}$ is proportional to $\vec{E}$ and $\overrightarrow{\nabla n}$ through a matrix $\bar{\bar{\sigma}}$, and a numerical coefficient α:

$$\vec{\Gamma} = \bar{\bar{\sigma}}(\vec{E} + \alpha \overrightarrow{\nabla n}), \qquad (7.6)$$

where $\alpha = \frac{n_s q_s}{k_b T_s}$, and $\bar{\bar{\sigma}}$ is:

$$\bar{\bar{\sigma}}_{x,y,z} = \frac{1}{v_s^2 + \omega_{c,x}^2 + \omega_{c,y}^2 + \omega_{c,z}^2} \begin{pmatrix} -(v_s^2 + \omega_{c,x}^2) & \omega_{c,x}\omega_{c,y} + v_s\omega_{c,z} & v_s\omega_{c,y} - \omega_{c,x}\omega_{c,y} \\ -\omega_{c,x}\omega_{c,y} + v_s\omega_{c,z} & -(v_s^2 + \omega_{c,y}^2) & -(v_s\omega_{c,x} - \omega_{c,y}\omega_{c,z}) \\ -(v_s\omega_{c,y} + \omega_{c,x}\omega_{c,z}) & v_s\omega_{c,x} - \omega_{c,y}\omega_{c,z} & -(v_s^2 + \omega_{c,z}^2) \end{pmatrix}.$$

$$(7.7)$$

We can now move to cylindrical coordinate system (r, θ, z), where r is the radial direction, θ the azimuthal angle and z the axial direction. By performing a rotation of the matrix $\bar{\bar{\sigma}}$, the components of Γ in the cylindrical coordinate system can be found. Moreover because of the plasma rotation symmetry, the matrix σ has to be rotational invariant. This condition is determined by imposing no electric field along the azimuthal direction, therefore $E_\theta = 0$. In cylindrical coordinates, the matrix $\bar{\bar{\sigma}}$ simplifies into:

$$\bar{\bar{\sigma}}_{r,\theta,z} = \begin{pmatrix} \frac{(\omega_{c,r}^2 + v_s^2)}{v_s} & \omega_{c,z} & \frac{\omega_{c,r}\omega_{c,z}}{v_s} \\ -\omega_{c,z} & v_s & \omega_{c,r} \\ \frac{\omega_{c,r}\omega_{c,z}}{v_s} & \omega_{c,r} & \frac{(v_s^2 + \omega_{c,z}^2)}{v_s} \end{pmatrix}. \qquad (7.8)$$

The matrix $\sigma_{r,\theta,z}$ is necessary to express the components of $\vec{\Gamma}$ in cylindrical coordinates, Γ_r, Γ_θ and Γ_z, which are inserted as the flux term variables in the model. The PDE module solves the system of Eq. 7.2 and 7.4 with respect to $\vec{\Gamma}$ for each plasma species s, taking into account the source and loss reaction rate terms S_s and L_s due to chemical reactions in the plasma.
Note that when $\vec{B} = 0$ this implies that $\omega_{c,x} = \omega_{c,y} = \omega_{c,z} = 0$, and the off-axis terms are then zero; and therefore the diffusion is isotropic.

Collision processes

We consider that each species has a Maxwellian distribution and we do not consider the time dependence but only the steady state equilibrium profiles. The H_2 density is calculated

	H^+	H_2^+	H_3^+	H^-	H
$\sigma_{i,H_2}\,(\cdot 10^{-20}\,\mathrm{m}^2)$	4.5	28	33	23	23

Table 7.2 – Collision cross sections for collisions between ions and H with the background H_2 gas.

from the perfect gas equation of state ($p = nk_b T$) assuming 0.3 Pa gas pressure uniform and constant and in thermal equilibrium with the positive ions, and a gas temperature of $T \approx 900\,\mathrm{K}$ [94]. This results in a H_2 density ($\sim 2.4 \cdot 10^{19}\,\mathrm{m}^{-3}$) at least ~ 20 higher than the plasma density ($\sim 1 \cdot 10^{18}\,\mathrm{m}^{-3}$, in the center), which allows using constant and uniform background of H_2, without solving a balance equation for H_2. Therefore the system can be considered as composed by *diluted* plasma species. Although this may be true for RAID for low pressures ($\lesssim 1\,\mathrm{Pa}$) and RF powers ($P \lesssim 5\,\mathrm{kW}$), this does not hold for high power operations, where neutral depletion may occur. Since the species we are considering in the model are neutrals and ions diluted in a H_2 gas, we only take into account neutral-neutral collisions and charged-neutral collisions. The collision frequency between a given species and the background gas can be written in the form:

$$\nu_s = n_{H_2}\,\sigma_s\,\nu_{th,s}, \tag{7.9}$$

where ν_{th} is the thermal velocity of the species s:

$$\nu_{th} = \sqrt{\frac{k_b T_i}{M_i}}, \tag{7.10}$$

where we assume that all atomic and ion species are thermalized, so that $T_i = T_H = T_{H_2} \approx 0.1\,\mathrm{eV}$, and uniform in all the domain. The collisions between neutral species and H_2 are approximated by hard sphere collisions, and their numerical value is reported in Tab. 7.2 [118]. The collision cross sections are computed as:

$$\sigma_s = \pi(r_s^2 + r_{H_2}^2), \tag{7.11}$$

where r_s is the radius of the species s and r_{H_2} is the effective radius of H_2.

Boundary conditions

Plasma particles can be produced and lost both in the volume and on the reactor walls. We assume that all ion species reaching the wall are lost by surface recombination i.e. they pick
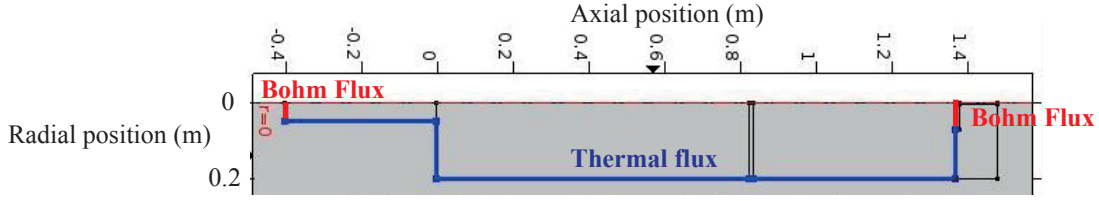
Figure 7.1 – Due to the strong axial magnetic field, positive ions (H$^+$, H$_2$$^+$ and H$_3$$^+$) are preferentially transported to the ends of the plasma column (red lines) where they are accelerated to the Bohm velocity. While diffusing across the magnetic field lines towards vessel side walls, positive ions are however thermalised by the gas.

up one electron and are then recycled into the plasma as neutrals keeping the background neutral pressure approximately constant.

Concerning the loss mechanisms of positive ions (H$^+$, H$_2$$^+$ and H$_3$$^+$) to the walls, we make a fundamental assumption depending on which part of the vessel they are lost. Because of the axial magnetic field, charged particles move preferentially along B field lines. This is expected to produce a quite important anisotropy on the ion transport and in equilibrium density profiles of positive ions. According to this argument, we separate the global wall losses into a loss flux along the axial and along the radial direction. We assume that ions impinging onto the extremities of the plasma column (marked by the red lines in Fig. 7.1), namely at the target and the antenna left side, are subject to free fall across the plasma sheath and are accelerated up to a speed given by the Bohm velocity $v_{B,s} = \sqrt{\frac{q_s T_e}{M_s}}$, where M_s is the ion mass, and assuming that $T_e \gg T_i$. The flux along the axial direction Γ for a positive ions, such as H$^+$, at the axial boundary is therefore:

$$\Gamma_{\text{H}^+}^{axial} = -n_{\text{H}^+}\sqrt{\frac{q_{\text{H}^+} T_e}{M_{\text{H}^+}}}. \tag{7.12}$$

The negative sign stems from the fact that ions are lost with respect to the vessel volume. In reality, this is actually the velocity at the end of pre-sheath, the minimal at which ions escape from the plasma.

The positive ions transported to the side walls of the vessel (marked by the blue contour in Fig. 7.1), diffuse across the magnetic field lines by performing multiple collisions and thermalising with the neutral gas of H$_2$. We assume that they are lost at thermal velocity $v_{th,\text{H}^+}^z = \sqrt{\frac{k_b T_{\text{H}^+}}{M_{\text{H}^+}}}$ and therefore the positive ion flux to the side walls is:

$$\Gamma_{\text{H}^+}^{radial} = -n_{\text{H}^+}\sqrt{\frac{k_b T_{\text{H}^+}}{M_{\text{H}^+}}}. \tag{7.13}$$

A more accurate estimate of the positive ion flux to the wall would require a detailed description of the plasma potential drop in the sheath region such as that described in Ref. [62], which

could be applied to the RAID plasma regime. However, this would require to restructure the current fluid model, and would add a degree of detail which goes beyond the scope of this model.

The H^- ion is however trapped into the plasma since the plasma potential acts like a potential well for them. The typical negative ion temperature $T_{H^-} \sim 0.1\,\text{eV}$ is far lower that the RAID typical plasma potential ($V_{plasma} = 12\,\text{V}$), measured by LPs and shown in Fig. 3.15. Thus, we assume zero flux of negative ions though the walls:

$$\Gamma_{H^-}^{wall} = 0. \tag{7.14}$$

Negative hydrogen ions are then produced and destroyed uniquely in the plasma volume. The atomic hydrogen H produced in the plasma volume, mostly by H_2 dissociation, not being affected by electromagnetic fields, diffuses to the wall at the thermal velocity. We therefore consider a thermal flux of H to all the vessel walls Γ_H:

$$\Gamma_H^{wall} = -n_H \sqrt{\frac{k_b T_H}{M_H}}. \tag{7.15}$$

H atom then sticks to the wall surface from which is then recycled into the plasma as a atom H or molecular H_2.

7.1.2 Plasma reactions

To determine the relative ratio between hydrogen plasma species, a large enough set of hydrogen plasma reactions has to be included in the model. In the plasma volume, ions and neutrals, when colliding, can change their molecular compositions and charge state. The source term S_s and the loss term L_s in Eq. 7.2 respectively take into account all possible processes that can produce or destroy a certain plasma species s, therefore:

$$S_s = \sum_i R_i \qquad \text{and} \qquad L_s = \sum_j R_j, \tag{7.16}$$

where R_i and R_j are the production and destruction reactions, respectively.

The source and loss terms $R_{i,j}$ for a certain species can be expressed as:

$$R_i = n_1 n_2 k_i, \tag{7.17}$$

where n_1 and n_2 are the density of reactant species and k_i the reaction rate coefficient. The rate coefficient is given by the convolution of the reaction cross section σ_i over the

particles energy distribution function $f(E, T)$:

$$k_i(T) = \int_0^\infty v(E)\sigma_i(E)f(E,T)dE.$$

(7.18)

We have initially used a set of 17 rate coefficients for hydrogen reactions rates given in Ref. [70] describing a mixture of argon and hydrogen plasma. However, the effect of the vibrational excitation on the dissociative attachment is not directly included and would have required 14 additional equations for each vibrational level of H_2. We have finally employed the list in Ref. [118] for the RAID model, containing 22 reaction rates in hydrogen and including the effect of the dissociative attachment through an "effective" reaction rate, which depends only on the equilibrium electron temperature. The list of hydrogen reactions with the respective reaction rates is given in Tab. 7.3.

The reaction rates are expressed in the Arrehnius form:

$$k(T) = A_1 T^{A_2} e^{\frac{A_3}{T+A_4}} + A_5 T^{A_6} e^{\frac{A_7}{T}},$$

(7.19)

where A_{1-7} are fit coefficients and T can be the electron, the ion or neutral temperature. Three body reactions are not considered here since their cross sections are negligible for the range of pressure considered (<1 Pa). By taking into account all the possible reactions of production and destruction for each species, we can express the source (and loss term) for each species, which are listed in Eq. 7.20.

$$
\begin{cases}
\begin{aligned}
\frac{\partial n_H}{\partial t} &= 2k_2 n_e n_{H_2} + k_3 n_e n_{H_2} - k_4 n_e n_H - k_5 n_{H_2^+} n_H + k_6 n_e n_{H_2^+} + k_8 n_{H_2} n_{H_2^+} + k_{10} n_{H_2^+} n_{H^-} + \\
&\quad + 3k_{11} n_H n_{H^-} + k_{12} n_e n_{H^-} + 2k_{13} n_e n_{H_3^+} + 2k_{15} n_e n_{H_2^+} + 3k_{16} n_e n_{H_3^+} + k_{17} n_e n_{H_3^+} + \\
&\quad - k_{18} n_H n_{H^-} + k_{19} n_{H_2} n_{H^-} + k_{20} n_H n_{H^-} + k_{21} n_{H_2} n_{H^+} - k_{22} n_e n_H, \\
\frac{\partial n_{H_2^+}}{\partial t} &= k_{11} n_e n_{H_2} - k_5 n_H n_{H_2^+} - k_6 n_e n_{H_2^+} + k_7 n_e n_{H_3^+} - k_8 n_{H_2} n_{H_2^+} - k_{10} n_{H_2^+} n_{H^-} - k_{15} n_e n_{H_2^+} + \\
&\quad + k_{21} n_{H_2} n_{H^+}, \\
\frac{\partial n_{H^-}}{\partial t} &= k_3 n_e n_{H_2} + k_7 n_e n_{H_2} - k_9 n_{H^+} n_{H^-} - k_{10} n_{H_2^+} n_{H^-} - k_{11} n_{H_3^+} n_{H^-} - k_{12} n_e n_{H^-} + \\
&\quad - k_{18} n_H n_{H^-} - k_{19} n_{H_2} n_{H^-} - k_{20} n_H n_{H^-} + k_{22} n_e n_H, \\
\frac{\partial n_{H^+}}{\partial t} &= k_4 n_e n_H + k_5 n_H n_{H_p^+} + k_6 n_e n_{H_2^+} - k_9 n_{H^+} n_{H^-} + k_{13} n_e n_{H_3^+} - k_{14} n_{H_2} n_H - k_{21} n_{H_2} n_{H^+}, \\
\frac{\partial n_{H_3^+}}{\partial t} &= -k_7 n_e n_{H_3^+} + k_8 n_{H_2} n_{H_2^+} - k_{11} n_{H_3^+} n_{H^-} - k_{13} n_e n_{H_3^+} + k_{14} n_{H_2} n_{H^+} - k_{16} n_e n_{H_3^+} + \\
&\quad - k_{17} n_e n_{H_3^+}.
\end{aligned}
\end{cases}
$$

(7.20)

	Reaction	Rate coefficient [$\mathrm{m^3s^{-1}}$]
1	$e + H_2 \rightarrow H_2^+ + 2e$	$7.27 \cdot 10^{-15} T_e^{0.549} e^{-15.5/(T_e - 0.001)} + 1.37 \cdot 10^{-14} T_e^{-0.557} e^{-20.3/T_e}$
2	$e + H_2 \rightarrow 2H + e$	$1.54 \cdot 10^{-14} T_e^{0.06} e^{8.63/T_e} + 1.11 \cdot 10^{-13} T_e^{-0.813} e^{-13.4/T_e}$
3	$e + H_2 \rightarrow H + H^-$	$4.43 \cdot 10^{-17} T_e^{-1.29} e^{-11.7/(T_e + 0.158)} + 1.33 \cdot 10^{-19} T_e^{-1.39} e^{-3.77/T_e}$
4	$e + H \rightarrow H^+ + 2e$	$9.74 \cdot 10^{-15} T_e^{-0.174} e^{-14.3/(T_e - 0.001)} + 6.35 \cdot 10^{-15} T_e^{0.433} e^{-16.4/T_e}$
5	$H + H_2^+ \rightarrow H_2 + H^+$	$1.54 \cdot 10^{-14} T_e^{-0.859} e^{-4.61/(T_1 - 0.786)} + 1.64 \cdot 10^{-15} T_i^{-0.353} e^{-0.258/T_i}$
6	$e + H_2^+ \rightarrow H + H^+ + e$	$3.50 \cdot 10^{-13} T_e^{-1.25} e^{-3.19/(T_e - 0.008)} + 1.77 \cdot 10^{-13} T_e^{-0.0924} e^{-3.04/T_e}$
7	$e + H_3^+ \rightarrow H_2^+ + H^-$	$1.93 \cdot 10^{-15} T_e^{-1.07} e^{-6.26/(T_e + 0.131)} + 5.35 \cdot 10^{-17} T_e^{-0.371} e^{-2.07/T_e}$
8	$H_2 + H_2^+ \rightarrow H + H_3^+$	$6.29 \cdot 10^{-15} T_i^{-1.46} e^{-2.22/(T_i + 0.356)} + 2.71 \cdot 10^{-16} T_e^{-1.30} e^{-0.317/T_i}$
9	$H^+ + H^- \rightarrow 2H$	$4.46 \cdot 10^{-14} T_i^{-0.281} + 1.26 \cdot 10^{-14} e^{-1.96/T_i}$
10	$H_2^+ + H^- \rightarrow H_2 + H$	$2.23 \cdot 10^{-14} T_i^{0.425} + 8.93 \cdot 10^{-14} T_i^{-0.261}$
11	$H_3^+ + H^- \rightarrow 0.5H_2 + 3H$	$1.70 \cdot 10^{-14} T_i^{0.313} + 5.75 \cdot 10^{-14} T_i^{-0.288}$
12	$e + H^- \rightarrow H + 2e$	$4.58 \cdot 10^{-13} T_e^{0.287} e^{-4.41/(T_e + 0.117)} + 2.71 \cdot 10^{-14} T_e^{0.62} e^{-1.82/T_e}$
13	$e + H_3^+ \rightarrow 2H + H^+ + 2e$	$2.69 \cdot 10^{-13} T_e^{-0.245} e^{-15.6/(T_e + 0.003)} + 1.01 \cdot 10^{-12} T_e^{-0.464} e^{-26.8/T_e}$
14	$H_2 + H^+ \rightarrow H_3^+ + h\nu$	$1.63 \cdot 10^{21}$
15	$e + H_2^+ \rightarrow 2H$	$2.29 \cdot 10^{-14} T_i^{-0.571} + 3.31 \cdot 10^{-15} T_i^{-0.152 T_e}$
16	$e + H_3^+ \rightarrow 3H$	$3.36 \cdot 10^{-15} T_e^{-0.716} + 3.73 \cdot 10^{-14} T_e^{-0.67} e^{6.40/T_e}$
17	$e + H_3^+ \rightarrow H + H_2$	$2.03 \cdot 10^{-15} (T_e^{-0.189} + 0.040 T_e^{-1.49}) + 5.57 \cdot 10^{-14} T_e^{1.23} e^{-6.21/T_e}$
18	$H + H^- \rightarrow H_2 + e$	$2.16 \cdot 10^{-13} T_i^{-1.89} e^{-12.7/(T_i + 1.17)} + 1.30 \cdot 10^{-15} T_i^{-0.418} e^{-0.192/T_i}$
19	$H_2 + H^- \rightarrow H + H_2 + e$	$1.62 \cdot 10^{-16} T_i^{0.417} e^{-6.47/(T_i + 0.132)} + 5.70 \cdot 10^{-16} T_i^{0.550} e^{-2.19/T_i}$
20	$H + H^- \rightarrow 2H + e$	$3.81 \cdot 10^{-15} T_i^{0.280} e^{-3.76/(T_i + 0.626)} + 4.55 \cdot 10^{-16} T_i^{0.603} e^{-0.375/T_i}$
21	$H_2 + H^+ \rightarrow H + H_2^+$	$5.54 \cdot 10^{-16} T_i^{-0.453} e^{-3.26/(T_i - 0.001)} + 5.98 \cdot 10^{-18} T_i^{-2.88} e^{-0.310/T_i}$
22	$e + H \rightarrow H^- + h\nu$	$5.75 \cdot 10^{-20} (T_e^{-0.0285} - 0.94 T_e^{-0.05}) + 6.54 \cdot 10^{-19} T_e^{-5.18} e^{-72.4/T_e}$

Table 7.3 – Plasma reactions and reaction rates used for RAID hydrogen plasma model (from [118]).
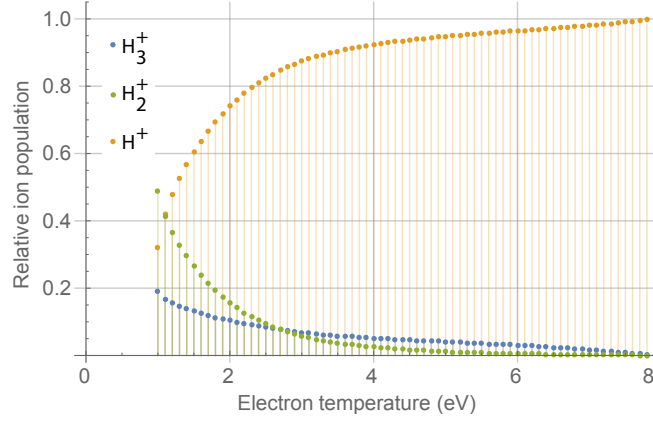
Figure 7.2 – Relative population of positive ions as a function of the electron temperature by inverting the system Eq. 7.20 in steady state regime for $n_e = 1.5 \cdot 10^{18} \mathrm{m}^{-3}$

Prior to the implementation of the COMSOL model, the equation set was solved with the software Mathematica in steady state regime to check if it resulted in reasonable solutions (and including a term for positive ion losses at the Bohm velocity). This was done by setting all derivatives to zero and solving the algebraic system by the inversion of the matrix. The resolution of the system was performed by considering reference parameters for a 3.5 kW hydrogen plasma discharge in RAID, for which: $n_e = 1.5 \times 10^{18}\,\mathrm{m}^{-3}$, the temperature of heavy species 0.1 eV and $p_{\mathrm{H}_2} = 0.3\,\mathrm{Pa}$. Fig. 7.2 shows the relative ion populations as a function of the electron temperature in the range [1-8] eV. We remark that in the center of the plasma column where $T_e \approx 5\,\mathrm{eV}$, we expect $\sim 95\%$ of H^+, $\sim 4\%$ of H_2^+ and $\sim 1\%$ of H_3^+, while at the plasma column edge, where $T_e \approx 1.5\,\mathrm{eV}$, we expect $\sim 60\%$ of H^+, $15\% \sim$ of H_2^+ and $\sim 25\%$ of H_3^+. This is a reasonable trend, since H^+ is expected to be efficiently produced at higher electron temperatures. Negative ions are considered in the following sections.

Reactions involving negative ions

The reaction set in Tab. 7.3 employed for this model contains a large variety of volume processes, including those regarding the production and the destruction of negative ions. There are three reactions producing H^-, which are: the dissociative attachment (DA), the attachment of electrons to H_3^+ and the attachment of electrons to H:

$$\mathrm{e} + \mathrm{H}_2 \rightarrow \mathrm{H} + \mathrm{H}^-, \tag{7.21}$$

$$\mathrm{e} + \mathrm{H}_3^+ \rightarrow \mathrm{H}_2^+ + \mathrm{H}^-, \tag{7.22}$$

$$\mathrm{e} + \mathrm{H} \rightarrow \mathrm{H}^- + \mathrm{h}\nu. \tag{7.23}$$

The hydrogen molecule can sustain a number of rovibrational excited states [120]. The dissociative attachment (DA) cross section is the main channel for H^- production and it shows
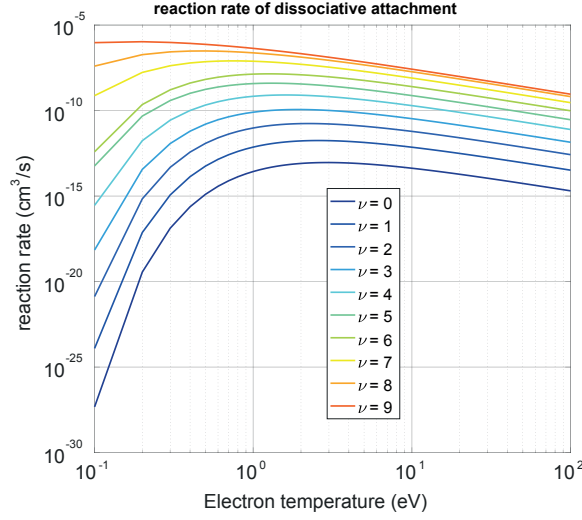
Figure 7.3 – Dissociative attachment reaction rate of H_2 [78] showing the peak at low electron temperature and the strong dependence on the vibrational state.

a rapid increase with large vibrational quantum number. Fig. 7.3 shows the reaction rate for DA for 10 vibrational states of $H(v)$, from $v = 0$ to $v = 10$ [78]. The effect of the rotational excitation on DA cross section is, however, small compared to the vibrational excitation [72]. Vibrational excited H_2 are produced by the processes described in Sec. 1.2.1. The inclusion of the 14 vibrational states of $H(v)$ would considerably increase the number of the terms in the balance equation and the computation complexity of the model without adding new physics. The DA reaction in Tab. 7.3 approximates the contribution of all the vibrational excited states with an effective coefficient based on the molecular activated rate coefficient provided in Ref. [108].

The reactions involving the destruction of H^- are the *mutual neutralization* (MN) with positive ions:

$$H^+ + H^- \rightarrow 2H, \tag{7.24}$$

$$H_2^+ + H^- \rightarrow H_2 + H, \tag{7.25}$$

$$H_3^+ + H^- \rightarrow 0.5H_2 + 3H, \tag{7.26}$$

the *associative detachment* (AD) with neutrals:

$$H + H^- \rightarrow H_2 + e, \tag{7.27}$$

$$H_2 + H^- \rightarrow H_2 + H + e, \tag{7.28}$$

$$H + H^- \rightarrow H_2 + e, \tag{7.29}$$
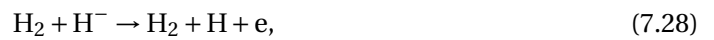
and the *electron detachment* (ED):

$$e + H^- \rightarrow H + 2e. \tag{7.30}$$

$$\tag{7.31}$$

The importance of each of these three processes can be evaluated by computing the mean free path (mfp). The knowledge of the mfp is important in the description of negative ion sources to evaluate the distance where negative ions can be extracted and also for source modeling [15]. In the case of RAID, the mfp for MN and the AD are constant along the radius and of the order of a few mm. The ED mfp is however of the order of 1 mm only for $r < 2\,\mathrm{cm}$, and about 10 cm where the density of negative ion peaks ($r \approx 5.5\,\mathrm{cm}$, according to LP photodetachment), suggesting that ED is negligible in the H^- rich shell.

7.1.3 Plasma equilibrium profile

Input profiles and parameters

The n_e and T_e are introduced in the model by fitting experimental profiles with analytical functions. Fig. 7.4 shows the input plasma 3D profiles of n_e (right) and T_e (left) for a typical H_2 plasma with 3 kW RF power, a magnetic field of $B = 200\,\mathrm{G}$ and 0.3 Pa gas pressure. Note that n_e is peaked downstream at $z \approx 0.8\,\mathrm{m}$ and in the antenna region. The n_e in the antenna ceramic tube is obtained by extrapolation of vessel measurements and considering that the electron density rises in the center of the antenna because of the superposition of the inductive regime and the helicon contribution. Also the T_e profile in the antenna region is extrapolated such that T_e varies monotonically from one end to the other of the plasma column. The extrapolated value of T_e in the antenna reaches about 8 eV which seems reasonable considering that the closest T_e measurement to the antenna is 7 eV and electrons are affected by the strong electric field close to the antenna legs, increasing their energy. A full mapping of n_e and T_e in the antenna region would be very helpful for completeness of the 3D model. This is however not feasible in the antenna because of RF coupling, as we discussed in Sec. 3.6. The drawback of this approach is that every simulation requires the introduction of new n_e and T_e 3D profiles, requiring full 3D LP measurements and calibration with microwave interferometry. The other input parameter is the radial profile of the plasma potential V_p, shown in Fig. 7.5, obtained by reproducing the experimental V_p radial experimental profile in Fig. 3.15 having a central flat top and decaying to zero at the grounded vessel wall. The resulting electric field is calculated as $\vec{E} = -\overrightarrow{\nabla V_p}$ and included in Eq. 7.6.
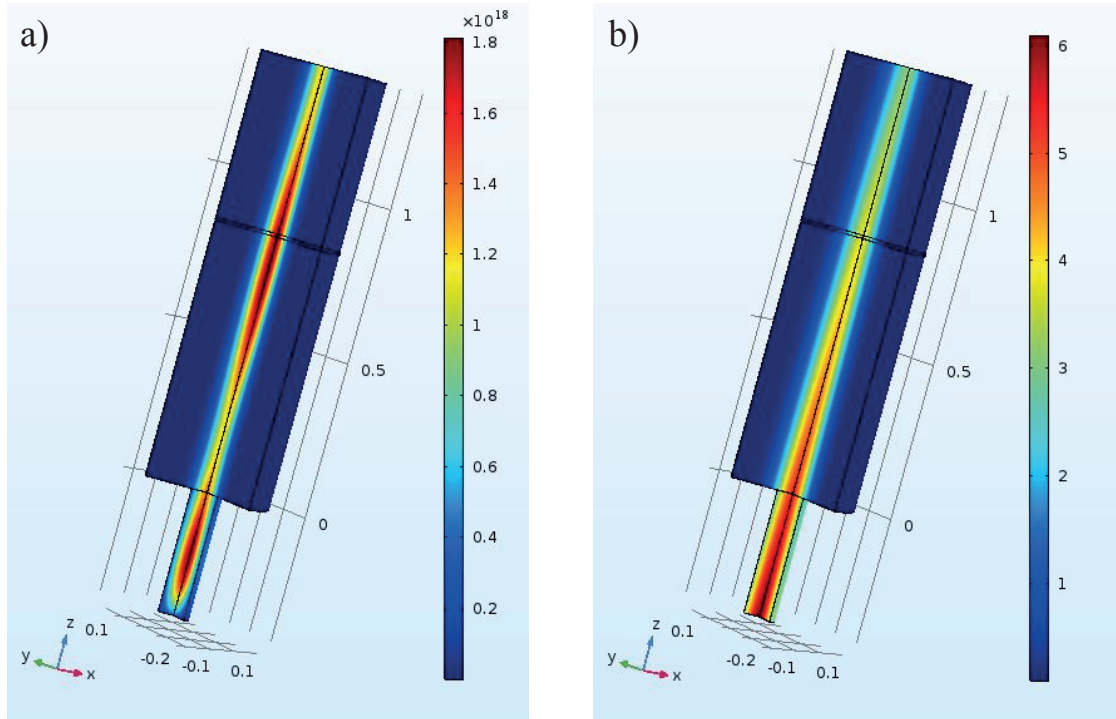
Figure 7.4 – Input plasma 3D experimental profiles of n_e (left) and T_e (right) for a typical H_2 plasma with 3 kW RF power and 0.3 Pa gas pressure.
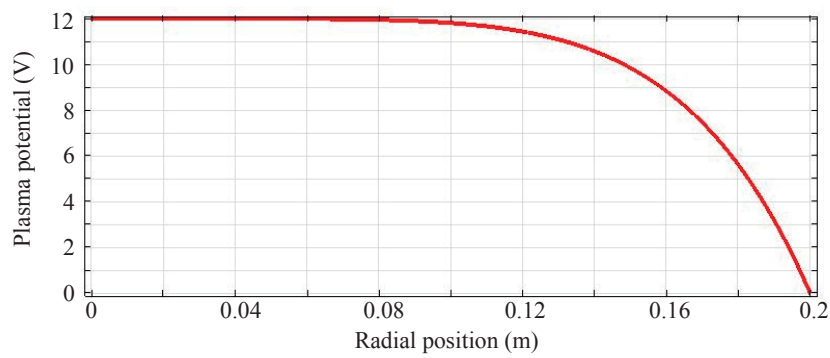

Figure 7.5 – Radial profile of the plasma potential obtained to approximately reproduce the experimental V_p radial profile in Fig. 7.5.

7.2 Ion species and H equilibrium profiles

7.2.1 3D profiles

Here we present the results of a numerical simulation for a typical hydrogen plasma in RAID with 3 kW RF power, 200 G of magnetic field and 0.3 Pa gas pressure. We show the results of the 3D profiles of ions and H resulting from the n_e and T_e profiles in Fig. 7.4. Fig. 7.6 shows the resulting equilibrium profiles for H^+, H_2^+, H_3^+, H^- and H. H^+ have a quite narrow distribution around the axis and peaks at $z \approx 0.5\,\text{m}$. H_2^+ however is mostly concentrated in the antenna region. H_3^+ ions look concentrated just in front of the antenna region and with a broader radial distribution compared to H^+ and H_2^+ ions.

It is worth noting that H^- are mostly localized at the edge of the plasma column and are distributed along the entire axial direction. This is promising for the development of a slit negative ion extractor (extracting along one radial direction) since it would provide a good homogeneity of n_{H^-} along the slit. We also observe an increase of n_{H^-} close to the target and a widening of the H^- ring. The H equilibrium profile peaks where n_e reaches its maximum value. We remark that n_H profiles are much wider compared to ion species since H is not affected by the strong axial magnetic field. We also note that a large quantity of H impinges on the surface walls, making the production of H^- ions by surface processes also practicable.

7.2.2 Radial profiles and comparison with experimental data

To appreciate the local distribution of plasma species it is helpful to fix an axial position and plot radial profiles. Since we are interested to compare the numerically simulated n_{H^-} radial profiles to the experimental measurements, we plot all plasma species profiles at the axial position where CRDS and laser photodetachment measurements were performed, namely at $z = 83\,\text{cm}$. Fig. 7.7 shows the radial density profiles of H^+ (on the top-left) and of H_2^+ (on the top-right). We remark that the n_{H^+} profile is very narrow and reaches $\sim 2 \cdot 10^{18}\,\text{m}^{-3}$; the $n_{H_2^+}$ profile is slightly broader and reaches $\sim 1.1 \times 10^{17}\,\text{m}^{-3}$. $n_{H_3^+}$ is broader that n_{H^+} and $n_{H_2^+}$ and reaches a peak density of $\sim 2.8 \times 10^{16}\,\text{m}^{-3}$. The relative density of the three positive ion species is in good agreement with the estimate with the 0D model in Fig. 7.2. n_{H^-} shows a clear peak at $r \approx 5.5\,\text{cm}$ which is in very good agreement with laser photodetachment measurements at 3kW RF power. Also the absolute peak value of $\sim 0.95 \times 10^{16}\,\text{m}^{-3}$ is not so far from the experimental value $\sim 1.2 \times 10^{16}\,\text{m}^{-3}$. These results indicate that the model is able to make prediction close to experimental values.

7.2.3 Physics mechanisms of negative ions

To examine the transport of the different species it is useful to compare the production rate (Eqs. 7.20) with the corresponding equilibrium profiles. In the case of negative ions we are interested to know if the effect of the transport has a relevant role in the formation of the equilibrium radial profile. Fig. 7.8 compares the normalized radial profile of the total
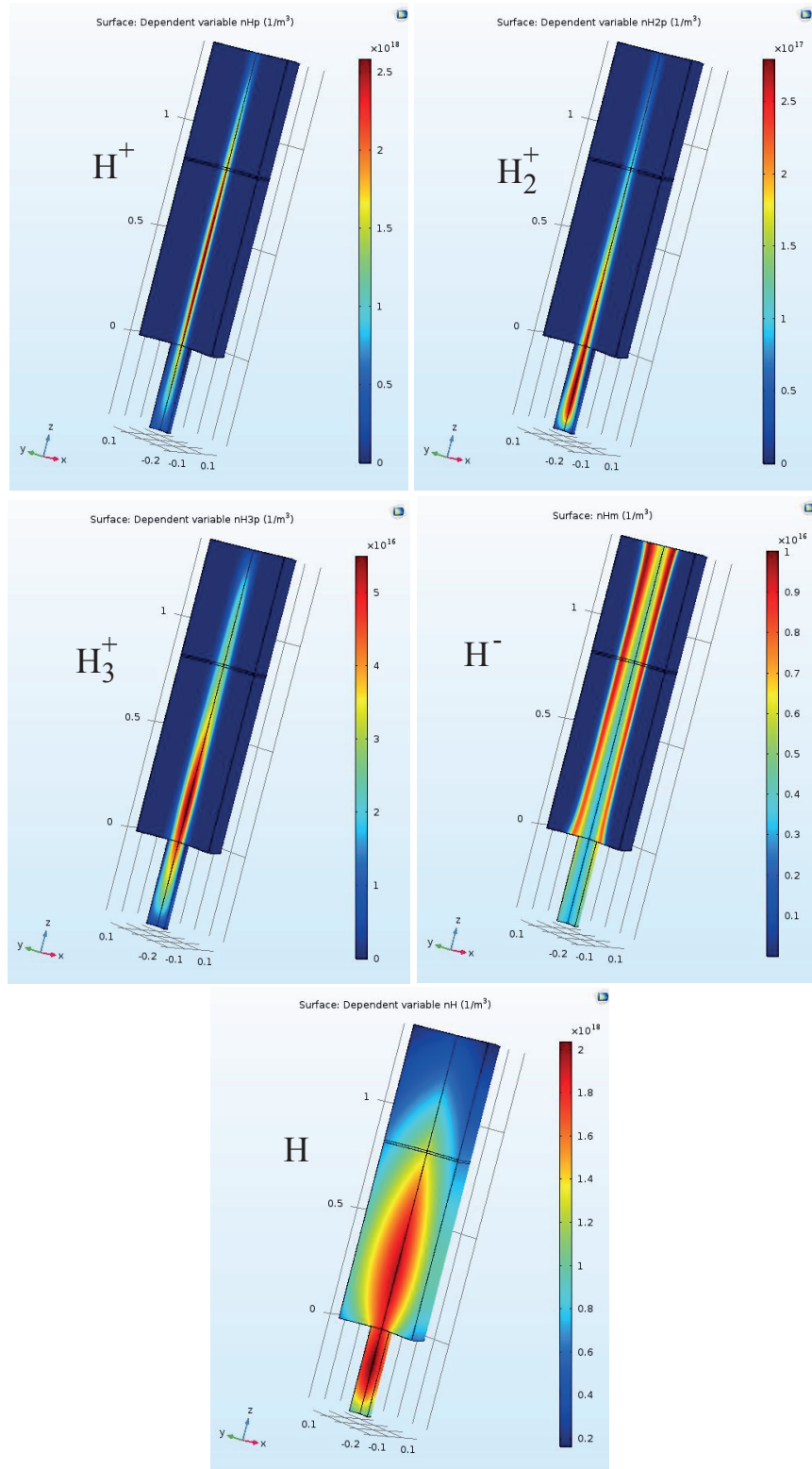
Figure 7.6 – Volumetric density profiles of H^+, H_2^+, H_3^+, H^- and H obtained from the experimental n_e and T_e profiles in Fig. 7.4 .
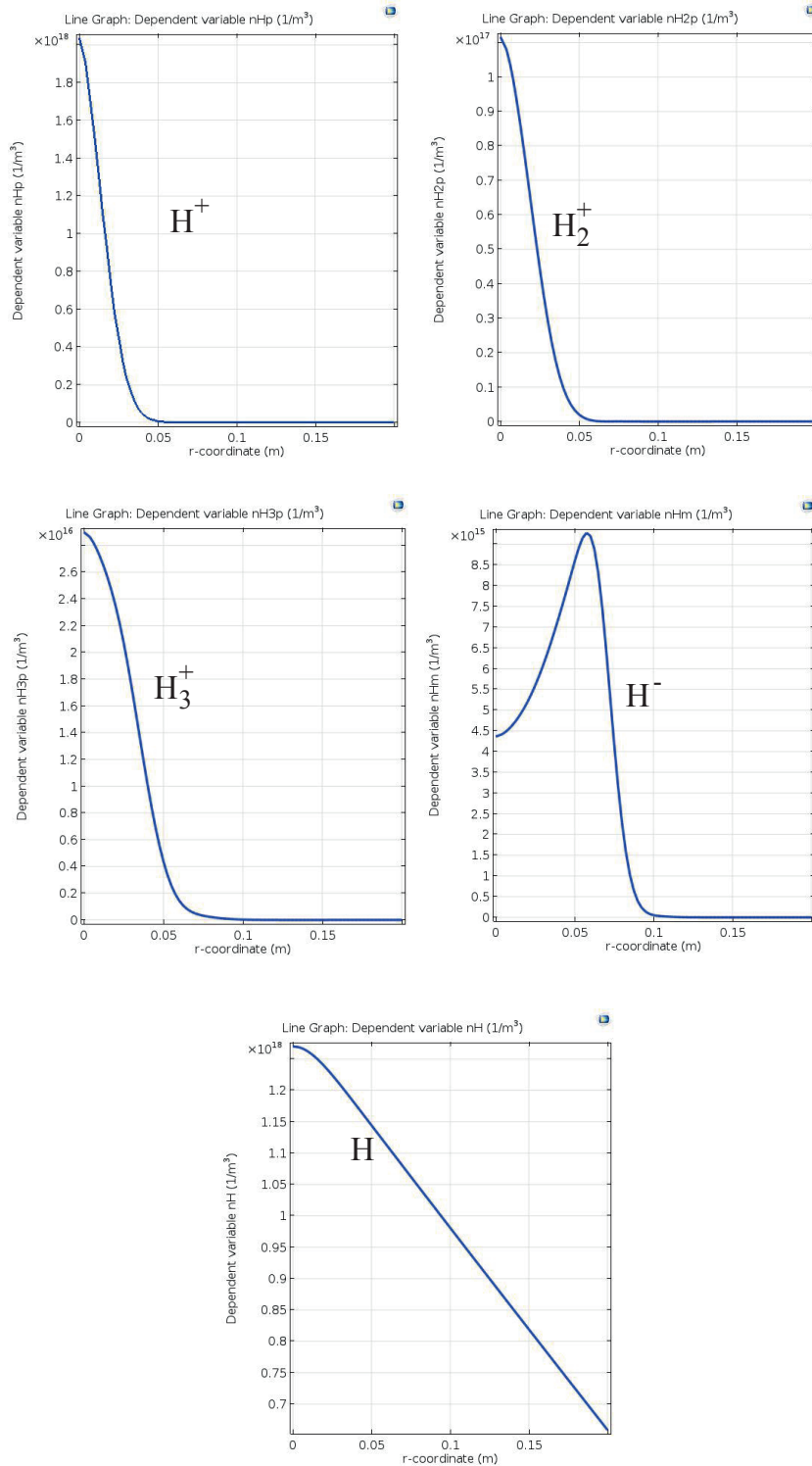
Figure 7.7 – Radial density profiles of H^+, H_2^+, H_3^+, H^- and H obtained from n_e and T_e profiles at the axial position $z = 0.83$ cm.
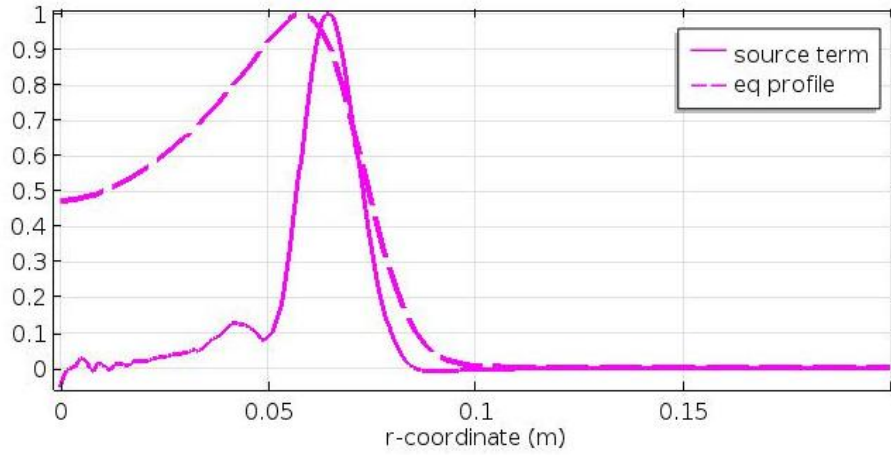
Figure 7.8 – Comparison between the normalized radial profiles of the total production rate of H⁻ (solid line) and the density equilibrium profile of H⁻ showing that radial diffusion of H⁻ plays an important role in the steady state profiles.

production rate of H⁻ (solid line) with the normalized radial equilibrium profile of n_{H^-}. It seems that most H⁻ are produced very close to the position of the peak H⁻ density in a region of ∼ 1.5 cm of FWHM, and a large number diffuse towards the plasma core. Thus, the extrapolation to $n_{H^-} \approx 0$ in the center of the plasma column used to fit the negative ion profiles measured by LP laser photodetachment in Sec. 4.2.5 might not correspond to reality. This, however, would not change the result of the analysis in Sec. 4.2.5 to determine the absolute negative ion density profiles.

Negative ions are mostly produced at the edge of the plasma column, where the electron density drops to ∼ $3 \times 10^{16} \, \mathrm{m}^{-3}$, this also seems compatible with the electronegativity of 0.3 measured by photodetachment. This suggests that H⁻ transport plays an important role in H⁻ equilibrium profiles, at least for this plasma regime.

An overall discussion concerning the production and destruction processes of H⁻ helps understanding the different constraints involved in the negative ion source development. The plasma parameters having a direct effect on the H⁻ production and destruction are: the electron density, the electron temperature and the background fill pressure. The equilibrium profiles are then determined by the plasma transport through the magnetic field topology and the collisionality. Also, turbulent phenomena could have an effect but they were not included in the previous model since these are not trivial to model. It appears that H⁻ profiles result from a combination of non linear processes and the only way to identify dominant processes is by numerical simulations. Experimental investigations with increasing RF power carried out in this thesis (see Sec. 4.1.5 and Sec. 4.2.4), in other hydrogen/deuterium plasma sources [19, 36, 26] and simple H⁻ balance models [14, 37] show that H⁻ density increases approximately linearly with power, and therefore with electron density. This can be qualitatively explained because, for RF low powers (a few kW), the production reaction rate is proportional to the square of the electron density and the destruction reaction rate is proportional to the H density

[37], according to the following equation:

$$n_{\mathrm{H}^-} = \frac{n_{\mathrm{H}_2^*}\langle\sigma v(DA)\rangle}{n_{\mathrm{H}^+}\langle\sigma v(MN)\rangle + \frac{n_{\mathrm{H}}}{n_e}\langle\sigma v(AD)\rangle + \frac{1}{\tau_{\mathrm{H}^-} n_e}}, \tag{7.32}$$

where $n_{\mathrm{H}_2^*}$ is the density of vibrationally excited H_2, $\langle\sigma v(DA)\rangle$, $\langle\sigma v(MN)\rangle$ and $\langle\sigma v(AD)\rangle$ are the dissociative attachment, the mutual neutralization and the associative detachment reaction rates, and τ_{H^-} is the lifetime for wall loss of H. Since $n_{\mathrm{H}_2^*} \propto n_e$ and $n_{\mathrm{H}^+} \propto n_e$, overall we have $n_{\mathrm{H}^-} \propto n_e$. However, as the electron density is further increased, the ionization limit approaches, also neutral depletion displaces H_2 molecule from the center of the plasma column and no further $n_{\mathrm{H}_2^*}$ molecule required for the DA are available. Also, the main destruction processes, the AD and the MN, continue to increase with electron density. The overall effect of the DA and the destruction processes is such that a saturation of H^- density is expected for higher powers. CRDS measurements in RAID 4.1.5 show, indeed, a flattening of n_{H^-} for RF power larger than 5 kW. Thus, it is unlikely that only by "brute force" increasing of the RF power, the target $n_{\mathrm{H}^-} \approx 10^{17}\,\mathrm{m}^{-3}$ could be achieved in the current RAID, and helicon devices in general.

The role of the electron temperature is more complex since, on the one hand, high electron temperatures $> 5\,\mathrm{eV}$ are required to rovibrationally excite the H_2 [78], and on the other, the DA cross section peaks for $T_e < 1\,\mathrm{eV}$ (see Fig. 7.3). Moreover, electron collisional losses start to become important from $T_e > 1\,\mathrm{eV}$, since the binding energy of the extra electron upon the H^- is only 0.75 eV. It is evident that it is an arduous task to keep these competitive processes separated in the same plasma volume. This problem, in conventional negative ion sources, is partially solved by the addition of a magnetic filter, separating two regions with different electron temperatures. Hence, RAID is already successful as a volume source of H^- since the vibrationally-hot H_2 is produced in the hot core, and dissociative attachment production of H^- occurs in the cold periphery without detachment by hot electrons. RAID provides in a natural way the two different electron temperature regions via the radial T_e profile. The reaction production mechanisms for H^- peaks at $r \approx 5\,\mathrm{cm}$, but then H^- are transported and the equilibrium profile is also dependent on the transport. LP measurements showed that the radial T_e profile is basically independent of the RF power. Perhaps, this could be conveniently modified in the expanding field geometry, discussed in Sec. 8.1, according to the envisaged extraction scheme. Clearly, dedicated numerical simulations for such a scheme would be required to accurately predict 3D H^- profiles.

The role of neutrals in negative ion production can be divided into that of H_2 and that of H. The volume production of negative ions is proportional to the number density of H_2^*, which is in turn proportional to the number density of H_2. We have experimentally observed that indeed large gas pressures and the injection of argon gas are favorable to achieve higher H^- densities, unfortunately for the purpose of NBI, 0.3 Pa is a stringent upper threshold. However, for surface production, a high flux of H is desirable to enhance surface H^- production, for example with caesium, although high H densities close to the extractor could destroy H^- by AD as well.

7.3 Conclusion and Outlook

A fluid model was developed to investigate the mechanisms determining the equilibrium 3D profile of ion and H species in the RAID plasmas. The model is based on the resolution of diffusion equations of multiple hydrogen plasma species considering a H_2 diluted magnetized collision plasma. Numerical simulations of a set of RAID experimental conditions show that positive ion species profiles are centrally peaked with central peak density of $2 \cdot 10^{18} \, \text{m}^{-3}$ for H^+, $1.1 \cdot 10^{17} \, \text{m}^{-3}$ for H_2^+ and $2.9 \cdot 10^{16} \, \text{m}^{-3}$ for H_3^+. Negative hydrogen radial density profiles show a very good agreement with experimental results, suggesting that this model could be used to extrapolate the source behavior at different regime and for source optimization.

Clearly, improvements of this model are possible. Firstly, the model requires as input data, the n_e and T_e 3D profiles, which are very time consuming to measure experimentally and, moreover, only a few data on the plasma parameters in the antenna region are available. Attempts to introduce a constraint on plasma quasi-neutrality resulted in non-convergent solutions. The current solutions for the charged species profile are displaced by the neutrality of only about a factor 10% in the center of the column but this can increase to even to an order of magnitude at the edge. The idea is to use the electric fields generated by the charge separations to "adjust" to the plasma quasi neutrality using Poisson's equation. A global approach would consist in introducing a power deposition profile, due to the helicon wave, and calculate the plasma formation by ionization and then allowing to diffuse and then repeat the calculation by iteration. Unfortunately the helicon wave - interaction mechanism is a combination of collision and collisionless power absorption mechanisms [31] which are not trivial to model, and actually even not very well understood theoretically .

Finally, for high power regimes, the hypothesis of H_2 diluted plasma does not hold. To describe high density regimes, the model should also include a balance equation for H_2. Some attempts to solve the system by considering also a balance equation for the set of Eq. 7.20 resulted in non-convergent solutions. Perhaps in order to reach convergence, a more realistic steady state flow of H_2, should be considered.

We believe that with some improvements this model can be used to accurately predict the equilibrium profiles of low temperature hydrogen plasmas in a wide range of input conditions of RF power, magnetic field and gas pressures and, furthermore, it could be employed to optimize existing negative ion sources for fusion.

8 Perspectives for Negative Ion Source Design

In previous chapters, we have discussed the overall physics of RAID helicon plasma including the formation of steady state profiles, the propagation of the helicon wave and the measurements of negative ion density, which are directly relevant to fusion applications. Leveraging these advances, we discuss herein the implications of RAID as a negative ion source including the preliminary design of a negative ion extractor. Although the negative ion density produced in volume does yet not meet the requirements for fusion application, RAID has the unique advantage, compared to other helicon sources, of producing hydrogen and deuterium steady state discharges fulfilling the low pressure requirements for fusion NBI application. In this chapter we discuss the plasma mechanisms relevant for negative ion extraction and possible extraction geometries from RAID-like plasmas, including the design of two extractors: one along the radius and the other along the axis of the device. The design of a RAID-like plasma to produce negative ions for fusion may very likely require the redesign of the source geometry to optimize the negative ion production. We believe that the first step in this direction is the axial homogenization, which can be improved by using multiple helicon antennas. We present preliminary tests with a double birdcage antenna setup, which also contribute to increase the power delivered to the plasma.

8.1   Extraction of negative ions

As mentioned in Sec. 1.2.4, the target parameters required for the negative ion source SPIDER, the prototype negative ion source for ITER, are quite challenging. SPIDER will most likely fulfill the required parameters since it is the outcome of more than one decade of physics and technology investigations on optimizing the operation of ICP sources from the surface production of negative ions to their extraction [19, 36].

However, concerning helicon plasma sources, it is quite premature to precisely foresee the performance of negative ion helicon-based systems at this early stage of development, for a number of reasons. First, the physics of volume production of negative ions in helicon plasmas is an emerging field, and research is currently ongoing. Although a very high negative ion density of $1.2 \times 10^{18}\,\mathrm{m}^{-3}$ was observed in a helicon plasma device [79], this was only achieved

during pulsed operation and for high gas pressure (>1Pa). The simultaneous achievement of all the requirements for an ITER negative ion source appears to be quite challenging and it is not clear whether this can be accomplished without the use of caesium. Very little is known on the possible use of caesium in such sources since caesium operation in helicon based devices has never been tested, to the best of author's knowledge. Second, negative ion extraction from helicon plasmas has never been attempted, and it is complex to extrapolate from the basis of the current ICP drivers, whose plasma production mechanisms are different from helicon, as well as their magnetic geometry. Third, their integration into a NBI system, including the compatibility with a neutralizer, has never been investigated.

The most remarkable achievements in RAID so far, regarding the source development, are the long duration of the plasma discharges, the low gas filling pressure of 0.3 Pa, the considerable amount of volume produced H^- and D^- and the high dissociation degree of $\sim 30\%$. To the best of the author's knowledge, no other helicon device was able to simultaneously achieve these parameters, which merit further fusion-related investigations.

Negative ion current density required for NBI applications are $355\,A/m^2$ for H^- and $285\,A/m^2$ for D^- corresponding to a volume density of $n_{H^-} \approx 1 \cdot 10^{17}\,m^{-3}$ in front of the extraction grid [36]. This is about 5 times higher than n_{H^-} and n_{D^-} measured in RAID by the techniques detailed in Sec. 4 and it is not certain if the gap could be bridged only by source optimization. Additionally, the co-extracted electron current ratio j_{H^-}/j_{n_e} (or j_{D^-}/j_{n_e}) has to be $\lesssim 0.5$ for H and $\lesssim 1$ for D. Although in the case of RAID we might expect a higher co-extracted electron current in D according to LP laser photodetachment (see Fig. 4.26), predicting accurately these values require modeling of the extraction geometry, including the magnetic topology of filter fields.

The experimental investigations detailed in Sec. 4.1 and 4.2 add relevant data on the volume production of H^- and D^- in hydrogen and deuterium helicon plasmas. Together with numerical simulations discussed in Sec. 7, it appears clear that negative ions have to be extracted from a shell-like structure around the plasma column. However, the design of a source based on a helicon plasma requires the investigation of different magnetic field geometries and the compatibility with an extractor and an acceleration system. Further experimental and numerical investigations relevant to the current setup would consist of characterizing negative ions along the plasma column and the study of different magnetic geometries, such as in the presence of an expanding magnetic field.

If used as part of a future volume ion source for a NBI system, direct extraction of the negative ions from the plasma column in the radial or axial direction should be possible. Three extraction geometries are foreseen:

1. If radial extraction is used, because of the inherent cylindrical nature of the helicon driven plasma, the beam would have to be long and narrow, such as that suggested in [127]. However, significant development may be required to avoid possible perturbation of plasma caused by the extractor. Moreover, the extraction system would need to be segmented, with each segment fitting between the magnetic coils.

2. Axial extraction seems unattractive as the annular region from which ions could be

extracted is narrow, and hence the extracted current would be low. Also, a transverse filter field would probably be needed to reduce the co-extracted electron current. It is also to be noted that the resulting annular beam shape has no particular advantage from the point of view of neutralisation or beamline design.

3. Using the helicon device to provide a plasma that expands towards a conventional multi-aperture system with a caesiated plasma grid should be considered because of the ease of operation at fill pressures < 0.3 Pa and the high efficiency of the helicon device. In this case, it needs to be established that the helicon driven plasma produces sufficient dissociation of the gas in order to have sufficient negative ion production via the impingement of the H/D atoms on the low work function of the plasma grid surface.

Recognising that the integration of a RAID-like plasma in a NBI injector would require a considerable numerical and experimental effort, the very first step is to experimentally demonstrate the possibility of extracting negative ions from the RAID plasma. Unlike the extraction from caesiated negative ions sources, where negative ions are produced by surface processes on the extraction grid, the extraction of negative ions from the bulk plasma volume requires the local disruption of the plasma potential. Fig. 1.9(c) showed the potential along the extraction direction for a plasma grid biased above the plasma potential immersed in a RAID plasma. In the framework of a collaboration with Consorzio RFX, hosted in Padova (Italy), we have initiated preliminary design of a radial and a axial extractor of negative ions for RAID, described in Sec. 8.1.1 and Sec. 8.1.2.

8.1.1 Design of a radial negative ion extractor for RAID

A radial extractor can be either a long and thin slit along the plasma column or can be segmented between coils. In Fig. 8.1 we show the schematic cross section of the radial extractor envisaged for RAID, for a proof-of-principle experiment, together with the CAD design. The idea is to extract negative ions located in the region of largest density, however, since the position of the peak negative ion density varies according to plasma parameters, the extraction slit should be free to move along the radial direction. The main components of the extractor are the plasma grid, which is a slit in our case, the extraction grid and the collector, where negative ions end up after having been extracted. The upper current density limit for space charge for electron and negative ions can be estimated by the Langmuir-Blodgett formula, in the the case of extraction from a system with cylindrical geometry [83]:

$$j = \frac{D}{r r_0 \beta^2},$$ (8.1)

where r is the radius of curvature of the equipotential lines imposed by the extractor, r_0 is the radius of curvature of the meniscus, $D = 2.336 \times 10^{-6} \text{V}^{-3/2}$ for electrons and $D = 5.455 \times 10^{-8} \text{V}^{-3/2}$ for H^- and $\beta^2 = 0.00274$. This results in a current density $j_e \approx 2850 \frac{\text{A}}{\text{m}^2}$ for electrons
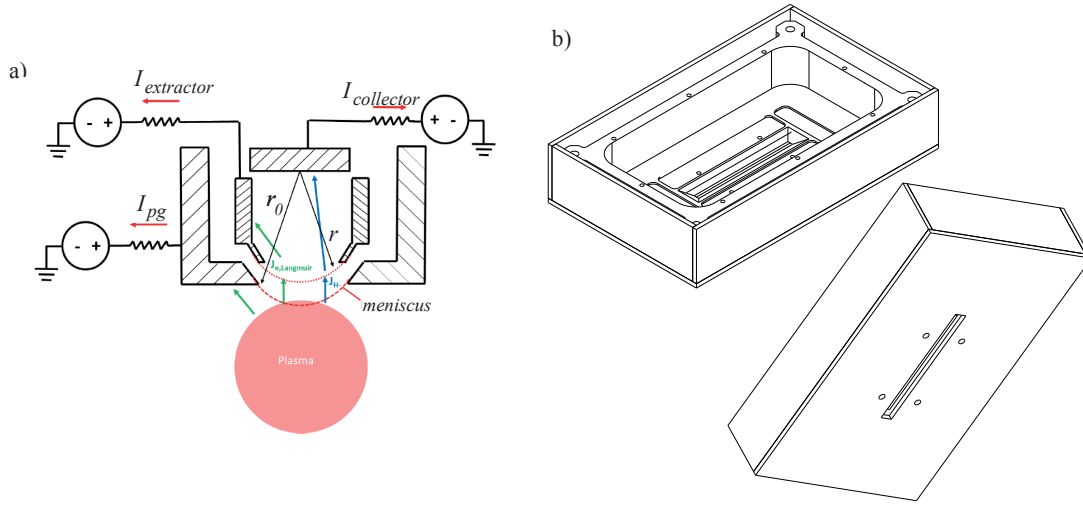
Figure 8.1 – a) Conceptual design of the radial negative ion extractor for RAID showing the main components of the prototype. b) CAD design of the radial extractor.

and $j_{\text{H}^-} \approx 67\frac{\text{A}}{\text{m}^2}$ for H$^-$ ions, for an applied voltage gap of 1 kV. This j_{H^-} would be 0.2 times the target j_{H^-} for SPIDER, nevertheless it would represent a first significant step in helicon source extraction development, provided that a large fraction of electrons is filtered, and large room for improvement and optimization is left. Supposing a rectangular slit of $100 \times 5\,\text{mm}^2$, this gives an electron current of $I_e \approx 1.5\,\text{A}$ and a H$^-$ current of $I_{\text{H}^-} \approx 0.035\,\text{A}$. Numerical simulations of particle trajectories for electron and negative ions for such a system show that plasma electrons with initial energy of 2 eV, typical for the edge of the plasma column, are deflected by the DC axial magnetic field. Therefore, a remarkable advantage of such an extraction configuration is that plasma electrons are expected to be largely filtered out by the intrinsic magnetic geometry of the plasma column. An additional filter field produced by small-size permanent magnets on the edge of the slit could, in any case, be inserted to further reduce the electron current. Concerning the H$^-$ ions, preliminary simulations shows that a few tens of volts of acceleration are sufficient to avoid significant ion deflection by the DC axial magnetic field.

8.1.2 Design of an axial negative ion extractor for RAID

Negative ions could be extracted along the axial direction by means of an annular extractor. The advantage of this set up is that this might be used in the perspective of the expanding plasma geometry employing the helicon as a plasma driver. Unlike the radial extractor, in the extraction along the axial direction, the electrons are not naturally filtered out by the DC axial magnetic field and they must be filtered from the extractor by additional filter fields. The idea is to add a strong local transverse magnetic field where negative ions are extracted. Fig. 8.2 shows the 3D model of the axial negative ion extractor for RAID, which will be installed on the downstream end flange. The annular extractor is surrounded by a circular array of SmCo
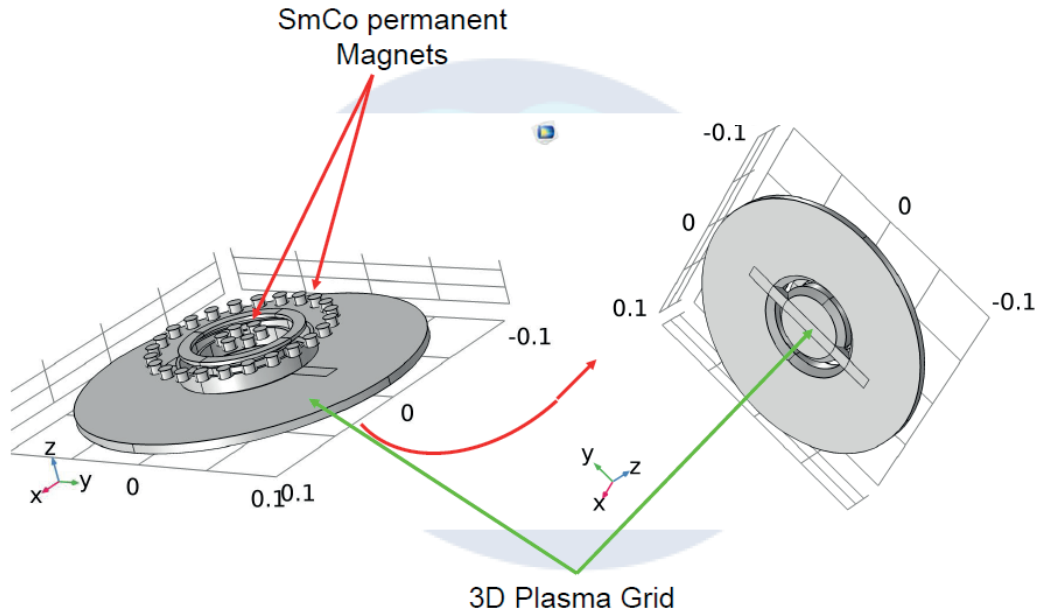
Figure 8.2 – 3D model of the axial negative ion extractor for RAID. Negative ions are extracted from across the filter field which is produced by a circular array of SmCo permanent magnets.

permanent magnets. Preliminary simulations show that such an arrangement would provide sufficient additional transverse magnetic field to filter out the plasma electrons. Unlike the radial extractor, in such a setup, a large portion of the plasma grid of the axial extractor directly faces the plasma, therefore, a water cooling system will be required. The large area of the extractor close to the plasma is also favorable to test the extraction with caesium. A caesium dispenser in a circular geometry is envisaged for an advanced stage of tests, once the volume operation (caesium-free) has been extensively investigated.

8.2 Preliminary tests with two Birdcage Antennas

We have recently installed a double birdcage setup as depicted in Fig. 8.3 in the framework of a collaboration within an EuroFusion Enabling Research on negative ion modeling, led by Dr. G. Fubiani of CNRS Toulouse, France. Installing a second birdcage antenna is motivated by two reasons: the first is that we want to increase the power delivered to the plasma up to 10 kW as an intermediate step to investigate the technology and physics issues of high power helicon plasmas; the second is that the use of two or more birdcage antennas can benefit the axial uniformity of the plasma column. The uniformity of the helicon plasma column is interesting for possible applications as source of negative ions for photoneutralization schemes, such as for the Cybele concept, detailed in Sec. 8.3 which requires a long and homogeneous plasma column. Such a system may require the use of multiple drivers to achieve high degrees of
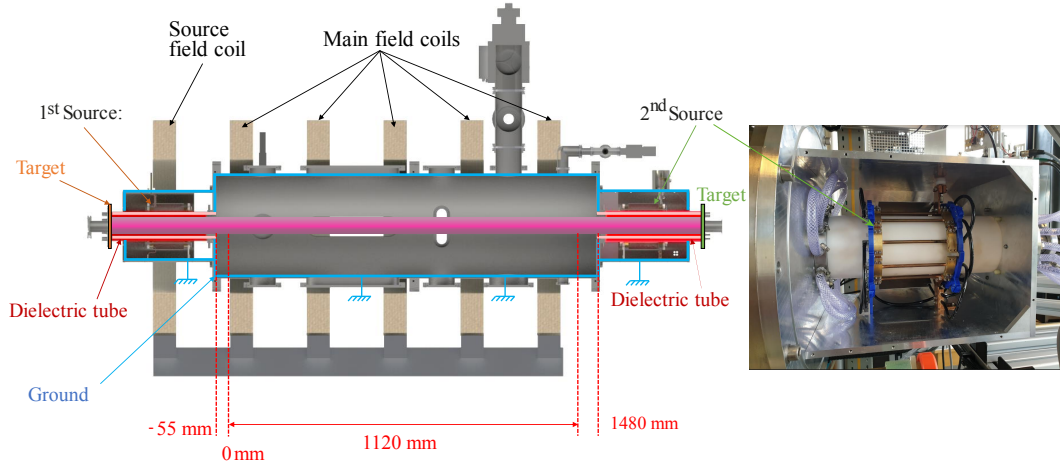
Figure 8.3 – On the left: schematic of the setup with two birdcage antennas to investigate a helicon plasma discharge generated by two identical birdcage antennas. Each birdcage is installed on the dielectric tube at the extremities of the vacuum vessel. On the right: picture of the second birdcage antenna installed on the alumina cylinder.

homogeneity. As detailed in Sec. 6.6, the production of helicon plasmas for AWAKE particle acceleration may also help achieving the required stringent degree of axial plasma density homogeneity (<0.2%). It is therefore helpful to study helicon plasma discharges induced by multiple helicon antennas.

In the setup on RAID in Fig. 8.3, two identical birdcage antennas are installed around two alumina tubes. Each antenna is powered by an independent RF power supply. The vessel walls are grounded and the targets at the ends of the alumina tubes are electrically floating.

We show in Fig. 8.4 preliminary measurements of the profiles of I_{sat} measured along the center of the plasma column for an argon plasma (on the left) and for hydrogen plasma (on the right). The red points are measurements with only the first antenna, the green points with only the second antenna and the blue points with both antennas. For each plasma species, the total RF power delivered to the plasma is the same, this allows comparing how the same RF power is distributed according to the set up. In the case of argon, the total power is 1500 W, for hydrogen it is 2000 W, equally shared between each antenna when both are used. In the case of hydrogen, we used 250 A current in the vessel coils corresponding to ~ 330 G peak field, and 150 A for argon, corresponding to ~ 200 G of peak field. In each test, there was no current flowing in the antenna coil, to make the magnetic field as symmetric as possible along the axial direction. We remark that, first of all, operations with two birdcage antennas are possible. Furthermore, the effect of using two antennas is to flatten the I_{sat} profiles, suggesting that plasma n_e axial profiles may flatten as well. These preliminary measurements suggest that the power deposition profiles along the axial direction are more homogeneous when both antennas are used.
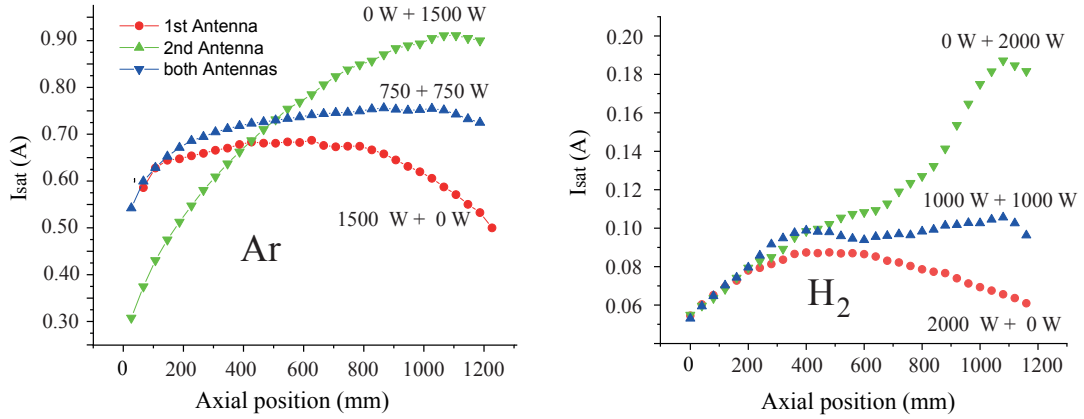
Figure 8.4 – Axial I_{sat} profiles with only the first antenna (red circles), with only second antenna (green triangles) and with two antennas (blue triangles), for argon plasma (on the left) and a hydrogen plasma (on the right). The I_{sat} profile tends to flatten when both antennas are used.

8.3 The Cybele concept of photoneutralization

Future NB systems will have to maximize the neutralization efficiency, above the expected efficiency of ∼ 60% of the gas neutralization. The neutralization of energetic negative ions is possible by photodetachment (a process called *photoneutralization*) with efficiency > 90 %. A concept for a full scale photoneutralization system for fusion devices, named *Cybele concept* [127], is currently being developed at CEA-IRFM (Institut de Recherche sur la Fusion par confinement Magnétique), in France. The main challenge of such a photoneutralization system, is the development of a high finesse (>10000) Fabry-Perot optical cavity powered by 1 kW CW high stability laser. To maximize the photoneutralization process, the negative ion beam (D⁻) has to be adapted to the optical cavity geometry, therefore it should consist of a laminar ion beam sheet to maximize the overlapping between the D⁻ beam and the laser beam. Fig. 8.5 shows a block schematic of the Cybele concept [5] consisting of an elongated negative ion source producing a blade-like negative ion beam which is converted to neutrals after passing through the photo-neutralization cells. The negative ion source required for this scheme should have a completely different topology compared to conventional ICP drivers, like those for ITER, since it should be long and narrow. Among the different ways to produce elongated plasmas, those produced by helicon waves could be a promising candidate, for the reasons which are detailed in Sec. 1.2.1.

In the framework of a collaboration with CEA-IRFM, a helicon antenna in a birdcage geometry was tested from 2016 to 2019 on the Cybele ion source, shown in Fig. 8.6(a), which consists of a tall and narrow rectangular volume (height 1.2 m, width 15 cm, depth 20 cm) facing a large vacuum vessel, envisaged for negative ion extraction. The magnetic field needed to confine the plasma was originally produced by an DC current flowing in the coils around an iron frame, as shown in Fig. 8.6(b). The magnetic field sustaining the plasma column was then the result of field lines leaking into the middle of the iron frame, providing a field of intensity
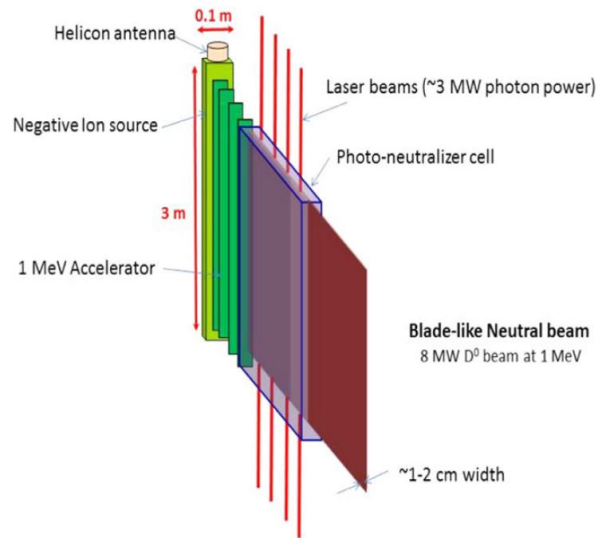
Figure 8.5 – Topology of a photoneutralization system of a negative ion sheet extracted by a helicon plasma column (from [5]).

~ 10 mT in the source volume. This arrangement had the advantage of providing a large available area for extraction, compatible to a radial extraction system such as that detailed in Sec. 8.1.1. This setup was tested with a birdcage antenna identical to that employed for RAID and installed on the top of the source. Measurements with LP showed that the plasma density was about 2 orders of magnitude lower than RAID and there were significant plasma losses on the vessel walls. This was perhaps mainly due to the magnetic field configuration which did not have the cylindrical symmetry favorable for helicon wave propagation, such as in the RAID magnetic field geometry. The Cybele magnetic field configuration was recently modified by using multiple internal coils along the plasma column to improve the homogeneity of the magnetic field and tests are currently underway to characterize this new configuration [5]. It is evident that the extraction of negative ions, in this case, would be performed by the available space between the coils, resulting in a segmented extractor, similar to the radial extraction scheme in RAID (see Sec. 8.1.1).

8.4 Discussion and Conclusions

Preliminary designs of two types of negative ion extractors to be installed on RAID are currently underway. The first consists of a $5 \times 100 \, \text{mm}^2$ slit extracting along the radial direction and exploiting the electron self-filtering effect due to the axial DC magnetic field. The second, is supposed to extract the negative ion ring along the axial direction and filter out the large electron flux by a circular array of permanent magnets. The primary issue which will be addressed is the compatibility of any electrically biased elements into the plasma and ascertain if the sustainment of a helicon discharge is possible even in the presence of a biased slit on the edge, or a large plate at the end of the plasma column. Experiments performed on the
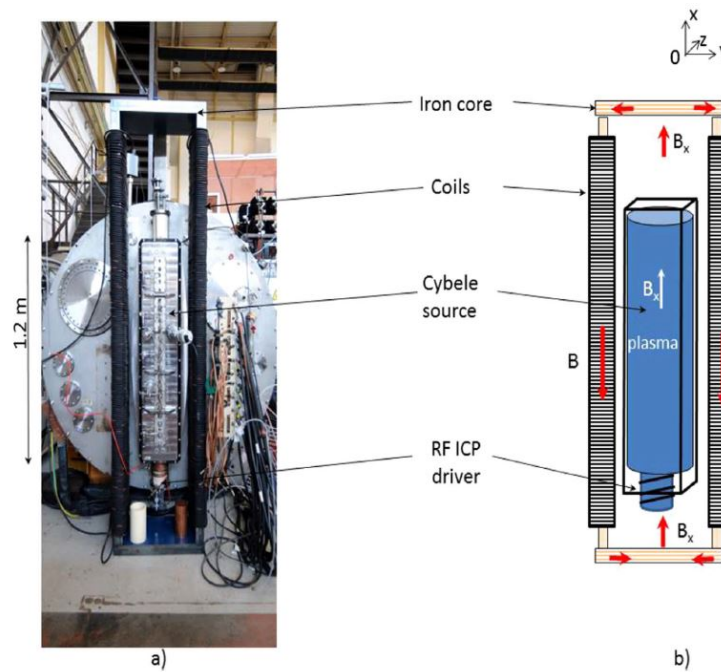
Figure 8.6 – (a) Picture of the Cybele source (b) scheme of the plasma region and the iron frame (from [127]).

Cybele source (see Sec. 8.3) with a birdcage antenna mounted on the top of a vessel with transverse dimensions smaller than RAID and a non cylindrical symmetric magnetic field topology, resulted in plasma densities ~2 orders of magnitude lower that RAID, suggesting that the helicon regime was not achieved. A smaller size extractor on RAID has the advantage of preserving the favorable magnetic field topology, successful for the achievement of H and D helicon plasma discharges, and maybe have only a local perturbing effect of the plasma column without interfering with the overall propagation of the helicon waves. Provided that negative ion extraction in RAID is practicable, the subsequent step would be the investigation of the issue of the co-extracted electrons and the related countermeasures to mitigate them. As an additional advancement in the comprehension of the system, the measurements of the extracted negative ion current should be correlated to source parameters. This would require the simultaneous use of plasma negative ion diagnostics, such as those described in Sec. 4.2 and in Sec. 4.1, and ion beam diagnostics, such as a retarded field energy analyzer. In parallel with extraction development, experimental efforts were devoted to the investigation of plasma discharges with multiple birdcages to improve the axial homogeneity and the power deposition efficiency.

9 | Summary and Conclusion

In this thesis, several aspects concerning the physics of the helicon plasmas are investigated both experimentally and numerically with the helicon source RAID (Resonant Antenna Ion Device), at the Swiss Plasma Center. This work is motivated by the necessity to study the possibility to employ helicon plasmas as sources of negative ions for the next generation of Neutral Beam Injectors (NBI), such as for DEMO (DEMOnstration Power Station). Helicon sources offer the advantage of producing high density plasmas with a few kW power and being compatible with high efficiency ($\gtrsim$ 93%) photoneutralization systems. A summary of the main results is provided below.

RAID plasma discharges are achieved using an alternative helicon antenna in a birdcage geometry, able to generate plasma columns with several gases including hydrogen and deuterium, relevant for fusion applications, and argon, helium, neon and nitrogen, for basic plasma physics. To characterize the plasma column, a combination of Langmuir Probes calibrated with a heterodyne microwave interferometer are employed. Microwave interferometry is often necessary to measure plasma density in RAID since it can reach $1 \cdot 10^{19} \, \mathrm{m}^{-3}$ with a few kW power and LPs suffer strong heating in this regime. Plasma radial profiles of electron density and temperature are centrally peaked reaching $\sim 5 \, \mathrm{eV}$ and decaying to $1 \, \mathrm{eV}$ over 5 cm along the radial direction. The entire plasma column was characterized, by means of a two axis LP, revealing a density peak at $\sim 50 \, \mathrm{cm}$ along the axial direction, suggesting the deposition of the helicon wave power away from the antenna region. To investigate the plasma dynamics, preliminary measurements of plasma density fluctuations by LPs in ion saturation were also performed. These showed that the plasma column exhibits an approximate azimuthal rigid rotation with a few kHz frequency. To compare the performance of the BirdCage (BC) antenna with a conventional antenna Half-Helix (HH), plasma radial profiles were compared, showing that the BC produces a plasma with much less density fluctuations, therefore suggesting a better RF coupling of the BC than the conventional HH antenna.

Following the characterization of global time-averaged and time-resolved features of RAID plasmas, experiments focused on laser-based diagnostics aimed at measuring the negative ion density in hydrogen and deuterium, directly relevant to fusion. H^- and D^- ions were

investigated by Cavity Ring-Down Spectroscopy (CRDS) and Langmuir Probe (LP) laser photodetachment. Major technical difficulties were initially encountered in the early phases of the CRDS installation in RAID due to the degradation of the HR (high reflectivity) coating when exposed to the plasma. By upgrading the setup with a number of technical improvements, it was then possible to obtain the first ever measurement of H^- and D^- CRDS in a helicon plasma source. By combining CRDS with LP laser photodetachment it was possible to extract the absolute radial density of H^- and D^-. It was found that H^- and D^- are located on a shell of radius ~ 5.5 cm and ~ 1.5 cm of FWHM attaining a density of ~ $2 \cdot 10^{16} \, m^{-3}$ in both H_2 and D_2 with 5 kW RF power. The shell-like profiles of negative ions is mainly due to the more efficient dissociative attachment reactions, producing H^- ions, on the cold plasma edge. These results show that a significant density of negative ions is formed in volume in helicon steady state plasma discharges. The attained value of negative ion density is still about 5 times lower than the target value for fusion applications (~ $1 \cdot 10^{17} \, m^{-3}$) and it is unlikely that they will be achieved only by higher power operation, because of competitive negative ion destruction processes. Perhaps, alternative magnetic field topologies, such as the expanding one, favorable to rapid electron cooling, should be considered.

To investigate the propagation of helicon waves in RAID a magnetic B-dot probe measuring the three components of the helicon wave field was designed and tested in RAID. The propagation of helicon waves was characterized in different conditions of densities, magnetic fields and pressures, and a good agreement with the helicon wave dispersion relation was ascertained. These results show that the Birdcage antenna can efficiently launch helicon waves in different gases. A numerical model in COMSOL Multiphysics, simulating the propagation of helicon waves in a RAID plasma produced by an antenna in a BirdCage geometry, supported the experimental observations. A good agreement was found when comparing the experimentally measured axial wavelength. A smaller, less invasive B-dot probe able to resolve finer radial helicon modes is currently envisaged.

In the framework of a collaboration with the AWAKE project (Advanced WAKefield Experiment) at CERN, aimed at the development of future plasma-based particle accelerators, a Thomson Scattering (TS) system was developed and tested in RAID. The purpose of this system is to perform precise and local measurements of plasma density and temperature in high density and uniform helicon plasmas, currently a promising candidate for particle acceleration. The results in RAID suggest that the current TS system could be used on the AWAKE helicon cell, with a limitation to density lower than $2 \cdot 10^{20} m^{-3}$ due to the partially coherent TS regime. Preliminary calculations to apply the current TS system in AWAKE and technical improvements, are presented. The TS was also an opportunity in RAID to benchmark the LP density measurements with an independent diagnostic. Plasma profiles in high power Ar plasma, were measured, showing hollow profiles, possibly a signature of neutral depletion. Further investigations may shed light on some not well understood phenomema of high power helicon plasmas.

To describe the transport of RAID hydrogen plasma and to compare with experimental results,

a fluid model was developed in COMSOL multiphysics. By introducing the experimental n_e and T_e profiles, the radial plasma potential, the magnetic field and considering a set of chemical reactions occurring in a hydrogen plasma, the transport equations for ion and neutral species i.e. H^+, H_2^+, H_3^+, H^- and H are solved, and equilibrium profiles are calculated. Negative hydrogen radial density profiles showed a very good agreement with experimental results, showing that negative ions are produced and survive in the cold plasma edge, and a significant fraction is transported to the hot, dense plasma center. The present model can be used to drive source optimization and the negative ion extraction envisaged for RAID. A significant step to improve helicon plasma modeling would be to couple the helicon propagation with the transport, but this requires the knowledge of the exact mechanisms of helicon power deposition, not completely understood. Moreover, since deuterium is ultimately relevant for fusion application, a deuterium transport model should be developed. It is expected that owing to the isotopic effect, the transport may significantly differ from hydrogen.

Leveraging the experimental and numerical efforts carried on RAID, the design of two types of negative ion extractors for RAID are currently under way. The first is a slit extractor along one radial direction, such as that initially envisaged for the *Cybele concept* [127] to investigate the photoneutralization of blade-like negative ion beams. The second is an annular extractor along the axis of the plasma column more similar to the extraction geometry from conventional ICP drivers. In the case where extraction of negative ions from RAID would be successful, this may open the road to further future investigations of the possible use of helicon plasmas as sources of negative ions for fusion.

Appendix

High Reflectivity (HR) mirrors for Cavity Ring-Down Spectroscopy

The use of suitable HR mirrors is mandatory for successful CRDS measurements. The gas temperature in the RAID vessel can reach $T \sim 800\,$K, according to OES spectroscopy measurements [94]. Therefore, mirror coatings may be subject to intense heat flux. Preliminary CRDS signals in the presence of plasma were acquired by using 0.8 in. diameter/ 6 m ROC (Radius Of Curvature), Fused Silica mirrors on a mirror mounting provided by the supplier. To minimize the flux of impinging hot gas particles on the mirrors' coating, hydrogen gas was continuously flushed by the purge channels welded onto the mirror mounting. Ring-down signals in vacuum with this first kind of mirrors resulted in $\tau \sim 20\,\mu$s, barely enough to detect negative ions. Tests in the presence of plasma were performed using the technique described in Sec. 4.1, consisting in the measurement of the jump of the Ring-Down time τ just after the plasma discharge. Following a few minutes of plasma exposure, however, the Ring-down dropped dramatically to $\tau \sim 2\,\mu$s, much lower than the sensitivity threshold and resulting in a reflectivity of $\sim 99.85\%$. Fig. 9.1 shows, on the right, a mirror exposed to plasma and, on the left, a mirror never exposed to plasma. A clear yellow nuance appeared on the surface exposed to the plasma, maybe as a result of the alteration of the coating due to hot gas exposure. To the naked eye, the nuance is quite homogeneous suggesting an isotropic source of alteration, perhaps a homogeneous flux of gas particles coming from the plasma. Since mirrors are very far from the plasma (40 cm at least), the only particles that can impinge on the mirrors are neutrals such as H_2 or H. Apart from the translational energy of the neutral particles, another source of energy deposition on the mirrors can be due to vibrationally excited H_2. These molecules are produced in the core of the plasma and could be transported to the mirrors' surface, where they de-excite by releasing their energy on the surface; the mirror coating in this case. Also, the recombination of H atoms on the surface, that are subsequently recycled as H_2 into the vessel, could be a potential source of energy that may alter the coating.

Apart from the appearance of the yellow nuance, the cause of such a drop of τ may be ascribed to the presence of dust deposited on the surface coating. Even a tiny grain of dust can scatter the light stored in the cavity and reduce the light confinement time in the optical cavity. Dust can come either from the gas purge channels, or from the vessel itself, since it is frequently opened to atmosphere for maintenance operations. Clear traces of grease were visible close to the vacuum ring on which the mirror is located. Because of the high temperature and the
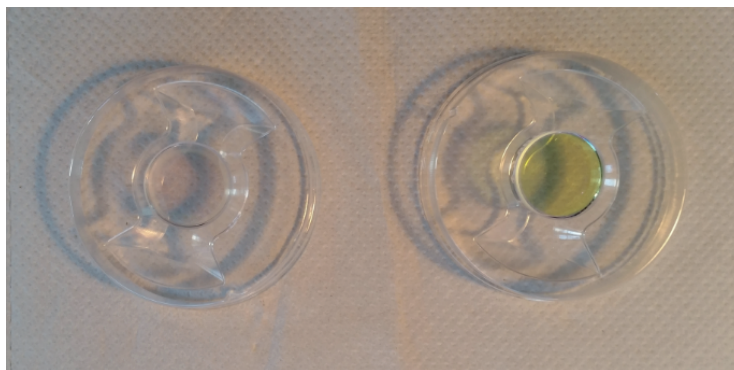
Figure 9.1 – On the left: mirror never exposed to plasma. On the right: mirror after a few minutes of plasma exposure.

adjustment movements of the HR mirrors during alignment, this grease could spread onto the surface up to the central part of the coating where light is reflected.

We therefore cleaned the surface of the mirrors as follows. Firstly, dust was removed by a jet of compressed air. Then, the coated surface was gently wiped with cleansing paper dipped in high purity acetone or methanol. Is is important to properly dry the surface and to avoid leaving traces of the cleaning product. Despite this cleaning with chemicals, the coating still showed the yellow nuance, suggesting that the HR coating probably irreversibly altered. Tests performed in the vessel in vacuum and in plasma did not show any recovery of the reflectivity. Other tests performed with another couple of the same kind of mirrors from the same supplier showed similar problems consisting of fast degradation of the coating after plasma exposures. Following the unfortunate experience with these first mirrors, we searched for another mirror supplier and we finally came up with Layertech [102]. Because of a different diameter standard (25mm diameter, 6.35 mm thick, fused silica), we re-machined new mirrors mountings, improving the mechanics. These mirrors were firstly characterized on an optical test bench separated from the vacuum vessel showing a reflectivity of 99.997%, as described in Sec. 4.1.1, largely satisfactory to detect negative ions. These mirrors were employed for the first CRDS experimental campaigns detailed in Sec. 4.1.4. After many hours of plasma exposures, they showed a considerable drop of the ring-down time (down to $\tau \sim 1\mu s$). Mirrors were therefore extracted from the mirror mountings to examine their condition. Fig. 9.2, on the right, depicts the Layertech mirrors after plasma exposure showing clear traces of grease deposited onto the surface. In Fig. 9.2, on the left, the plasma exposed mirror and a never exposed mirror are compared. However, despite the plasma exposure, the Layertech mirrors did not show any remarkable alteration of the colour, such as the aforementioned yellowish layer on the first sets of mirrors. After cleaning the surface with the procedure described above, it was possible to almost restore the original reflectivity, resulting in a ringdown time of $\tau \sim 40\mu s$, corresponding to R= 99.992%.

It was then possible to perform the second CRDS experimental campaign consisting of parameter scans in power, pressure and magnetic field which is detailed in Sec. 4.1.5. Fig. 9.3 shows the ring-down time during multiple plasma discharges of increasing power from 2 to 8
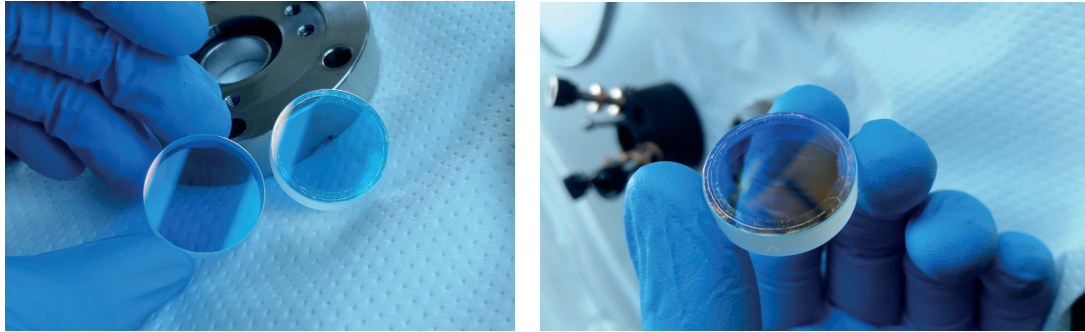
Figure 9.2 – On the right: Layertech mirror after many hours of plasma exposure showing traces of dirt on the coating. Its reflectivity was restored to almost the original value by cleaning with chemicals. On the left: comparison of Layertec mirror never exposed to plasma with one exposed to plasma.
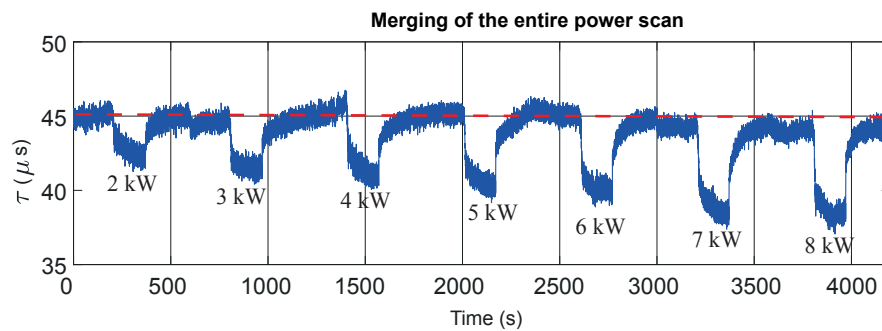
Figure 9.3 – Ring-down time during multiple plasma discharges of increasing RF power from 2 to 8 kW in hydrogen and 0.3 Pa gas pressure. Each plasma discharge is followed by an approximate recovery of the original ring-down time in vacuum ($\tau \sim 45\mu$s), marked by the red dashed line.

kW in hydrogen and 0.3 Pa gas pressure. By increasing the power of the plasma discharge the depth of the τ drop increases because of the increasing density of H^- ions. For each plasma discharge the negative ion density was computed by the technique described in Sec. 4.1.4. Each plasma discharge is followed by an approximate recovery of the original ring-down time in vacuum ($\tau \sim 45\mu$s), marked by the red dashed line.

To conclude, when proper HR mirrors are used in a plasma device such as RAID, where any particular cleaning standard for vacuum is taken, cleaning of the coating of the HR mirrors with chemicals may be the solution to keep the reflectivity sufficiently high.
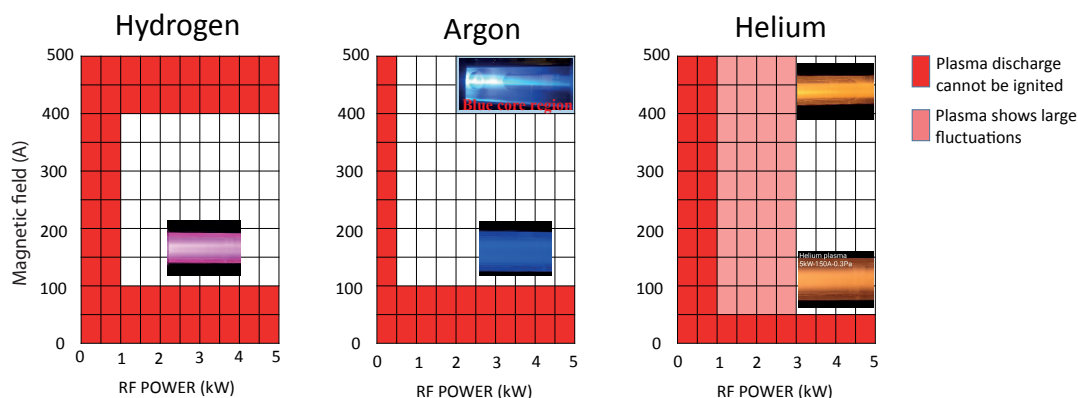
Figure 9.4 – Colour mapping showing the stability/instability regions in the plane RF power vs-magnetic field for H_2, He and Ar, and visible pictures of plasma in the corresponding areas.
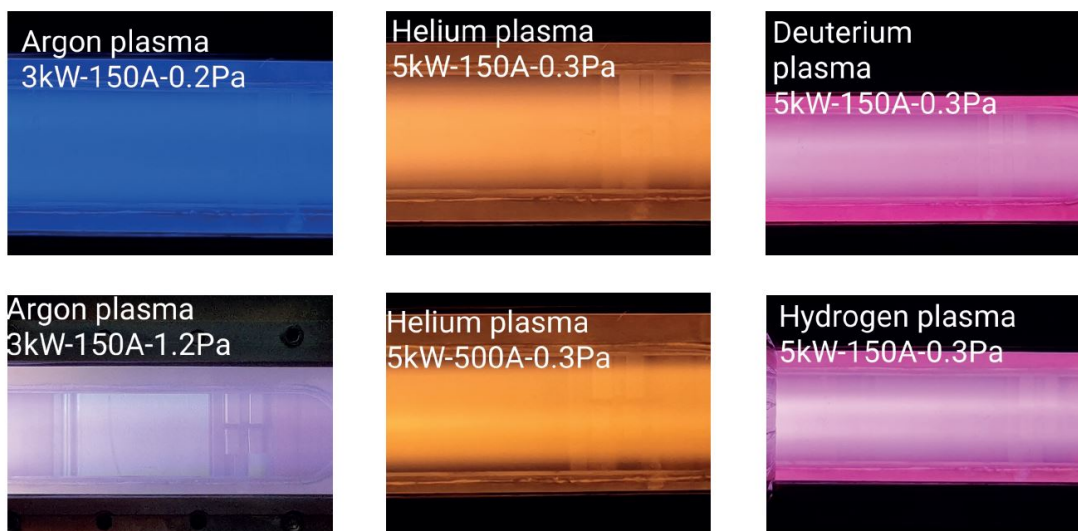
Figure 9.5 – Pictures of the plasma column in visible light for H_2, D_2, He and Ar.

Stability mapping and plasma pictures

The parameter space over which a plasma discharge can be achieved in RAID depends on the plasma species. Fig. 9.4 is a colour mapping showing the stability/instability regions for H_2, He and Ar plasma discharges in the magnetic field vs. RF power plane. Plasma discharges cannot be ignited in the red region, probably because the helicon wave cannot propagate and then deposit its energy into the plasma. In the case of helium gas, the plasma discharge is possible but plasma shows large fluctuations in visible light in the region of power 1-3 kW. Fig.9.5 shows pictures of the plasma in visible light. Plasma parameters are written on the pictures.
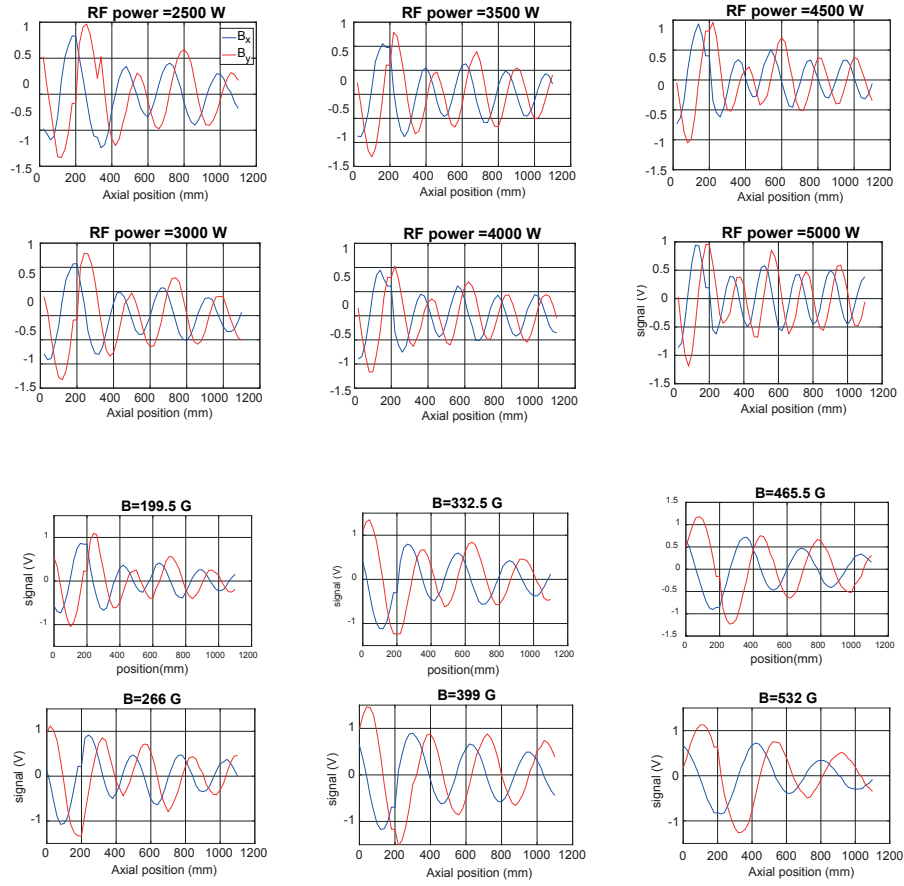
Figure 9.6 – B-dot measurements of the transverse components B_x and B_y of the helicon wave for different RF powers (first and second row) and different magnetic field (third and fourth row) in a H_2 plasma, at $r = 4.5\,$cm and 0.3 Pa gas pressure.

Helicon wave wavelength measurements

Fig. 9.6 shows the transverse components of the helicon wave measured in a H_2 plasma for different RF power (first and second row) and for different magnetic field (third and fourth row). By increasing the RF power, and thus the electron density, the axial wavelength is decreased. By increasing the magnetic field, the axial wavelength is increased. These trends are in agreement with the simple helicon wave dispersion relation.

Notations

List of acronyms

AD	Associative Detachment
Ar	Argon
AWAKE	Advanced WAKefield Experiment
CEA	Commissariat à l'Energie Atomique et aux énergies alternatives
CRDS	Cavity Ring Down Spectroscopy
DA	Dissociative Attachment
ED	Electron Detachment
EEDF	Electron Energy Distribution Function
FWHM	Full Width at Half Maximum
HR	High Reflectivity
ICP	Inductively Coupled Plasmas
ITER	International Experimental Thermonuclear Reactor
LoS	Lign of Sight
LP	Langmuir Probe
MITICA	Megavolt ITER Injector and Concept Advancement
MN	Mutual Neutralization
mw interferometry	microwave interferometry
NBI	Neutral Beam Injection
OES	Optical Emission Spectroscopy
O-mode	Ordinary mode
RAID	Resonant Antenna Ion Device
RAMI	Reliability, Availability, Maintainability and Inspectability
RF	Radio-Frequency
SNR	Signal-to-noise ratio
SOL	Scrape-Off Layer
TCV	Tokamak à Configuration Variable

TS	Thomson Scattering
SPIDER	Source for the Production of Ions of Deuterium Extracted from a Radio frequency plasma
SPC	Swiss Plasma Center
X-mode	Extraordinary mode

List of repeatedly used symbols

B	Magnetic field
B_0	axial magnetic field
σ	standard deviation of a quantity
$\langle \sigma v(.) \rangle$	reaction rate of a process
c	speed of light
e	elementary charge
f	frequency
I_{sat}	ion saturation current
j_{H^-}	extracted H^- current
j_{D^-}	extracted D^- current
j_e	extracted electron current
$\vec{k}$	wave vector
m_e	electron mass
m_i	mass of an ion
n_c	cut-off density
n_e	electron density
n_{H^-}	H^- density
t	time
T_e	electron temperature
T_i	ion temperature
T	neutral temperature
w	beam diameter
w_0	beam waist
ϵ_0	vacuum permittivity
λ	wavelength
λ_D	Debye length
τ	decay time
ω	pulsation of the wave
ω_{pe}	plasma frequency
ω_{ce}	electron cyclotron frequency
ω_{ci}	ion cyclotron frequency

Bibliography

[1] LF–2.7 GHz rf/if gain and phase detector - AD8302. Technical report, Analog Devices, 2002.

[2] E. Adli, A. Ahuja, and O. Apsimon *et al.* Acceleration of electrons in the plasma wakefield of a proton bunch. *Nature*, 561:363–367, 2018.

[3] R. Agnello, M. Barbisan, I. Furno, P. Guittienne, A. A. Howling, R. Jacquier, R. Pasqualotto, G. Plyushchev, Y. Andrebe, S. Béchu, I. Morgal, and A. Simonin. Cavity ring-down spectroscopy to measure negative ion density in a helicon plasma source for fusion neutral beams. *Rev. Sci. Instrum.*, 89:103504, 2018.

[4] R. Agnello, S. Béchu, I. Furno, P. Guittienne, , A. A. Howling, R. Jacquier, G. Plyushchev, M. Barbisan, , R. Pasqualotto, I. Morgal, and A. Simonin. Negative ion characterization in a helicon plasma source for fusion neutral beams by cavity ring-down spectroscopy and Langmuir probe laser photodetachment. *Nucl. Fusion*, 60:026007, 2020.

[5] K. M. Ahmed, R. Agnello, S. Béchu, G. Cartry, H. P. L. de Esch, I. Furno, P. Guittienne, A. Howling, R. Jacquier, I. Morgal, N. Sadeghi, and A. Simonin. Magnetic field configurational study on a helicon-based plasma source for future neutral beam systems. *Plasma Sources Sci. Technol.*, 28:095005, 2019.

[6] S. Aleiferis. *Experimental Study of* H$^-$ *negative ion production by electron cyclotron resonance plasmas*. PhD thesis, Université Grenoble-Aples, 2016.

[7] E. V. Appleton. Wireless studies of the ionosphere. *J. Inst. Elec. Engrs.*, 71:642, 1932.

[8] H. Arnichand, Y. Andrebe, P. Blanchard, S. Antonioni, S. Couturier, J. Decker, B. Duval, F. Felici, C. Galperti, P.-F. Isoz, P. Lavanchy, X. Llobet, B. Marlétaz, P. Marmillod, and J. Masur. New capabilities of the incoherent Thomson scattering diagnostics in the TCV tokamak: divertor and real-time measurements. *Journal of Instrumentation*, 14(09):C09013, sep 2019.

[9] F. Avino. *Turbulence at the boundary of toroidal plasmas with open and closed magnetic flux surfaces*. PhD thesis, Lausanne, 2015.

Bibliography

[10] AWAKEcollaboration. Awake Design Report. Technical Report SPSC-2013-013, CERN, 2013.

[11] AWAKEcollaboration. Acceleration of electrons in the plasma wakefield of a proton bunch. *Nature*, 561:363–367, 2018.

[12] M. Bacal. Photodetachment diagnostic techniques for measuring negative ion densities and temperatures in plasmas. *Rev. Sci. Instrum.*, 71:3981, 2001.

[13] M. Bacal. Physics aspects of negative ion sources. *Nucl. Fusion*, 46:S250–S259, 2006.

[14] M. Bacal, A. M. Bruneteau, and M. Nachman. Negative ion production in hydrogen plasmas confined by a multicusp magnetic field. *Journal of Applied Physics*, 55:15, 1984.

[15] M. Bacal, R. McAdams, and B. Lepetit. The Negative Ion Mean Free Path And Its Possible Implications. *AIP Conf. Proc.*, 13:1390, 2011.

[16] M. Bagatin, A. Coniglio, M. D'Arienzo, A. D. Lorenzi, S. Gerardin, A. Paccagnella, R. Pasqualotto, S. Peruzzo, and S. Sandri. Radiation Environment in the ITER neutral beam injector prototype. *IEEE Trans. Nucl. Sci.*, 59:1099, 2012.

[17] F. E. Baghiti-Sube, F. Basht, and M. Bacal. Photodetachment diagnostics of plasma with a high n_-/n_e ratio. *Rev. Sci. Instrum.*, 67:2221, 1996.

[18] J. Bardsley. Configuration interaction in the continuum states of molecules. *J. Phys. B:At. Mol. Phys.*, 1:349, 1968.

[19] M. Berger, U. Fantz, and S. C.-K. and. Cavity ring-down spectroscopy on a high power RF driven source for negative hydrogen ions. *Plasma Sources Science and Technology*, 18(2):025004, feb 2009.

[20] T. Biewer, S. J. Meitner, J. Rapp, H. Ray, and G. Shaw. First results from the Thomson scattering diagnostic on the proto-MPEX. *Rev. Sci. Instrum.*, 87:11E518, 2016.

[21] T. M. Biewer and G. Shaw. Initial implementation of a Thomson scattering diagnostic for Proto-MPEX. *Rev. Sci. Instrum.*, 85:11D812, 2014.

[22] G. G. Borg and T. Jahreisa. Radio-Frequency power combiner for cw and pulsed applications. *Rev. Sci. Intrum.*, 65:452, 1994.

[23] R. W. Boswell. Plasma production using a standing helicon wave. *Physics Letters*, 33A(7):457–458, 1970.

[24] S. A. Bozhenkov, M. Beurskensa, A. Dal Molinb, G. Fucherta, E. Pascha, M. Stoneking, M. Hirscha, U. Hofela, J. Knauera, and J. Svenssona. The Thomson scattering diagnostic at the Wendelstein 7-X and its performances in the first operation phase. *J. Instrumentation*, 87:P10004, 2017.

[25] S. Briefi and U. Fantz. "Investigation of helicon discharges as rf coupling concept of negative hydrogen ion sources". *AIP Conference Proceedings*, 278:1515, 2013.

[26] A. M. Bruneteau, C. Courteille, R. Leroy, and M. Bacal. Investigation of two negative hydrogen and deuterium ion sources: Effect of the volume. *Rev. Sci. Intrum.*, 67:3827, 1996.

[27] B. Buttenschön, N. Fahrenkamp, and O. Grulke. A high power, high density helicon discharge for the plasma wakefield accelerator experiment AWAKE. *Plasma Phys. Control. Fusion*, 60:075005, 2018.

[28] S. Béchu. Master professionnel "Technologies et applications des plasmas. Technical report, Centre de Recherche Plasma-Matériaux-Nanostructures, Grenoble (France), 2010.

[29] S. Béchu, A. Soum-Glaude, A. Bès, A. Lacoste, P. Svarnas, S. Aleiferis, A. A. Ivanov, and M. Bacal. Multi-dipolar microwave plasmas and their applicaiton to negative ion production. *Physics of Plasmas*, 20:101601, 2013.

[30] T. N. Carlstrom, C. L. Hsieh, R. Stockdale, D. G. Nilson, and D. N. Hill. Initial operation of the divertor Thomson scattering diagnostic on DIII-D. *Rev. Sci. Instrum.*, 68:1195, 1997.

[31] P. Chabert and N. Braithwaite. *Physics of Radio-Frequency Plasmas.* Cambridge, 2011.

[32] O. Chellaï. *Oulfa Chellaï.* PhD thesis, Millimeter-Wave Beam Scattering by Edge Turbulence in Magnetically-Confined Plasmas, 2019.

[33] F. F. Chen. Plasma ionization by helicon waves. *Plasma Physics and Controlled Fusion*, 33:339, 1991.

[34] F. F. Chen. *Introduction to plasma physics and controlled fusion.* Springer, 2006.

[35] F. F. Chen, I. D. Sudit, and M. Light. Downstream physics of the helicon discharge. *Plasma Sources Sci. Technol.*, 5:173–180, 1996.

[36] S. Christ-Koch, U. Fantz, and M. B. and. Laser photodetachment on a high power, low pressure rf-driven negative hydrogen ion source. *Plasma Sources Science and Technology*, 18(2):025003, feb 2009.

[37] C. Courteille, A. M. Bruneteau, and M. Bacal. Investigation of a large volume negative hydrogen ion source. *Rev. Sci. Instrum.*, 66:2533, 1995.

[38] S. B. D Rauner and U. Fantz. "RF power transfer efficiency of inductively coupled low pressure h2 and d2 discharges". *Plasma Sources Sci. Technol.*, 26:095004, 2017.

[39] A. W. Degeling, C. O. Jung, R. W. Boswell, and R. E. A. Plasma production from helicon waves. *Physics of Plasmas*, 3:7, 1996.

Bibliography

[40] P. Devynck, J. Auvray, M. Bacal, P. Berlemont, J. Bruneteau, R. Leroy, and R. A. Stern. "photodetachment technique for measuring H- velocities in a hydrogen plasma". *Rev. Sci. Intrum.*, 50:2944, 1989.

[41] K. Dittmann, C. Küllig, and J. Meichsner. 160 GHz gaussian beam microwave interferometry in low-density rf plasmas. *Plasma Sources Science and Technology*, 21(2):024001, apr 2012.

[42] A. J. H. Donné. High spatial resolution interferometry and polarimetry in hot plasmas. *Rev. Sci, Instrum.*, 66:3407, 1995.

[43] M. J. Druyvesteyn. Der Niedervoltbogen. *ZS. f. Phys.*, 69:781, 1930.

[44] M. K. et al. High fusion performance from deuterium–tritium plasmas in jet. *Nucl. Fusion*, 39, 1999.

[45] U. Fantz, H. Falter, P. Franzen, D. Wünderlich, M. Berger, A. Lorenz, W. Kraus, P. McNeely, R. Riedl, and E. Speth. Spectroscopy—a powerful diagnostic tool in source development. *Nucl. Fusion*, 46(6):S297–S306, may 2006.

[46] A. Fasoli, B. Labit, M. McGrath, S. H. Müller, G. Plyushchev, M. Podestà, and F. M. Poli. Electrostatic turbulence and transport in a simple magnetized plasma. *Phys. of Plasmas*, 13:55902, 2006.

[47] G. Federici, C. Bachmann, L. Barucca, C. Baylard, W. Biel, L. Boccaccini, C. Bustreo, S. Ciattaglia, F. Cismondi, V. Corato, C. Day, E. Diegele, T. Franke, E. Gaio, C. Gliss, T. Haertl, A. Ibarra, J. Holden, G. Keech, R. Kembleton, A. Loving, F. Maviglia, J. Morris, B. Meszaros, I. Moscato, G. Pintsuk, M. Siccinio, N. Taylor, M. Tran, C. Vorpahl, H. Walden, and J. You. Overview of the DEMO staged design approach in europe. *Nucl. Fusion*, 59(6):066013, apr 2019.

[48] S. Franke. *Application of Thomson scattering at* 1.06 µm *as a diagnostic for spatial profile measurements of electron temperature and density on the TCV tokamak*. PhD thesis, Ecole Polytechnique Fédérale de Lausanne, 1997.

[49] L. Friedland, C. I. Ciubotariu, and M. Bacal. "Dynamic plasma response in laser-photodetachment experiments in hydrogen plasmas". *Phys. Rev. E*, 49:4353, 1994.

[50] G. Fubiani, L. Garrigues, G. Hagelaar, N. Kohen, and J. P. Boeuf. Modeling of plasma transport and negative ion extraction in a magnetized radio-frequency plasma source. *New Journal of Physics*, 19(1):015002, jan 2017.

[51] O. Fukumasa and K. Yoshino. Isotope effect and cesium dependence of negative ion production in volume and ion sources. *Rev. Sci. Intrum.*, 69:941, 1998.

[52] I. Furno. *Fast transient phenomena measured by soft X-ray emission in TCV Tokamak*. PhD thesis, Ecole Polytechnique Fédérale de Lausanne, 2001.

[53] I. Furno, R. Agnello, U. Fantz, A. Howling, R. Jacquier, C. Marini, G. Plyushchev, P. Guit-tienne, and A. Simonin. Helicon wave-generated plasmas for negative ion beams for fusion. *EPJ Web of Conferences*, 157:03014, 2017.

[54] I. Furno, H. Reimerdes, and B. Labit. Plasma diagnostics in basic plasma devices and tokamaks: form principles to practice. Technical report, Swiss Plasma Center, 2018.

[55] S. Ghosh, P. K. Chattopadhyay, J. Ghosh, and D. Bora. Rf compensation of single Lang-muir probe in low density helicon plasma. *Fusion Engineering and Design*, 112:915 – 918, 2016.

[56] P. F. Goldsmith. *Quasioptical Systems*. IEEE press, 0000.

[57] C. Gorse, R. Celiberto, M. Cacciatore, A. Laganà, and M. Capitelli. From dynamics to modeling of plasma complex systems: negative ion (H-) sources. *Chemical Physics*, 161:211–227, 1992.

[58] R. H. Goulding, J. B. O. Caughman, J. Rapp, T. M. Biewer, T. S. Bigelow, I. H. Campbell, J. F. Caneses, D. Donovan, N. Kafle, E. H. Martin, H. B. Ray, G. C. Shaw, and M. A. Showers. Progress in the Development of a High Power Helicon Plasma Source for the Materials Plasma Exposure Experiment. *Fusion Science and Technology*, 72:588–592, 2017.

[59] T. S. Green. Intense ion beams. *Reports on Progress in Physics*, 37(10):1257–1344, oct 1974.

[60] L. R. Grisham. Lithium Jet Neutralizer to Improve Negative Ion Neutral Beam Perfor-mance. *AIP conference proceedings*, 1097:364, 2009.

[61] P. Guittienne, E. Chevalier, and C. Hollenstein. Towards an optimal antenna for helicon wave excitation. *Journal of Applied Physics*, 98:083304, 2005.

[62] P. Guittienne, A. A. Howling, and I. Furno. Two-fluid solutions for langmuir probes in collisionless and isothermal plasma, over all space and bias potential. *Phys. Plasmas*, 25:093519, 2018.

[63] H.-J. Hartfuss and T. Geist. *Fusion Plasma Diagnostics with mm-Waves*. Wiley, 2013.

[64] A. Hatayama, S. Nishioka, K. Nishida, S. Mattei, J. Lettry, K. Miyamoto, T. Shibata, M. Onai, S. Abe, S. Fujita, S. Yamada, and A. Fukano. Present status of numerical mod-eling of hydrogen negative ion source plasmas and its comparison with experiments: Japanese activities and their collaboration with experimental groups. *New Journal of Physics*, 20(6):065001, jun 2018.

[65] J. Hawke, Y. Andrebe, P. Bertizzolo, R. Blanchard, R. Chavan, J. Decker, B. Duval, P. La-vanchy, X. Llobet, B. Marlétaz, P. Marmillod, G. Pochon, and M. Toussaint. Improving spatial and spectral resolution of TCV Thomson scattering. *J. Instrumentaion*, 12:C12005, 2017.

[66] R. Hemsworth, H. Decamps, J. Graceffa, B. Schunke, M. Tanaka, M. Dremel, A. Tanga, H. D. Esch, F. Geli, J. Milnes, T. Inoue, D. Marcuzzi, P. Sonato, and P. Zaccaria. Status of the ITER heating neutral beam system. *Nuclear Fusion*, 49(4):045006, mar 2009.

[67] R. S. Hemsworth, D. Boilson, P. Blatchford, M. D. Palma, G. Chitarin, H. P. L. de Esch, F. Geli, M. Dremel, J. Graceffa, D. Marcuzzi, G. Serianni, D. Shah, M. Singh, M. Urbani, and P. Zaccaria. Overview of the design of the ITER heating neutral beam injectors. *New Journal of Physics*, 19(2):025005, feb 2017.

[68] R. S. Hemsworth and T. Inoue. Positive and Negative Ion Sources for Magnetic Fusion. *Transaction on Plasma Science*, 33(6):1799, dec 2005.

[69] J. R. Hiskes. Cross section for the vibrational excitation of state via electron collisional excitation of the higher singlet states. *J. Appl. Phys.*, 51:4592, 1980.

[70] A. T. Hjartarson, E. G. Thorsteinsson, and J. T. Gudmundsson. Low pressure hydrogen discharges diluted with argon explored using a global model. *Plasma Sources Science and Technology*, 19(6):065008, nov 2010.

[71] C. Hollenstein, P. Guittienne, and A. A. Howling. Resonant rf network antennas for large-area and large-volume inductively coupled plasma source. *Plasma Sources Sci. Technol.*, 22:055021, 2013.

[72] J. Horáček, M. Čížek, K. Houfek, P. Kolorenč, and W. Domcke. Dissociative electron attachment and vibrational excitation of H2 by low-energy electrons: Calculations based on an improved non local resonance model. II. Vibrational excitation. *Phys. Rev.*, 73:022701, 2004.

[73] A. A. Howling and D. C. Robinson. Coherent mode activity in the edge of tosca tokamako. *Plasma Phys. Control. Fusion*, 39:1863, 1988.

[74] M. Huang and G. M. Hieftje. A new procedure for determination of electron temperatures and electron concentrations by Thomson scattering from analytical plasmas. *Spectrochim. Acta Part B*, 44B:291–305, 1989.

[75] I. H. Hutchinson. *Principle of Plasma Diagnostics*. Cambridge, 1981.

[76] L. Ibba. Microwave Interferometry Plasma Diagnostic in TORPEX. Technical report, Swiss Plasma Center, 2016.

[77] R. Jacquier, R. Agnello, B. P. Duteil, P. Guittienne, A. Howling, G. Plyushchev, C. Marini, A. Simonin, I. Morgal, S. Bechu, and I. Furno. First B-dot measurements in the RAID device, an alternative negative ion source for DEMO neutral beams. *Fusion Engineering and design*, 146:1140–1144, 2019.

[78] R. K. Janev, D. Reiter, and U. Samm. Collision processes in low-temperature hydrogen plasmas. *Berichte des Forschungszentrums Jülich*, 2003.

[79] H. V. W. Jesse Santoso and C. S. Corr. High density negative hydrogen ion production in a high power pulsed helicon discharge. *Plasma Sources Sci. Technol.*, 27:10LT03, 2018.

[80] A. Kiejna and K. Wojciechowski. Work function of metals: relation between theory and experiment. *Progress in Surface Science*, 11:308, 1981.

[81] E. Krishnakumar, S. Denifl, C. I, S. Markelj, and N. J. Mason. Dissociative electron attachment cross sections for H_2 and D_2. *Physical Review Letters*, 106:243201, 2011.

[82] A. Lachat. Experimental investigation of the RF power coupling efficiency of different helicon antennas for plasma generation. EPFL, 2019.

[83] I. Langmuir and K. B. Blodgett. Currents limited by space charge between concentric spheres. *Phys. Rev.*, 24:10LT03, 1924.

[84] J. D. Lawson. Some Criteria for a Power Producing Thermonuclear Reactors. *Proc. Phys. Soc*, 60:6, 1957.

[85] B. P. LeBlanc. Thomson scattering density calibration by rayleigh and rotational raman scattering on nstx. *Rev. Sci. Instrum.*, 79:10E737, 2008.

[86] K. Y. Lee, K. I. Lee, J. H. Kim, and T. Lho. High resolution Thomson scattering system for steady-state linear plasma sources. *Rev. Sci. Intrum.*, 89:013508, 2018.

[87] K. K. Lehmann and D. Romanini. The superposition principle and cavity ring-down spectroscopy. *The Journal of Chemical Physics*, 105:10263, 1996.

[88] J. Lesurf. *Millimeter-wave Optics, Devices and Systems.* CRC Press, 1990.

[89] M. A. Lieberman and A. J. Lichtenberg. *Principles of plasma discharges and material processing.* Wiley, 1994.

[90] M. Light and F. F. Chen. Helicon wave excitation with helical antennas. *Physics of Plasma*, 2:1084, 1994.

[91] M. Light, I. D. Sudit, F. F. Chen, and D. Arnush. Axial propagation of helicon waves. *Physics of Plasmas*, 2:4094, 1995.

[92] R. M. Magee, M. E. Galante, J. Carr, Jr., G. Lusk, D. W. McCarren, and E. E. Scime. Neutral depletion and the helicon density limit r. *Physics of Plasmas*, 20:123511, 2013.

[93] J. F. C. Marin. *Helicon wave propagation and plasma equilibrium in high-density hydrogen plasma in converging magnetic field.* PhD thesis, Australian National University, 2015.

[94] C. Marini, R. Agnello, B. P. Duval, I. Furno, A. A. Howling, R. Jacquier, A. N. Karpushov, G. Plyushchev, K. Verhaegh, and P. Guittienne. Spectroscopic characterization of H_2 and D_2 helicon plasmas generated by a resonant antenna for neutral beam applications in fusion. *Nucl. Fusion*, 57:036024, 2017.

[95] A. G. McLean, V. A. Soukhanovskii, S. L. Allen, T. N. Carlstrom, B. P. LeBlanc, M. Ono, and B. C. Stratton. Conceptual design of a divertor Thomson scattering diagnostic for NSTX-Ua. *Rev. Sci. Intrum.*, 85:11E825, 2014.

[96] v. d. H. J. Meiden. *Thomson scattering on low and high temperature plasmas.* PhD thesis, Technische Universiteit Eindhoven, 2002.

[97] D. G. Miljaky and F. F. Chen. Density limit in helicon discharges. *Plasma Sources Sci. Technol.*, 7:537–549, 1998.

[98] O. Motojima. The ITER project construction status. *Nucl. Fusion*, 55:20pp, 2015.

[99] S. H. Müller, A. Diallo, A. Fasoli, I. Furno, B. Labit, and M. Podestà. "Plasma blobs in a basic toroidal experiment: Origin, dynamics, and induced transport". *Physics of Plasmas*, 14:110704, 2007.

[100] H. Nakano, K. Tsumori, M. Shibuya, S. Geng, M. Kisaki, K. Ikeda, K. Nagaoka, M. Osakabe, Y. Takeiri, and O. Kaneko. Cavity ringdown technique for negative-hydrogen-ion measurement in ion source for neutral beam injector. *Journal of Instrumentation*, 11(03):C03018–C03018, mar 2016.

[101] O'Keefe and D. G. Deacon. Cavity ring-down optical spectrometer for absorption measurements using pulsed laser sources. *Rev.Sci. Intrum.*, 59:2544, 1988.

[102] L. optical coating optics. Measurement Report of HR mirrors, private communication. Technical report, Layertech, 2018.

[103] N. Oudini, N. Sirse, F. Taccogna, A. R. Ellingboe, and A. Bendib. Photo-detachment signal analysis to accurately determine electronegativity, electron temperature, and charged species density. *APPLIED PHYSICS LETTERS*, 109:124101, 2016.

[104] A. Pandey, D. Mukherjee, D. Borah, M. Bandyopadhyay, H. Tyagi, R. Yadav, and A. Chakraborty. Characterization of hydrogen plasma in a permanent ring magnet based helicon plasma source for negative ion source research. *Plasma Phys. Control. Fusion*, 61:065003, 2019.

[105] R. Pasqualotto, M. Agostini, M. Barbisan, M. Brombin, R. Cavazzana, G. Croci, M. D. Palma, R. Delogu, M. D. Muri, A. Muraro, S. Peruzzo, A. Pimazzoni, N. Pomaro, M. Rebai, A. Rizzolo, E. Sartori, G. Serianni, S. Spagnolo, M. Spolaore, M. Tardocchi, B. Zaniol, and M. Zaupa. A suite of diagnostics to validate and optimize the prototype ITER neutral beam injector. *Journal of Instrumentation*, 12(10):C10009–C10009, oct 2017.

[106] R. pasqualotto, A. Alfier, and L. Lotto. Design of a cavity ring-down spectroscopy diagnostic for negative ion rf source SPIDER. *Rev. Sci. Intrum.*, 81:10D710, 2010.

[107] R. Pasqualotto, P. Nielsen, C. Gowers, M. Beuskens, M. Kempenaars, T. Carlstrom, D. Johnson, and J.-E. Contributors. High resolution Thomson scattering for Joint European Torus (JET). *Rev. Sci. Instrum.*, 75:3891, 2004.

[108] A. Pigarov and I. Krasheninnikov. Application of the collisional-radiative, atomic-molecular model to the recombining divertor plasma. *Physics Letters*, 222:251–257, 1996.

[109] A. Pitzschke. *Pedestal Characteristics and MHD Sability of H-mode in TCV*. PhD thesis, Ecole Polytechnique Fédérale de Lausanne, 2011.

[110] G. Plyushchev, R. Kersevan, A. Petrenko, and P. Muggli. A rubidium vapor source for plasma source for AWAKE. *J. Phys. D: Appl. Phys.*, 51:025205, 2018.

[111] T. K. Popov, M. Mitov, A. Bankova, P. Ivanova, M. Dimitrova, S. Rupnik, J. Kovačič, T. Gyergyek, M. Cerček, and F. M. Dias. Langmuir probe method for precise evaluation of negative-ion density in electronegative gas discharge magnetized plasma. *Contrib. Plasma Phys.*, 53:51–56, 2013.

[112] P. N. R. Pasqualotto and L. Giudicotti. *Rev. Sci. Instrum.*, 72:1134, 2001.

[113] J. Rapp, L. W. Owen, J. Canik, J. D. Lore, J. F. Caneses, N. Kafle, H. Ray, and M. Showers. Radial transport modeling of high density deuterium plasmas in proto-MPEX with the B2.5-Eirene code. *Physics of Plasma*, 26:042513, 2019.

[114] M. P. Reilly, W. Lewis, and G. H. Miley. Magnetic field probes for use in radio frequency plasma. *Rev. Sci. Intrum.*, 80:053508, 2009.

[115] B. E. A. Saleh. *Fundamentals of Photonics*. Wiley, 1991.

[116] E. E. Salpeter. Electron Density Fluctuations in Plasma. *Phys. Rev.*, 120:1528–1535, 1960.

[117] J. Santoso, R. Manoharan, S. O'Byrne, and C. S. Corr. Negative hydrogen ion production in a helicon plasma source. *Phys. Plasma*, 22:093513, 2015.

[118] J. S. Santoso. *Production of Negative Hydrogen Ions in a High-Powered Helicon Plasma Source*. PhD thesis, 2018.

[119] M. N. M. Sasao and M. Bacal. H^- laser photodetachment at 1064, 532, and 355 nm in plasma. *Journal of Applied Physics*, 83:2944, 1998.

[120] K. Sawada and T. Fujimoto. Effective ionization and dissociation rate coefficients of molecular hydrogen in plasma. *Journal of Applied Physics*, 78:2913, 1995.

[121] R. Scannell, M. Beurskens, M. Kempenaars, G. Naylor, M. Walsh, T. O'Gorman, and R. Pasqualotto. Absolute calibration of LINDAR Thomson scattering system by rotational Raman scattering. *Rev. Sci. Intrum.*, 81:045107, 2010.

[122] E. E. Scime, A. Kesee, and R. W. Boswell. Mini-conference on helicon plasma sources. *Phys. Plasmas*, 15:058301, 2008.

[123] A. C. Selden. Simple analytic form of the relativistic Thomson scattering spectrum. *Physics letters*, 79A:2221, 1980.

[124] B. Seo, S. You, J. Kim, D. S. b, Y. Shin, and H. Chang. Measurements of electron energy probability functions in helicon discharge by laser Thomson scattering. *Thin Solid Films*, 547:52–56, 2013.

[125] S. Shinohara, D. Kuwahara, T. Furukawa, S. Nishimura, T. Yamase, Y. Ishigami, H. Horita, A. Igarashi, and S. Nishimoto. Development of featured high-density helicon sources and their application to electrodeless plasma thruster. *Plasma Physics and Controlled Fusion*, 61(1):014017, nov 2018.

[126] T. Shoji, Y. Sakawa, S. Nakazawa, K. Kadota, and T. Sato. Plasma production by helicon waves. *Plasma Sources Sci. Technol.*, 2:5–10, 1993.

[127] A. Simonin, R. Agnello, S. Bechu, J. M. Bernard, C. Blondel, J. P. Boeuf, D. Bresteau, G. Cartry, W. Chaibi, C. Drag, B. P. Duval, H. P. L. de Esch, G. Fubiani, I. Furno, C. Grand, P. Guittienne, A. Howling, R. Jacquier, C. Marini, and I. Morgal. Negative ion source development for a photoneutralization based neutral beam system for future fusion reactors. *New Journal of Physics*, 18(12):125005, dec 2016.

[128] D. A. Skinner, A. M. Bruneteau, P. Berlemont, C. Courteille, R. Leroy, , and M. Bacal. Isotope effect and electron-temperature dependence in volume h and d ion sources. *PHYSICAL REVIEW E*, 48:2122, 1993.

[129] V. Smil. *Energy and civilizations*. Massachusetts Institute of Technology, 2017.

[130] P. Sonato, P. Agostinetti, U. Fantz, T. Franke, I. Furno, A. Simonin, and M. Q. Tran. Conceptual design of the beam source for the DEMO neutral beam injectors. *New Journal of Physics*, 18(12):125002, dec 2016.

[131] E. Speth, H. Falter, P. Franzen, U. Fantz, M. Bandyopadhyay, S. Christ, A. Encheva, M. Fröschle, D. Holtum, B. Heinemann, W. Kraus, A. Lorenz, C. Martens, P. McNeely, S. Obermayer, R. Riedl, R. Süss, A. Tanga, R. Wilhelm, and D. Wünderlich. Overview of the RF source development programme at IPP garching. *Nucl. Fusion*, 46(6):S220–S238, may 2006.

[132] I. D. Sudit and F. F. Chen. Discharge equilibrium of a helicon plasma. *Plasma Sources Sci. Technol.*, 5:43–53, 1995.

[133] J. D. Swift. *Electrical probes for plasma diagnostics*. 1970.

[134] T. Tajima and J. M. Dawson. Laser Electron Accelerator. *Phys. Rev. Lett.*, 43:267, 1979.

[135] K. Takahashi, S. Takayama, A. Komuro, and A. Ando. Standing helicon wave induced by a rapidly bent magnetic field in plasmas. *Physical Review Letters*, 116:135001, 2016.

[136] S. C. Thakur, C. Brandt, L. Cui, J. J. Gosselin, , and G. R. Tynan. Formation of the Blue Core in Argon Helicon Plasma. *IEEE TRANSACTIONS ON PLASMA SCIENCE*, 43:2754, 2015.

[137] C. Theiler, I. Furno, A. Kuenlin, P. Marmillod, and A. Fasoli. Practical solutions for reliable triple probe measurements in magnetized plasmas. *Rev. Sci. Instrum.*, 82:82, 2011.

[138] D. Thompson, R. Agnello, I. Furno, A. Howling, R. Jacquier, G. Plyushchev, and E. Scime. Ion heating and flows in a high power helicon source. *Phys. Plasmas*, 24:063517, 2017.

[139] V. Toigo, S. D. Bello, E. Gaio, A. Luchetta, R. Pasqualotto, P. Zaccaria, M. Bigi, G. Chitarin, D. Marcuzzi, N. Pomaro, G. Serianni, P. Agostinetti, M. Agostini, V. Antoni, D. Aprile, C. Baltador, M. Barbisan, M. Battistella, M. Boldrin, M. Brombin, M. D. Palma, A. D. Lorenzi, R. Delogu, M. D. Muri, F. Fellin, A. Ferro, G. Gambetta, L. Grando, P. Jain, A. Maistrello, G. Manduchi, N. Marconato, M. Pavei, S. Peruzzo, N. Pilan, A. Pimazzoni, R. Piovan, M. Recchia, A. Rizzolo, E. Sartori, M. Siragusa, E. Spada, S. Spagnolo, M. Spolaore, C. Taliercio, M. Valente, P. Veltri, A. Zamengo, B. Zaniol, L. Zanotto, M. Zaupa, D. Boilson, J. Graceffa, L. Svensson, B. Schunke, H. Decamps, M. Urbani, M. Kushwah, J. Chareyre, M. Singh, T. Bonicelli, G. Agarici, A. Garbuglia, A. Masiello, F. Paolucci, M. Simon, L. Bailly-Maitre, E. Bragulat, G. Gomez, D. Gutierrez, G. Mico, J.-F. Moreno, V. Pilard, A. Chakraborty, U. Baruah, C. Rotti, H. Patel, M. Nagaraju, N. Singh, A. Patel, H. Dhola, B. Raval, U. Fantz, M. Fröschle, B. Heinemann, W. Kraus, R. Nocentini, R. Riedl, L. Schiesko, C. Wimmer, D. Wünderlich, M. Cavenago, G. Croci, G. Gorini, M. Rebai, A. Muraro, M. Tardocchi, and R. Hemsworth. The ITER neutral beam test facility towards SPIDER operation. *Nuclear Fusion*, 57(8):086027, jul 2017.

[140] J. L. Toulouzan, J. J. Locquet, D. Allano, P. Savary, and R. D'Arrigo. Inversion d'Abel d'un plasma cylindrique d'hélium réalisation d'un spectrographe stigmatique à détecteur vidicon. *J. Opt.*, 12:369, 1981.

[141] O. Tudisco, A. L. Fabris, C. Falcetta, L. Accatino, R. D. Angelis, M. Manente, M. F. F. Ferri, C. Neri, C. Mazzotta, D. Pavarin, F. Pollastrone, G. Rocchi, A. Selmo, L. Tasinato, F. Trezzolani, and A. A. Tuccillo. A microwave interferometer for small and tenuous plasma density measurements. *Rev. Sci. Instrum.*, 84:033505, 2013.

[142] J. M. Urrutia and R. L. Stenzel. Helicons in uniform fields. I. Wave diagnostics with hodograms. *Phys. Plasmas*, 25:032111, 2018.

[143] J. Vieira, R. A. Fonseca, W. B. Mori, and L. O. Silva. Ion Motion in Self-Modulated Plasma Wakefield Accelerators. *Phys. Rev. Lett.*, 109:145005, 2018.

[144] K. Warner and G. M. Hieftje. Thomson scattering from analytical plasmas. *Spectrochim. Acta Part B*, 57:201–241, 2002.

[145] J. Wesson. *Tokamaks.* Oxford Science publication, 2004.

[146] B. Wolf. *Handbook of Ion Sources.* CRC Press, 1995.

[147] D. Wünderlich, D. Dietrich, and U. Fantz. Application of a collisional radiative mode to atomic hydrogen for diagnostic purposes. *Journal of Quantitative Spectroscopy and Radiative Transfer*, 110(1):62–71, 2006.

[148] W. Yang, S. N. Averkin, A. V. Khrabrov, I. D. Kaganovich, Y.-N. Wang, S. Aleiferis, and P. Svarnas. Benchmarking and validation of global model code for negative hydrogen ion sources. *Phys. Plasmas*, 25:113509, 2018.

[149] L. Zhang and J. Ouyang. Microwaves Scattering by Underdense Inhomogeneous Plasma Column. *Plasma Science and Technology*, 18:267, 2016.

[150] V. Zhil'tsov, E. Klimenko, P. Kosarev, V. Kulygin, V. Platonov, N. Semashko, A. Skovoroda, V. Ukhov, and A. Mehed'kin. The development of a negative ion beam plasma neutralizer for ITER NBI. *Nuclear Fusion*, 40(3Y):509–513, mar 2000.

Acknowledgements/Remerciements

During my four year experience at the Swiss Plasma Center I had the chance to work in a stimulating environment surrounded by many scientifically outstanding people. I want to express my sincere gratitude to my supervisor, Prof. Ivo Furno, for his constant guidance during this academic journey, his powerful encouragement in pursuing the objectives and his strong commitment. My activities were also strongly supported by my co-supervisor, Dr. Alan Howling, for the patience in carefully correcting all my manuscripts, contributing to improve the quality of my work and for being always available to discuss any scientific issue.

Au cours de ma thèse j'ai eu la chance et l'honneur de travailler dans le group de plasma industriel, caractérisé par une ambience agréable, joyeuse et amusante. Pendant ces quatre années j'ai été entouré par des collègues et amis qui m'ont constamments soutenu et bien conseillé. J'aimerais remercier tout d'abord Rémy Jacquier pour son enorme support technique et aide precieux, sans son soutien au labo je n'aurais jamais été en mesure de mettre en place autant d'experiences sur le RAID. Je suis reconnaisant à Philippe Guittienne pour les innombrable discussions sur la physique des plasmas, son indispensable soutien dans les simulations numériques mais surtout pour sa constante disponibilité pour clarifier mes doutes et questions toujours avec bienveillance. Merci à Gennady pour sa façon speciale de contribuer à apporter le sourire dans le groupe et pour l'organisation quotidienne de la pause de midi et des tournois des fléchèttes. C'était aussi un très grand plaisir de collaborer avec les étudiants de master, en particulier une pensée de remerciement est dediée à Rita, Tristan et Basile. It was a pleasure to share the office with my facing neighbour Alexandra Waskow. Thank you for all the short breaks with funny discussions during our hard working times! Thanks Maurizio Giacomin for our frequent fruitful discussions on plasma modeling.

Je tiens à remercier l'atelier et bureau de construction pour avoir dessiné et usiné plusieurs composantes mechaniques qui m'ont permi de mettre en oeuvre nombreuses diagnostiques sur le RAID. Je remercie également la direction de l'SPC pour l'efficacité et le professionalisme.

Un pensiero speciale va alla mia famiglia, per l'affetto costante e incondizionato.

Lausanne, 17 avril 2020   R. A.

Riccardo Agnello

Curriculum Vitae

✆ *(+41) 789754352*
✆ *(+39) 3336732097*
✉ *riccardo.agnello@epfl.ch*

▬▬▬ Education

2016-2020	**Ph.D. in Physics**, *Swiss Plasma Center, Ecole Polytechnique Fédérale de Lausanne (EPFL), Lausanne, Switzerland*.
2015	**Master Degree in Physics**, *Università di Catania and Laboratori Nazionali di Fisica Nucleare (INFN), Catania, Italy*. Graduated with 110 cum laude/110
nov-dec 2014	**Internship**, *Department of Physics, Ohio State University, Columbus, USA*.
2009-2012	**Bachelor Degree in Physics**, *Dipartimento di Fisica, Università di Catania and Scuola Superiore di Catania, Catania, Italy*. Graduated with 110 cum laude/110

▬▬▬ Peer-reviewed publications

○ **R. Agnello**, S. Béchu, I. Furno, Ph. Guittienne, A.A. Howling, R. Jacquier, G. Plyushchev, M. Barbisan, R. Pasqualotto , I. Morgal and A. Simonin, *"Negative ion characterization in a helicon plasma source for fusion neutral beams by Cavity Ring-Down spectroscopy and Langmuir probe laser photodetachments"* Nucl. Fusion **60**, 026007 (2020).

○ **R. Agnello**, M. Barbisan, I. Furno, Ph. Guittienne, A. A. Howling, R. Jacquier, R. Pasqualotto, G. Plyushchev, Y. Andrebe, S. Béchu, I. Morgal and A. Simonin, *"Cavity Ring-Down Spectroscopy to measure negative ion density in a helicon plasma source for fusion neutral beams"* Rev. Sci. Instrum. **89**, 103504 (2018).

○ **R. Agnello**, Y. Andrebe, H. Arnichand, P. Blanchard, T. De Kerchove, I. Furno, A. A. Howling, R. Jacquier and A. Sublet *"Application of Thomson scattering to helicon plasma sources"*, Journal of Plasma Physics (submitted).

○ **R. Agnello**, I. Furno, A. A. Howling, , Ph. Guittienne, R. Jacquier *"Model and simulation of a hydrogen helicon plasma"* (in preparation).

○ Kamal M Ahmed, **Riccardo Agnello**, Stéphane Béchu, Gilles Cartry, H P L de Esch, Ivo Furno, Philippe Guittienne, Alan Howling, Rémy Jacquier, Iaroslav Morgal, Nader Sadeghi and Alain Simonin, *Magnetic field configurational study on a helicon-based plasma source for future neutral beam systems*, Plasma Sources Sci. Technol. 28 (2019) 095005 (14pp).

○ Ivo Furno, **Riccardo Agnello**, U. Fantz, Alan Howling, Rémy Jacquier, Claudio Marini, Gennady Plyushchev, Philippe Guittienne and Alain Simonin, *Helicon wave-generated plasmas for negative ion beams for fusion*, EPJ Web of Conferences 157, 03014 (2017).

○ R. Jacquier, **R. Agnello**, B. P. Duteil, C. Marini, P. Guittienne, A. Howling, Ivo Furno, G. Plyushchev, A. Simonin, I. Morgal, and S. Bechu, *First B-dot measurements in the RAID device, an alternative negative ion source for DEMO neutral beams*, Fusion Engineering and Design, March 2019.

○ D. S. Thompson, **R. Agnello**, I. Furno, A. Howling, R. Jacquier, G. Plyushchev and E. E. Scime, *Ion heating flows in a high power helicon source*, Phys. Plasmas 24, 063517 (2017).

- C. Marini, **R. Agnello**, B. P Duval, I. Furno, A. A, Howling, R. Jacquier, A.N. Karpushov, G. Plyushchev, K. Verhaegh, Ph. Guittienne, U. Fantz, D. Wünderlich, S. Béchu and A. Simonin, *Spectroscopic characterization of H2 and D2 helicon plasmas generated by a resonant antenna for neutral beam applications in fusion*, Nucl. Fusion 57, 036024 (2017).

- A. Simonin, **R. Agnello**, S. Béchu, J. M. Bernard, C. Blondel, J.P.Boeuf, D. Bresteau, G. Cartry, W. Chaibi, C. Drag, B. P. Duval, H P L de Esch, G Fubiani, I Furno, C Grand, Ph Guittienne, A Howling,R Jacquier, C Marini and I Morgal, *Negative ion source development for a photoneutralization based neutral beam system for future fusion fusion reactors*, New J. Phys. 18, 125005 (2016).

- G. Castro, D. Mascali, **R. Agnello**, L. Celona, O. Leonardi, L. Neri, D. Nicolosi, G. Torrisi, and S. Gammino *Experimental investigation of non-linear wave to plasma interaction in a quasi-flat magnetostatic field*, Rev. Sci. Instrum. 87, 02A507 (2016).

- G. Torrisi, D. Mascali, L. Neri, O. Leonardi, G. Sorbello, L. Celona, G. Castro, **R. Agnello**, A. Caruso, S. Passarello, A. Longhitano, T. Isernia, and S. Gammino, *Microwave frequency sweep interferometer for plasma density measurements in ECR ion sources: Design and preliminary results*, Rev. Sci. Instrum. 87, 02B909 (2016).

- D. Mascali, G. Torrisi, O. Leonardi, G. Sorbello, G. Castro, L. G. Celona, R. Miracoli, **R. Agnello**, and S. Gammino, *The first measurement of plasma density in an ECRIS-like device by means of frequency sweep microwave interferometer*, Rev. Sci. Instrum. 87, 095109 (2016).

Teaching experiences

2019 **Physique Générale I**, *EPFL*.
2017-2019 **Physique des Plasmas I**, *EPFL*.
2017 **Physique Générale I**, *EPFL*.
2016 **Laboratoire de Physique I**, *EPFL*.
2015 **Fisica Generale II**, *Mechanical Engineering, Università di Catania, Catania, Italy*.
2014 **Fisica Generale I**, *Mechanical Engineering, Università di Catania, Catania, Italy*.

Student (Co)-Supervision

2019 **Master thesis**, *Politecnico di Torino, R. Agus.*
2019 **Master thesis**, *EPFL, T. De Kerchove.*
2018 **Master thesis**, *EPFL, A. Lachat.*
2018 **Travail Pratique (TP4)**, *A. B. Pouradier.*
2017 **Travail Pratique (TP4)**, *A. Lachat.*
2017 **Travail Pratique (TP4)**, *D. Zullino.*
2016 **Travail Pratique (TP4)**, *A. Lachat.*

Languages

Italian, *Mother tongue.*
English, *Fluent - working language.*
French, *Fluent - working language.*
German, *Basic knowledge.*